2022

Across-Scale Energy Transfer In The Southern Ocean

Laur Ferris
William & Mary - Virginia Institute of Marine Science, lnferris@alum.mit.edu

Across-scale energy transfer in the Southern Ocean

A Dissertation

Presented to

The Faculty of the School of Marine Science

William & Mary

In Partial Fulfillment

of the Requirements for the Degree of

Doctor of Philosophy

by

Laur Ferris

January 2022

APPROVAL PAGE

This dissertation is submitted in partial fulfillment of

the requirements for the degree of

Doctor of Philosophy

Lauren [Laur] Newell Ferris

Approved by the Committee, December 2021

Donglai Gong, PhD
Committee Chair / Advisor
Virginia Institute of Marine Science - William & Mary
Gloucester Point, Virginia, United States

Louis St. Laurent, PhD
Applied Physics Laboratory - University of Washington
Seattle, Washington, United States

John M. Klinck, PhD
Center for Coastal Physical Oceanography - Old Dominion University
Norfolk, Virginia, United States

Alison M. Macdonald, PhD
Woods Hole Oceanographic Institution
Woods Hole, Massachusetts, United States

Marjorie A. M. Friedrichs, PhD
Virginia Institute of Marine Science - William & Mary
Gloucester Point, Virginia, United States

Carl T. Friedrichs, PhD
Virginia Institute of Marine Science - William & Mary
Gloucester Point, Virginia, United States

I dedicate this dissertation to the cousin squad (Byron, John, Will, Tyler, Chris, Justin, and Ben), my persistent source of motivation, amusement, and friendship.

TABLE OF CONTENTS

ACKNOWLEDGEMENTS……..……..……...vi

ABSTRACT……..…..……vii

CHAPTER 1: INTRODUCTION……2

CHAPTER 2: OCEAN_DATA_TOOLS: A MATLAB TOOLBOX FOR INTERACTING WITH BULK FREELY-AVAILABLE OCEANOGRAPHIC DATA……21

CHAPTER 3: ASSESSING SURFACE BOUNDARY LAYER SCALINGS OF SHEAR TURBULENCE IN THE HIGH-WIND SOUTHERN OCEAN USING DIRECT MEASUREMENTS…….……..26

CHAPTER 4: CONTAMINATION OF FINESCALE STRAIN ESTIMATES OF TURBULENT KINETIC ENERGY DISSIPATION BY FRONTAL PHYSICS…..…..…64

CHAPTER 5: SYMMETRIC INSTABILITY AS A MECHANISM FOR TOPOGRAPHICALLY-ENHANCED MIXING IN THE SOUTHERN OCEAN.……114

CHAPTER 6: CONCLUSION……166

BIBLIOGRAPHY…….……..175

TABLE OF ACRONYMS

AABW	Antarctic Bottom Water
AAIW	Antarctic Intermediate Water
ABI	ageostrophic baroclinic instability
ACC	Antarctic Circumpolar Current
AML	actively mixing layer
APE	available potential energy
APL-UW	Applied Physics Laboratory - University of Washington
AUSSOM	Autonomous Sampling of Southern Ocean Mixing
AUV	autonomous underwater vehicle
(B)CI	(barotropic) centrifugal instability
BLS	boundary layer scaling
CESM	Community Earth System Model
CCPO-ODU	Center for Coastal Physical Oceanography - Old Dominion University
CCSM	Community Climate System Model
CLIVAR	Climate Variability and Predictability Program
CROCO	Coastal and Regional Ocean Community Model
CSI	centrifugal-symmetric instability
CTD	conductivity, temperature, depth
DIMES	Diapycnal and Isopycnal Mixing Experiment
DNS	direct numerical simulation
EBF	Ekman buoyancy flux
ECMWF	European Centre for Medium-Range Weather Forecasts
EKE	eddy kinetic energy
ENSO	El Niño Southern Oscillation
FSI	forced symmetric instability
FSP	finescale strain parameterization
GI	gravitational instability
GM	Garrett-Munk
GSI	gravitational-symmetric instability
GSW	Gibbs-SeaWater
HRP	High Resolution Profiler
HYCOM	HYbrid Coordinate Ocean Model
IDW	Indian Deep Water
IW	internal wave

KPP	K-Profile Parameterization
(L)ADCP	(Lowered) Acoustic Doppler Current Profiler
LES	large eddy simulation
MLD	mixed layer depth
MLI	mixed layer instability
MITgcm	MIT General Circulation Model
MO	Monin-Obukhov
MOC	meridional overturning circulation
MOM3	Modular Ocean Model, version 5
NADW	North Atlantic Deep Water
NetCDF	Network Common Data Form
NI(W)	near-inertial (wave)
ODE	ordinary differential equation
OI	overturning instability
OSBL	ocean surface boundary layer
PDF	probability density function
PDW	Pacific Deep Water
PF	Polar Front
PV	potential vorticity
ROMS	Regional Ocean Modeling System
SACCF	Southern ACC Front
SAF	Subantarctic Front
SAMW	Subantarctic Mode Water
SI	symmetric instability
SIO	Scripps Institution of Oceanography
SMILES	Surface Mixed Layer Evolution at Submesoscales
SOFine	Southern Ocean Fine structure
SOSE	Southern Ocean State Estimate
SPURS	Salinity Processes in the Upper Ocean Regional Study
SSI	stratified shear instability
TEM	Transformed Eulerian Mean
TKE	turbulent kinetic energy
T/S	temperature-salinity
UAF	University of Alaska Fairbanks
UCDW	Upper Circumpolar Deep Water

VIMS	Virginia Institute of Marine Science
VMP	vertical microstructure profiler
WBP	wave breaking production
WHOI	Woods Hole Oceanographic Institution
WOCE	World Ocean Circulation Experiment

ACKNOWLEDGEMENTS

I came to work with Donglai Gong in 2016 and had no plans to stay and become an oceanographer. First and foremost I want to thank Donglai for bringing me into this purposeful rabbit hole, supporting my out-of-wheelhouse ideas, and shaping me into a scientist. Whether it be all-hours Slack conversations, scheming about ideas, or life advice, I couldn't have been luckier than to stumble into his lab five years ago and walk out with a mentor, colleague, and friend. This research and my development as a turbulent person would not be possible without Lou St. Laurent. I am grateful for the guidance, teaching me how to sarcasm, and unwavering enthusiasm for my spam a.k.a. plots, questions, and wonderings. I am not sure if he knew what he was getting himself into, but am indebted to him for adopting me as a turbulence student. I am grateful to John Klinck for single-handedly teaching me most of what I know about dynamics, answering my endless barrage of highly-specific questions, and providing invaluable insight on research. I am grateful to Alison Macdonald for teaching me what it means to be a seagoing oceanographer and for welcoming me into the WHOI community. I would like to thank Marjy and Carl for serving on my committee. Justin Shapiro was central to the production of this amazing dataset and this is not lost on me. His talent for all things gliders is something to strive for, and I thank him for sharing some of his wisdom. Similarly, I wish to thank Harper Simmons for his encouraging enthusiasm for my project and thoughtful production of the model data used in this dissertation; I excitedly look forward to working with Donglai, Harper, Lou, and Justin for many years to come. I wish to thank my dad (James Ferris) for the afternoon conversations and inspiration regarding all things scratch hunting. I thank my mom (Jennifer Ferris) for kayaking and hiking escapes, effervescent excitement about research travels, and providing a home for Turkey whilst at ocean. The rest of my family is also awesome, and I wish to thank Will Ferris, Caitlin King, Renee Newell, Kim & Eva, Newell & Richie cousins, Mike Rubino, Sophie, and Hedge House (Alison Bazylinski, Jack Conroy, Kate Bemis, Grace Molino, Schuyler Nardelli, Andrew Corso, Vanessa Strohm, Lexi, Turk). I am grateful for friends (Taylor Njaka, Amin Manna, Brett Buzzanga, Mar Arroyo, Nicole Cai, Fei Da, Qubin Qin, Marta Faulkner, Jackie Friedman). The tireless work of Linda Schaffner, Jen Hay, Cathy Cake, and John Griffin made my student experience delightful. The research was funded by NSF Award #1558639 (PIs St. Laurent & Merrifield). My time and computers were funded by VIMS Academic Studies, MARACOOS, Office of Naval Research, VIMS Ocean-Atmosphere & Climate Change Research Fund (Emeritus John Boon), and the VIMS Olsson Family Fellowship. I received at-sea training from US GO-SHIP, Oregon State University (OSU) Ocean Observatories Initiative, OSU Ocean Mixing Group. Finally, I thank WHOI Physical Oceanography for hosting me as a guest student.

ABSTRACT

Numerous physics are responsible for forward energy cascade at oceanic fronts but their roles are not fully clear. This dissertation investigates wind-sheared turbulence in the ocean surface boundary layer (OSBL), internal wave interactions in the ocean interior, and instability-driven turbulence in energetic jets; with attention paid to the parameterizations used to quantify them. At the OSBL, meteorological forcing injects turbulent kinetic energy (TKE), mixing the upper ocean and rapidly transforming its density structure. In the absence of direct observations or capability to resolve sub-grid scale turbulence in ocean models, the community relies on boundary layer scalings (BLS) of shear and convective turbulence to represent this mixing. Despite the importance of near-surface mixing, ubiquitous BLS representations of these processes have been under-assessed in high energy forcing regimes such as the Southern Ocean. Glider microstructure from AUSSOM (Autonomous Sampling of Southern Ocean Mixing), a long-duration glider mission, is leveraged to show BLS of shear turbulence exhibits a consistent bias in estimating TKE dissipation rates in the OSBL.

In the interior, finescale strain parameterization (FSP) of the TKE dissipation rate has become a widely used method for observing mixing, solving a coverage problem where only CTD profiles are available. However there are limitations in its application to intense frontal regions where adjacent warm/salty and cold/fresh waters create double diffusive instability. Direct turbulence measurements from DIMES (Diapycnal and Isopycnal Mixing Experiment in the Southern Ocean) and AUSSOM are used to show FSP can have biases of up to 8 orders of magnitude below the mixed layer when physics associated with T/S fronts are present. FSP often fails to produce reliable results in frontal zones where temperature-salinity (T/S) intrusive features contaminate the CTD strain spectrum, as well as where the aspect ratio of the internal wave spectrum is known to vary greatly with depth (as in the Southern Ocean). We propose that the FSP methodology be modified to include a density ratio-based data exclusion rule to avoid contamination by double diffusive instabilities in frontal zones.

At energetic frontal jets, symmetric instability (SI) has gained momentum for explaining enhanced turbulence. Submesoscale frontal instabilities are well-established by idealized analytical and numerical studies to be a significant source of TKE in the global ocean. However, observations of TKE dissipation enhanced by SI are few, and it is unknown to what order in the real ocean this process is active. AUSSOM measured elevated TKE dissipation rates throughout the core of the Polar Front (PF). Motivated by this finding, we use a 1-km Regional Ocean Modeling System hindcast to investigate the role of SI in energy cascade and Southern Ocean mixing. We extend popular overturning instability criteria for application to ageostrophic flows. SI of the centrifugal/inertial variety is widespread along the northern continental margins of the Antarctic Circumpolar Current due to topographic shearing of the anticyclonic side of PF-associated jets but is notably limited (above 1-km scale) to the mixed layer at open-ocean fronts. Contrarily, modeled velocity fields are strongly indicative of critical layers and other internal wave interactions dominating the open-ocean elevated TKE budget even at energetic fronts.

Across-scale energy transfer in the Southern Ocean

Chapter 1
Introduction

1. Introduction

A study called Autonomous Sampling of Southern Ocean Mixing (AUSSOM) was conducted in the Drake Passage region (Fig. 1) between the end of Austral Winter (November 2017) and the beginning of Austral Spring (February 2018). As part of this, a Slocum glider *Starbuck* with CTD and microstructure sensing was used to collect a 6-week turbulence record spanning 800 km from the Shackleton Fracture Zone to the Falkland Plateau. This dataset

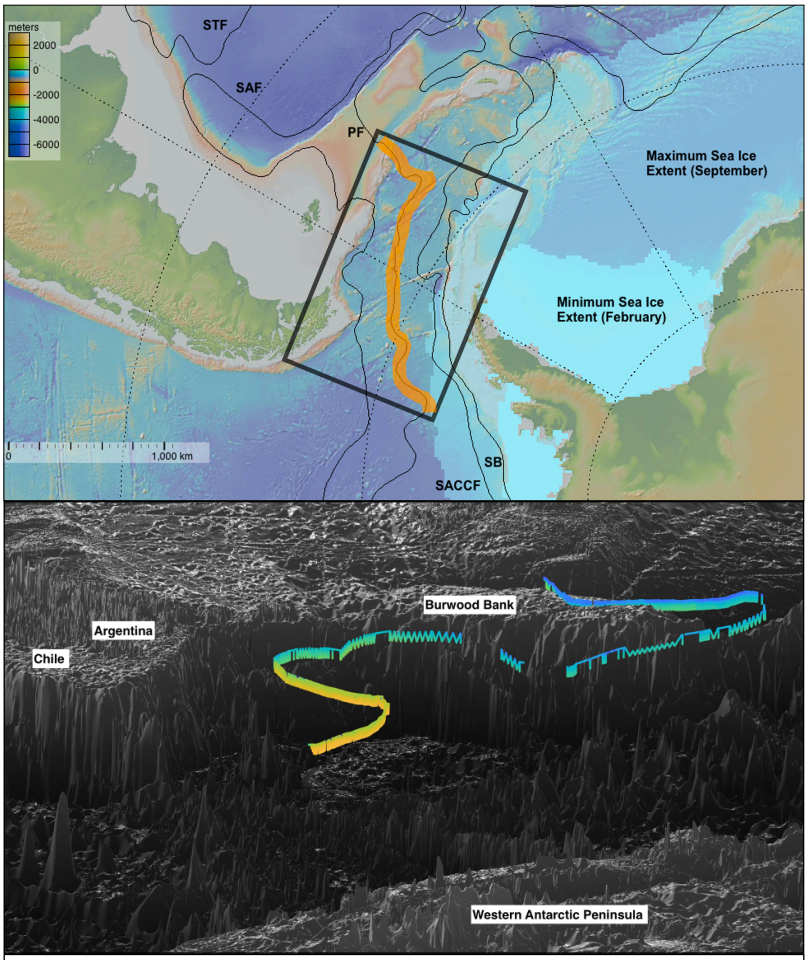

Figure 1: AUSSOM glider survey conducted in the Drake Passage region between end of Austral Winter (Nov. 2017) and beginning of Austral Spring (Feb. 2018). Upper: study region with location of inset (lower panel) and Polar Front in orange. Lower: glider-measured density. Prepared in GeoMapApp. Bathymetry from Smith & Sandwell Database (v. 18.1). Capriciously we open with the Orsi et al. (1995) representation of Southern Ocean fronts, which was in no way consistent with the Polar Front location during AUSSOM, because it emphasizes how little we know about the Antarctic Circumpolar Current and its structure.

was the launchpad for and opportunity to address questions in following dissertation. This research aims elucidate energetic pathways to turbulent mixing in the upper Southern Ocean through autonomous sampling, as well as set the stage for future community observation and model construction efforts.

Energetic forcing of the ocean happens at scale of internal tides and wind-generated near inertial (NI) internal waves. It is unknown exactly how energy transfers from the mesoscale to dissipative scale. Beneath the surface boundary layer in which wind stress drives the turbulent mixing, the widely accepted mechanism in the ocean interior is internal wave-wave interactions. There are other options such as wave-flow interactions, double diffusive instabilities, and baroclinic-symmetric instabilities. My dissertation aims to elucidate energy transfer across scales of the ocean. Understanding across-scale energy transfer is necessary for building ocean circulation models which accurately simulate upper ocean structure in energetic frontal regions on operational to climatic timescales. By quantifying the path to turbulence in several dynamical regimes using several parameterizations, we study different mechanisms of forward energy cascade and aim to provide new insight into this problem and where our abilities stand.

2. Background

2.1 Southern Ocean Closure of the Global Overturning Circulation

The mesoscale processes and turbulent mixing within the Southern Ocean play critical roles in global ocean circulation. As a major water mass component of the global overturning circulation, North Atlantic Deep Water (NADW) is formed in marginal seas at high latitude, flows southward, and upwells in the Southern Ocean. A large fraction of

this upwelled NADW is eventually modified on the continental shelves of the Ross Sea, Weddell Sea, and Adelie Coast to become the Antarctic Bottom Water (AABW). Remaining NADW diverges northward and combines with Indian and Pacific Deep Water (IDW/PDW) to become the upper return cell of the Atlantic meridional overturning circulation (MOC) (Talley, 2013).

Buoyancy forcing through air-sea exchange and interior mixing transforms NADW into Subantarctic Mode Water (SAMW) and Antarctic Intermediate Water (AAIW) (Abernathey et al., 2016). The Scotia Sea east of the Drake Passage is believed to be a critical site of SAMW and AAIW modification and subduction (Talley, 1996; Sallee et al., 2010). This Southern Ocean upwelling process is thought to be predominantly wind-driven quasi-adiabatic isopycnal upwelling (Talley, 2013) facilitated by wind stress. Mean eastward wind stress over the Southern Ocean causes a northward surface Ekman transport, while the curl of this wind stress creates a divergence—and thus downwelling (upwelling) north (south) of the wind stress maximum—in the Ekman transport that steepens Antarctic Circumpolar Current (ACC) isopycnals. The meridional equatorward temperature gradient helps to maintain this slope. While the northward Ekman transport generates an Eulerian overturning circulation (Eq. 1, term 2), baroclinic instability (where mesoscale eddies pinch off at density fronts) counteracts most of this circulation (Eq. 1, term 3). The remainder is a quasi-adiabatic, wind-forced residual circulation (Eq. 1, term 1) forming the high latitude segment of NADW-fed upper return cell of the MOC.

$$-f_0\overline{v}^* = \frac{\partial \tau}{\partial z} + \frac{\partial}{\partial z}\left(\frac{f_0\overline{v'b'}}{N^2}\right) \tag{1}$$

where f_0 is the f-plane Coriolis parameter, $\overline{v}^*$ is the residual meridional component of velocity (mean minus eddy-associated), τ is the kinematic wind stress, and $v'b'$ is the eddy-associated buoyancy flux. This residual circulation can be seen from Transformed Eulerian Mean (TEM) formulation (Vallis, 2019) of meridional steady momentum equation in the ACC, with large positive stress at the surface and seafloor. Meridional density gradient drives zonal geostrophic current (Eq. 2).

$$\phi = \frac{\delta p}{\rho_o}, \qquad b = -g\frac{\delta \rho}{\rho_o}, \qquad f u_g = -\frac{\partial \phi}{\partial y}, \qquad f\frac{\partial u_g}{\partial z} = -\frac{\partial b}{\partial y} \tag{2}$$

where ϕ is the kinematic pressure (omitting hydrostatic contribution), b is buoyancy, and u_g is geostrophic velocity.

While this paradigm of quasi-adiabatic upwelling is generally supported by numerical models (Thompson, 2008), the models do not have realistic mixing schemes and the role of ocean interior mixing on Southern Ocean dynamics is still poorly understood (Waterhouse et al., 2014). Furthermore, the relative importance of isopycnal versus diapycnal upwelling is unclear, and it is an area of active research (Tamsitt et al., 2017). Distinct from ocean gyres, the ACC lacks a full-depth western boundary. Shallower than the sill depth of the Drake Passage (~2000m), the ACC cannot support a zonal pressure gradient or meridional geostrophic current. In lieu of this, it is eddy flux that accomplishes meridional water mass transport and upwelling. The mesoscale eddies (~20km), generated by baroclinic instabilities, mediate transfer of momentum between

the surface (wind stress) and underlying topography (bottom form stress). These eddies are concentrated along zonal fronts, which coincide with potential vorticity gradients (Thompson, 2008) and deep-reaching geostrophic flow. Potential energy is released from the water column when eddies are pinched off at density fronts and decay (Ferrari & Wunsch, 2009; Marshall & Speer, 2012). Accurate estimate of the eddy fluxes requires characterization of eddy dynamics down to submesoscale.

2.2 Southern Ocean Vertical Transport: Inhomogeneous and Unconstrained

The locations and mechanisms for eddy-mediated diapycnal upwelling and downwelling in the Southern Ocean remain open research questions. The regional distribution of upwelling is inhomogeneous, with enhanced activity mediated by site-specific flow-eddy-topography interactions (Adams et al., 2017). The site-specific dynamics of upwelling depend on water mass transformation processes operating at both the meso- and the submesoscale. Critically, the vertical profile of eddy diffusivity in relation to water mass distribution determines where diapycnal upwelling/downwelling in the water column occurs. Using the MITgcm simulation of south Indian ACC, Rosso et al. (2015) found that topographically influenced submesoscale features in the ACC are

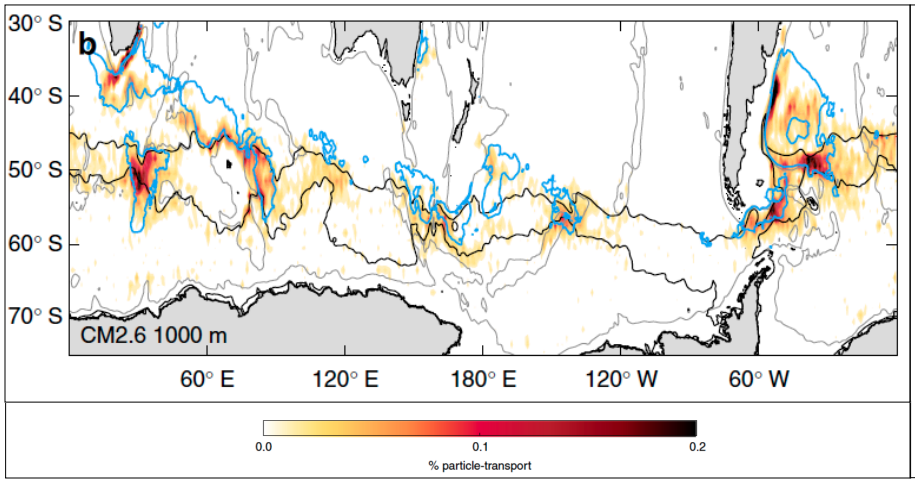

Figure 2: Upwelling hotspots in the ACC from Tamsitt et al. (2017). Showing percentage of particle transport crossing 1000m in each grid cell in the CM2.6 model between release at 30ºS and arrival in mixed layer at high latitude. Mean EKE higher than 75 cm^2 s^{-2} are indicated by blue contours.

generated indirectly, primarily as mesoscale eddies and meanders which subsequently destabilize into smaller length scales. In a Lagrangian tracer study, Tamsitt et al. (2017) used particle tracking numerical models (CESM, CM2.6, and SOSE) to find the locations of concentrated upwelling, identifying five major topographic features within the ACC that have high eddy kinetic energy (EKE). The EKE hotspot east of the Drake Passage (54-60°S, 69-35°W) is simulated to have a disproportionately critical role in Southern Ocean upwelling (Fig. 2, green). However, this hotspot has never been observed at a resolution sufficient to resolve submesoscale features and linking them to mesoscale dynamics.

2.3 Fronts of the Antarctic Circumpolar Current

As the site of the only deep-reaching geostrophic current that flows completely around Earth, the ACC's over 100 Sv transport is the junction between the Pacific, Atlantic, and Indian Oceans. Direct Pacific-Atlantic and Pacific-Indian transports outside of the ACC are 1 Sv and 10-15 Sv, respectively (Talley, 2011). Water masses are formed, modified, and exported northward from this junction. Central to this system are ACC fronts. Fronts in the ACC are water mass boundaries which demarcate abrupt changes in T/S relation, while an ACC jet (Fig. 3a) is a strong zonal geostrophic current (and region of concentrated eddying). While the popular Orsi et al. (1995) depiction (Fig. 1a) is useful, it is important to note that ACC fronts are collections of filaments (Fig. 3b) rather than contiguous barriers. While there is much support that ACC jets are primarily constrained by topography and wind stress, planetary control has alternatively been suggested as the source of the current's zonation (Naveira Garabato et al., 2001).

Major fronts include the Southern ACC Front (SACCF), Polar Front (PF), and Subantarctic Front (SAF). The SAF is the northern edge of the ACC and is the Upper Circumpolar Deep Water (UCDW)-SAMW/AAIW front. Here a thick layer of SAWM overlies low-salinity Antarctic Intermediate Water. Further south the PF is demarcated by abrupt changes in sea surface temperature and the subduction of Antarctic Surface Water beneath SAMW. The SACCF is the southern edge of the ACC. The zone between SAF-PF is prone to interleaving between warms/saline waters north of SAF to isothermal T/S curve south of PF.

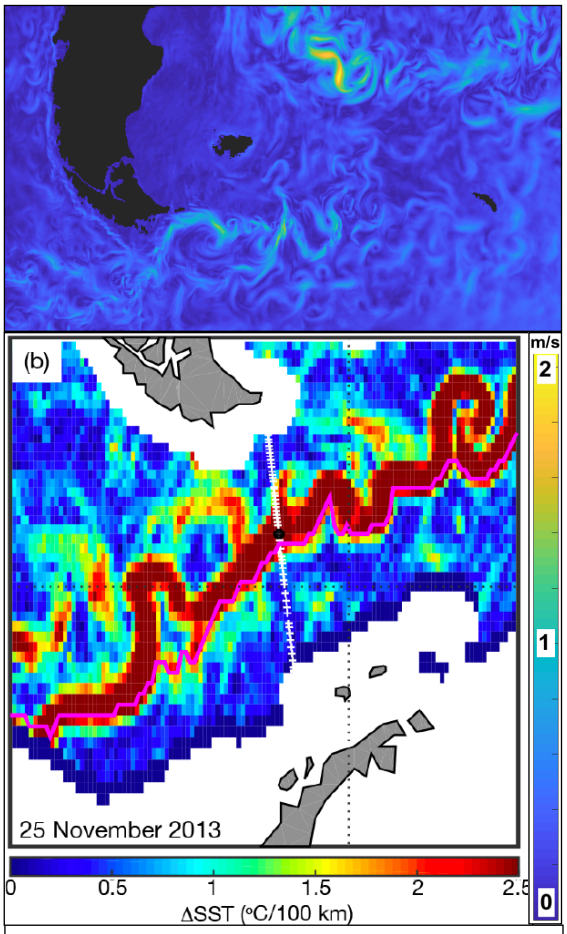

Figure 3: Fronts and jets. Showing (a) Jets in surface energetic flow in the Western Scotia Sea region, generated from GOFS 3.1: 41-layer HYCOM + NCODA Global 1/12° Analysis. (b) a weekly Polar Front location identified using SST gradient algorithm (magenta line) and XBT (black dot). White pixels from quality control measures. From Freeman & Lovenduski (2016).

These fronts augment modification and mixing of water masses in the Southern Ocean. The circumpolar outcropping of isopycnals means horizontal juxtaposition of water masses with contrasting T/S relationships, which predisposes them to unique mixing mechanisms. The region around the PF is predisposed to interleaving and intrusive mixing because there are warm/salty subantarctic waters north of the PF and

cold/fresh Southern Ocean waters south of the PF (Merrifield et al., 2016). The density ratio favors salt fingering north of the PF and in the frontal region, and diffusive convection south of the PF. The phenomenology of turbulent mixing varies in different environments, and sometimes an identical eddy, heat, and salt diffusivity is used in models which can be problematic for representing double-diffusive mixing mechanisms. Overall, intrusive processes are especially important source of enhanced dissipation at intermediate depth and should be accounted for in large-scale ocean models. Understanding of double diffusive mechanisms and lesser understood mechanisms of mesoscale turbulence are both critical for representing water mass transformation and thus MOC in models (e.g. the correct diffusivity profiles).

2.4 Topographic Enhancement of Energetic Mixing & Eddies

The Southern Ocean is populated with mesoscale eddies and Scotia Sea is an eddy generation hotspot (Fig. 4, green circle). Many ACC eddies are beneath a threshold length scale of $L = 2\pi R_d$ and will drive a forward energy cascade (Scott & Wang, 2005; Ferrari & Wunsch, 2009; McWilliams, 2016). There are a two well-known ways for mesoscale eddies to lose energy: (1) energy loss to frontal instability and frontogenesis in the surface layer (D'Asaro et al., 2011), (2) energy loss to bottom friction and dissipation of internal waves in the bottom boundary layer (Munk & Wunsch, 1998). However, the reality of Southern Ocean energy cascade is more complicated. Due to weak stratification, large injection of kinetic energy, and the absence of continuous zonal jets, the Southern Ocean is highly influenced by topographic interaction in addition to geostrophic turbulence (Ferrari & Wunsch, 2009). Deep flow impinging on topography

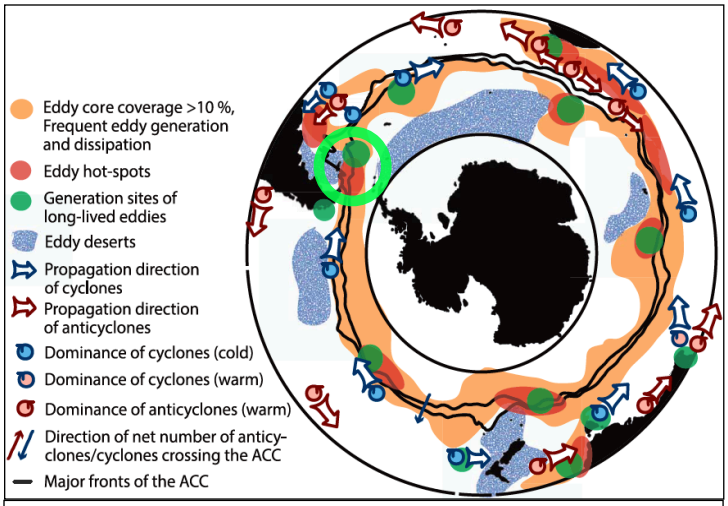

Figure 4: Spatial description of eddies >50km in the Southern Ocean. Based on satellite AVISO altimetry and identification using the Okubo-Weiss parameter (OW), which is a metric of the dominance of vorticity over strain. From Frenger et al. (2015).

will generate internal lee waves, which can break mid-water column at critical layers causing enhanced turbulent mixing (Ferrari & Wunsch, 2009; Nikurashin et al. 2014). Observation of turbulent mixing in and around a mesoscale eddy shows that turbulent dissipation is enhanced on the edge and lower in the middle of the eddy suggestive of critical layer interactions while internal wave energy fluxes from above and below the eddy are reflected (Sheen et al., 2015). In short, topographic interaction interferes with intersecting flow to produce a complex energy cascade from EKE to turbulent dissipation. The exact dynamics of the coupling between mesoscale eddies and turbulent dissipation remains poorly observed and understood (Naveira Garabato et al., 2004).

Turbulent kinetic energy may dissipate at the site of internal wave generation (via wave breaking) or internal waves may propagate energy away from the site of generation, dissipating at continental margins (Waterhouse et al., 2014). An important result of this is that, away from continental margins, the measured turbulent energy dissipation rate is a "floor" value for the local generation and mixing. Vertical eddy diffusivity of density $K_\rho = \Gamma\epsilon/\overline{N}^2$ can be estimated using a measured turbulent dissipation rate and an

assumed efficiency factor Γ (which relates removal of energy by buoyancy forced to shear production of turbulent TKE; Thorpe, 2005). It follows that observed rates of both turbulent dissipation ϵ and diapycnal diffusivity K, are elevated in regions of enhanced mixing. Usually $\Gamma = 0.2$ is used for the efficiency factor but this assumption does not hold for regimes that are not 3-D isotropic small-scale turbulence. Double diffusive instability carries extra consideration when interpreting turbulent mixing because most general parameterizations assume small-scale isotropic turbulence. Salt fingering, for example, requires less energy per diapycnal transfer of properties; it has a much higher efficiency factor (Γ) than 0.2 and thus converts more kinetic energy to potential energy than small-scale turbulence.

2.5 Upper Ocean Mixing Dynamics in the Southern Ocean

Most energy for turbulent mixing in the surface mixed layer comes from buoyancy flux (convection) and wind stress (breaking surface gravity waves and Langmuir circulation) (Mackinnon et al., 2013). In addition to directly driving turbulent dissipation in the actively mixing layer, wind stress generates near-inertial (NI) motions which modulate the base of the mixed layer, sending NI internal waves into the interior ocean (Mackinnon et al., 2013). However, internal waves are limited to frequencies between the Coriolis frequency and the stratification frequency $f \leq \omega \leq N$, where $N^2 = -(g/\rho_o)(d\rho/dz)$. A sharp upper thermocline (characterized by maximum N) can act as a barrier, decoupling the water column into two layers for near-inertial frequency waves (Cushman-Roisin & Beckers, 2011). Convective engulfment of thermocline waters and entrainment by shear instabilities are active at the base of the mixed layer. Less than

5% of 65 TW imparted to the surface ocean by wind makes it into the interior (Mackinnon et al., 2013), but considering slightly less than 2.1 TW (corresponding to $1 \times 10^{-4} m^2\ s^{-1}$ average density diffusivity) is required to maintain the MOC (i.e., to allow deep water to rise to the isopycnal levels at which Ekman transport in the Southern Ocean takes effect) this is amount is extremely significant.

Relevant processes that drive mixing and energy transfer in the main thermocline include double-diffusive convection and interleaving/layering, shear-driven instabilities (e.g. Kelvin-Helmholtz), internal wave-eddy interactions (e.g. strain of mesoscale features trapping internal waves, critical layers), and internal wave-wave interactions. Internal waves interact with each other (presumably in the universal manner of the Garrett-Munk spectrum, [Garrett & Munk, 1972; 1975]) until they break and relinquish their energy as turbulent dissipation. This forward cascade to smaller scales is carried out between interactions between three internal waves with summatively resonant wavenumbers and frequencies (Hasselmann's theorem).

Baroclinic frontal instability converts available potential energy (APE) from sharp horizontal buoyancy gradients to eddy kinetic energy (EKE); where wind stress opposing an along-front flow can further destratify the frontal region, enhancing diapycnal mixing (D'Asaro et al., 2011; Thomas et al., 2013; Mackinnon et al., 2013). Along-front wind stress causes an Ekman advective transport of buoyancy that further destratifies PF regions by pushing dense water over less dense water, enhancing baroclinic instability. The water mass structure of the Polar Front is also susceptible to double-diffusive mixing

regimes; which are more efficient at transferring salinity, as well as kinetic energy to potential energy, than 3D isotropic turbulence (Schmitt, 1994).

2.6 Controls on deep ocean mixing: Fronts and Terrain

Flow-bathymetry interaction and deep ocean mixing are key factors in driving the dynamics of topography-enhanced upwelling in the ACC. Microstructure measurements of turbulence in the ACC are sparse. St. Laurent et al. (2012) conducted microstructure measurements of turbulent energy dissipation rate in the Drake Passage (Fig. 5, left panel), as part of the Diapycnal and Isopycnal Mixing Experiment (DIMES). Turbulent dissipation was enhanced by two orders of magnitude to O(10^{-8}) W kg^{-1} upwards through 1000m depth along the SACCF, PF, and SAF; compared to O(10^{-10}) W kg^{-1} outside of frontal regions. In addition to the speed and depth of incident flow, the terrain of underlying bathymetry influences enhancement of turbulent mixing and upwelling. Turbulent diffusivity is enhanced over rough topography and abrupt isolated ridges in the

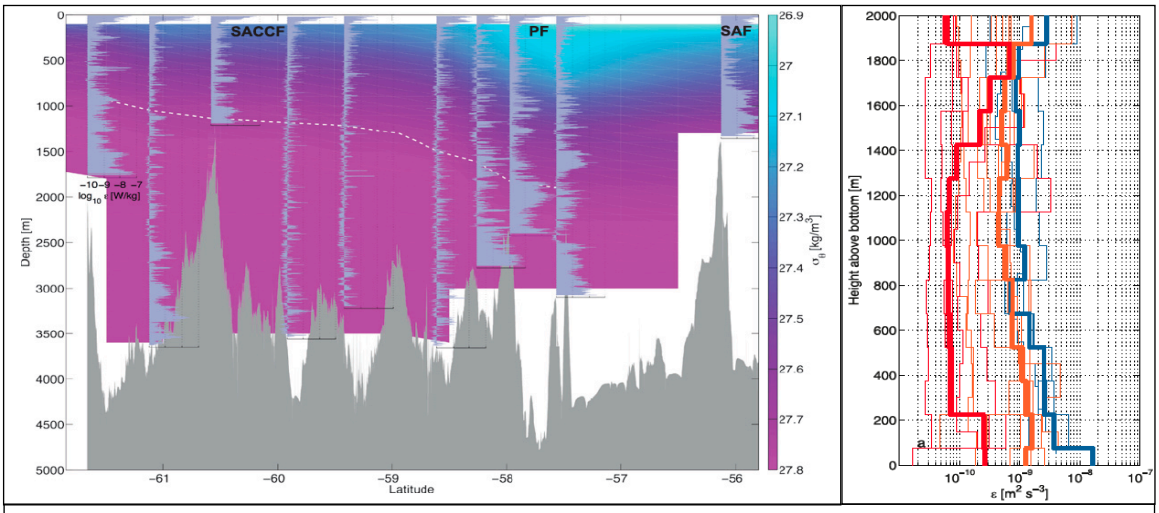

Figure 5: Turbulence enhanced by ACC fronts and rough topography. **(left)** Microstructure measurements of turbulent dissipation (10^{-10} to 10^{-7} W kg^{-1} log scale) from DIMES Phoenix Ridge transect; note enhancement at ACC fronts. From St. Laurent et al. (2012). **(right)** Turbulent dissipation from global microstructure profiles sorted into smooth (red), rough (orange), and ridge (blue) topography. From Waterhouse et al. (2014).

abyssal ocean (Polzin et al., 1997; Waterhouse et al., 2014). The geometry of these features is important. Turbulent dissipation in abyssal mixing is enhanced over ridge crests and bathymetric slopes but not valleys (Ledwell et al., 2000; Naveira Garabato et al., 2004). Waterhouse et al. (2014) compiled 5200 global microstructure profiles over various topography and found that enhanced dissipation and diapycnal diffusivity reach far into the water column (Fig. 5, right panel) over rough topography and ridges. In a general sense, enhanced turbulent mixing is likely controlled by (1) incident flow, (2) bathymetry, and (3) geometry of topographic features.

3. Data Acquisition

A glider-based sensor package for making direct turbulence measurement is the Rockland MicroRider (Fig. 6a) which was used for AUSSOM, the core dataset of this dissertation. The processes of measuring turbulence from a glider will be briefly explained now. The rate of kinetic energy loss through viscosity is given by (Eq. 3):

$$\epsilon = \frac{\nu}{2}\langle s_{ij}s_{ij}\rangle \text{ where } s_{ij} = \begin{pmatrix} s_{11} & s_{12} & s_{13} \\ s_{21} & s_{22} & s_{23} \\ s_{31} & s_{32} & s_{33} \end{pmatrix} \text{ and } s_{12} = \left(\frac{\partial u_1}{\partial x_2} + \frac{\partial u_2}{\partial x_1}\right) \tag{3}$$

where ϵ is turbulent kinetic energy dissipation rate [W/kg], ν is the molecular kinematic viscosity of water [1×10^{-6}m^{2}s^{-1}], s_{ij} is the shear tensor, $\partial u_i/\partial x_j$ are velocity fluctuations (Fig. 6b). Direct measurement of turbulence from a free fall platform assumes isotropy, which allows (Eq. 3) to be approximated as (Eq. 4):

$$\epsilon = \frac{15}{2}\nu\left\langle (du'/dz')^2 \right\rangle \text{ where } \frac{du'}{dz'} = \frac{\partial u'}{\partial t}\frac{\partial t}{\partial z'} = \frac{\partial u'}{\partial t}\frac{1}{V} \tag{4a}$$

$$V = \frac{W}{\sin(\phi + \alpha)} \tag{4b}$$

Above z' is the coordinate aligned with the shear probes and u' is the water velocity component normal to z' measured by the shear probes. When using this package knowing the velocity of the instrument through the water (V) is critical for measuring turbulent dissipation. It is possible to calculate vertical glider speed using a flight model (Merckelbach et al., 2019), but the pressure-derived vertical velocity (W) is a close

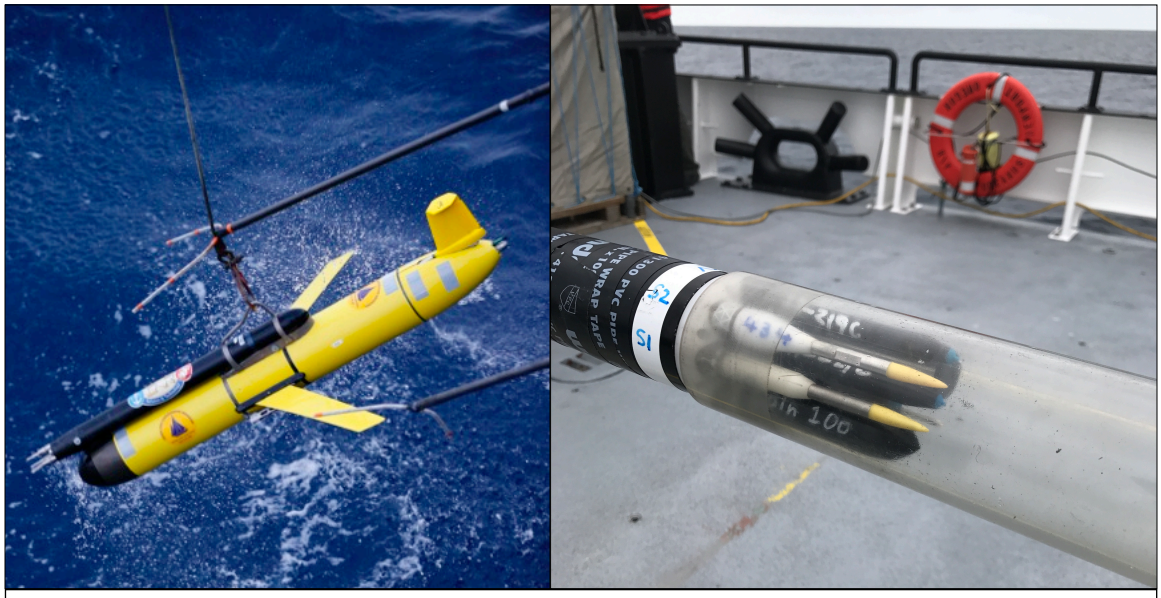

Figure 6: (a) Slocum glider *Starbuck* with a Rockland MicroRider. (b) An example of shear probes on the OSU Ocean Mixing Group's Chameleon microstructure profiler (Pijuana et al., 2018).

enough fit (Fer et al., 2014). Glider speed V is calculated using the vertical velocity W and trigonometry of glide angle (Eq. 4b), where glide angle is the sum of pitch angle ϕ and the angle of attack α (St. Laurent & Merrifield, 2017). Due to the resolution limit of the shear probe being larger than the Kolmogorov length scale, spectral estimates of the spatial gradients (measured by the probe) are referenced to the Nasmyth spectrum (Fig. 7)

(Lueck et al., 2016) for quality control and integrated to obtain the bracketed term in (Eq. 4a).

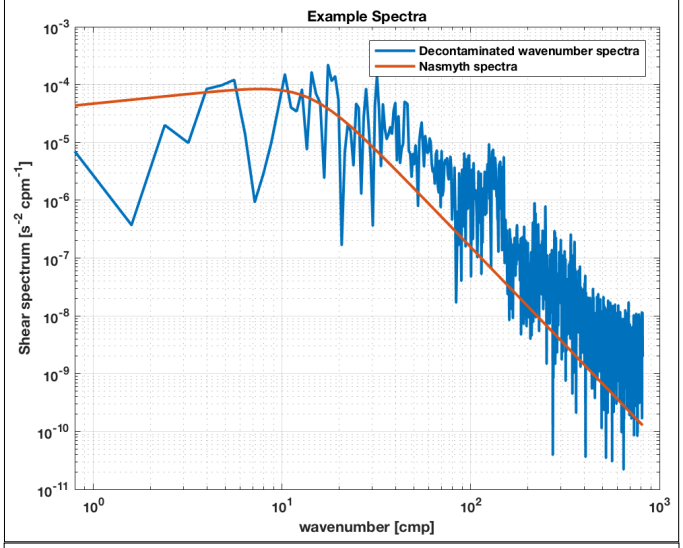

Figure 7: Example shear spectrum from AUSSOM.

4. Motivation

A high-value target for the ocean physics, climate, and naval communities alike is the prospect of constraining both global and regional values for turbulent kinetic energy (TKE) dissipation rate and diapycnal diffusivity (Waterhouse et al., 2014) such that ocean circulation models can be built with or calibrated against realistic representations of mixing. Aside from global patterns of mixing which impact prediction of the climate timescale, poorly understood energetic events such as storms and intense frontal regions are both regimes that have traditionally been challenging for numerical ocean models to predict ocean dynamics on the operational timescale. Models as they stand are limited by existing commonly-used turbulence closure schemes, which generally implement interior mixing when shear instability produces an unstable flow state as diagnosed by Richardson number. These schemes can only represent the physical processes which they have been constructed to represent, and are generally unaware of elevated mixing efficiency by wave breaking, Langmuir circulation, frontal instabilities, and other special mechanisms. Kinetic energy can cascade to a smaller scale through interactions with internal waves or participate in submesoscale instabilities which can

happen when certain arrangements of buoyancy and velocity gradient are present and are more common at sharp fronts. These instabilities are not represented in most hydrostatic ocean models; their significance is their ability to release KE at sub-grid scale, providing an energy source for mixing and creating an ocean state that is potentially different from the state that was numerically predicted. A baseline understanding of the physical processes contributing to the TKE budget in polar frontal regions is necessary to develop the skill of circulation models in these unique but important environments.

In the absence of adequate availability of true microstructure measurements, a question is if — and to what extent — alternative parameterizations of TKE dissipation rate (which leverage more easily-acquired data such as wind speed, buoyancy flux, or density) can be used to fill these knowledge gaps. These parameterizations are not physical laws; rather, they are mathematical expressions derived through simplification of the Navier-Stokes equations, empirically, or some combination thereof. Two such parameterizations for TKE dissipation rate are boundary layer similarity scaling (BLS) in the surface ocean (Chapter 3) and strain-based finescale parameterization (FSP) in the ocean interior (Chapter 4). A recent and notable effort to apply FSP to elucidate global

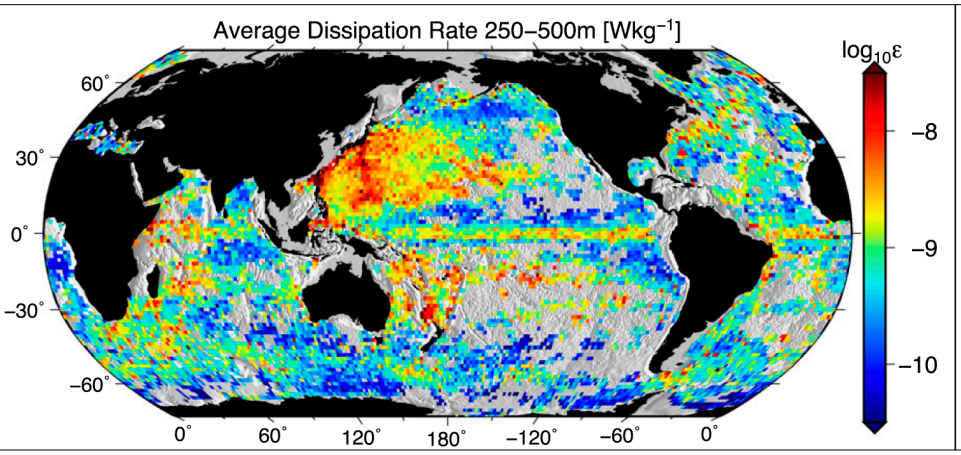

Figure 8: 1.5° climatological average TKE dissipation rates (ϵ) estimated from Argo profiles using strain-based finescale parameterization, from Whalen et al. (2015).

patterns of mixing was Whalen et al. (2015)'s TKE dissipation maps constructed from the global Argo array (Fig. 8). The scope of these results and their inevitable usage gives an urgency to understanding FSP-estimated TKE dissipation rate and how it relates to energy contained by the true rate of TKE dissipation at the microscale.

5. Outline

This dissertation reflects the coordination of different data sources to study forward energy cascade, turbulence, and its parameterizations. Expediting this coordination are clean, reusable tools to efficiently format and analyze different data sources. Chapter 2 presents a new open-source MATLAB toolbox for processing and manipulating freely-available oceanographic data sources. I include it in this dissertation to underscore the utility of community-managed software tools. Oceanographers should ideally produce software tools as if they were destined to be used and maintained by others. While our community more or less functions in small units, sharing useful (but globally redundant) scripts and tools within laboratories, departments, or informal alliances; production quality code is probably a gateway to exponentially increasing the connectivity and pace of ocean physics.

The subsequent three chapters investigate energetic pathways to turbulent mixing in the Antarctic Circumpolar Current and surrounding Southern Ocean as an archetype (but also nuance) for mixing in energetic frontal zones. Each chapter has a guiding high-level guiding question:

- Chapter 3: Correctable bias in surface boundary layer scalings of shear turbulence in the Southern Ocean

How does energy transfer between the atmosphere and interior ocean in the Polar Front and does it match our law-of-the-wall understanding?

- Chapter 4: Contamination of finescale strain estimates of turbulent kinetic energy dissipation by frontal physics

How realistic is assumption that energy in internal wave field smoothly transfers to turbulent dissipation in the Southern Ocean?

- Chapter 5: Roles of internal waves and frontal instability in downscale energy transfer in Antarctic Circumpolar Current jets

Which processes are responsible for energy transfer into the microscale in the Antarctic Circumpolar Current?

Chapter 3 examines the transfer of TKE into the surface of the ocean, the ubiquitous parametric representations we use to calculate it, and the physical assumptions which make these representations vulnerable. It combines microstructure measurements from a novel glider program called Autonomous Sampling of Southern Ocean Mixing (AUSSOM) with satellite-derived meteorological data to test "law of the wall" surface boundary layer scalings of shear turbulence, which are believed to hold in all wind-dominated regions and seasons of the global ocean when accepting a rigid boundary paradigm.

Chapter 4 explores the transfer of energy through the ocean; namely the connection between kinetic energy at the oceanic finescale and oceanic microscale, and critically examines the use of strain-based finescale parameterizations of TKE dissipation in regions with intense frontal structure such as all major geostrophic currents. It

leverages microstructure data and CTD collected though DIMES US5, AUSSOM, and the Argo program to demonstrate that front-associated physics contaminate finescale strain estimates of TKE dissipation. It explores the consequences of assuming a Garrett-Munk internal wave spectrum as well as technical challenges associated with estimating mixing rates from the global Argo array as a solution to poor microstructure coverage.

Chapter 5 addresses physical processes that fall outside our paradigm of across-scale energy transfer driven primarily by internal wave-wave collisions — frontal instabilities as well as interactions between internal waves and the background flow of the Antarctic Circumpolar Current. It combines observations from AUSSOM with a simulation produced using the Regional Ocean Modeling System (ROMS) to connect dynamics at the mesoscale (and submesoscale) to TKE dissipation at the microscale.

The collection of research presented in this dissertation blends data from several platforms and scales to elucidate the physics driving forward energy cascade and upper ocean structure in energetic frontal regions, identify vulnerabilities of the parameterizations currently used to represent these physics, and inform the construction of future numerical ocean models which aim to simulate the submesoscale and smaller. While principally based in the Antarctic Circumpolar Current, the relevancy of its findings extend to energetic currents around the world.

Chapter 2
ocean_data_tools: A MATLAB toolbox for interacting with bulk freely-available oceanographic data

1. Statement of Need

`ocean_data_tools` simplifies the process of extracting, formatting, and visualizing freely-available oceanographic data. A wealth of oceanographic data (from research cruises, autonomous floats, global ocean models, etc.) are accessible online. However, many oceanographers and environmental scientists (particularly those from subdisciplines not accustomed to working with large datasets) can be dissuaded from utilizing these data because of the overhead associated with determining how to batch download data and format them into easily-manipulable data structures. `ocean_data_tools` solves this problem by allowing the user to transform common oceanographic data sources into uniform structure arrays, call general functions on these structure arrays, perform custom calculations, and make graphics.

2. Summary

Structure arrays, the common currency of `ocean_data_tools`, are more user-friendly than the native data storage underlying many of the datasets because they allow the user to neatly group related data of any type or size into containers called fields. Both the structure array and its fields are mutable, and data is directly visible and accessible in the Matlab workspace (unlike NetCDF which requires a function call to read variables).

Matlab was chosen as the language of choice for this toolbox because it is already extensively used within the oceanographic community. It is also a primary language for much of the community, which is important because this toolbox aims to lower the barrier to entry for using the growing variety of freely-available field- and model-derived oceanographic datasets. The workflow of ocean_data_tools is to build uniform structure arrays (e.g. `argo`, `cruise`, `hycom`, `mercator`, `woa`, `wod`) from raw datasets and call

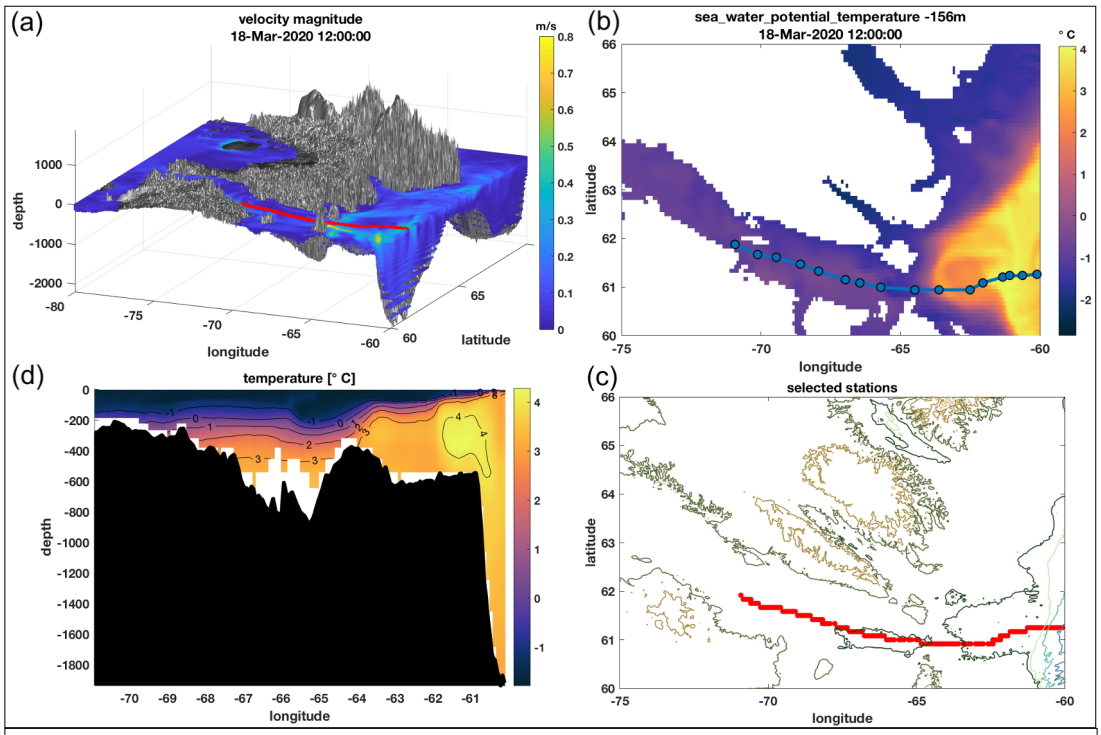

Figure 1: Building a virtual cruise from the Operational Mercator global ocean analysis and forecast system at 1/12 degree with 3D bathymetry (Smith & Sandwell, 1997). Showing (a) a 3D velocity plot created using `model_domain_plot`, (b) virtual cruise selection using `transect_select`, and `model_build_profiles`, (c) coordinates of the resulting uniform structure array, and (d) a temperature section plotted using `general_section` with `bathymetry_section`. Three of the subplots use colormaps from `cmocean` (Thyng, Greene, Hetland, Zimmerle, & DiMarco, 2016).

general functions on these structure arrays to map, subset, or plot. Functions with the `\_build` suffix load raw data into uniform structure arrays. Structure arrays are compatible with all `general_` functions, and serve to neatly contain the data for use

with custom user-defined calculations or other toolboxes such as the commonly-used Gibbs-SeaWater (GSW) Oceanographic Toolbox (McDougall & Barker, 2011). One application of the `\_build` feature is to create virtual cruises from model output Fig. 1. The user draws transects on a map (or passes coordinates as an argument) to build vertical profiles from model data. This may be used as a cruise planning tool, to facilitate comparison of observations with model output, or to support decision-making in

Table 1: Current ocean_data_tools data sources.

Data Source	DOI, Product Code, or Link
Argo floats	doi:10.17882/42182
Smith & Sandwell bathymetry	doi:10.1126/science.277.5334.1956
IOOS Glider DAC	https://gliders.ioos.us/
MOCHA Climatology	doi:10.7282/T3XW4N4M
HYbrid Coordinate Ocean Model	https://hycom.org
CMEMS Global Ocean 1/12° Physics Analysis and Forecast	GLOBAL_ANALYSIS_FORECAST_PHY_001_024
GO-SHIP hydrographic cruises	https://www.go-ship.org/
World Ocean Atlas 2018	https://www.ncei.noaa.gov/products/world-ocean-atlas
World Ocean Database	https://www.ncei.noaa.gov/products/world-ocean-database

underwater glider piloting (using model forecasts to inform ballasting or adjust flight for ocean currents). Some `ocean_data_tools` functions employ `nctoolbox` (Schlining, Signell, & Crosby, 2009).

There are several high-quality ocean and/or climate related Matlab toolboxes such as Climate Data Toolbox for Matlab (Greene et al., 2019), those part of SEA-MAT: Matlab Tools for Oceanographic Analysis, and Gibbs-SeaWater (GSW) Oceanographic Toolbox (McDougall & Barker, 2011). However, there are no other documented and designed-to-be-shared toolboxes filling the same data exploration niche as this one.

`ocean_data_tools` is unique in encouraging the user to invoke a variety of freely-available data into their exploration and does not expect the user to provide privately-collected measurements or privately-generated model output. It connects users to specific, well-documented data sources (Table 1). `ocean_data_tools` has already been used for data exploration in support of scientific publications (Bemis et al., 2020; Crear et al., 2020). This toolbox is built for extensibility; the objective is to welcome contributors and continuously add support for additional datasets such as Remote Sensing Systems products and European Centre for Medium-Range Weather Forecasts (ECMWF) products. The source code for `ocean_data_tools` has been archived to Zenodo with the linked DOI: Ferris (2020).

Acknowledgements

The Virginia Institute of Marine Science (VIMS) provided financial support for this project. I am grateful to Donglai Gong for ongoing mentorship. I thank the many organizations providing freely-available data to the oceanography community including (but not limited to) Argo, the HYCOM consortium, the Copernicus Programme, the International Global Ship-based Hydrographic Investigations Program (GO-SHIP), and the National Oceanic and Atmospheric Administration (NOAA). I also thank the two reviewers for helpful feedback, especially Kelly Kearney for her insightful suggestions. The figure was generated using E.U. Copernicus Marine Service Information. This paper is Contribution No.3960 of the Virginia Institute of Marine Science, William & Mary.

Endnotes

The full text of this chapter is published as: *Ferris, L., (2020). ocean_data_tools: A MATLAB toolbox for interacting with bulk freely-available oceanographic data. Journal of Open Source Software, 5(54), 2497. https://doi.org/10.21105/joss.02497*

Chapter 3
Assessing surface boundary layer scalings of shear turbulence in the high-wind Southern Ocean using direct measurements

Abstract

The ocean surface boundary layer is a gateway of energy transfer into the ocean. Wind shear and meteorologically-forced convection inject turbulent kinetic energy into the surface boundary layer, mixing the upper ocean and transforming its density structure. In the absence of direct observations or the capability to resolve sub-grid scale 3D turbulence in operational ocean models, the oceanography community relies on surface boundary layer similarity scalings (BLS) of shear and convective turbulence, based on "law of the wall" relationships, to represent this mixing. Despite their importance, near-surface mixing processes, and ubiquitous BLS representations of these processes, have been under-sampled and under-assessed in high energy forcing regimes such as the Southern Ocean. With the maturing of autonomous sampling platforms, there is now an opportunity to collect high-resolution spatial and temporal measurements in the full range of forcing conditions. Here we leverage the results of the first long-duration glider microstructure survey of the Southern Ocean to show that BLS of shear turbulence exhibit a significant but correctable bias, underestimating (overestimating) turbulent

dissipation rates in the shallower (deeper) parts of the surface boundary layer, and are applicable in medium to strong wind forcing conditions.

Introduction

The surface boundary layer is the gateway for heat, momentum, and gas transfer between the atmosphere and interior ocean. Turbulent kinetic energy (TKE) injected into the upper ocean boundary layer, together with the surface buoyancy flux, directly affects the depth of mixing, controls water mass transformation, and mixes water to increase potential energy of the upper ocean structure (at the expense of TKE). As the only sector of the global ocean that connects all three major ocean basins through the meridional overturning circulation (MOC), the Southern Ocean is an especially important site of water mass transformation. Much of the energy for turbulent mixing in the surface mixed layer comes from shear flow, buoyancy flux (convection), and wind stress (breaking surface gravity waves and Langmuir circulation) (Mackinnon et al., 2013). Buoyancy forcing through air-sea exchange and interior mixing driven by internal waves transforms North Atlantic Deep Water (NADW) first into Subantarctic Mode Water (SAMW) and eventually into Antarctic Intermediate Water (AAIW) (Abernathey et al., 2016). The Scotia Sea east of the Drake Passage is believed to be a critical site of SAMW and AAIW modification and subduction (Talley, 1996; Sallee et al., 2010), but little is known about the formation of these water masses. Despite its importance, mixing processes in the Southern Ocean have been under-sampled, largely due to its remote location and severe conditions.

An autonomous glider program called Autonomous Sampling of Southern Ocean Mixing (AUSSOM) was conducted in the Drake Passage region between the end of Austral Winter and the beginning of Austral Spring in 2017-1018. AUSSOM represents the first extended glider deployment in the Drake Passage region of the ACC (Fig. 1) and is the longest continuous glider microstructure record ever collected. Unlike shipboard

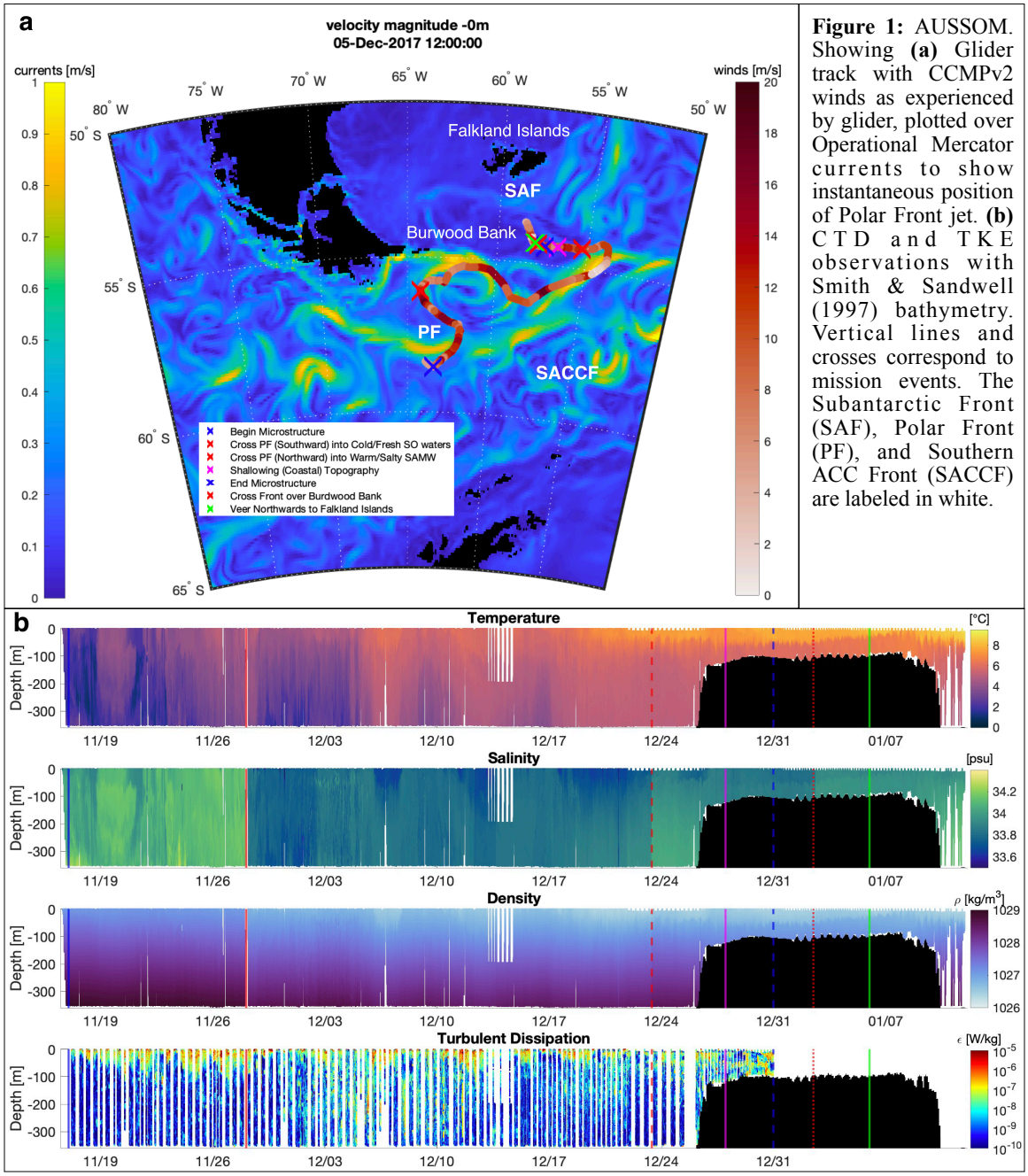

Figure 1: AUSSOM. Showing **(a)** Glider track with CCMPv2 winds as experienced by glider, plotted over Operational Mercator currents to show instantaneous position of Polar Front jet. **(b)** CTD and TKE observations with Smith & Sandwell (1997) bathymetry. Vertical lines and crosses correspond to mission events. The Subantarctic Front (SAF), Polar Front (PF), and Southern ACC Front (SACCF) are labeled in white.

methods, gliders remain deployed for months at a time sampling though all sea states, thus it is a first opportunity to understand turbulent dissipation rate and mixing variations in the Polar Front (PF) of the Southern Ocean though a full range of atmospheric forcing conditions. The high spatial resolution and temporal extent of this dataset is also an opportunity to understand the performance of boundary layer similarity scaling (BLS) through the full range of meteorological forcing.

We rely on similarity scaling to estimate surface boundary layer turbulence in a variety of observational, analytical, and modeling pursuits; operational models such as HYCOM and ROMS utilize similarity scaling embedded in K-Profile Parameterization (KPP) mixing algorithms (Monin & Obukhov, 1954; Large et al., 1994). Turbulence parameterizations based on law-of-the-wall BLS are common in models (Umlauf et al., 2005), as well as analytical and observational studies. BLS leverages fundamental results for fluid behavior at a boundary to estimate the turbulent dissipation caused by shear and convective forcing at the boundary. Just outside the region closest to the boundary where viscous effects dominate (the viscous sublayer), there exists a logarithmic layer (or inertial sublayer) in which the turbulence budget is a first-order balance between shear production, dissipation, and buoyancy. The equation describing this TKE budget (assuming that locally the ocean is in steady state such that TKE per unit volume is constant) is given in horizontally homogenous form by

$$0 = -\frac{1}{\rho_0}\frac{\partial}{\partial z}\langle wp' \rangle + \nu \frac{\partial^2}{\partial z^2} e - \langle uw \rangle \frac{dU}{dz} - \epsilon - \frac{g}{\rho_0}\langle \rho' w \rangle - \frac{\partial}{\partial z}\langle we \rangle \qquad \text{(Eq. 1)}$$

where u, v, and w are turbulent velocity components, p' is the pressure fluctuation, $\langle _ \rangle$are averages, ν is kinematic viscosity, $e = (u^2 + v^2 + w^2)/2$, dU/dz is vertical shear of the mean flow, ϵ is TKE dissipation rate, g is gravity, and $\rho' \approx -\rho_0(\alpha T' - \beta S')$ is the density fluctuation due to temperature and salinity fluctuations T' and S'. The terms on the right-hand side are (1) work of pressure fluctuations, (2) viscous divergence of TKE, (3) shear production, (4) dissipation, (5) buoyancy production, and (6) divergence of vertical transport. Terms 3-5 dominate the balance in all cases such that the first terms 1-2 are generally neglected. Term 6 is zero in the absence of additional vertical transport of TKE.

In the real ocean surface boundary layer, there is addition production due to Stokes drift (U_s) and shear is not necessarily aligned with the momentum flux $\langle uw \rangle$ such that more correct theoretical representation of (Eq. 2a) is:

$$\epsilon = -\langle uw \rangle \, (dU/dz) \cos \mathrm{A} - \langle uw \rangle \, (dU_S/dz) \cos \mathrm{B} - g\langle \rho' w \rangle \qquad \text{(Eq. 2a)}$$

where $-\langle uw \rangle < u_*^2$ decreases nearly linearly from the surface, and angles A and B are the wind direction relative to the shear. Angles A and B are rarely both near zero, and A can exceed 90 degrees in some real ocean conditions due to varying wind direction, such that energy is extracted. However, there is no validated method for obtaining the shear of the Stokes drift (dU_s/dz), the angles, and $\langle uw \rangle$ from observations, limiting their usage beyond analytical and modeling applications.

For practical application of BLS, examining the shear production term (term 3 of Eq. 1), the mean vertical rate of transfer of horizontal momentum in the x direction by fluctuations in vertical velocity is assumed to be constant (Thorpe, 2005) and it is

dominated by fluctuations in velocity rather than density such that Reynolds stress in the logarithmic layer is also assumed to be constant $\tau/\rho_0 = -\langle uw \rangle$ and the shear-dominated simplification of (Eq. 1) is:

$$\epsilon = (\tau/\rho_0) dU/dz \qquad \text{(Eq. 2b)}$$

Friction velocity (of the *water* at the boundary) is given by $u_* = \sqrt{\tau/\rho_0}$ where τ is wind stress and ρ_0 is water density at the surface. In light of the assumption that viscous effects are negligible in the logarithmic layer, dimensional grounds demand $dU/dz = u_*/kz$ where $k = 0.41$ is von Karman's constant. Substituting into (Eq. 2b) gives the principal equation for BLS of shear turbulence

$$\epsilon = u_*^3/kz \qquad \text{(Eq. 3a)}$$

In conditions where ϵ is driven by the wave field and Stokes drift, and the user has a full menu of state variables from which to derive the necessary terms (such as in a modeling application) a useful alternative equation is:

$$\epsilon = -\langle uw \rangle \left(\frac{u_*}{k} \right) F(U_S) F(z) \cos A - \langle uw \rangle \left(\frac{dU_S}{dz} \right) \cos B - g \langle \rho' w \rangle + WBP \qquad \text{(Eq. 3b)}$$

where added to (Eq. 2a) is the effect of surface gravity waves to reduce the shear by a function of the Stokes drift $F(U_S)$ (Large, et al. 2019), there is wave breaking production (WBP), and the Reynolds stress is a none-constant function of depth $F(z)$.

In the presence of convection induced by buoyancy flux, (Eq. 3a) is adapted to include the effects of buoyancy flux (J_b). One such adaptation (Lombardo & Gregg, 1989) based on similarity scaling of the atmospheric boundary layer is given in Table 1, where buoyancy production is represented as a constant function of surface flux

Table 1. Boundary layer similarity scaling (Lombardo & Gregg, 1989)

Buoyancy flux sign	Depth ratio	Scaling	Profiles of 932	Regime
$J_b < 0$		$\epsilon \approx u_*^3/kz$	700	Wind-Dominated
$0 < J_b$	$AML/L_{MO} < 1$		218	
	$1 < AML/L_{MO} < 10$	$\epsilon \approx 1.76u_*^3/kz + 0.58J_b$	7	Intermediate
	$10 < AML/L_{MO}$	$\epsilon \approx J_b$	0	Convection-Dominated
	No AML identified		7	

$cJ_b = -g\langle\rho' w\rangle$. It is piecewise, neglecting either wind shear or convection as determined by the ratio between the vertical extent of the actively mixing layer (AML) (the layer of active turbulence) and the Monin-Obukhov length scale L_{MO} (the depth at which the effects of wind shear are equivalent to convection in turbulent flows). L_{MO}, which is negative in destabilizing conditions, describes the scale inside of which turbulence generated by wind shear dominates that generated by convection.

We reconsider two key assumptions of the logarithmic layer paradigm. The first assumption is that Reynolds stress within the logarithmic layer is approximately equal to surface wind stress (Kundu, 1990). Momentum flux is principally balanced by this Reynolds stress and depends on the relative fluid velocity between water and interface (Newman, 2018). We know this assumption breaks down when there is substantial momentum transport into the breaking surface gravity wave field (Agrawal et al., 1992; Thorpe, 2005). The second assumption of BLS is that shear production, convection, and turbulent dissipation dominate the turbulent kinetic energy equation (Eq. 1). While wind shear and convection are assumed to dominate the near-surface turbulence budget, other

dynamics could impact turbulent dissipation in an intense frontal region such as the Polar Front. These other dynamics are ignored because they are rarer and/or their TKE contributions are smaller near the surface boundary of the ocean.

We assume that energy transfer from mesoscale-and-larger forcing to the dissipative scale is principally accomplished by wind shear and convection in the surface boundary layer, and internal wave-wave interactions (elastic scattering, induced diffusion, parametric instability) in the interior ocean. There are several other processes through which it is physically possible for energy to enter the microscale; these are not included in BLS, and their potential impacts will be revisited in Discussion. Convective engulfment of thermocline waters and entrainment by shear instabilities (e.g. Holmboe instabilities or Kelvin-Helmholtz billows) are active at the bottom of the mixed layer and important for communicating heat and momentum between the atmosphere and interior ocean (Thorpe, 2005). Other processes include wave-driven mixing (Langmuir cells and wave breaking processes), wave-flow interactions (critical layers), double diffusive instabilities (which are more efficient transferring kinetic energy to potential energy than 3D isotropic turbulence; Schmitt, 1994), and baroclinic-symmetric instabilities (Thomas et al., 2013; Smyth & Carpenter, 2019). Langmuir circulation develops when a horizontal perturbation in the downwind stress causes unequal stress on the surface of the ocean, causing horizontal vorticity (vorticity vector normal to surface). Stokes drift further imparts a vertical vorticity (vorticity vector parallel to wind direction) generating Langmuir circulation cells, which converge at areas of maximum horizontal perturbation, causing downward flow. Turbulence is observed to be enhanced below Langmuir

suspected downwelling, due to either the advection of turbulence generation by breaking surface waves or the circulation itself. Aside from mixing the surface layer, Langmuir circulation serves to deepen or undulate the mixed layer (Thorpe, 2004; MacKinnon et al., 2013).

Waves are known play a significant role in contributing to the near-surface TKE budget, increasing TKE dissipation rate when energy transfers from surface waves to turbulence through wave breaking and other wave-enhanced turbulence. Sutherland et al. (2013) found TKE dissipation rates to be consistent with law-of-the-wall boundary layer scaling of shear turbulence, but noticed some individual profiles also scaled with the Stokes shear. D'Asaro et al. (2014) studied the effects of surface wave by comparing inferred turbulence (from the square root of the average of the squared vertical velocity) in a low-wave lake with that in a high-wave ocean; concluding that waves Stokes drift and not breaking could explain the difference (such that attention should be focused on the parameterization of Langmuir turbulence). Sutherland et al. (2014) used direct measurements from an air-sea interaction profiler to find that TKE dissipation rate is inversely proportional with the Langmuir number (La) squared. Sutherland et al. (2016) observed a diurnally intensified, wind-driven jet in the subtropical Atlantic during the SPURS (Salinity Processes in the Upper Ocean Regional Study) project to find that diurnal increase in stratification restricts vertical diffusion of wind stress and depth of momentum flux, increasing near-surface shear instability (an additional source of near-surface TKE). Lacking wave measurements, we focus on law-of-the-wall boundary layer scaling of shear turbulence (Large et al., 1994) and do not aim to partition TKE sources.

Fox-Kemper et al. (in press) provide a comprehensive review of MO theory and current theoretical understanding about surface wave effects. A research topic is whether wave effects are already included in MO theory, based on the wind stress which generates waves. Fox-Kemper et al. (in press) note that systematic inconsistencies arise when wind waves deviate in direction from the wind stress itself or propagate from a nonlocal generation site. An issue of wave effects is that they decay with depth due to the decay of wave orbital velocity. Near-surface mixing is a combination of convective, wind shear, and wave (e.g., non-breaking and Langmuir forcing) effects (Fox-Kemper et al., in press).

Observations of turbulent dissipation are globally sparse (Waterhouse et al., 2014) and climate model Southern Oceans are believed to exhibit large biases in mixed layer depth (e.g. CESM; CCSM, Danabasoglu et al., 2012). Testing boundary layer scalings using atmospheric forcing against direct turbulence measurements in AUSSOM will have broad impacts for our understanding of Southern Ocean climate, as well as how surface boundary layer turbulence is built into numerical models. This study focuses on the surface AML and its parameterization to assess the extent to which BLS can be used to estimate upper ocean mixing across the full range of wind forcing, and is the first step in a larger effort to combine BLS with satellite data products to provide a time-varying estimate of upper ocean mixing in the Southern Ocean. AML depth can change on a faster (~20m/hr) timescale than the mixed layer depth (MLD). Whereas the AML is defined by elevated turbulent dissipation, the MLD is defined by homogenous density (Fig. 2). Turbulence of the AML is the kinetic energy source which homogenizes the water column via diffusivity of density ($K_\rho = \Gamma\langle\epsilon\rangle/\overline{N^2}$) and produces a mixed layer,

where Γ is the efficiency factor. Understanding the physical processes and associated parameterizations for turbulent mixing in the surface mixed layer is critical for (1) understanding energy transfer into the mixed layer, (2) improving OSBL flux schemes embedded in circulation models, and (3) expanding turbulence estimations to satellite platforms.

2. Methods

A Teledyne Webb Research Slocum glider equipped with a Rockland Scientific MicroRider was used to collect a 6-week record of upper-ocean turbulence spanning 800 km from the Shackleton Fracture Zone to the Falkland Plateau. This glider-based methodology of measuring turbulence is well-documented in published literature (Fer et al., 2014; St Laurent & Merrifield, 2017; Zippel et al., 2021). The glider was deployed at 58°S, 64°W at the southern edge of the Polar Front (PF) on November 16th, 2017 from the R/V Laurence M. Gould, conducted 82-day mission in the PF, sampled for 60 days until sensing disabled to preserve battery, and was recovered near Port Stanley, Falkland Islands on February 5th, 2018. The dataset is one of the largest microstructure datasets ever collected, totaling over 3028 CTD profiles and 932 microstructure profiles from 0-350 meters (approximately 300,000 meters of microstructure profiles in 60 days). For context, DIMES (Diapycnal and Isopycnal Mixing Experiment in the Southern Ocean) collected 800,000 meters of profiles over 5 years, 8 cruises, and 1 year of ship time. It is likely the most ever microstructure collected by a single instrument system. To address key questions, we implement BLS, compare to glider microstructure, and determine the bias associated with applying BLS estimates of mixing to the high-wind Southern Ocean.

In the absence of direct meteorological measurements, we harness satellite data for records of meteorological forcing. Latent and sensible heat fluxes are from the SeaFlux CDR dataset (Clayson & Brown, 2016). The buoyancy flux is calculated from SeaFlux turbulent fluxes, SST (Version 5 MW OISST Product from REMSS), salinity (Copernicus product Global SSS/SSD L4 Processor V1.1), precipitation (GPCP V1.3 Daily Rainfall), and surface radiation flux (CERES_SYN1deg_Ed4A) using

$$J_b = g\left[\frac{\alpha}{\rho c_p} Q_{tot} + \beta S_o (E - P)\right] \quad \text{(Eq. 4)}$$

where α and β are the expansion coefficients for heat and salinity, c_p is the specific heat of seawater, Q_{tot} is the total (sensible and latent) heat flux, S_o is surface salinity, E is the evaporation rate, and P is precipitation. Friction velocity (u_*) is computed from surface radiation flux (CERES_SYN1deg_Ed4A), winds (CCMPv2), near-surface specific humidity (from SeaFlux CDR), near-surface temperature (from SeaFlux CDR), and SST (from SeaFLUX CDR) using the COARE Met Flux Algorithm v3.5 (Edson et al., 2013). Windsea significant wave height (H_s) is obtained from the Copernicus Global Ocean Waves Multi Year product, which is a global wave reanalysis on a 1/5° grid, at a 3-hourly temporal resolution.

The MicroRider, a glider-based sensor package for making direct turbulence measurements, was used for AUSSOM. In general, direct measurement of turbulence from a free fall platform assumes 3-D isotropy, which allows viscous dissipation (ϵ) of turbulent kinetic energy to be approximated by

$$\epsilon = 15/2\nu\langle(du'/dz')^2\rangle \quad \text{(Eq. 5)}$$

where z' is the coordinate aligned with the shear probes, u' is the water velocity component normal to z', and $du'/dz' = (\partial u'/\partial t)(\partial t/\partial z') = (\partial u'/\partial t)V$. Here ν is the molecular kinematic viscosity of water [~10^{-6}m^{2}s^{-1}] and $\partial u'/\partial t$ are velocity fluctuations measured by the shear probes. When using any package, velocity of the instrument through the water (V) is required to calculate turbulent dissipation. Glider microstructure differs from free-fall microstructure in that the velocity of shear probes through the water is not the same as its fall rate. It is possible to calculate vertical glider speed using a flight model (Merckelbach et al., 2019), but the pressure-derived vertical velocity W is sufficiently accurate for this application (Fer et al., 2014). The velocity [m/s] of the glider through the water $V = W/\sin(\phi + \alpha)$ is calculated using the vertical component of that velocity and glide angle, where glide angle is the sum of pitch angle (ϕ) and the angle of attack (α) (St. Laurent & Merrifield, 2017). Vertical eddy diffusivity of density $K_\rho = \Gamma\langle\epsilon\rangle/\overline{N^2}$ is estimated using measured turbulent dissipation rate (ϵ), buoyancy frequency (N) calculated from CTD using adiabatic leveling, and an assumed efficiency factor of $\Gamma = 0.2$.

A metric of AML is necessary to understand where BLS applies, as well as to facilitate depth normalization and temporal averaging of turbulent dissipation. With over 900 microstructure profiles, AML identification is completed using a simple algorithm. The steps for each microstructure profile are to: (a) Find the depth at which a log-linear fit of surface (upper 100 meters) falls to an empirically determined background $\epsilon = 10^{-8}$ W/kg (Fig. 2d). (b) Discard obviously wrong fits using automatic checks. (c) Interpolate good AML depths. A critical step in the process is excluding enhanced turbulence at

depth that is unrelated to direct surface (wind or buoyancy) forcing; restricting polynomial fitting to the upper 100m—empirically selected to focus on surface-forced turbulence—avoids mixing events that are unrelated to surface boundary layer physics

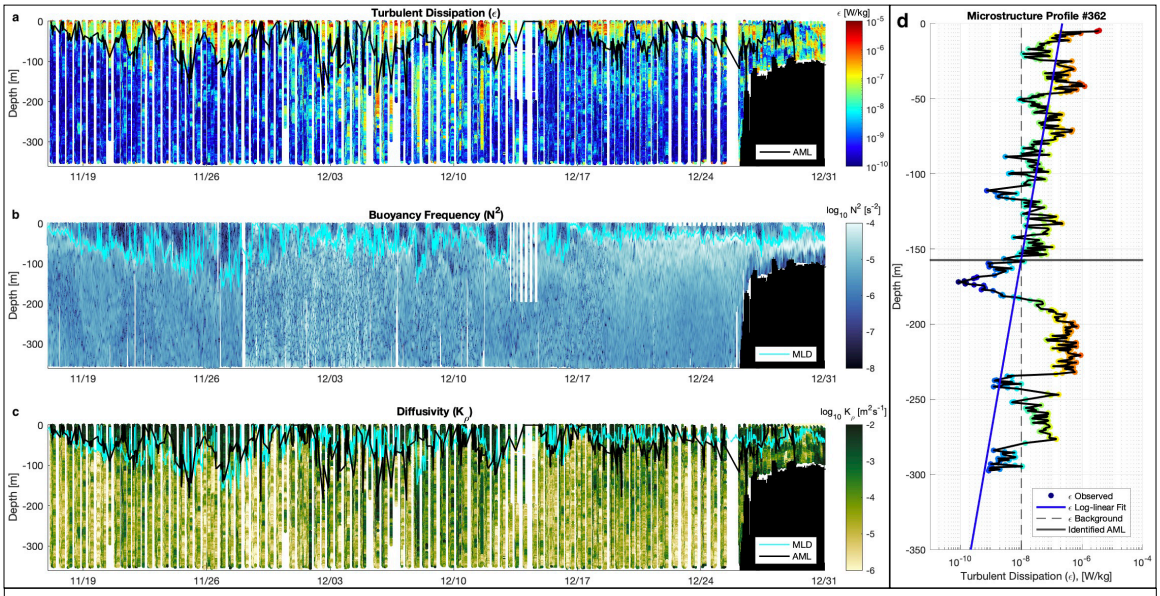

Figure 2: Mixing sections. Showing **(a)** turbulent dissipation with actively mixing layer (AML) depth, **(b)** buoyancy frequency with mixed layer depth (MLD), **(c)** diffusivity with AML and MLD, and **(d)** a case of AML identification using log-linear fit.

(e.g. internal wave and forward cascade). To be clear, while the polynomial coefficients are determined from data in the the upper 100m the resulting fit is allowed to extend below this depth. The result is a working AML depth dataset that avoids deep (e.g. internal wave-related) mixing (Fig 2a). For comparison, MLD is from glider CTD using a surface-density difference criterion of $\Delta\rho = 0.03$ kg/m^3 and $\Delta T = 0.2°$ C, where the two estimates of MLD are compared for sensitivity and shallower estimate is generally used (Dong et al., 2008). The algorithm effectively tracks the base of the mixing layer over time (Fig. 2b). The MLD is not the equivalent to the AML, but there are order-of-magnitude close (such that MLD might be used as a coarse proxy for AML).

Two versions of boundary layer similarity scaling (BLS) are implemented (Fig. 4). The standard version (using COARE variables) applies the full wind and buoyancy flux scaling (Table 1) using u_* and J_b. Upon inspection (Fig. 3) it is clear that our study is almost entirely wind dominated (with less than 1% of cases invoking buoyancy flux into BLS) such that we can neglect convection. As a matter of intrigue, we also implemented a simplified version of BLS using solely u_* interpolated from CCMPv2, the easily-

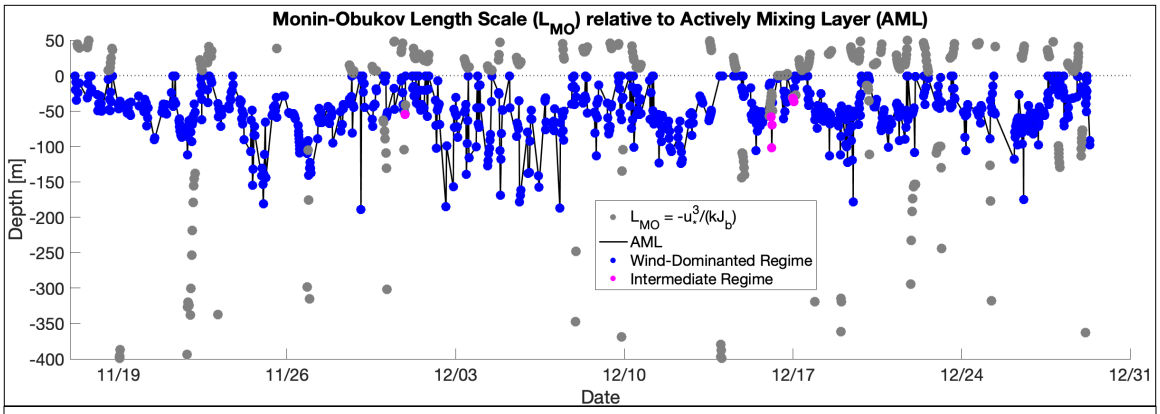

Figure 3: Monin-Obukhov length scale (L_{MO}) in comparison to the actively mixing layer (AML).

accessible wind product available from Remote Sensing Systems (http://www.remss.com/). With close agreement, the reader may consider for themself (Fig. 4b, 4d) whether it might be appropriate to just apply this simplified version of BLS in wind-dominated situations. However, the rest of our paper uses the standard version of BLS.

Individual microstructure and synchronous BLS profiles were also integrated (Eq. 6) to obtain the dissipated power associated with the observations and scaled estimates (Fig. 4d).

$$\Phi = \int_{z_{AML}}^{z_{min}} \rho \epsilon dz \qquad \text{(Eq. 6)}$$

Turbulence observations and estimates were temporally averaged prior to calculating the observed bias in BLS, $\log_{10}(\epsilon_{BLS}/\epsilon)$. Because the timescale of mixing events is shorter than the temporal resolution (6 hours) of the CCMPv2 wind data, it is not meaningful to compare individual microstructure profiles to wind-based BLS profiles; rather profiles must be averaged over some timescale to produce useful comparison. Averaging intervals must be long enough that the wind product adequately represents mean turbulent dissipation, and there are enough microstructure instances available for averaging, but short enough that comparisons assess the strength of BLS over a range of conditions. The inertial period is used as the averaging interval. Finally, polynomial fits are used to generate two variations of bias function (a curve fit and a probability density function).

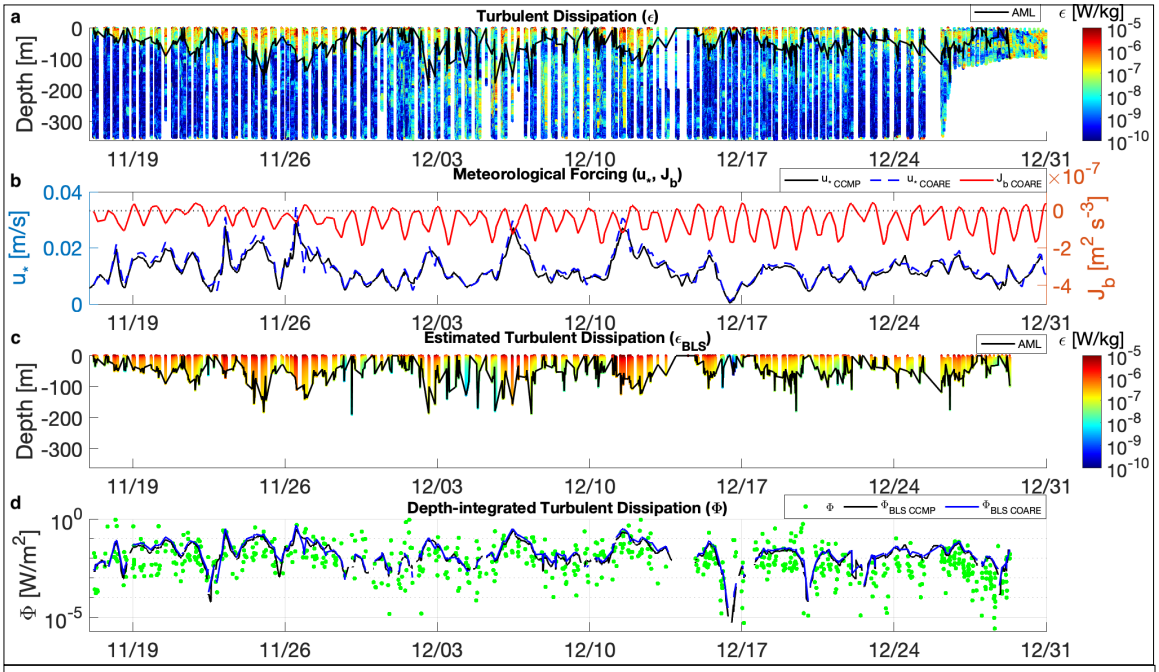

Figure 4: Boundary layer similarity scaling (BLS). Showing **(a)** observed turbulent dissipation with actively mixing layer (AML) depth, (b), direct meteorological forcing of near-surface turbulence, (c) turbulent dissipation estimated using BLS, and (d) depth-integrated energy levels (units of flux) for each observed and derived profile. Note that estimated turbulent dissipation section derived from COARE (wind and buoyancy flux) and CCMP (wind) are visually identical such that only the latter is shown.

Surface boundary layer turbulence is normalized by the AML depth, and data outside of the AML is excluded. 30 vertical bins are used to facilitate temporally averaging with adjacent profiles.

3. Results

Focusing our attention on the surface boundary layer, comparing AML to L_{MO} using the depth ratios in Table 1, we find that buoyancy flux played a minimal role in forcing the AML during the study, with buoyancy rarely removed from the upper ocean and energy for near-surface mixing predominately supplied by wind stress. An analysis of time-averaged microstructure and BLS profiles computed with boundary layer scaling (Lombardo & Gregg, 1989) demonstrates that the BLS underestimates turbulent dissipation in the shallowest depths and overestimates turbulent dissipation deeper within the AML (Fig. 5), consistent with Merrifield's (2016) bulk analysis of tow-yo VMP transects from DIMES US5. BLS bias exhibits a

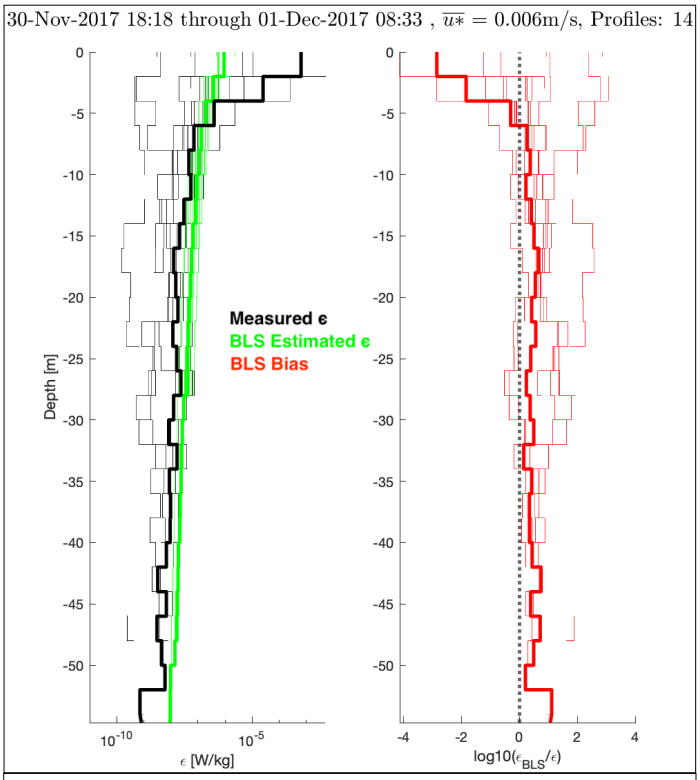

Figure 5: One centered interval of BLS, time-averaging (over inertial period) turbulent dissipation (left panel) and bias expressed as ratio of ϵ_{BLS} to measured ϵ (right panel) in depth space. Hereafter time-averaging is performed in AML-normalized (dimensionless) depth space. Averaged profiles are bold.

characteristic vertical profile throughout the survey for nearly all centered averages of observed and estimated turbulent dissipation.

A section of this bias is shown in Fig. 6c, with blue (red) hues indicating underestimation (overestimation) of observed turbulence in the AML-normalized surface boundary layer, with underestimation in the near-surface by up to 4 orders of magnitude. The vertical extent of this underestimation varies in depth, with three strong events lagging 2-3 days after intense storms; these will be revisited in the Discussion. A few cases (red hues near the surface) do not have the characteristic bias profile, raising the important question of why; examining normalized bias against friction velocity (u_*), windsea significant wave height (H_s), and profiles available within the 14.5-hour interval for averaging (Fig. 6a) it is apparent that these cases are colocated with instances in which there are few (<5) microstructure profiles available for averaging (Fig. 6b). Wind forcing (u_*) and windsea significant wave heights (H_s) mirror each other such that they are a reasonable proxy for one another. Insufficient number of profiles available for averaging is the most obvious factor in inconsistent BLS bias due to higher statistical uncertainty. The scale of temporal averaging (in other words, selecting a sufficiently coarse timescale such that the wind product meaningfully represents shear turbulence in the surface boundary layer) is critical to producing reliable BLS estimates of meteorologically forced turbulent dissipation. In our observations, accuracy of BLS does not depend on whether wind inflection (whether it is increasing or decreasing), nor proximity to Polar Front.

We aim to quantify this bias, placing several quality controls on the data. Profiles

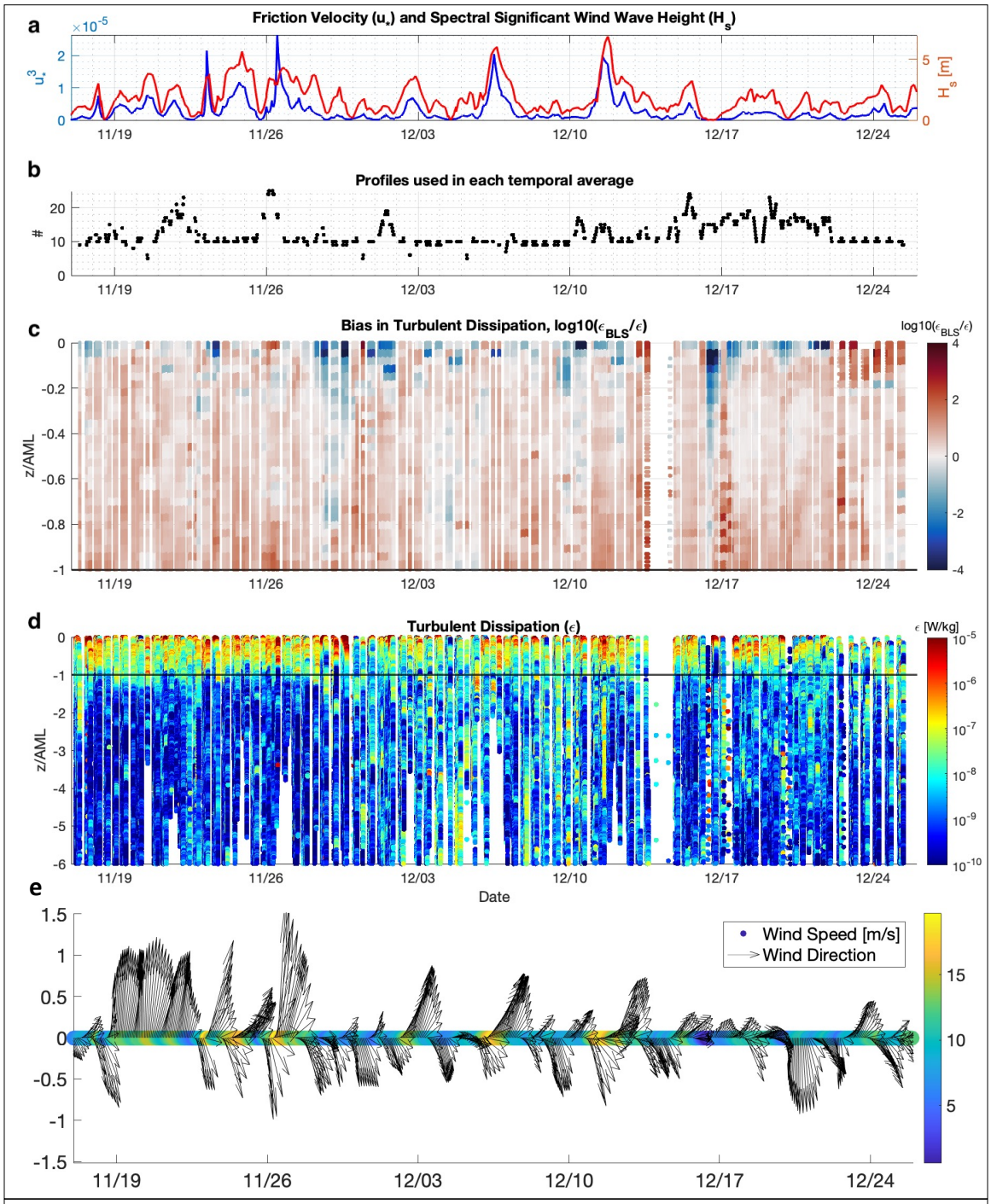

Figure 6: Bias of boundary layer similarity scaling (BLS). Showing (a) friction velocity u_* and windsea significant wave height H_s over glider, (b) availability of microstructure and associated BLS profiles for temporal averaging, (c) BLS bias in the normalized AML, and (d) observed turbulent dissipation rates depth-normalized by the AML. In normalized space, the AML is from *z/AML* = [0,1]. Also showing (e) wind direction as a function of time with northward wind speed [m/s] on the y-axis and total wind speed [m/s] as color axis.

are excluded (181 profiles or ~19.4%) because (a) the profile does not have a recognizable AML, (b) the profile is over the continental rise or shelf and thus likely contaminated by elevated bottom boundary layer mixing, or (c) there are no measurements in an entire vertical bin of a temporal average. Profiles are normalized by AML depth and measurements beyond the AML are omitted from analysis. After quality control, bias is quantified in two ways (Fig. 7b): a full dataset polynomial fit, and polynomial fit for the mean $\mu(z) = \ln(\epsilon_{BLS}/\epsilon)$ and the standard deviation $\sigma(z)$ of the

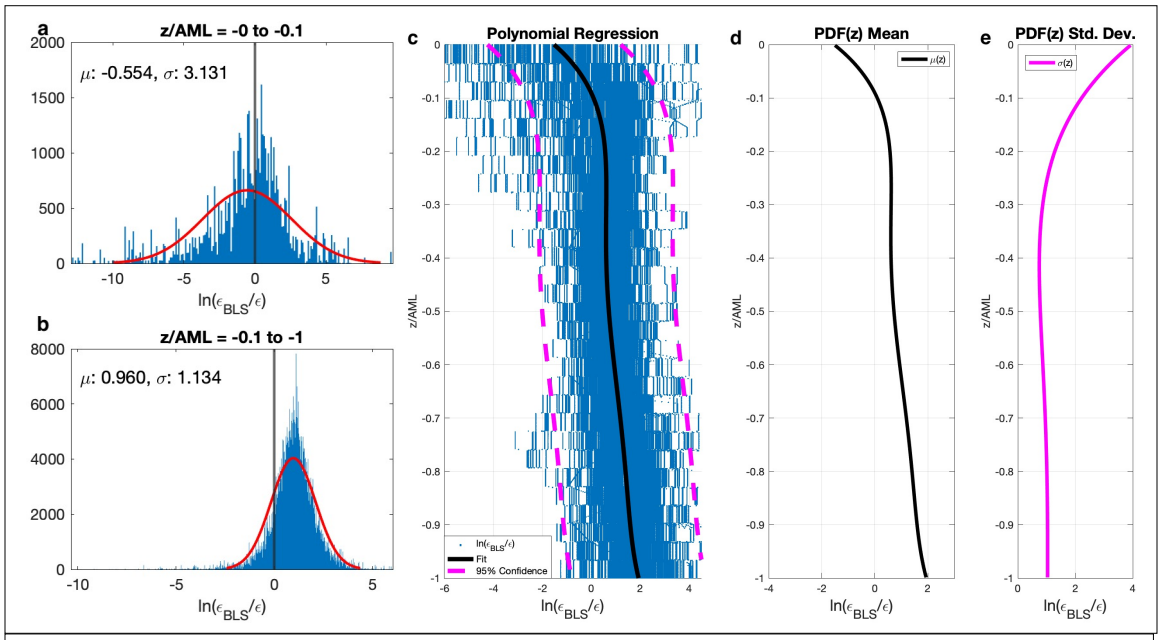

Figure 7: Showing histograms for bias in the **(a)** near-surface and **(b)** deeper AML, with **(c-e)** polynomial fits of BLS bias. **(c)** shows a full dataset polynomial fit with 95% confidence intervals. Additionally, polynomial fits for the **(d)** mean and **(e)** standard deviation of BLS bias are computed using a moving vertical window.

depth-dependent probability distribution function (PDF) fit to individual PDF computed from a moving vertical window. Polynomial fits $\xi(\hat{z})$ of $\ln(\epsilon_{BLS}/\epsilon)$ and its standard deviation are given by (Eq. 7):

$$\xi(\hat{z}) = \xi_5(\hat{z})^5 + \xi_4(\hat{z})^4 + \xi_3(\hat{z})^3 + \xi_2(\hat{z})^2 + \xi_1(\hat{z}) + \xi \qquad \text{(Eq. 7)}$$

where $\hat{z} = z/AML$ is the magnitude of the distance from the surface and coefficients are provided in Table 2. We used a 5th-degree polynomial because it best described the data

Table 2. Coefficients for bias polynomials

	ξ_5	ξ_4	ξ_3	ξ_2	ξ_1	ξ_0
Curve Fit $\mu(z)$	65.8318	-195.7996	217.5514	-109.1612	25.0325	-1.5199
PDF $\mu(\hat{z})$	67.0843	-199.1266	220.7982	-110.5756	25.2952	-1.5352
PDF $\sigma(\hat{z})$	-8.2071	37.8270	-67.6796	57.5501	-22.4064	3.9510

(there is no a priori theoretical reason for its selection). Note that where earlier we wished to describe bias in orders of magnitude of underestimation/overestimation $\log_{10}(\epsilon_{BLS}/\epsilon)$, bias is quantified using a natural logarithm $\ln(\epsilon_{BLS}/\epsilon)$ to facilitate correction in exponential form (which will be tested in Section 4 with Eq. 8).

Depth regimes for Fig. 7a are partitioned by the zero crossing of bias polynomials (Fig. 7b), $z/AML = -0.1$, which is the same regardless of whether bias is defined for qualitative description $\log_{10}(\epsilon_{BLS}/\epsilon)$ or quantitative correction $\ln(\epsilon_{BLS}/\epsilon)$. The near-surface AML exhibits a larger standard deviation in bias (Fig. 7a) than the deeper AML, suggesting wave dynamics at the air-sea interface might impact this. Partitioning the dataset into less-than-average and greater-than-average wave conditions demonstrates a counterintuitive result. In the *near-surface AML*, the mean underestimate and standard deviation of BLS is larger in *low* wind conditions (Fig. 8); in the *deeper AML*, the mean overestimate of BLS is larger in *high* wind conditions. The near-surface underestimation is more severe during breaking wave conditions (Fig. 9) and when Langmuir circulation is more likely active (Fig. 10), though wind friction velocity (Fig. 8) seems to have more

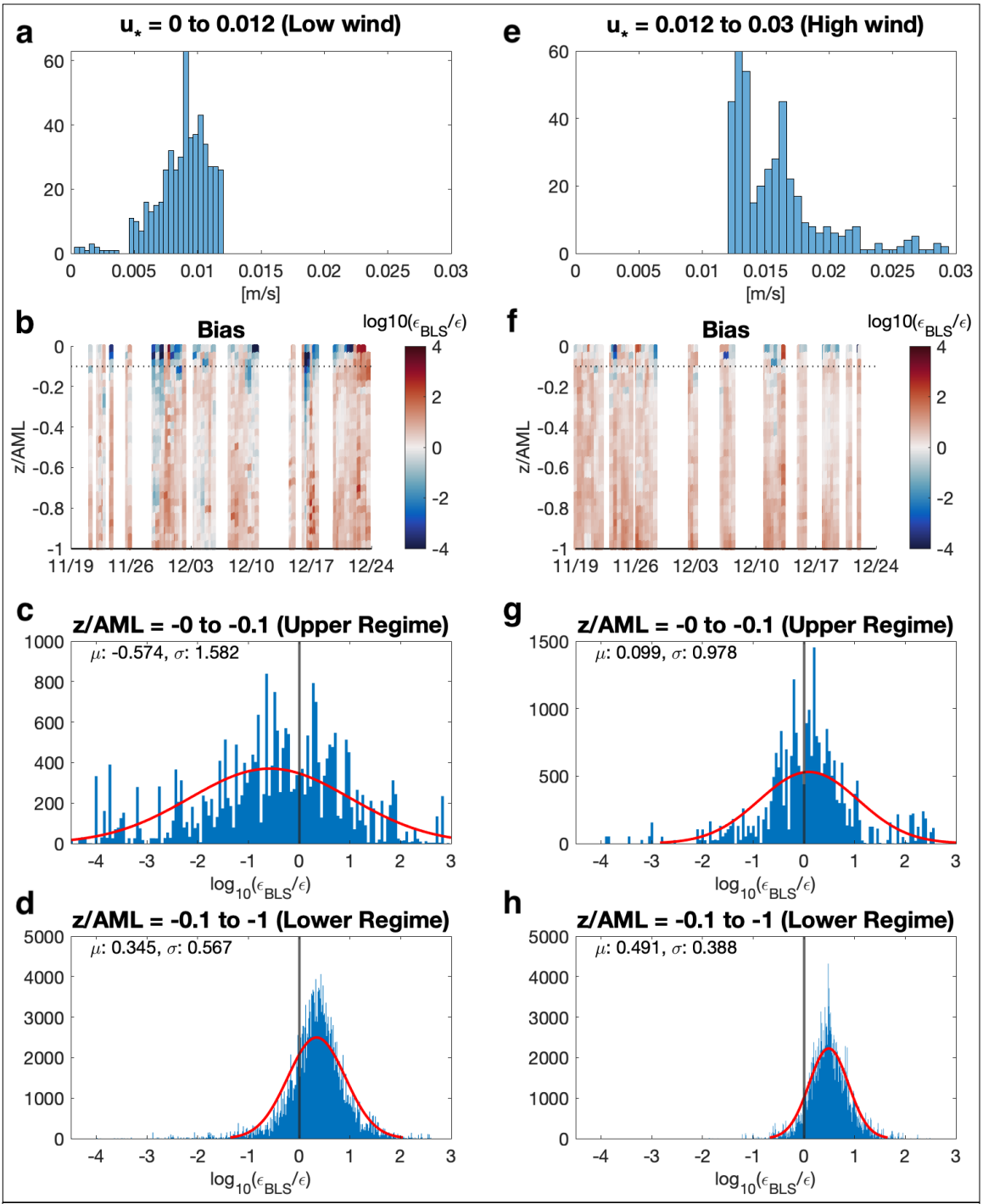

Figure 8: Histograms for BLS separated by water friction velocity (u_*) and position within the AML. **(a-d)** shows a bias section, near-surface histogram, and deeper AML histogram for low-wind conditions. **(e-h)** is the same for high-wind conditions.

influence on near-surface underestimation than wave steepness or Langmuir number. The shape of these bias profiles and their physical origins will now be discussed.

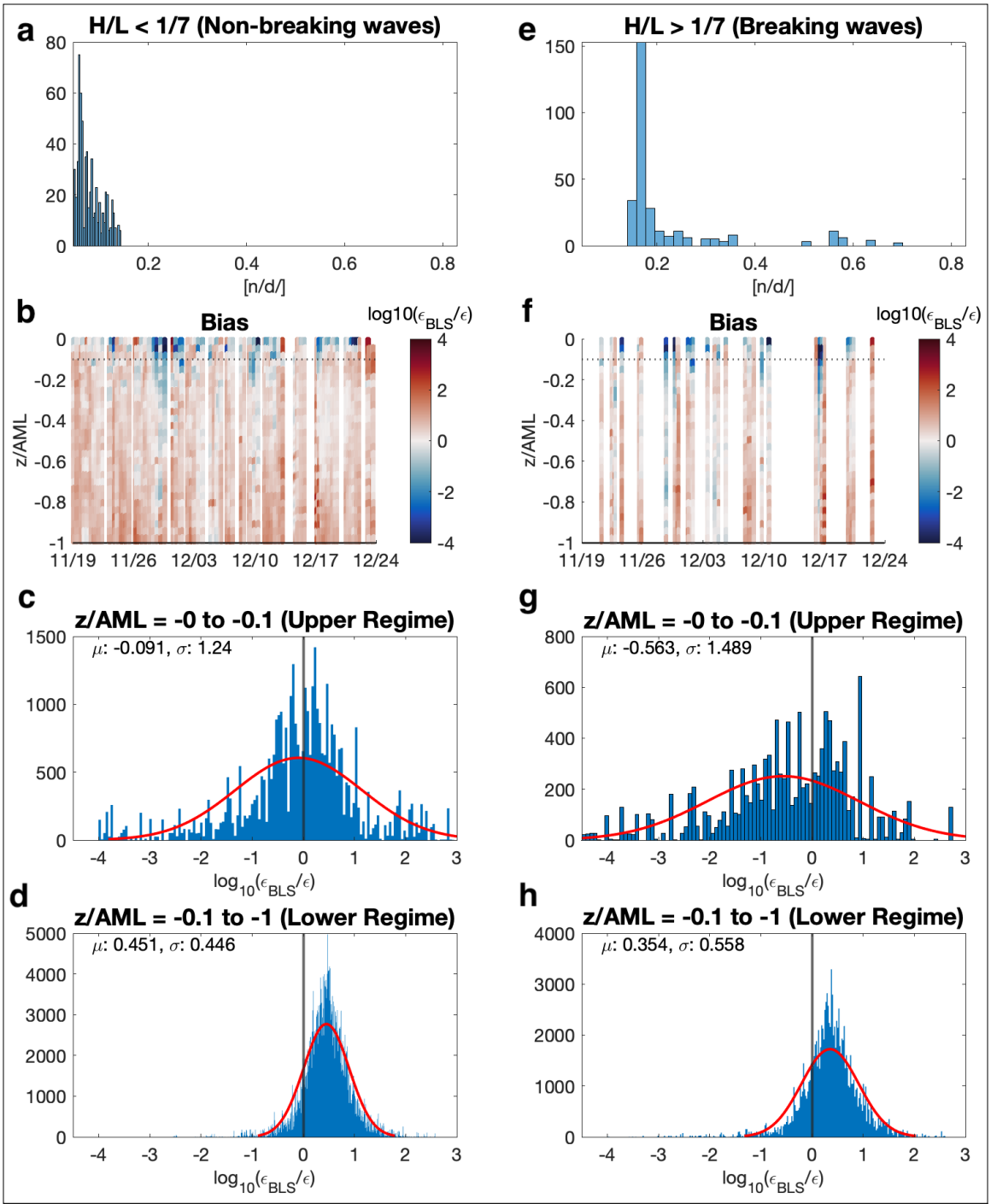

Figure 9: Histograms for BLS separated by wave steepness (*H/L*) and position within the AML. **(a-d)** shows a bias section, near-surface histogram, and deeper AML histogram for low-wind conditions. **(e-h)** is the same for high-steepness conditions. Wave steepness is calculated from Copernicus Global Ocean Waves Multi Year product (1/5° grid, at a 3-hourly temporal resolution) using wind wave mean period (*T*) and significant wave height from wind and swells (*H*) using ($L=2\pi H/gT^2$).

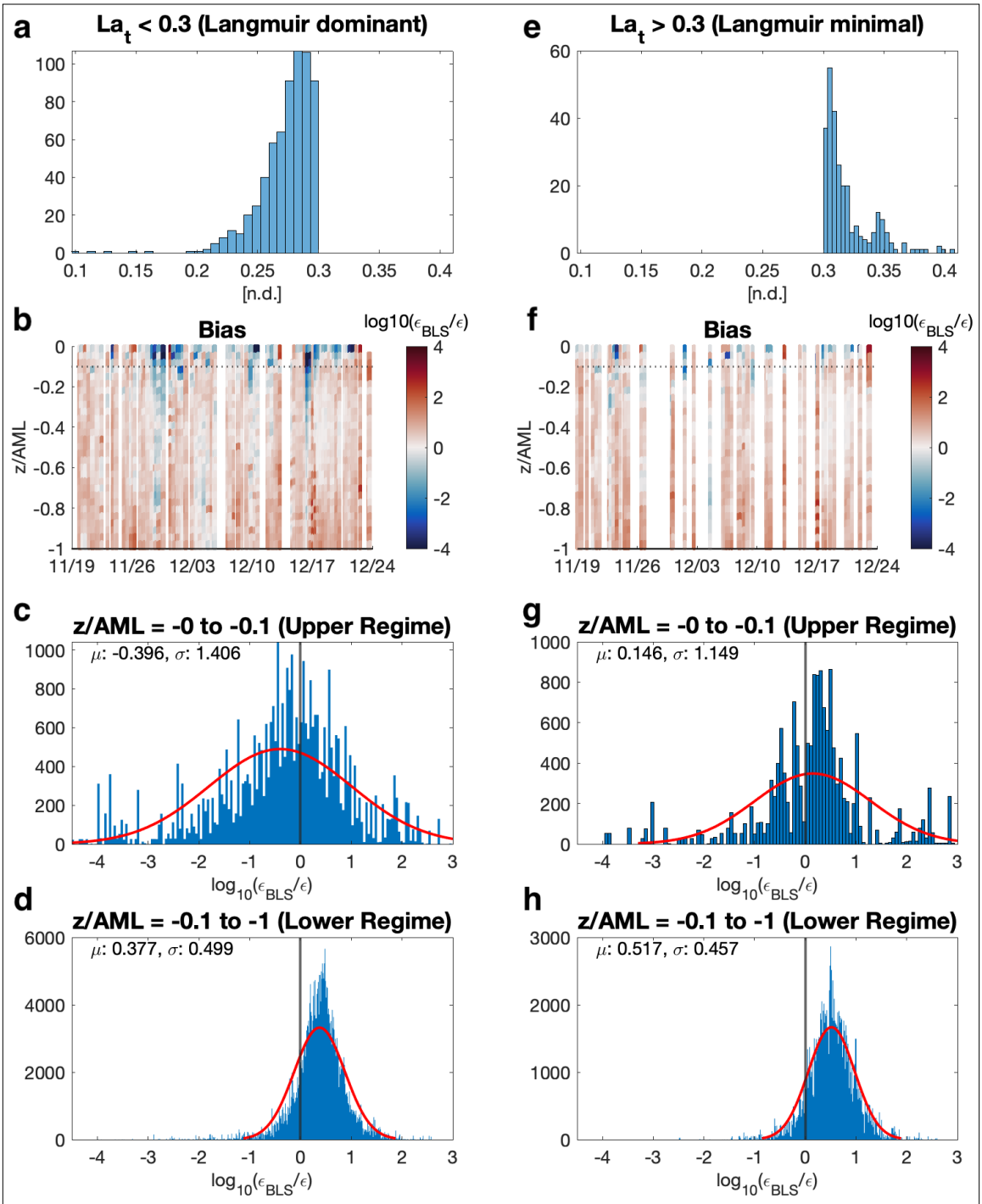

Figure 10: Histograms for BLS separated by Langmuir number and position within the AML. **(a-d)** shows a bias section, near-surface histogram, and deeper AML histogram for low-wind conditions. **(e-h)** is the same for Langmuir-stable conditions. Wave steepness is calculated from Copernicus Global Ocean Waves Multi Year product (1/5° grid, at a 3-hourly temporal resolution) using $La_t = (u*/u_{s0})^{1/2}$ where u_{s0} is surface velocity of Stokes drift.

4. Discussion

Overall, glider survey revealed interesting subsurface physics, observing elevated turbulent dissipation rates ($\epsilon = 10^{-7}$ W/kg) for the entire duration for which the glider sampled the core of the Polar Front. Glider CTD observed some salt fingering and double diffusive staircases north of the PF (consistent with Merrifield et al., 2016) and sporadic diffusive/oscillatory convection (Ferris et al., 2020). Subsurface phenomena will be discussed in a follow-on paper. We observe an interesting relationship between frontal hydrography and shallow mixing which warrants brief discussion. The glider crossed south into the PF on 11/28, marking a sharp reduction in density and mixed layer depth (Fig. 2). Here there is also a transition in the relationship between MLD and AML (Fig 9). North of the PF the AML rarely develops beyond the mixed layer; but beyond the PF in the cold, fresh, dense Southern Ocean waters the AML routinely develops beyond the MLD with little compliance from the mixed layer itself. TKE erodes the base of MLD, mixing away this interface. MLD and AML track well in November, but their relationship changes in December onward. At depth, starting at and exceeding the mixed layer, front has different physics than the outside of the front. This could be due to greater observed stratification resisting mixed layer deepening despite churning by TKE of the AML with little complicate from the mixed layer (Fig. 2); intense lateral density gradients within the PF core creating stability and preventing convection. Another possibility is that some TKE source other than wind-shear is contributing to AML development; DIMES (St. Laurent et al., 2012) observed lee wave interactions and enhanced TKE in the ACC fronts. The relationship between water masses and AML:MLD is complicated by

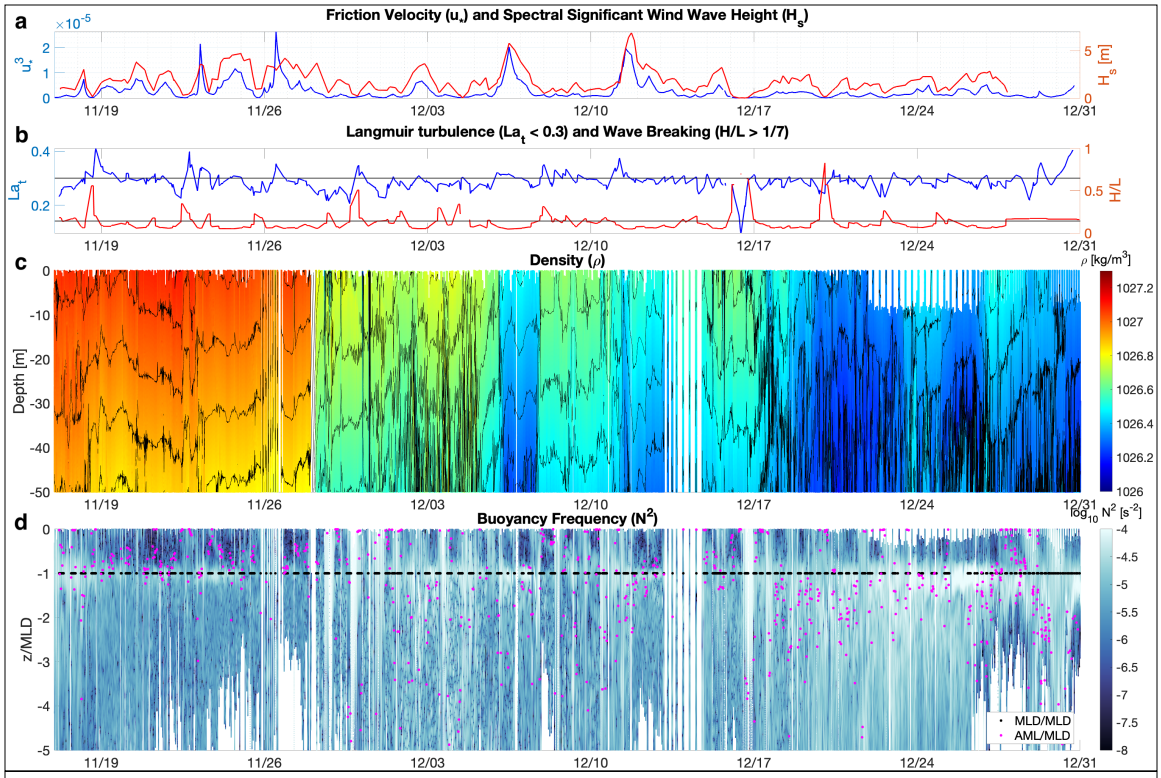

Figure 11: Near surface hydrography. Showing **(a)** friction velocity and significant wind wave height, **(b)** turbulent Langmuir number and wave steepness (*H/L*), **(c)** shallow density with isopycnal contours at 0.07 kg/m^3 intervals, and **(d)** stratification with AML and MLD depth-normalized by MLD.

seasonal transition from winter to summer—and increasing stratification—of the upper Southern Ocean, similar to that observed by Du Plessis et al., (2019). A shallowing of dense isopycnals occurs during the December 3 and December 12 storm events (Fig. 11), as well as on December 17 following wind and wave conditions strongly conducive to Langmuir circulation. In summary, mixing dynamics are highly influenced by the front (as well as seasonal transition) and worthy of further investigation.

Boundary layer similarity scaling (BLS) underestimates turbulent dissipation in the near-surface and overestimates turbulent dissipation below the near-surface, consistent with Merrifield (2016). This result holds regardless of wind speed and depends on only sufficient temporal averaging (i.e., the inertial period). MLD is not equivalent to

the AML but overall average MLD and AML depths are comparable such that we suggest it as a crude but reasonable proxy for AML depth (when a cutoff depth is required for implementation of boundary layer scaling). Boundary layer scaling in its current form can be responsibly used to estimate surface boundary layer mixing from meteorological data (from remote sensing or in situ sources), given (1) an appropriate spatial and temporal resolution is selected and (2) a depth-based correction is applied to the estimate. Recapitulating assumptions, we confirm that within the AML, shear production and turbulent dissipation dominate the turbulent kinetic energy (TKE) equation such that BLS can still be used to estimate surface boundary layer mixing with minor adjustment (which is possible due to the predictable, depth-based based form of its bias).

The BLS underestimates energy input into the near-surface ocean because it does not sufficiently account for surface gravity wave breaking, and/or TKE from alternative sources in the high-wind Southern Ocean environment. Our observations suggest that accuracy of BLS does not depend on the rate at which wind friction velocity is increasing (decreasing). It also does not depend on proximity to Polar Front, which makes sense because water column structure and its geographic variation impacts the diffusivity (amount of homogenization) resulting from turbulent kinetic energy dissipation, rather than the level of turbulent dissipation itself. BLS of shear turbulence in the Southern Ocean exhibit a correctable bias, underestimating (overestimating) turbulent dissipation rates in the shallower (deeper) parts of the surface boundary layer. While this result holds regardless of wind speed or inflection and depends only on sufficient temporal averaging, the magnitude of the shallower underestimate varies with wind speed and sea state,

performing with greater bias during the mildest wind forcing. Returning the key assumptions, BLS assumes Reynolds stress is approximately a constant function of boundary stress. In other words, stress due to wind shear near the air-sea interface is approximately equal to wind stress within the inertial sublayer, which is not true when there is substantial momentum transport into the breaking surface gravity wave field. Another assumption of BLS is that this shear production (from this wind stress, along with buoyancy forcing which is negligible in this study) dominates the TKE budget and matches turbulent dissipation.

BLS in its current form is a rigid-boundary theory and assumes that the TKE budget (Eq. 1) is dominated by shear production, buoyancy production, and dissipation. In general surface gravity waves are thought to play a role in boundary layer structure within 1-2 significant wave heights (H_s) of the surface. Gerbi et al. (2009) used an

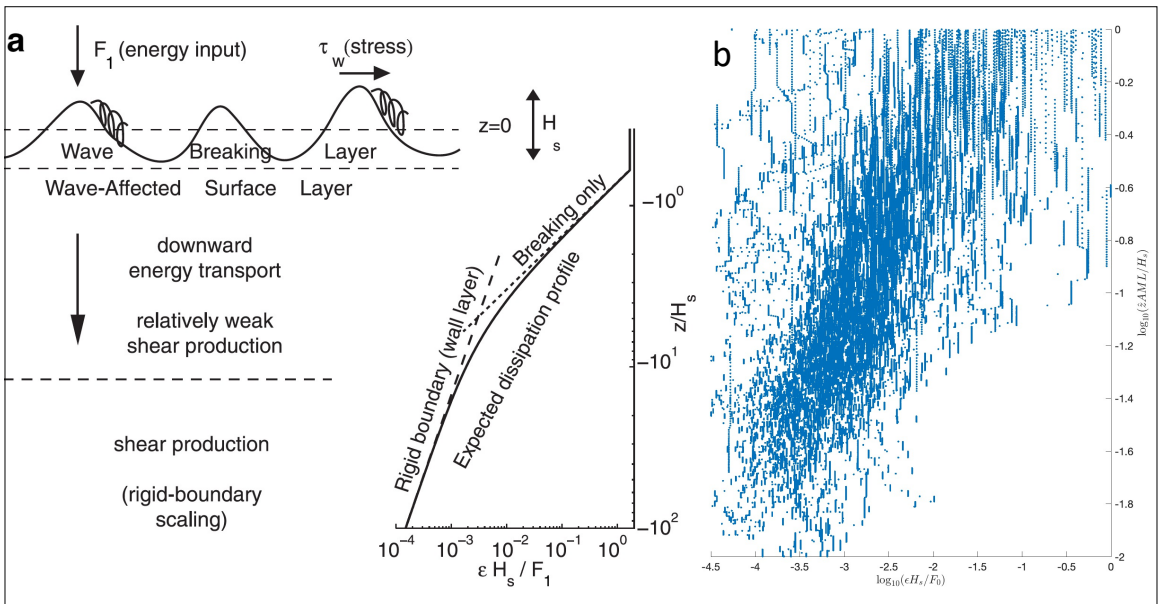

Figure 12: Boundary layer structure. Showing **(a)** cartoon schematic from Gerbi et al., (2009) and **(b)** the same figure constructed using AUSSOM glider microstructure dissipation measurements, windsea significant wave height H_s, and wind forcing $F_1=u_*^3 G_t$, where G_t is an empirical function of approximate wave age. Scatter (blue) includes 1 in 5 profiles for clarity.

analytical model with observations from the Coupled Boundary Layers and Air Sea Transfer low winds experiment (CBLAST-Low) to estimate terms of the TKE equation (Eq. 1) and found that production alone was unable to balance dissipation in the wave affected-surface layer, a conceptual region which lies above the rigid boundary or logarithmic layer (Terray et al., 1996). The inclusion of a transport term (representing the nonspecific effects of wave breaking, nonlinear wave-turbulence interactions, and Langmuir turbulence) improved the model, though the contribution of Langmuir turbulence was thought to be unimportant relative to wave breaking. We have reproduced this result (Fig. 12) using our Lagrangian measurements, which should be identical to the statistics of wave breaking turbulence were they computed from an Eulerian platform (Derakhti et al, 2020). Two alternative scalings are tested in comparison to depth-integrated TKE (Fig. 13), including $F_1 = G_t u_*^3$ (Craig & Banner, 1994) and $F_2 = c_e u_*^2$ (Gemmrich et al., 1994). Thomson et al., (2016) tested these scalings—and three others which we abstain from testing without in-situ wave observations—and found that F_2 had

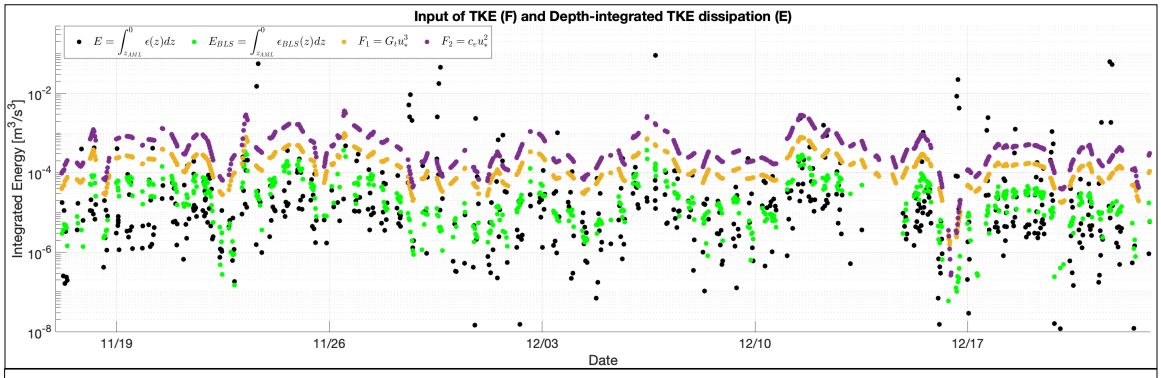

Figure 13: Depth-integrated TKE in comparison to inputs of TKE from wind estimated by alternative scalings. is an empirical function of wave age (Terray et al., 1996) which ranges from 37 to 182 for our dataset. Wave age is calculated using an approximation of data published in Edson et al. (2013), given by $u_{*a}/c_p \sim= 0.004U_{10}-0.003$ (Edson, pers. comm, Nov. 2020). Effective energy transfer velocity $c_e \sim= 0.148U_{10}+1.11$ is calculated after Hwang (2009) and is generally 1.5 to 3 m/s in the ocean.

the best agreement with observations, though marginally so. Our data is not consistent with this result; we find that both of these scalings produced inflated energy levels relative to (Eq. 3a).

Numerical modeling literature has aimed to understand the implications of breaking surface waves and Langmuir turbulence, which are not included wall-bounded (e.g. BLS) turbulence parameterizations and sub-grid schemes unless explicitly added (e.g. Kantha & Clayson, 2004). The inclusion of Langmuir (or Craik-Leibovich) schemes in ocean general circulation model (OGCM) turbulent boundary layer mixing parameterizations produces mixed layers of 2-25% deeper in extratropical, weak-convection regions such as the austral summer Southern Ocean (Li et al., 2019). A TKE contribution of wave breaking, if present, decays rapidly from surface (impacting mostly the near-surface), while a TKE contribution of Langmuir turbulence acts throughout the depth of the Langmuir circulation and its inclusion can fix some of the discrepancy in modeled too-shallow MLDs (D'Asaro et al., 2014). Sullivan et al. (2007) used large-eddy simulation (LES) and found that the wave age (c_p/u_{*a}), where c_p is phase speed of the spectral peak and u_{*a} is air friction velocity) impacted the near-surface effects, with younger wave groups and higher wind speeds exhibiting a larger positive feedback with Langmuir turbulence (in which breaking wave vorticity seeds Langmuir circulation) and generally increases near-surface dissipation. While producing mixed layers more similar to reality, unconfirmed is whether Langmuir turbulence is the actual physical mechanism producing deeper mixed layers (than BLS alone) in the ocean (D'Asaro, 2014). We propose two physical interpretations which may be contributing to BLS bias in tandem.

A first explanation is that BLS may underestimate energy input into the near-surface ocean because it does not sufficiently account for surface gravity wave breaking in the high-wind Southern Ocean environment. This violates the first assumption of BLS (that vertical transfer of horizontal momentum in the logarithmic layer is constant and dominated by velocity fluctuations such that Reynolds stresses are constant function of wind speed). However, this explanation alone (in light of the observation that near-surface bias is more severe during the mildest winds) does not necessarily capture the complete story. Low estimation of turbulent dissipation in the near-surface layer low-wind case could still be wave related. The presence of swell not related to the low winds could be a factor. It is possible that surface gravity waves bias BLS in all cases but it is more noticeable in low-wind cases (due to the lower overall magnitude of observed turbulent dissipation) and waves have the biggest impact near the surface. The near-surface underestimation and deeper-AML overestimation of turbulent dissipation is likely coupled. If more energy is lost in the shallowest depth, less energy will make it to the deeper AML, resulting in lower levels of turbulent dissipation (and a BLS overestimation) than previously parameterized. The near-surface underestimation by BLS is worse when there are breaking wave conditions and, and low wind shear. Meanwhile, the deeper histograms of Figs. 8-10 are remarkably consistent. One factor resulting in this could be that $\langle u\,w \rangle$ is realistically non-constant with depth, decreasing proportional to u_*^2 over the AML. However, mild inconsistency in the lower regime histograms in Fig. 8 and Fig. 9 suggest there must be other wind-related physical processes at work.

A second explanation is that there are sources of turbulent kinetic energy (TKE) other than wind shear and buoyancy flux which are contributing to observed turbulent dissipation but not accounted for by BLS. We assume that energy injection into the dissipative scale is principally accomplished by direct meteorological forcing (wind shear and convection) in the surface boundary layer, but other processes such as Langmuir driven turbulence, shear instabilities, and symmetric instabilities could be active in an intense wind-sheared frontal zone. BLS would not represent these processes. Belcher et al. (2012) concluded that Stokes shear is a dominant source in the Southern Ocean. Mixing in the Antarctic Circumpolar Current (ACC) might be further complicated by the numerous other processes turbulently transforming the upper ocean, such as internal wave driven mixing (St. Laurent et al., 2012) and double diffusion (Merrifield et al., 2016). It should be emphasized that this second explanation is not a complete explanation by itself - it does not account for the lack of turbulence (BLS overestimation) at depth. Moreover, deep over estimation events would worsen if overall positive bias (to accommodate $\langle u\,w \rangle$decreasing from the surface) were corrected. Furthermore, Langmuir circulation cannot be the only additional source of TKE because the presence or absence of this mechanism does not explain deep underestimation events (Fig. 10).

Improved parameterization of turbulent mixing in the surface boundary layer is necessary for more accurate representation of upper ocean structure in observation settings and numerical models. A direct consequence of this near-surface turbulence underestimation for the diffusivity (Fig. 2) is a misrepresentation of mixed layer development and upper ocean structure in representations that utilize dissipation and/or

TKE. Momentum is removed by breaking waves at the near surface to the point that there is less energy available for mixing in the deep (contributing to the overestimation of turbulent dissipation by BLS in the deeper AML. This means that using BLS as-is produces a slightly distorted view of mixed layer development and near-surface ocean structure. In other words, biases in the upper ocean structure of turbulent dissipation are disadvantageous even if the integrated energy of BLS is correct. The vertical location of this energy dissipation matters because it controls the reorganization of water parcels and thus the upper ocean structure (of density, temperature, salinity) itself.

BLS consistently misrepresents the structure of turbulent dissipation in our observations, underestimating turbulent dissipation in the very near-surface and overestimating turbulent dissipation further down, but the consistency of this bias suggests it can be corrected. A practical solution (which does not require estimating and adding the missing TKE associated with wave-related and other sources) could be implemented by applying a bulk depth-dependent correction based on the "Full" or $\mu(z)$ polynomial (Table 2) to existing BLS such that

$$\epsilon(\hat{z}) \approx \epsilon_{BLS}(\hat{z})e^{-\xi(\hat{z})} \quad \text{(Eq. 8)}$$

would give a statistically-improved BLS of each estimated profile. Here $\xi(\hat{z}) = \mu(\hat{z})$, either of the two polynomials describing BLS bias $\ln(\epsilon_{BLS}/\epsilon)$. A solution which could be more useful in a numerical modeling applications is to conduct Monte Carlo simulation using the $\mu(z)$ and $\sigma(z)$ probably density functions (PDFs) to obtain realistic BLS with uncertainty information. The bulk depth-dependent correction (Eq. 8) is applied to the BLS estimate, and the results are shown in Fig. 14. Depth-integrating TKE over different

parts of the water column demonstrates the distinct near-surface and deeper dynamical

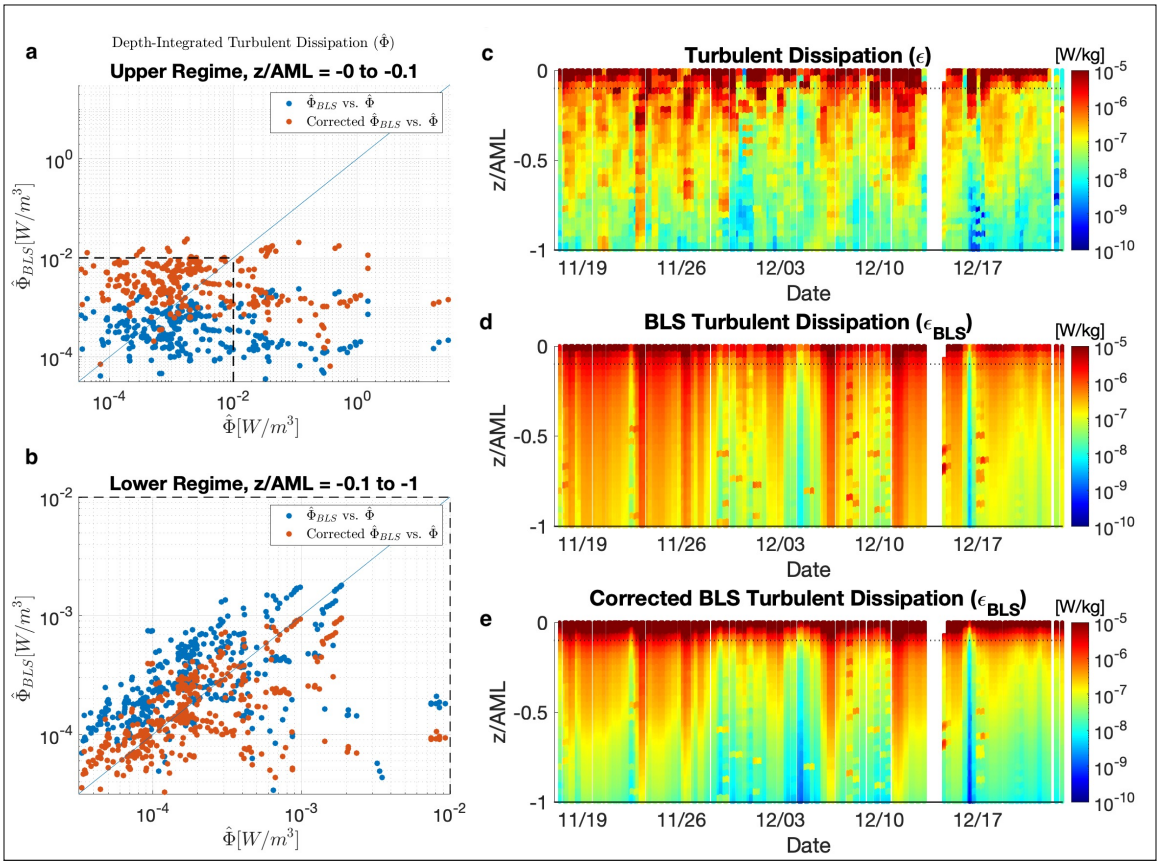

Figure 14: Energetic performance of BLS adjustment using bulk depth-dependent correction (Eq. 8). Showing integrated AML energy levels for observed and BLS-estimated turbulent dissipation in the **(a)** near-surface and **(b)** deeper regimes. Sections of turbulent dissipation (observed, BLS, corrected BLS) are shown in **(c-e).**

regimes. In both cases (Fig. 14a) the correction yields energy levels closer to those observed, improving representation of wind-forced shear production of TKE in the AML. From an ensemble perspective, BLS prediction of logarithmic layer energetics is most representative of true energetics below the near-surface. In an integrated sense, uncorrected BLS is an underestimation of TKE into the AML. BLS bias has greater consequences in the shallowest parts of the AML, because turbulent dissipation rate is largest nearest to the surface. In other words, shallow bias dominates integrated energy levels to underestimate the overall energy transfer into the ocean surface boundary layer

by wind stress. A correction is important not only for predicting the vertical structure of mixing in the upper ocean, but for bulk energy fluxes.

We revisit the cause of the deeper underestimation events (Fig. 6c); restated, patches of elevated observed turbulence (blue hues) extending deeper into the AML which were not accurately captured by BLS. There is some second-order dynamical effect; the timescale of this effect is much longer than the inertial period (~14.5 hours), and timescale for a storm system to pass the glider (from CCMPv2) is less than one day. Glider depth-averaged current is comparable to ACC velocity (from Operational Mercator, Fig. 1) extracted along the track of the glider such that the platform is effectively Lagrangian; it is not the case that ACC velocity is advecting/distorting patches of turbulence (associated with wave breaking) faster than the glider such that they appear lagged in the turbulence record.

A plausible physical mechanism explaining these deeper underestimation events is described in Dohan & Davis (2011), who observed a storm to excite near-inertial oscillations & currents in mixed layer with sufficient current shear to cause elevated mixing for 3 days after the storm itself. A key element was that wind direction turned with the direction of inertial rotation such that it resonantly excited the oscillations. We similarly see a wind direction turn in the direction of inertial rotation (Fig. 6e) during storm events. The shear associated with the inertial currents lowers Richardson number sufficiently to participate in current shear-driven mixing. But why would the TKE contribution of this current shear-driven mixing appear in BLS bias $\log_{10}(\epsilon_{BLS}/\epsilon)$ as a *delayed* underestimation event and not immediately? During the storm itself, the

calculation of bias would be heavily buffered by the wind-forced shear turbulence, such that the secondary component would perhaps not become noticeable until the wind died down and only the current shear remained. As wind subsides, the contribution of mixing due to current shear would subside, both and become smaller and this additional contribution becomes more noticeable. We speculate that this mechanism could similarly create a delayed TKE contribution from the storms, though this cannot be confirmed with the available data.

A final point of discussion is the origin of near-surface underestimation of turbulence dissipation in the current BLS. Importantly Lombardo & Gregg (1989) focused on times when the ocean steadily lost buoyancy to the atmosphere, such that buoyancy flux played a large role in forcing dissipation through convection. The assumptions of momentum balancing a constant Reynolds stress in the logarithmic layer worked for this regime. Here we build on this work and show that a wind-dominated regime is characterized by significant momentum loss, alternative TKE sources, or both in the upper ocean. There is greater turbulent dissipation than the BLS predicts. Representing this additional energy input into near surface is critical for understanding mixed layer dynamics, water mass transformation, and energy input in regions (and seasons) where wind shear dominates convection in the global ocean. The conclusions drawn from this study are expected to hold where and when wind shear dominates convection. AUSSOM was wind-dominated such that this assessment is broadly extensible to similarity scalings of shear turbulence (Monin & Obukhov, 1954), not specific to the Lombardo & Gregg (1989) scaling; which tested BLS in mild/moderate

wind, forced convection conditions. Before more recent studies, it was unknown how the scaling performs during high wind conditions, when law-of-the-wall possibly ceases to hold and the Monin-Obukhov length scale can be very deep. Throughout AUSSOM buoyancy flux played a minimal role in deepening the AML in the Drake Passage and Scotia Sea region (perhaps even extracting energy and reducing its development), with energy for near-surface mixing supplied almost solely by wind stress. AUSSOM tested boundary layer scaling in high-wind, non-convective conditions, but future investigations are needed for assessment of even stronger winds, and for cases where both wind-shear and buoyancy loss are significant.

Acknowledgments

Computational resources were provided by the VIMS Ocean-Atmosphere & Climate Change Research Fund. AUSSOM was supported by the OCE Division of the National Science Foundation. We thank the Captain and crew of the R/V Gould for their excellent support during the field program, and Justin Shapiro for the recovery mission. We also thank the two anonymous reviewers whose invaluable feedback greatly improved the paper. This study has been conducted using E.U. Copernicus Marine Service Information. CCMP Version-2.0 vector wind analyses are produced by Remote Sensing Systems.

Data Availability Statement.

All glider data used in the paper will be shared at microstructure.ucsd.edu, the NSF-funded Microstructure Database. The COARE 3.5 algorithm and its associated data products are publicly available. This includes surface radiation data from the CERES project (https://ceres.larc.nasa.gov/products-info.php?product=SYN1deg), CCMPv2

winds (www.remss.com; Wentz et al., 2015), near-surface temperature and humidity from SeaFlux CDR (https://www.ncdc.noaa.gov/cdr/atmospheric/ocean-near-surface-atmospheric-properties; Clayson et al., 2016b), sea surface temperature from SeaFlux Ocean CDR (https://www.ncdc.noaa.gov/cdr/oceanic/sea-surface-temperature-whoi; Clayson et al., 2016a), GPCP V1.3 daily rainfall product (https://www.ncdc.noaa.gov/cdr/atmospheric/precipitation-gpcp-daily; Adler et al., 2017), and aforementioned CMEMS products.

Endnotes

I gratefully acknowledge the contributions of my collaborators for this project: Donglai Gong (VIMS), Sophia Merrifield (SIO), Carole Anne Clayson (WHOI), and Louis St. Laurent (APL-UW).

Chapter 4
Contamination of finescale strain estimates of turbulent kinetic energy dissipation by frontal physics

Abstract

Finescale strain parameterization (hereafter, FSP) of the turbulent kinetic energy dissipation rate has become a widely used method for observing ocean mixing, solving a coverage problem where direct turbulence measurements are absent but CTD profiles are available. This method can offer significant value, but there are limitations in its broad application to the global ocean. In particular, FSP often fails to produce reliable results in frontal zones where temperature-salinity (T/S) intrusive features contaminate the CTD strain spectrum, as well as where the aspect ratio of the internal wave spectrum is known to vary greatly with depth, as frequently occurs in the Southern Ocean. In this study we use direct turbulence measurements from DIMES (Diapycnal and Isopycnal Mixing Experiment in the Southern Ocean) and glider microstructure measurements from AUSSOM (Autonomous Sampling of Southern Ocean Mixing) to show that FSP can have large biases (compared to direct turbulence measurement) below the mixed layer when physics associated with T/S fronts are meaningfully present. We propose that the FSP methodology be modified to (1) include a density ratio (R_ρ)-based data exclusion rule to avoid contamination by double diffusive instabilities in frontal zones such as the Antarctic Circumpolar Current, the Gulf Stream, and the Kuroshio Current, and (2)

conduct (or leverage available) microstructure measurements of the depth-varying shear-to-strain ratio $R_\omega(z)$ prior to performing FSP in each dynamically-unique region of the global ocean.

1. Introduction

Mesoscale processes, submesoscale processes, and turbulent mixing within the Southern Ocean play critical roles in global ocean circulation. As a major water mass component of the global overturning circulation, North Atlantic Deep Water (NADW) upwells in the Southern Ocean; much of this upwelled NADW is modified to become the Antarctic Bottom Water (AABW) while remaining NADW diverges northward and combines with Indian and Pacific Deep Water to become the upper cell of the Atlantic Meridional Overturning Circulation (Talley, 2013). While this paradigm of quasi-adiabatic upwelling is generally supported by numerical models (e.g., Thompson, 2008), models do not capture realistic mixing physics. The role of ocean interior mixing, in particular the relative importance of isopycnal versus diapycnal upwelling in Southern Ocean dynamics, is still poorly understood (Waterhouse et al., 2014; Tamsitt et al., 2017). We are just beginning to understand the spatial and temporal inhomogeneity of upper ocean mixing in the Southern Ocean (Ferris et al., in revision). The vertical structure of eddy diffusivity in relation to water mass distribution determines where diapycnal mixing and upwelling (downwelling) in the water column occurs. With the obvious sparsity of turbulent kinetic energy (TKE) dissipation measurements, it is tempting to widely apply FSP as a substitute tool to extract turbulence information from much more plentiful CTD

measurements collected by ships and autonomous platforms in order to study global ocean mixing.

The processes that drive mixing in the Southern Ocean are numerous. Focusing on the ocean interior below the surface mixed layer, these processes include double diffusive convection and interleaving/layering, shear-driven instabilities, internal wave-eddy interactions, and internal wave-wave interactions. Of these, internal wave-wave interactions are most central to across-scale energy transfer. The process of forward energy cascade moves energy from the mesoscale (10 to 100 km), governed mainly by geostrophy, to the sub-mesoscale (10 m to 10 km), which consists of nonlinear flows and internal waves, and eventually down to the TKE dissipation microscale (1 cm to 1 m) (St. Laurent et al., 2012; Sheen et al., 2015). While the details of this downscale energy transfer are active areas of research, it is widely accepted that forward energy cascade in the interior ocean is principally accomplished through internal wave-wave interactions. Internal waves interact with each other (presumably in the universal manner of the Garrett-Munk spectrum [Garrett & Munk 1972; 1975]) until they break and release their energy as turbulent dissipation. This forward cascade to smaller scales is carried out through interactions between triads of internal waves with additively (subtractively) resonant wavenumbers and frequencies (i.e. Hasselmann's theorem). Turbulent kinetic energy may dissipate locally at the site of internal wave generation via wave breaking, or internal waves may propagate energy away from the site of generation and dissipate at continental margins (Waterhouse et al., 2014).

The oceanic finescale is defined as features that exist and vary on vertical scales from 1-10m to 100-1000m, whereas the microscale is characterized by features 1cm to 1m. The Ozmidov scale, $L_{oz} = \varepsilon^{1/2}/N^{3/2}$ (~1m), is the key scale delineating the finescale adiabatic processes (i.e. internal waves) from the microscale diabatic dissipative processes and describes the largest eddies that can overturn in a stably stratified water column thereby contributing to forward energy cascade. There are numerous finescale parameterizations leveraging CTD and/or velocity profiles to estimate TKE dissipation rate (ε); including Thorpe scales (Gargett & Garner, 2008), shear- and/or strain-based finescale parameterizations (Polzin et al., 1995), and newer lesser-adopted techniques such as the large eddy method (Beaird et al., 2012). All the approaches rely on measurements of finescale features and the assumption that energy at the finescale dissipates at the microscale.

Thorpe scale analysis consists of algorithmically sorting the fluid elements from a measured density (CTD) profile into a theoretical stably-stratified profile, while keeping track of the vertical displacements required to sort these fluid elements (Thorpe, 1977). A Thorpe length scale L_T is obtained from the root-mean-square of these tracked displacements. The rate of turbulent dissipation ε is inferred from the empirical relationship with Ozmidov length scale (L_{oz}). Dillon (1982) adopted the method for oceanic application (using the assumption that density in surface layers and seasonal thermoclines is dominated by temperature), with subsequent groups such as Alford & Pinkel (2000) applying the same temperature-only method to depth-restricted regions where temperature alone is indicative of density overturns. Gargett & Garner (2008)

extended the method to density overturns measured by wire-lowered CTD. Mater et al. (2015) with its companion paper (Scotti, 2015) demonstrated clear bias (due to L_T/L_{oz} increasing with overturn size) in the Thorpe scale method using Vertical Microstructure Profiler (VMP) observations but it remains a common method despite this known issue.

Shear- and/or strain-based finescale parameterizations leverage the wave-driven forward energy cascade to estimate TKE dissipation rate. The parameterization of mixing associated with internal wave interactions consists of assuming the energy budget, $P \cong -\rho\varepsilon + B$, such that turbulent production P is matched by turbulent dissipation ε and buoyancy flux B. This spectral energy transfer occurs in a cascade of increasing wavenumbers (i.e. decreasing length scale nonlinear wave motions), of which an estimation (for the Garrett-Munk spectrum) is calculated from vertical CTD and ADCP profile measurements (Polzin et al., 2014). Gregg (1989) first developed the shear-based finescale parameterization. Observations used to characterized the oceanic shear and strain spectra in relation to microstructure measurements (Gregg & Kunze, 1991) led to the development of the shear and strain-based method by Polzin et al. (1995), with the generalization of the Gregg-Henyey parametrization to different latitudes using measurements of velocity and density via High Resolution Profiler (HRP). Kunze et al. (2006) offers a comprehensive discussion of applying Polzin et al. (1995)'s shear and strain-based method to lower-frequency (e.g. 50-meter) LADCP data such as that from global hydrography. Mauritzen et al., (2002) then introduced the method of strain-only finescale parameterization in their study of the Mid-Atlantic Ridge. Whalen et al. (2012) and Whalen et al. (2015) are known for the application of strain-only finescale

parameterization to the Argo float array. There are numerous variations of the above parameterization such as the “MG parameterization” modified for use on the continental shelf (Mackinnon & Gregg, 2003).

Finescale parameterizations based on shear and/or strain variance measurements assume turbulent mixing in the ocean is primarily driven by internal wave-wave interactions (i.e. elastic scattering, induced diffusion, parametric instability) that is characterized by the Garrett-Munk (GM) wave spectrum in the ocean. The GM model is an empirical representation of the canonical internal wave spectrum based on data collected from many regions of the ocean (Munk, 1981; Gregg & Kunze, 1999). The empirically derived parameters in the GM model represent numerous elements of spectral cascade physics, including energy transfers due to wave-wave, wave-eddy and eddy-eddy interactions at scales larger than viscous dissipation. These interactions have been studied in stratified turbulence literature: direction numerical simulation (DNS)-based inquires have supported a highly anisotropic forward energy cascade in the inertial subrange characterized by wave features in the vertical and formation of layers in the horizontal; such that energy transfer from horizontal to vertical modes is a universal feature (Lindborg, 2006; Kimura & Herring, 2012). Velocity structure functions reveal the vortical and wave-attributable spectra to have distinct transition wavenumbers from 2D turbulence to 3D turbulence, complicating structure of energy spectra (Kimura & Herring, 2012). Stratification is also shown to enhance non-local energy transfer between large and small horizontal scales (Khani & Waite, 2013). Nevertheless, extremely fine numerical grids are required to confirm the spectra behavior observed in many of these

studies (Bartello & Tobias (2013), leaving us to the continued observation of oceanic forward energy cascade. As such, the variation in stratification (N^2) or "strain spectra" is attributed to an internal wave field described by the GM spectrum and its associated energetics. This is a somewhat precarious assumption for the Southern Ocean (Kunze et al., 2006; Frants et al. 2013; St. Laurent et al., 2012; Sheen et al., 2013) as observations have shown that finescale parametrization techniques routinely overestimate turbulent kinetic energy dissipation rates even when a conservative shear-to-strain ratio (R_ω) is assumed (Merrifield, 2016). The best agreement is thought to be found in the deep ocean interior where the assumption of the dominance of wave-wave interactions likely holds, and the presence of fronts and eddies can further modify the observed shear and strain in ways that deviate from the presumed GM spectrum.

Adopting the methodology of Whalen et al. (2012) and Huussen et al. (2012) the finescale strain parametrization of TKE dissipation rate is given by (Eq. 1).

$$\epsilon_{strain} = \epsilon_0 \frac{\overline{N^2}}{N_0^2} \frac{\langle \xi_z^2 \rangle^2}{\langle \xi_{zGM}^2 \rangle^2} h(R_\omega) L(f, N) \tag{1}$$

The term $\langle \xi_z^2 \rangle$ is the strain variance determined by integrating the strain spectra, leveraging the property that the area under a one-sided power spectrum is equal to its variance. $L(f, N)$ is the latitudinal correction of the ocean internal wave field and represents the internal wave field frequency content. $h(R_\omega)$ is the dependence on the internal wave field's shear-to-strain ratio R_ω (Kunze et al., 2006; Polzin et al., 1995),

which must be assumed in the absence of shear, typically $R_\omega \sim 3$. More detail is provided in Methods.

Recently strain-only finescale parameterization has been used to infer climatological patterns of global mixing from WOCE/CLIVAR lowered CTD (Huussen et al., 2012) as well as Argo profiling floats (Whalen et al., 2015); and in the latter case this technique is uniformly applied to the global ocean including the frontal zones such as the Drake Passage of the Antarctic Circumpolar Current (ACC), Gulf Stream, and Kuroshio Current. These studies produce turbulent dissipation estimates on the climatological scale rather than in a time-varying sense. Frants et al., (2013) performed FSP and Thorpe scale analysis on DIMES CTD but did not examine how their efficacy changes in the context of the intense frontal zone. These methods have not yet been widely adopted for use by glider platforms; but Johnston & Rudnick (2015) applied the strain-only finescale parameterization to glider data, with agreement between shear-and-strain and strain-only estimates of diffusivity within a factor of 1.7 and standard deviation 1.6. An important consideration is that gliders, contrary to free-falling vertical profilers, sample the water column at an angle. Whereas Thorpe scales depend on careful measurement of the vertical organization of water parcels and could underestimate turbulent dissipation rates associated with high aspect ratio Kelvin-Helmoholz billows or through the observation of false overturns (Thorpe, 2012), finescale strain parameterization leverages the assumed isotropy of a somewhat universal wavenumber spectra and is more robust to use with autonomous underwater gliders.

We examine several key assumptions of FSP, which overall assumes that energy in the internal wave field smoothly transfers to turbulent dissipation. By measuring both the internal wave scale (using FSP) and the microscale we can assess this paradigm. Strain is mathematically defined as the distance between two isopycnal surfaces divided by their mean separation (Thorpe, 2005). There are three assumptions confounding this comparison: (Assumption 1) that observed strain-like features are in fact internal wave strain, (Assumption 2) that the shear-to-strain ratio is similar to the Garrett-Munk (GM) spectrum such that its value R_ω may be assumed, and (Assumption 3) downscale energy transfer steadily occurs such that for a control volume the production of turbulent kinetic energy by shear matches the dissipation by molecular viscosity and buoyancy flux—ignoring the divergence, pressure work, and transport terms of the turbulent kinetic energy equation; nonlinear interactions between internal waves accomplish this transfer (Polzin et al., 2014).

Assumption 1 is that variations in buoyancy frequency (N^2) are from strain. Double diffusive instabilities (endemic to Southern Ocean and other intense frontal regions) could contaminate the strain spectrum via temperature-salinity (T/S) intrusive features. A key feature of the ACC system are its numerous named fronts, water mass boundaries where collections of filaments demarcate abrupt changes in T/S relation. The Subantarctic Front (SAF) is the northern edge of the ACC and divides Upper Circumpolar Deep Water from Subantarctic Mode Water (SAMW) which overlies low-salinity Antarctic Intermediate Water. Further south the Polar Front (PF) is demarcated by abrupt changes in sea surface temperature and the subduction of Antarctic Surface Water

beneath SAMW. The outcropping of isopycnals in this frontal system creates horizontal juxtapositions of water masses with contrasting T/S relationships, predisposing them to double diffusive instabilities. The region around the PF is predisposed to double diffusive instabilities (Schmitt, 1994) because there are warm/salty subantarctic waters to the north and cold/fresh Southern Ocean waters to the south.

Double diffusive instabilities occur because thermal diffusivity is much greater than salt diffusivity ($\kappa_S \approx 1 \times 10^{-9} m^2 s^{-1}$, $\kappa_T \approx 1.5 \times 10^{-7} m^2 s^{-1}$). In its salt fingering regime (Schmitt, 1994), warm/salty water overlies cold/fresh water; and a parcel displaced into the upper layer warms faster than it experiences a salinity change such that it becomes as warm/fresh particle and continues to rise. In its diffusive/oscillatory regime, cold/fresh water overlies warm/salty water; and a particle displaced upward conductively loses heat before sinking as lukewarm/salty water back to the initial position, subsequently overshooting its initial position (producing a growing oscillation). The oscillation forms its own well-mixed layer until the temperature gradient between the mixed layer and the adjacent water grows until it becomes critically unstable and forms a convective layer. Double diffusive instabilities need not be vertical; horizontal double diffusive instabilities (interleaving and intrusive layering) are know to occur in the Drake Passage, contributing heavily to lateral mixing. They are expected to be 10-100m in scale. North of the PF and its vicinity are predisposed to salt fingering, while south of the PF is predisposed to diffusive convection (Merrifield et al., 2016). A T/S-intrusive signal would manifest itself in FSP as the potential energy (strain) spectra having an unusual rolloff at high wave numbers (i.e. its values would be too high). T/S-intrusive signals can

be identified using the density ratio $R_\rho = \alpha T_z / \beta S_z$, useful for predicting whether a profile is prone to the diffusive ($0.5 < R_\rho < 1$) or the salt fingering ($1 < R_\rho < 2$) regime. Ranges here are those for which instability can develop faster than local buoyancy period $2\pi/N$ (Schmitt, 1994).

Assumption 2 arises specifically for FSP (which uses only strain, different from shear-and-strain finescale parameterization). FSP assumes an idealized, universal Garrett-Munk (GM) spectrum; which is an empirically-determined imagined-to-be universal function which describes the variation of wave energy in horizontal wavenumber, vertical wavenumber, and frequency space. By assuming a GM shear-to-strain ratio (R_ω) we assume GM shear characteristics and thus make an assumption about the frequency content of the internal wave field. Internal wave-wave interactions on smooth shape of spectrum (e.g. induced diffusion) and make it more red. The GM spectrum is intended to apply far away from contamination by boundaries and specific internal waves sources such that internal waves have had sufficient time and space to collide and smooth the spectrum such that there is no longer any prominence in wavenumber or frequency (Polzin & Lvov, 2011). FSP is could potentially fail in the Southern Ocean because it is not necessarily meet this criterion.

Due to weak stratification, large injection of kinetic energy, and the presence of continuous zonal jets, the Southern Ocean is highly influenced by topographic interaction in addition to geostrophic turbulence (Ferrari & Wunsch, 2009). Deep flow (e.g. a mesoscale eddy, jet, barotropic tide) impinging on rough topography $h = h_0 \sin[k(x + Ut)]$ generates topographic lee waves with frequency $\omega = Uk$, where

k is the horizontal wavenumber of the seafloor topographic feature and U is the horizontal flow velocity. In reality the seafloor is a combination of features with different wavenumbers such that the lee wave spectra is realistically a summation of Fourier modes. Internal lee waves generated by flow-topography interactions appear to dissipate only a fraction of the total lee wave energy locally (Brearley et al., 2013); waves in the "hydrostatic non-rotating range" $U/N < k^{-1} < U/f$ can radiate upward, such that internal lee waves have an intrinsic frequency range of $f^2 < k^2 U(z)^2 < N^2$ (Bell, 1975). Lee waves are hypothesized to be more dominant in Southern Ocean than is ubiquitous in the global ocean (MacKinnon et al., 2017), and an internal wave spectrum with a prominent lee wave peak in wavenumber and frequency space is not a GM spectrum and implies a departure from the assumed $R_\omega = 3$. Furthermore R_ω is fixed for a single wave and is inherently a biased estimator of the full spectrum (Polzin et al., 1995; Polzin et al., 2014).

If the true shear-to-strain ratio is higher (lower) than assumed R_ω in any part of the water column, ϵ_{FSP} will be an underestimate (overestimate) of true TKE dissipation rate ϵ with an error directly proportional to the value of R_ω. Internal waves at tidal frequency are associated with lower R_ω, while internal waves at near-inertial frequency are associated with higher R_ω. Chinn et al. (2016) find values ranging from 1 to 10; Waterman et al. (2013) report 7 over the Kerguelen Plateau, implying more energy in the near-inertial peak than the GM model spectrum. From studies of the Drake Passage and Scotia Sea (Fig. 16 from Kunze et al., 2006; Nikurashin & Ferrari, 2010) $R_\omega = 10$ is appropriate. R_ω is effectively a ratio of horizontal kinetic to potential energy. Near-

inertial internal waves (those with frequencies close to f) are considered part of the *hydrostatic rotating wave regime* and have motions which are dominantly horizontal and rotational, while waves with frequencies close to N are part of the *non-hydrostatic wave regime* and have motions which are predominately vertical (Gill, 1982). This can been seen from the expression for lee wave vertical wavenumber $m^2/k^2 = (N^2 - \omega^2)/(\omega^2 - f^2)$. It follows that waves with frequencies near f (near N) have a high (low) shear-to-strain ratio. Nikurashin & Ferrari attribute this high $R_\omega = 10$ to inertial oscillations triggered by momentum flux divergence (caused by large-amplitude internal waves).

Assumption 3 is that the energy feeding turbulent dissipation comes from nonlinear internal wave-wave interactions. In some way, FSP estimates the turbulent dissipation attributable to internal wave driven interactions. If internal waves are predominately driving TKE injection into the microscale, then FSP should hold. If physical processes which can shortcut the steady forward energy cascade are active, FSP would be biased low (e.g. there is more energy disputing at the microscale than contained by the internal wave field). TKE shortcuts include surface forcing (wind shear and buoyancy flux), wave-flow interactions (critical layers), and frontal instabilities (e.g parallel shear, centrifugal, inertial, baroclinic-symmetric). Observational studies of Southern Ocean mixing (e.g. SOFine and DIMES) have found enhanced TKE dissipation over regions of complex topography leads to the generation of internal waves (Nikurashin et al., 2014; St Laurent et al., 2012; Waterman et al., 2013) suggesting that this system is sufficiently dominated by internal wave-wave interactions and this assumption

(sufficiently deeper than the surface boundary layer) is likely less of an issue than Assumptions 1 and 2.

In the absence of microstructure coverage, the use of FSP to estimate turbulence from lowered CTD and autonomous profiling floats is useful for our understanding of mixing in the global ocean; and the numerical models we construct from our understood reality. Acknowledging that some of the core assumptions of FSP may be incompatible with frontal physics it is important to reexamine the use of FSP in frontal zones, especially in the Southern Ocean. In this study we pair the wealth of microstructure data

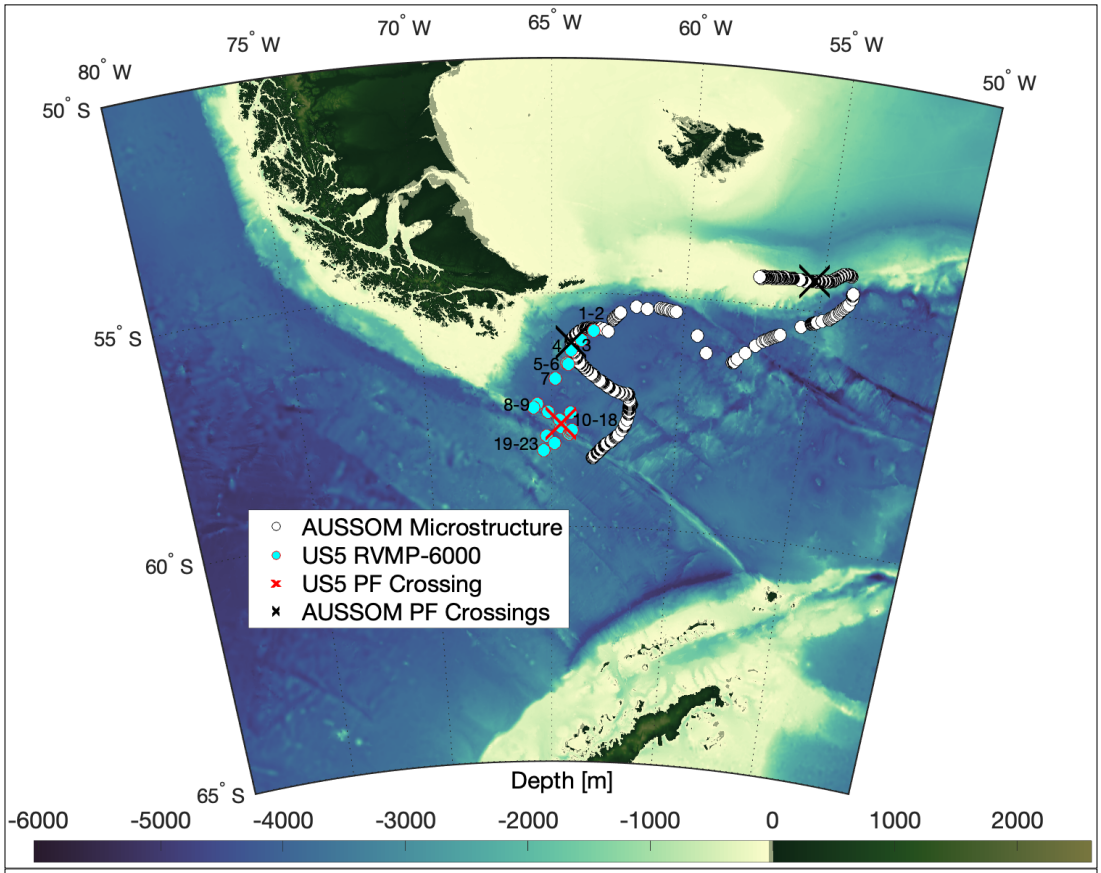

Figure 1: Field data. Showing synchronous microstructure and CTD profiles from the DIMES US5 cruise (Oct.-Nov.2013) and AUSSOM glider survey (Nov.-Dec.2017) used for comparison of TKE dissipation rate estimated from finescale strain parameterization (FSP) to direct measurements. The Polar Front (PF) is a dynamic, meandering structure which changes location over time and marks the subduction of cold, fresh Southern Ocean water beneath warm, salty Subantarctic water.

collected during DIMES with a first-of-its-kind glider survey (Fig. 1) to test FSP in an intense frontal zone — the Drake Passage and Scotia Sea regions of the Antarctic Circumpolar Current. Understanding FSP and its representation of downscale energy transfer in frontal regions is necessary for progressing TKE estimation from unmanned platforms and our fundamental understanding of ocean circulation, as well as understanding the global patterns of diapycnal diffusivity from which we calibrate large-scale circulation models.

2. Methods

The Autonomous Sampling of Southern Ocean Mixing (AUSSOM) study was conducted in the Drake Passage region between the end of Austral Winter (November 2017) and the beginning of Austral Spring (February 2018). As part of this study, a Slocum glider *Starbuck* with a pumped Seabird CTD and a Rockland MicroRider microstructure sensor was used to collect a 6-week turbulence record spanning 800 km from the Shackleton Fracture Zone to the Falkland Plateau. Slocum glider *Starbuck* was deployed on 16-November-2017 during LMG-1802 from the R/V Laurence M. Gould, conducted an 82 day mission in the Polar Front, and was recovered near Port Stanley, Falkland Islands on February 5th. The glider sampled for 60 days until sampling was disabled to preserve battery. The AUSSOM mission collected 3,028 CTD profiles and 932 microstructure profiles at depths between 0 and 350 meters. The details of glider microstructure data processing are described in St. Laurent & Merrifield (2017). Ferris et al. (in revision) previously used this dataset to quantify correctable bias in surface boundary layer scalings of shear turbulence.

Cruise US5 (or NBP1310A) was the Drake Passage leg of the Diapycnal and Isopycnal Mixing Experiment in the Southern Ocean (DIMES) and took place at the end of Austral Winter in 2013 (from October 26th through November 13th) on the RVIB Nathaniel B. Palmer. The cruise included 48 CTD and LADCP stations, with 23 full-depth microstructure profiles downstream of Phoenix Ridge and over the Shackleton Fracture Zone. Many of the 23 stations were in and around the SAF and PF. Full-depth turbulence measurements were collected using a free-falling Rockland VMP-6000 with dual shear and thermistor probes. The cruise also included 5 tow-yo segments of a Rockland VMP-250. Cruise reports for DIMES US5 and other DIMES cruises are available at http://dimes.ucsd.edu. The DIMES US5 VMP-6000 and AUSSOM glider were each equipped with a Sea-Bird CTD (a pumped CTD in the case of the glider). CTD data from both were used for FSP analysis. Our analysis utilizes these two datasets and proceeds as follows: (1) For DIMES, we compute ϵ_{FSP} from CTD data collected at the 23 microstructure stations and compare it to directly measured ϵ from the VMP. (2) For AUSSOM, we similarly compute ϵ_{FSP} from the glider CTD and compare it to measured ϵ from the Rockland microstructure sensor. (3) Calculate the density ratio (R_ρ) for each of these CTD records to identify T/S-intrusive regions. (4) Examine the FSP bias $\log_{10}(\epsilon_{FSP}/\epsilon)$ inside (outside) of fronts and the T/S-intrusive regions.

We apply the FSP methodology as follows. The first step is to subdivide CTD profiles into vertical segments; we use half-overlapping segments 100 meters in length and average the primary segments with secondary (staggered) segments to produce FSP estimates over 50-meter intervals. For DIMES US5, segments span from 200m to 4200m

Table 1. Variables of finescale strain parameterization (FSP)

Variable	Unit	Description
ϵ_{strain}	W/kg	Estimated TKE dissipation rate (Eq. 1).
ϵ_0	W/kg	6.73×10^{-10}, canonical GM dissipation rate for N_0 at latitude 30°.
N_0	rad/s	5.24×10^{-3}, canonical GM buoyancy frequency.
N	rad/s	Buoyancy frequency computed from CTD e.g. via Gibbs-SeaWater Oceanographic Toolbox.
$\overline{N}$	rad/s	Mean buoyancy frequency for each segment, bin-averaged from N.
N_{smooth}	rad/s	Buoyancy frequency smoothed using quadratic fitting (Kunze et al., 2006) or calculated from CTD using adiabatic leveling (Huussen et al., 2012) e.g. via github.com/OceanMixingCommunity/Standard-Mixing-Routines. The latter is used here.
$\langle \xi_z^2 \rangle$	n.d.	Observed strain variance (Eq. 4).
$\langle \xi_{zGM}^2 \rangle$	n.d.	GM strain variance (Eq. 4).
S_{str}	[rad/m]$^{-1}$	Strain spectrum computed from ξ_z for each segment using Welch's power spectral density estimate (Welch, 1967).
S_{strGM}	[rad/m]$^{-1}$	GM model strain spectrum computed from f and $\overline{N}$ for each segment, e.g. via github.com/jklymak/GarrettMunkMatlab. Gregg & Kunze (1991) parameters are used here.
$k_{min} = \frac{2\pi}{\lambda_{max}}$	rad/m	Low-wavenumber integration limit, $2\pi/100$m is used here. λ_{max} should not be larger than the segment length (i.e. the fundamental wavenumber), nor ~150m to avoid accidental eddy contributions (Kunze et al., 2006).
$k_{max} = \frac{2\pi}{\lambda_{min}}$	rad/m	High-wavenumber integration limit, $2\pi/10$m is used here. This should be chosen to avoid the high-wavenumber roll-off, as well as be below the Nyquist wavenumber of sampling resolution Δz.
L	n.d.	Correction for latitudinal variability of internal wavefield (Eq. 5).
f	rad/s	Coriolis frequency.
f_{30}	rad/s	7.2921×10^{-5}, reference Coriolis frequency at latitude 30°.
h	n.d.	Dependence on shear-to-strain ratio (Eq. 3), reduces to 1 when $R_\omega = 3$.
R_ω	n.d.	Shear-to-strain ratio, 3 assumes GM frequency spectrum but we use 10 after Kunze et al. (2006); Nikurashin & Ferrari (2010).
ξ_z	n.d.	Strain computed for each segment (Eq. 2).
Δz	m	Sampling resolution within each segment, typically $\Delta z \approx 1$m for DIMES US5 and $\Delta z \approx 0.3$m for AUSSOM.

(or the VMP profile depth), following the practice of removing shallow depths from analysis. For AUSSOM, segments span from 150m to 350m. We are confident that this slightly-shallower choice is a safe one after analyzing actively mixing layer and mixed layer dynamics in Ferris et al. (2020b) and Ferris et al. (in revision) because it is well below the surface mixed layer features. TKE dissipation rate (Eq. 1) is computed for each segment of each profile. Next we calculate the strain (Eq. 2), which utilizes three forms of buoyancy frequency (Table 1) to quantify the density deformation of the water column:

$$\xi_z = \frac{N^2 - N^2_{smooth}}{\overline{N^2}} \qquad (2)$$

Fluid strain is similar to mechanical strain (a tensor metric of material deformation); one might think of (Eq. 2) as quantifying the deformation in stratification, assumed to be caused by internal waves (IW). Of course (Eq. 2) is not the formal definition of fluid strain, but is used because time-mean density profiles are not available; in their absence the scale of the segments is assumed to represent the time mean and variations within this scale represent internal wave

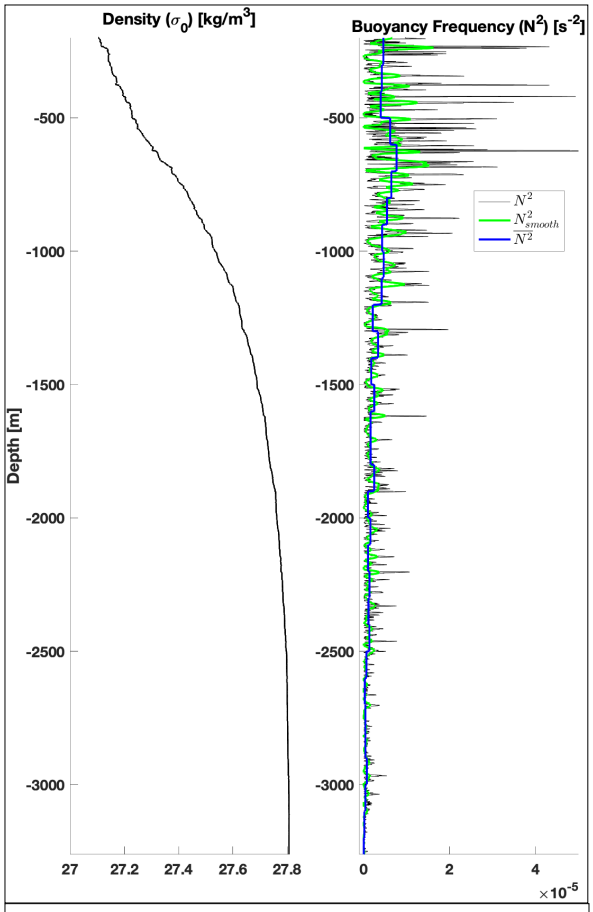

Figure 2: Three forms of buoyancy frequency used in (Eq. 1), calculated for DIMES US5 profile 17. To be clear, the density profile is not directly involved in the calculation of strain and is just provided for reference.

activities (discussed in Mauritzen et al., 2002). The calculation is performed in only one spatial direction (down in the case of DIMES US5, or along the glider's flight path in the case of AUSSOM) and do not require 3-D strain tensor representation. By estimating the deformation (allegedly caused by internal waves), we can estimate the internal wavefield itself (and its energy content) and assume that this energy content at the finescale will dissipate as TKE at the microscale.

The connection between fluid deformation at the finescale and IW energy contained at that scale is the GM model spectrum, which is used as a reference to estimate IW energy from strain. The GM spectrum describes internal wave energy as a function of IW wavenumber (relatable to strain) and IW frequency (relatable to shear). In the absence of fluid velocity information, dependence on shear is calculated (Eq. 3) from an assumed shear-to-strain ratio R_ω:

$$h(R_\omega) = \frac{1}{6\sqrt{2}} \frac{R_\omega(R_\omega + 1)}{\sqrt{R_\omega - 1}} \tag{3}$$

and our focus is narrowed to comparing the observed strain to reference strain using the ratio of their variance $\langle \xi_z^2 \rangle / \langle \xi_{zGM}^2 \rangle$. For a stationary ergodic random process, spatial-domain variance of a signal (strain in this case) is equal to its spectrum integrated over wavenumber in the wavenumber domain (i.e. Parseval's theorem). It is advantageous to compute the variance of each strain segment in the wavenumber domain (rather than the spatial domain) because this facilitates comparison with the GM spectrum (which is function of wavenumber). Observed and GM strain variances ($\langle \xi_z^2 \rangle$ and $\langle \xi_{zGM}^2 \rangle$) are

calculated from their respective spectra (S_{str} and S_{strGM}) over an identical range of wavenumbers (k) using (Eq. 4) (Fig. 3):

$$\langle \xi_z^2 \rangle = \int_{k_{min}}^{k_{max}} S_{str}(k) dk \tag{4}$$

Prior to calculating the observed strain spectrum S_{str} each strain segment ξ_z is de-trended; and a convolution window with 10% $\sin^2$ taper is applied in order to minimize spectral distortion of the segment's wavenumber content due to discontinuity at the edges. In other words, first and last tenth of the segment are smoothly brought to zero using multiplicative factor $\sin^2\left(0.1\frac{\pi z}{2n}\right)$, where n is the length of the strain segment. The spectrum S_{str} is corrected for power lost to windowing and multiplied by transfer function $\mathbf{sinc}^{-2}(k\Delta z/2\pi)$, where $\mathbf{sinc}(x) = \sin(\pi x)/(\pi x)$ to correct

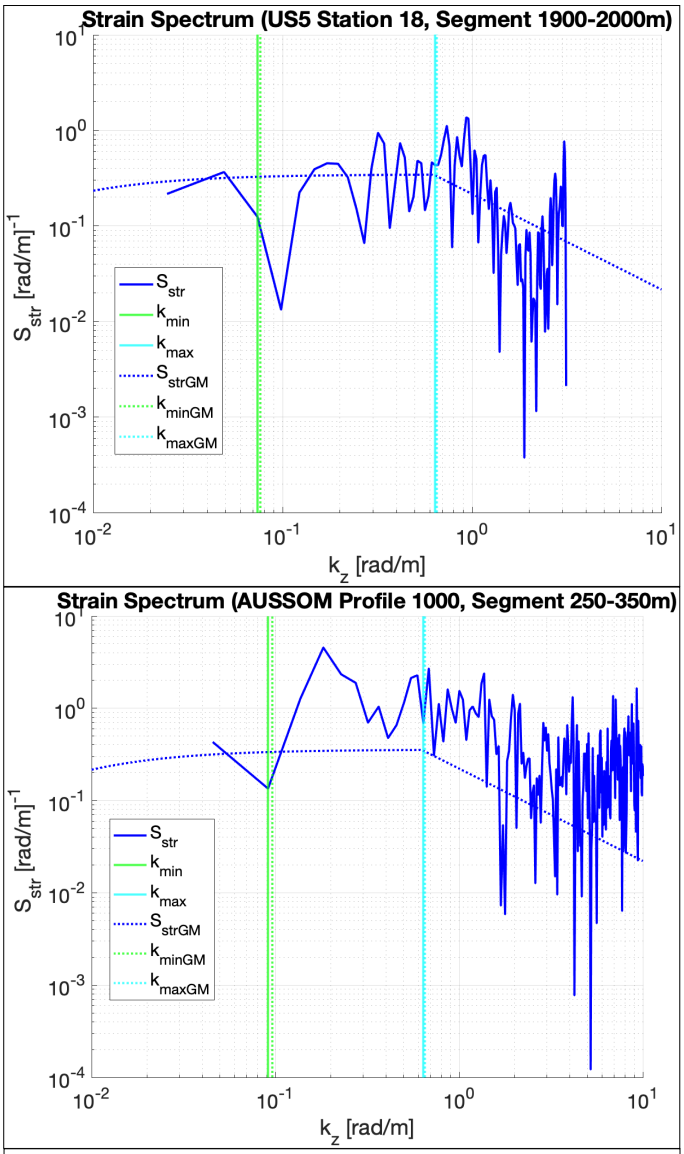

Figure 3: Example strain spectra and limits of integration (Eq. 4) for one segment of DIMES US5 and one segment of AUSSOM (corresponding to 13-Dec-2017 09:15:17).

for finite differencing, where Δz is the vertical resolution of each segment.

Following concerns that at high energy levels the measured strain spectrum could become saturated (transition to 3D turbulence) before the high energy roll-off point k_c (Gargett, 1990) such that (Eq. 4) erroneously include part of the dissipation scale and overestimate the strain variance, it has been popular in the literature to adjust the high wavenumber (low wavelength) integration limit until $\langle \xi_z^2 \rangle \leq 0.1$ or 0.2 (Huussen et al., 2012; Whalen et al., 2015). The practice evolved from the sensible usage of this integral constraint in Kunze et al. (2006), but we suggest the reconsideration of this convention for two reasons. The first reason is that significant advance in sensing technology since 1990 has rendered the practice of calculating the strain spectrum down to 10 meter scale obsolete. We have the ability to measure strain to much smaller scale (e.g. 1 meter for DIMES US5 and ~0.3 meters for AUSSOM, which are furthermore free-falling and uncontaminated by ship heave around the 10 meter scale), have greater confidence that k_c seen in the spectrum is truly the roll-off point, and do not need to discard that much of the internal wave subrange (Klymak & Moum, 2007). Our ability to select $k_{max} \approx k_c$ makes this study robust to additional sources of bias such as wave-flow (critical layer) interactions which are problematic when $k_{max} \ll k_c$ (Polzin et al., 2014; Waterman et al., 2013)

The second reason is purely logical. Deliberately constraining the integration limits (Eq. 4) beyond the observed roll-off point (to always produce a strain variance of $\langle \xi_z^2 \rangle \leq 0.1$) manipulates the observed strain variance $\langle \xi_z^2 \rangle$ until it matches what we wish it to be. The internal wave subrange is not necessarily parallel to GM spectrum, therefore

picking and choosing different subsets of the internal wave subrange to include in our calculation of strain variance can produce wildly different strain variances; it is most accurate to use as much of the inertial subrange as possible. There is no ontological reason for applying this criterion other than as a workaround for not being able to consistently determine k_c given measurement limitations (applicable when resolved strain was coarser). From inspection of S_{str} vs. k, a choice of $k_{max} = 2\pi/\lambda_{min} = 10\mathbf{m}$ is a suitable k_c for our datasets.

A correction for latitudinal variability of internal wavefield is also calculated (Eq. 5) for each segment. All variables, their units, and their sources are summarized in Table 1.

$$L(f,N) = \mathfrak{R}\left\{\frac{f\cosh^{-1}(\overline{N}/f)}{f_{30}\cosh^{-1}(N_0/f_{30})}\right\} \tag{5}$$

Shear- and/or strain-based finescale parameterizations do not apply to the continental shelf where the assumption of a broadband, source-agnostic IW wave spectrum fails outright (MacKinnon & Gregg, 2003), and so we omit AUSSOM profiles beyond the beginning of the continental rise. This constraint leaves 1504 CTD profiles, 739 of which have synchronous microstructure. Due to the large spatial extend of the AUSSOM dataset and immense spatial variability of TKE dissipation rates in the Drake Passage and Scotia Sea, we elect not to average adjacent CTD profiles (as one might be tempted to do) in order to investigate the success or failure of each individual application of FSP. Finally, before proceeding we wish to discuss a nuance of averaging that is often not discussed in literature involving measurements or estimates of TKE dissipation rate.

The arithmetic mean is commonly used to estimate the first probability moment (average) when data is normally-distributed or close to it. TKE dissipation rate is not remotely normally-distributed as the values often span multiple orders of magnitude (rather, it is log-skew-normally distributed [Cael & Mashayek, 2021]), such that the arithmetic mean is close to a maximum rather than unbiased estimator of centroid. This issue of large values dominating the arithmetic mean is discussed in Waterman et al. (2013). Arithmetic means can be used to obtain average energetics from uniformly-distributed turbulent kinetic energy dissipation rates, but should not be used to evaluate biases in the the statistical ensemble of turbulence parameterizations. As such, we apply logarithmic transformation before taking the mean, giving the better estimator (Eq. 6), which is also the geometric mean:

$$\hat{\epsilon} = \frac{1}{n}\sum_{n=1}^{n} \log_{10} \epsilon_n \tag{6}$$

We will revisit the choice of geometric vs. arithmetic mean in the Discussion section.

Finally, to find density ratio R_ρ for each segment (Fig. 4), the procedure is to take a moving average of absolute salinity and conservative temperature with a window of approximately 33-meters. Then R_ρ is calculated using the Gibbs SeaWater (GSW) Oceanographic Toolbox of TEOS-10. For section plots (i.e. Fig. 7a, 8a, 13) R_ρ is averaged in 10-meter vertical bins, chosen based on the expected scale of TS intrusions) to facilitate visual comparison with TKE dissipation rate. For instances requiring a single representative value of $\overline{R_\rho}$ for each half-segment (i.e. Fig. 7b, 8b, 15a), R_ρ is averaged in

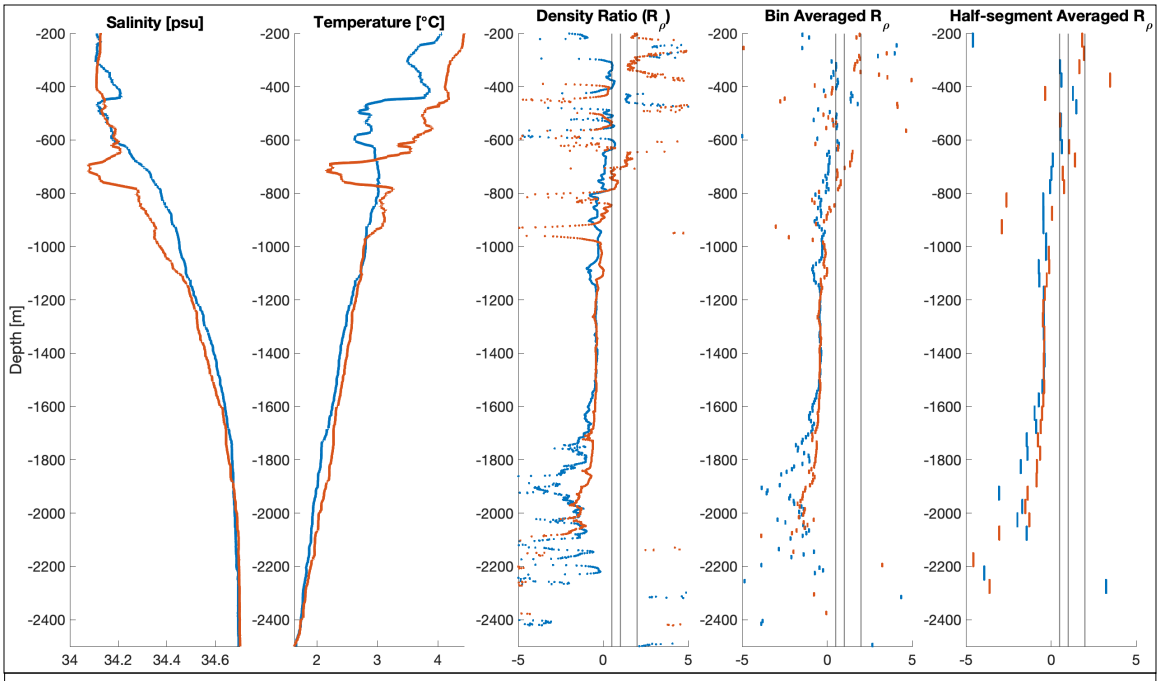

Figure 4: Calculation of density ratio R_ρ for two profiles (Station 2 and 14) of US5. Values falling between vertical lines indicate stratification favorable to double diffusive instability.

50-meter vertical bins. In both cases, the procedure is to first check for the presence of $0.5 < R_\rho < 2$ (indicative of double diffusive instability) within a bin; then take the average of doubly-unstable values if present, or all values if no unstable R_ρ are found. In rare cases where multiple stable values ($R_\rho < 0.5$ or $2 < R_\rho$) average to produce a mean falsely indicative of stratification unstable to double diffusive instability, only R_ρ of the dominant side are averaged e.g. $\overline{R_\rho} = (-100 + 51 + 52)/3 = 1$ would become $\overline{R_\rho} = (51 + 52)/2 = 51.5$. The purpose of this scheme is to ensure the identification of bins containing subparts favorable to double diffusive instability when the entire segment is not doubly-unstable. This method is could create a discontinuity near $\overline{R_\rho} = 0.5 \cup 2$ in the x-axis ($\overline{R_\rho}$) but has no influence on the y-axis (bias or magnitude of ϵ_{FSP}).

3. Results

For DIMES US5, at first glance (Fig. 5a) FSP estimates of TKE dissipation show good agreement with the microstructure TKE measurements below the main thermocline.

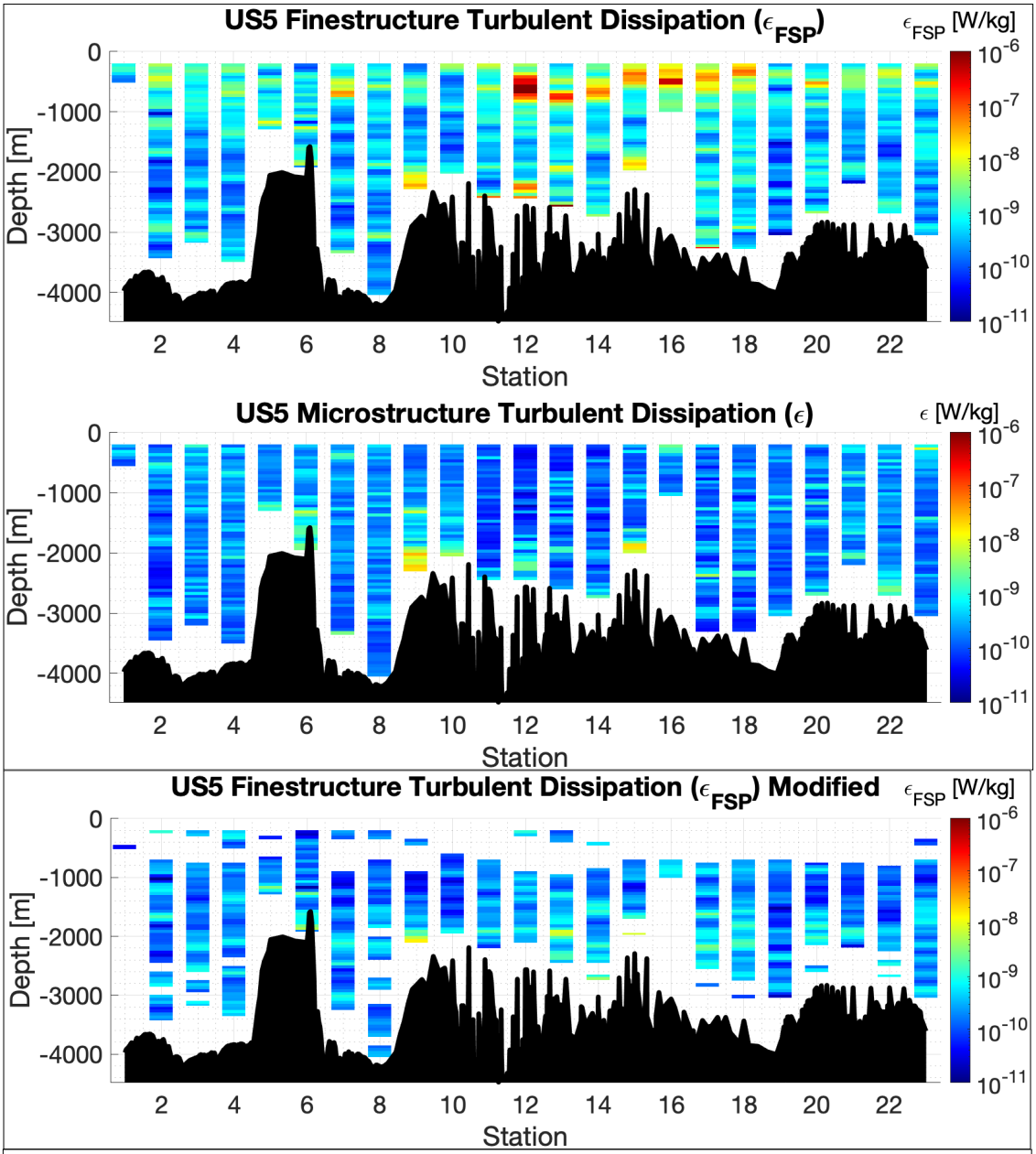

Figure 5: FSP-estimated and measured TKE dissipation rate for US5. Measured dissipation rate has been bin-averaged to facilitate comparison with estimated dissipation. The bottom panel corresponds to modified FSP (Fig. 11, discussed later) and uses a shear-to-strain ratio R_ω which transitions from 3 to 10 as in Fig. 10. Additionally all data prone to T/S-intrusive features has been removed from use.

FSP captures but underestimates bottom-intensified TKE dissipation rates at stations 6, 9, 12, and 15 as would be expected; the GM spectrum does not represent this efficient boundary layer pathway of energy cascade into the microscale. Enhanced dissipation at these stations (Fig. 5b) is consistent with past findings of internal lee waves being generated over topography, radiating energy upward, and breaking (Nikurashin & Ferrari,

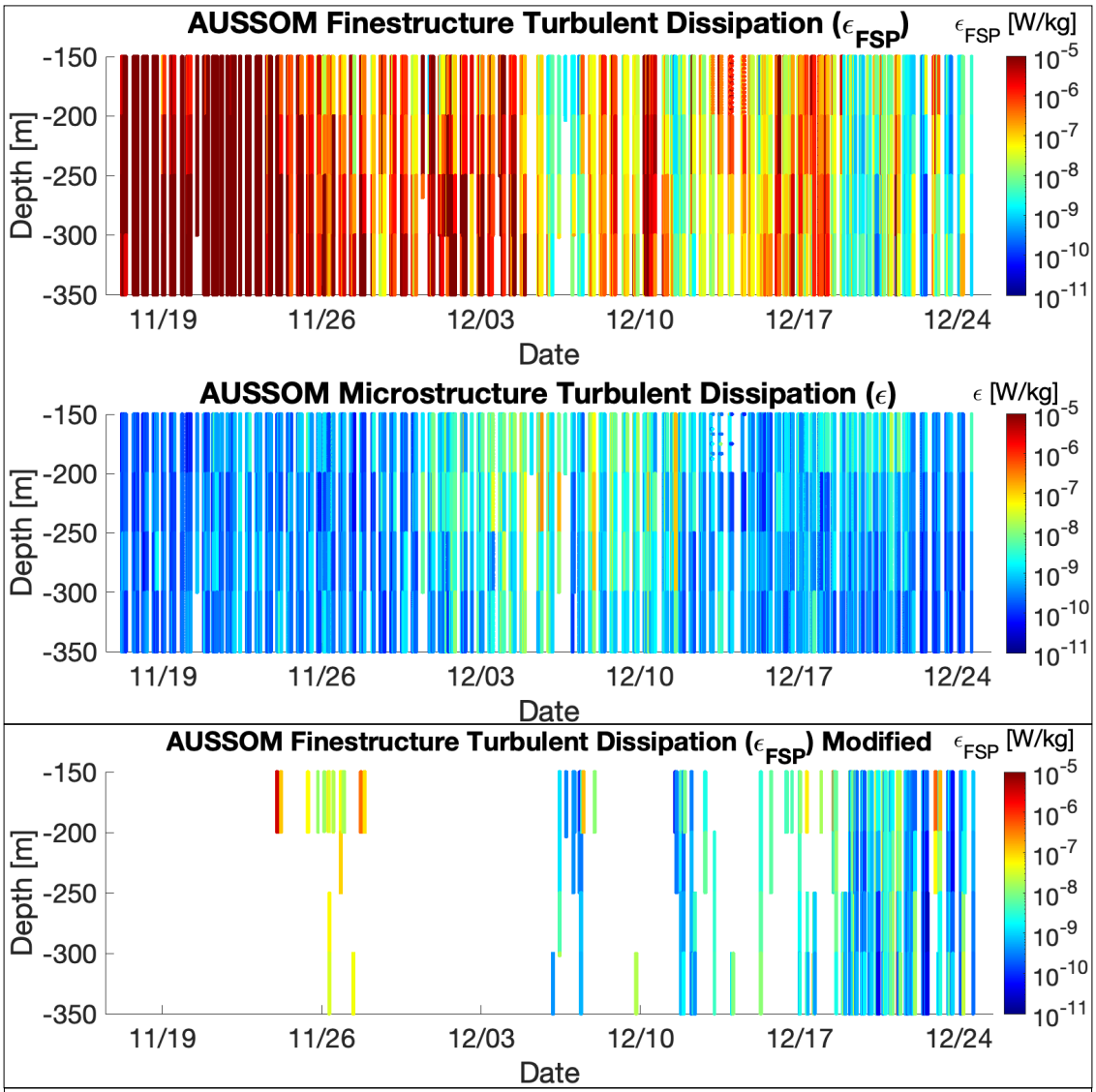

Figure 6: FSP-estimated and measured TKE dissipation rate for AUSSOM. Measured dissipation rate has been bin-averaged to facilitate comparison with estimated dissipation. The bottom panel corresponds to modified FSP (Fig. 11, discussed later) and uses a shear-to-strain ratio R_ω which transitions from 3 to 10 as in Fig. 10. Additionally all data prone to T/S-intrusive features has been removed from use.

2010; St. Laurent et al., 2012); the GM spectrum does not represent such a lee wave contribution, which has been shown to raise TKE dissipation rates to 10^{-8} W/kg. FSP estimates are in general too high in the main thermocline and above, and there is spatial variation in this overestimation. For AUSSOM, the mild overestimation by FSP at shallower depths (Fig. 6a) is consistent with the same depth levels of DIMES US5 but varies intensely during the record, with severe bias before 12/03. DIMES US5 and AUSSOM are fundamentally different in that DIMES US5 was targeted at sampling throughout the Drake Passage, while AUSSOM crossed in the Polar Front on 11/28 and remained in the core of the front though 12/23. FSP methodology does not capture frontally intensified mixing processes between 12/01 and 12/12 (Fig. 6b) which are attributed to internal wave interactions. These are briefly addressed in Ferris et al. (in revision) and will be investigated in a follow-on paper dedicated to the role of internal waves and frontal instability in downscale energy cascade in ACC jets.

Focusing on the upper 2500 meters of DIMES US5 (Fig. 7) where FSP exhibits the greatest bias and is most susceptible to T/S intrusions (Merrifield et al., 2016) around the Polar Front (south of 57º) where there are more instances of doubly-unstable stratification. The bias $\log_{10}(\epsilon_{FSP}/\epsilon)$ and density ratio R_ρ for each segment in Fig. 7a are scattered in Fig. 7b, with segments collocated with doubly-unstable stratification colored in pink and yellow for the diffusive and salt fingering regimes of double diffusive instability, respectively (both regimes of double diffusive instability are possible when $R_\rho \approx 1$). The worst biases (i.e. above 1.5 orders of magnitude) are collocated with unstable segments. This exercise is repeated for AUSSOM (Fig. 8) and produces similar

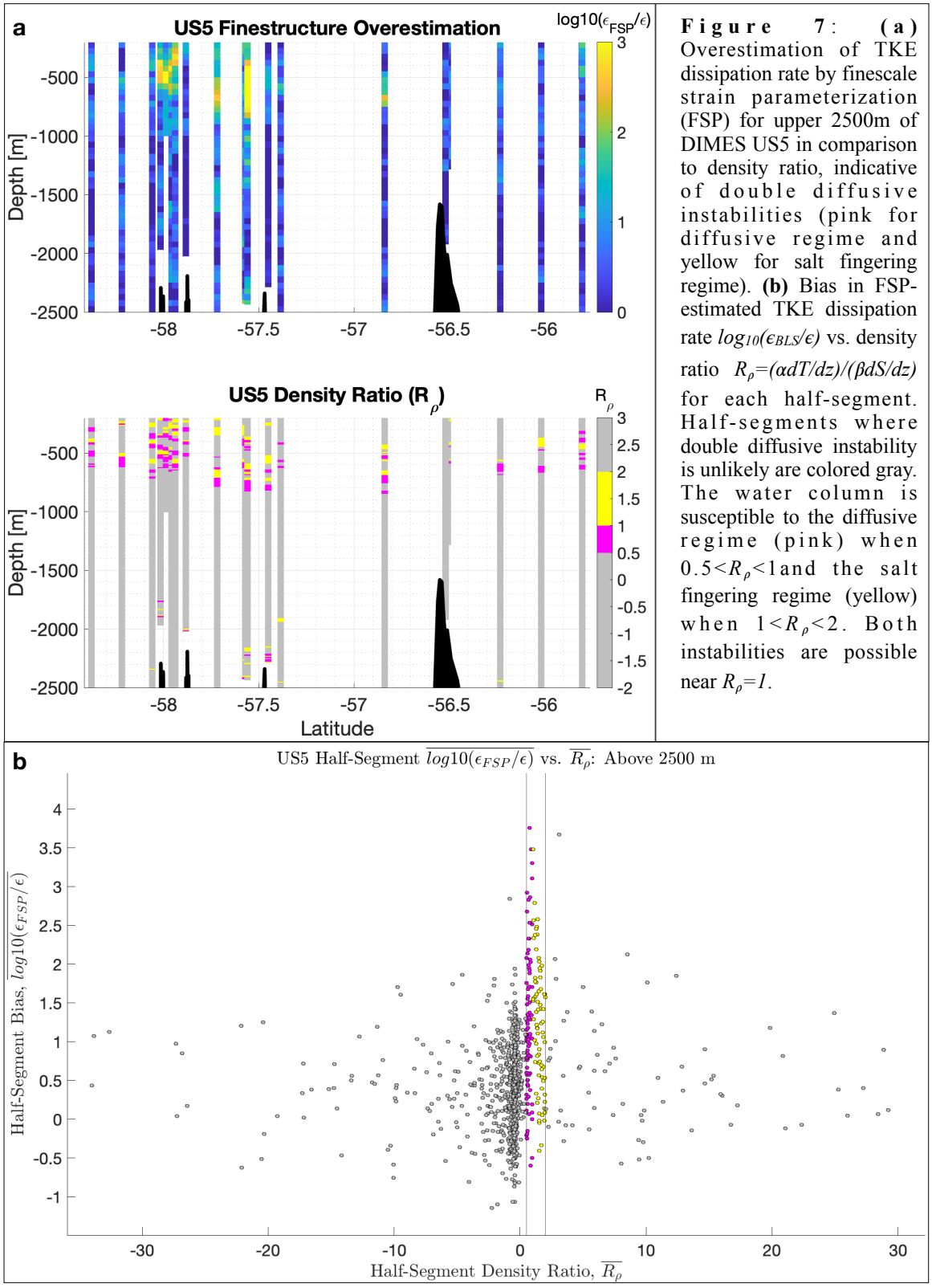

Figure 7: (a) Overestimation of TKE dissipation rate by finescale strain parameterization (FSP) for upper 2500m of DIMES US5 in comparison to density ratio, indicative of double diffusive instabilities (pink for diffusive regime and yellow for salt fingering regime). **(b)** Bias in FSP-estimated TKE dissipation rate $log_{10}(\epsilon_{BLS}/\epsilon)$ vs. density ratio $R_\rho=(\alpha dT/dz)/(\beta dS/dz)$ for each half-segment. Half-segments where double diffusive instability is unlikely are colored gray. The water column is susceptible to the diffusive regime (pink) when $0.5<R_\rho<1$ and the salt fingering regime (yellow) when $1<R_\rho<2$. Both instabilities are possible near $R_\rho=1$.

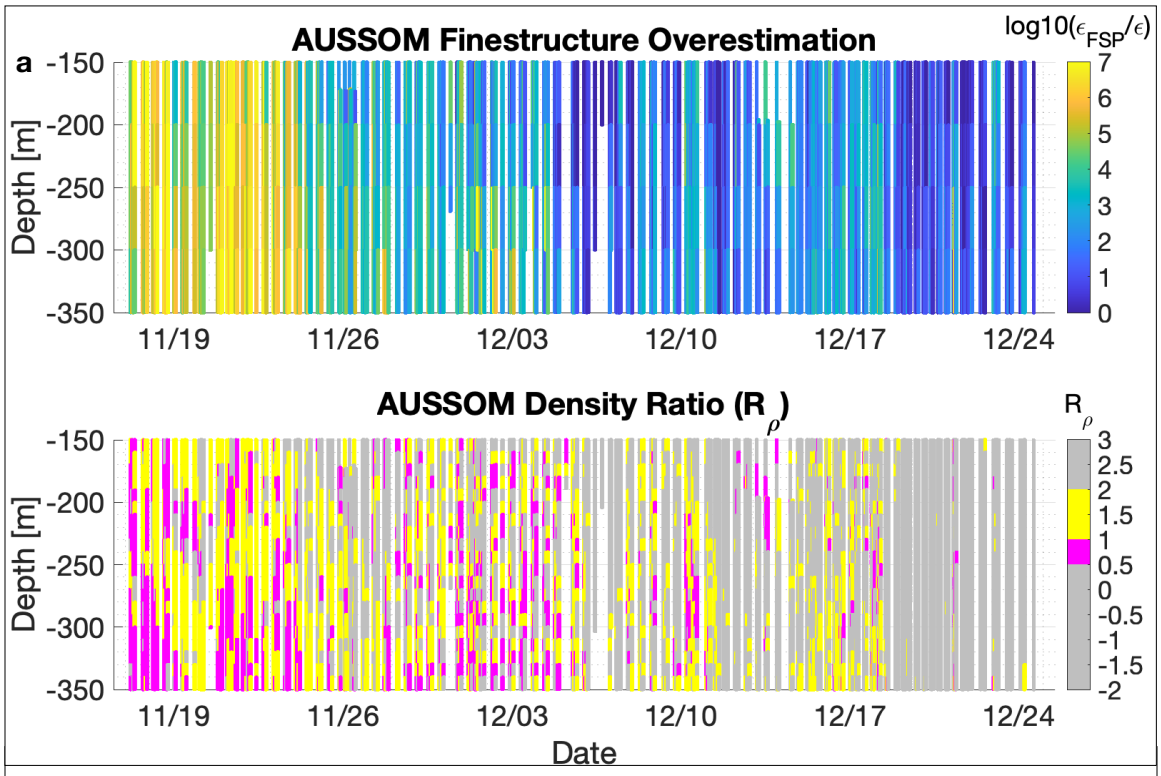

Figure 8: **(a)** Overestimation of TKE dissipation rate by finescale strain parameterization (FSP) for AUSSOM in comparison to density ratio, indicative of double diffusive instabilities (pink for diffusive regime and yellow for salt fingering regime) (same as Fig. 7a). **(b)** Bias in FSP-estimated TKE dissipation rate $log_{10}(\epsilon_{BLS}/\epsilon)$ vs. density ratio $R_\rho=(\alpha dT/dz)/(\beta dS/dz)$ for each half-segment (same as Fig. 7b).

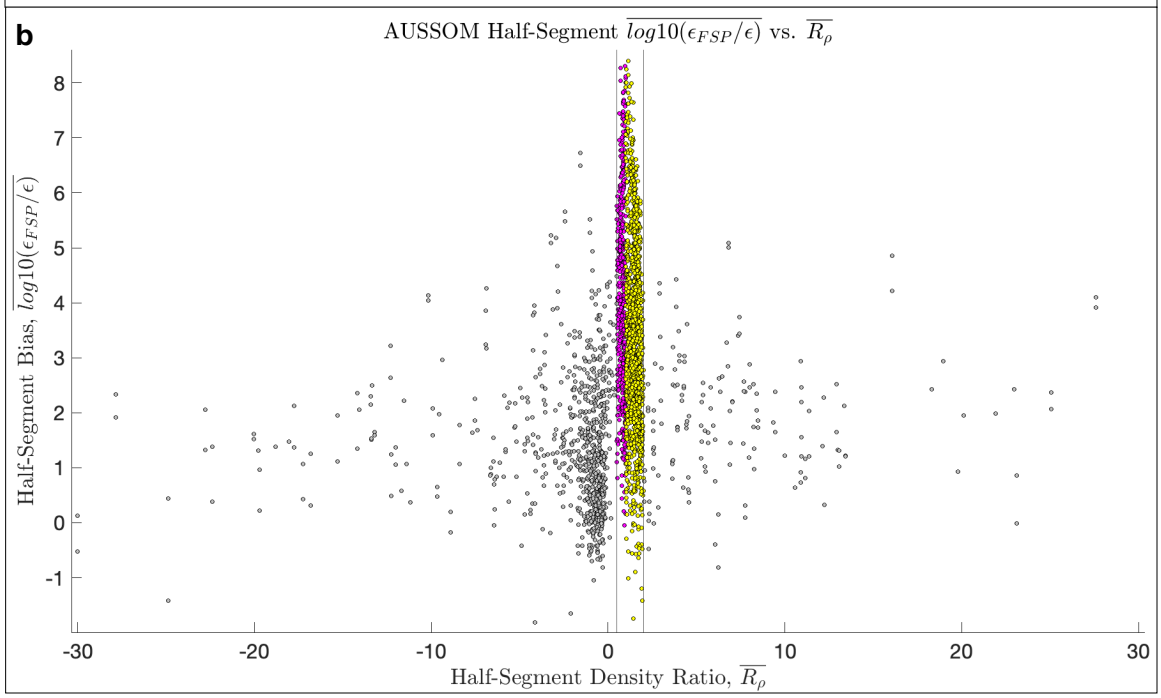

results. Segments corresponding to doubly-unstable stratification are associated with biases of up to 8 orders of magnitude. In other words, FSP estimates 100,000,000 times the amount of TKE dissipating in the water than is actually dissipating (though it should be noted that this the compound error from all physical sources and cannot entirely be attributed to double diffusive instability.

The established practice for applying FSP to autonomous platforms is to average as many profiles as are available for a given region to produce a climatological estimate for TKE dissipation rate. Ensemble averages with 90% bootstrapped confidence intervals are given for DIMES US5 and AUSSOM (Fig. 9). After Whalen et al (2015) and other literature applications of FSP, for the purposes of calculating confidence intervals the epsilon value for each half-segment is treated as one sample rather than each singular CTD sample that went into the TKE estimate for that half-segment. Contaminated segments, including the 50m segments above and below each segment containing 0.5 <Rp <2, are removed from the left average (red) to produce the right average (green). (Due to half-overlapping segments used to obtain FSP epsilon, a T/S-intrusive feature in a given 50m half-segment could theoretically contaminate the 50m half-segments above and below a contaminated segments. For Fig. 7 and Fig. 8, sensitivity analysis was performed to determine the effect of considering contamination in adjacent bins and its effects were found to be negligible.) Upon removing contaminated segments, DIMES US5 shows improvement by up to half an order of magnitude above 900m but this is confounded by fewer measurements within each bin, widening confidence intervals. It is misleading to draw conclusions from the DIMES US5 profiles because eliminating

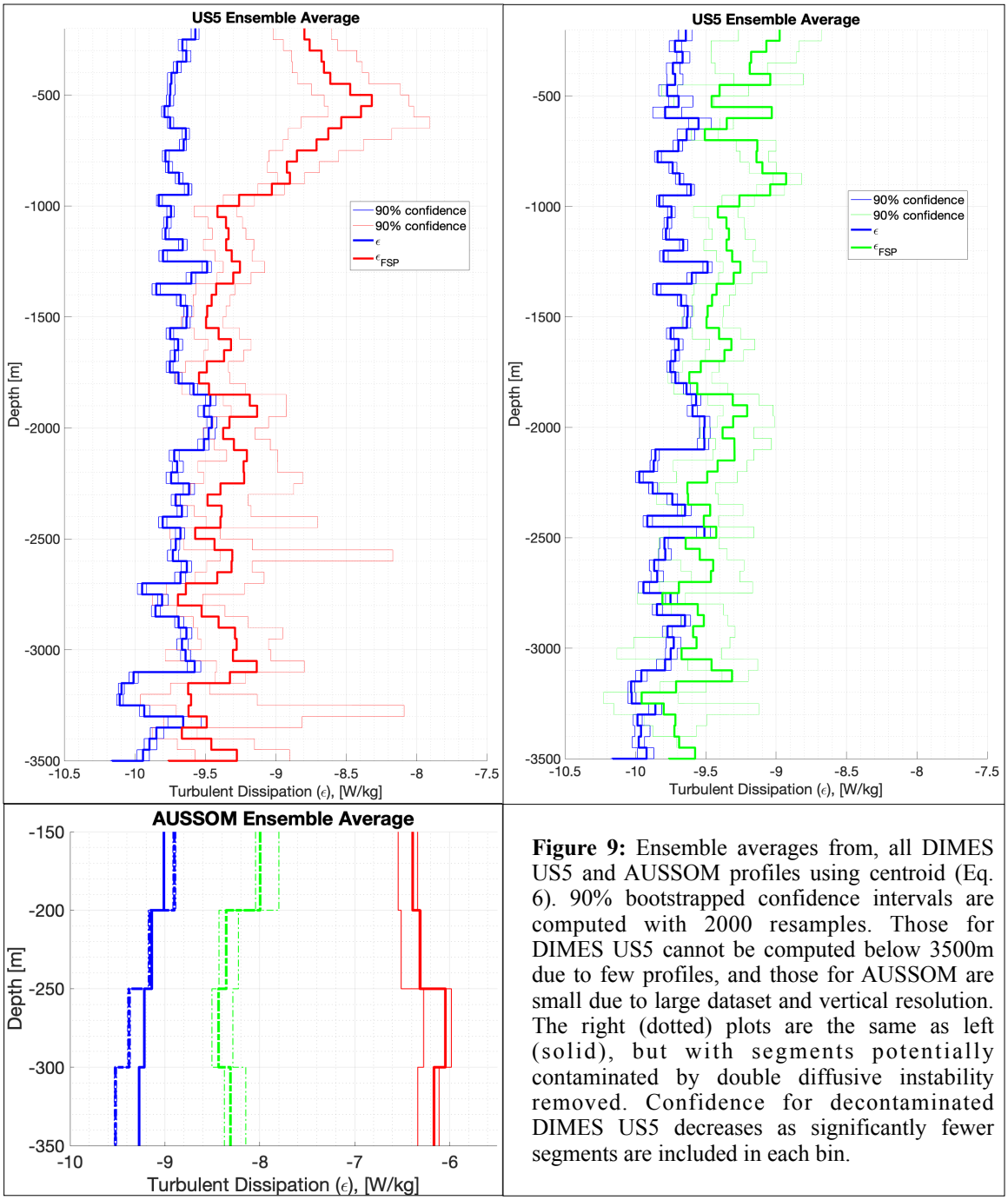

Figure 9: Ensemble averages from, all DIMES US5 and AUSSOM profiles using centroid (Eq. 6). 90% bootstrapped confidence intervals are computed with 2000 resamples. Those for DIMES US5 cannot be computed below 3500m due to few profiles, and those for AUSSOM are small due to large dataset and vertical resolution. The right (dotted) plots are the same as left (solid), but with segments potentially contaminated by double diffusive instability removed. Confidence for decontaminated DIMES US5 decreases as significantly fewer segments are included in each bin.

contaminated segments from the average drastically reduces the number of profiles contributing to each bin, with sometimes only a single profile in a bin such that a confidence interval cannot be computed, for example the 550-650m bin.

In contrast, the large sample size (739 profiles) of AUSSOM makes this a more reliable practice, and it is evident that removing contaminated segments improves the ensemble average by approximately an order of magnitude. However, the ensemble average for FSP-estimated TKE dissipation rate (ϵ_{FSP}) remains 1-2 orders of magnitude higher than microstructure TKE dissipation rate (ϵ) suggesting a remaining discrepancy due to Assumption 2 and Assumption 3. The remaining bias suggests that implementation of depth-varying shear-to-strain ratio might be appropriate, contrary to the general practice of choosing a constant shear-to-strain ratio. Similarly, departure in the Southern Ocean internal wave spectrum from the GM spectrum could explain the residual overestimation by FSP. The GM spectrum does not account for enhanced internal lee wave content in the Southern Ocean produced by strong geostrophic flow impinging on complex topography. In the future, it may be worth employing a methodology leveraging alternative spectral presentations as motivated by stratified turbulence literature.

4. Discussion

For both DIMES US5 and AUSSOM, we have used FSP to estimate TKE dissipation rate from CTD and compared to direct microstructure measurements to show that double diffusive instabilities are associated with large biases. In other words, double diffusive instabilities contaminate FSP, compounding with other sources of bias to estimate up to 10^8 times the TKE dissipation in the Polar Front than actually occurs in the ocean. Strain-based methodology (FSP) is vulnerable to failure in intrusive water mass regions and likely falls outside of the widely reported agreement factor of 2-3 in frontal regions of the global ocean where double diffusive instabilities are active. This is notable

because the community might otherwise consider applying FSP as-is to the global CTD from the international Argo program to solve ocean mixing problems. Sites of elevated TKE dissipation as estimated from Argo floats (Whalen et al., 2015) are in many places collocated with frontal regions where frontal physics might contaminate the internal wave-associated strain spectrum with a double diffusive instability spectrum. In other words, the observed strain spectrum attributed to internal waves is actually convolved with a second strain spectrum attributable to double diffusive instabilities. Recall that the core assumptions of FSP are that observed strain-like features are internal wave strain (Assumption 1), the internal wave spectrum is well-represented by the GM spectrum (Assumption 2), and downscale energy transfer steadily occurs via nonlinear wave-wave interactions such that for a control volume the production of turbulent kinetic energy by shear matches the dissipation by molecular viscosity and buoyancy flux (Assumption 3). As such, FSP (Eq. 1) violates Assumption 1 and should be paired with a R_ρ-based data selection rule when applied anywhere in the ocean but especially

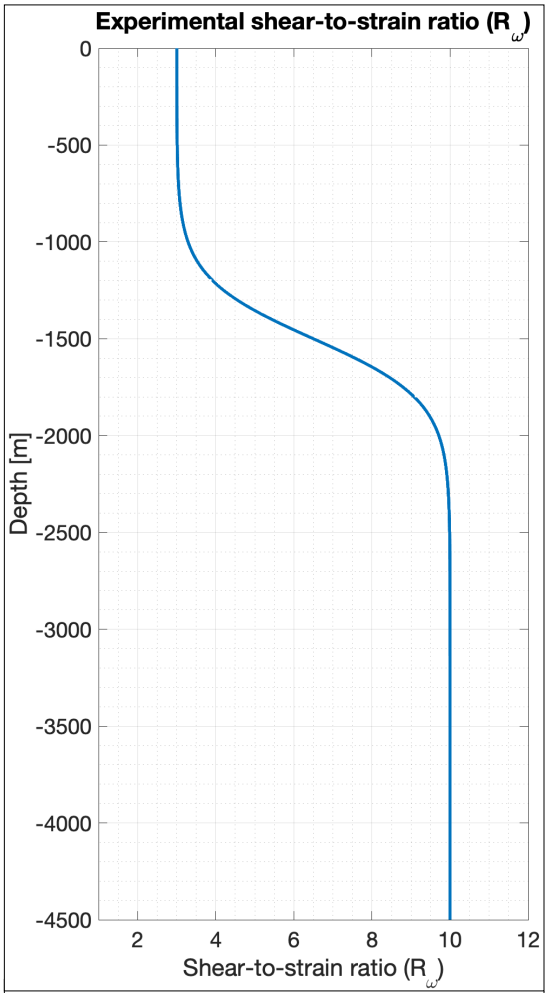

Figure 10: Experimental depth-varying shear-to-strain ratio used to produce Fig. 11. This is a hybrid of G-M theory $R_\omega=3$ and the inertial oscillation-enhanced $R_\omega=10$ and has equation $R_\omega(z)=3.5\tanh[2\pi(z-1500)/2000)]+6.5$.

frontal regions. Succinctly, FP should not be performed when R_ρ indicates that double diffusive instabilities are possible.

Assumption 3 is difficult to assess with the high-resolution data available (e.g. AUSSOM does not have associated velocity measurements) which leaves us to speculate about Assumption 2, that the content shear-to-strain ratio chosen from the literature ($R_\omega = 10$) reasonably represented the aspect ratio of the internal wave spectrum in all parts of the water column. We recall that if the true shear-to-strain ratio is lower than the assumed constant R_ω in any part of the water column, ϵ_{FSP} will be an overestimate of true TKE dissipation rate ϵ. Furthermore, the physical mechanism justifying high shear-to-strain ratio (bottom-intensified inertial oscillations) in Nikurashin & Ferrari (2010) should become less dominant away from the bottom boundary. As a matter of speculation, we test a shear-to-strain ratio $R_\omega(z)$ which smoothly transitions from the GM assumed $R_\omega = 3$ above 1000m to the literature-supported $R_\omega = 10$ below 2000m (Fig. 10). FSP is repeated for both DIMES US5 and AUSSOM with $R_\omega(z) = 3.5\tanh[2\pi(z - 1500)/2000)] + 6.5$ and the ensemble averages resulting from this exercise are given in Fig. 11. For US5 (which is considerably less contaminated by double diffusive instability to begin with, relative to AUSSOM) the ensemble average for FSP TKE dissipation rate collapses onto the true ensemble average. The ensemble average for AUSSOM improves by 2 orders of magnitude. Repeating Fig. 9, averages with doubly unstable segments removed are provided on the right in green. Drawing conclusions from DIMES US5 is once again precarious (due to few available profiles remaining in each 50-meter bin in and above the main thermocline) but both DIMES US5

and AUSSOM show further improvement. Section plots with the transitional $R_\omega(z)$ and doubly-unstable segments removed are provided in Fig. 5 and Fig. 6. Removal of doubly-unstable segments substantially restricts the amount of the dataset available for FSP, but to the benefit of markedly-improved TKE dissipation rate estimates.

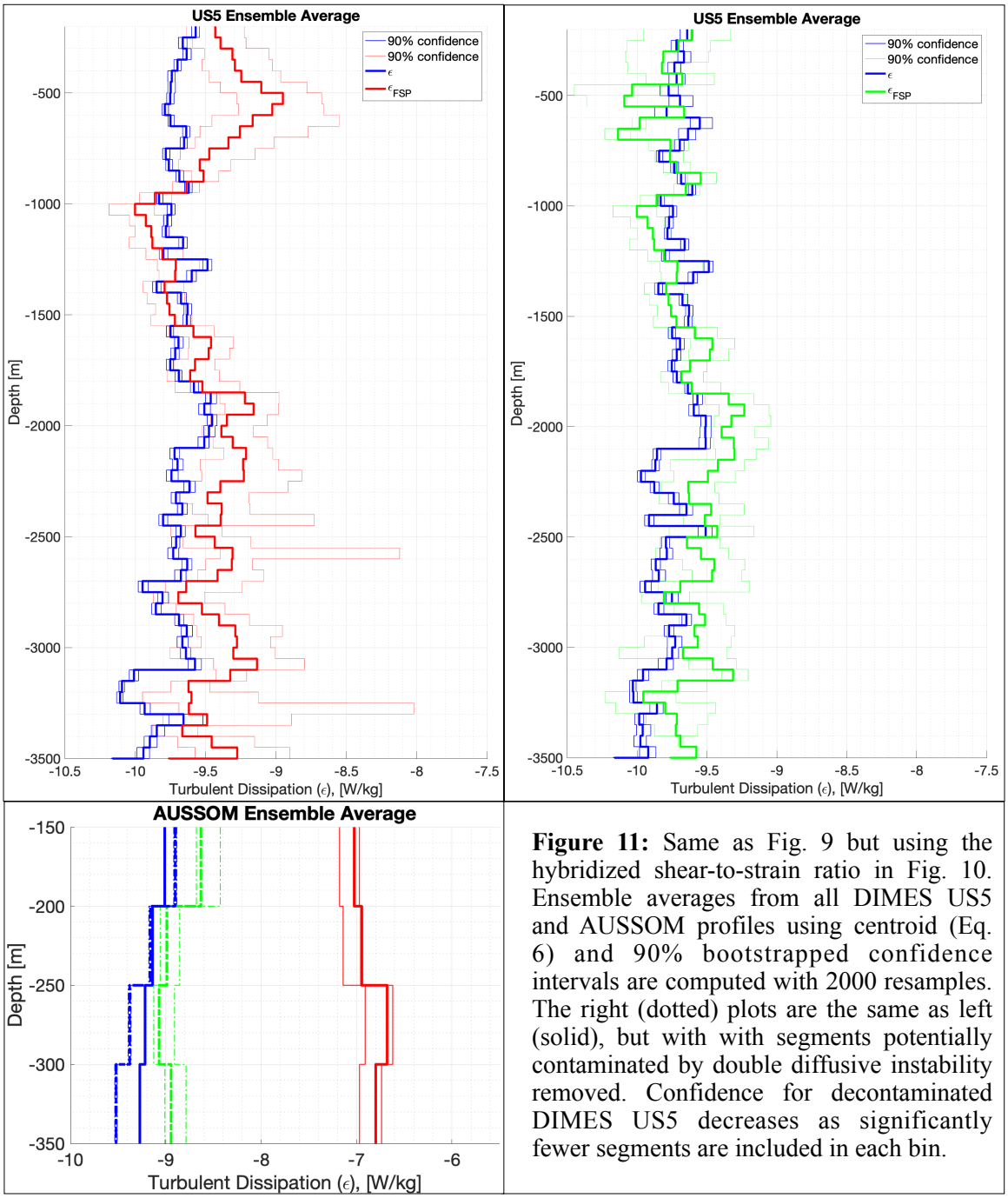

Figure 11: Same as Fig. 9 but using the hybridized shear-to-strain ratio in Fig. 10. Ensemble averages from all DIMES US5 and AUSSOM profiles using centroid (Eq. 6) and 90% bootstrapped confidence intervals are computed with 2000 resamples. The right (dotted) plots are the same as left (solid), but with with segments potentially contaminated by double diffusive instability removed. Confidence for decontaminated DIMES US5 decreases as significantly fewer segments are included in each bin.

The Southern Ocean has a spectrum that deviates from the GM spectrum in the deep because it has a steady zonally-uninhibited current impinging on underling seamounts to produce its own internal wave spectrum with internal lee wave origins. It is straightforward to substantiate the apparent $R_\omega = 10$ in the deep ocean by substituting expected internal lee wave frequencies into the ratio of the internal wave shear to strain variance for a single wave (Polzin et al., 1995),

$$\frac{\langle V_z^2 \rangle}{N^2 \langle \xi_z^2 \rangle} = \frac{(\omega^2 + f^2)(N^2 - \omega^2)}{N^2(\omega^2 - f^2)} = R_\omega \tag{7}$$

where $\langle V_z^2 \rangle$is the shear variance. Using the mean Coriolis frequency for DIMES US5, an assumed ocean velocity of $U = 0.1$ m/s, and observed stratification (Fig. 12a), internal waves can exist from about $785\text{m} < 2\pi/k < 5235\text{m}$ for the deep ocean and down to 315m in the main thermocline. The range of shear-to-strain ratios (Eq. 7) which can exists for possible internal wave frequencies are given in Fig. 12b. Near-internal oscillations have a higher shear-to-strain ratio (R_ω) and can exist in the deep ocean which

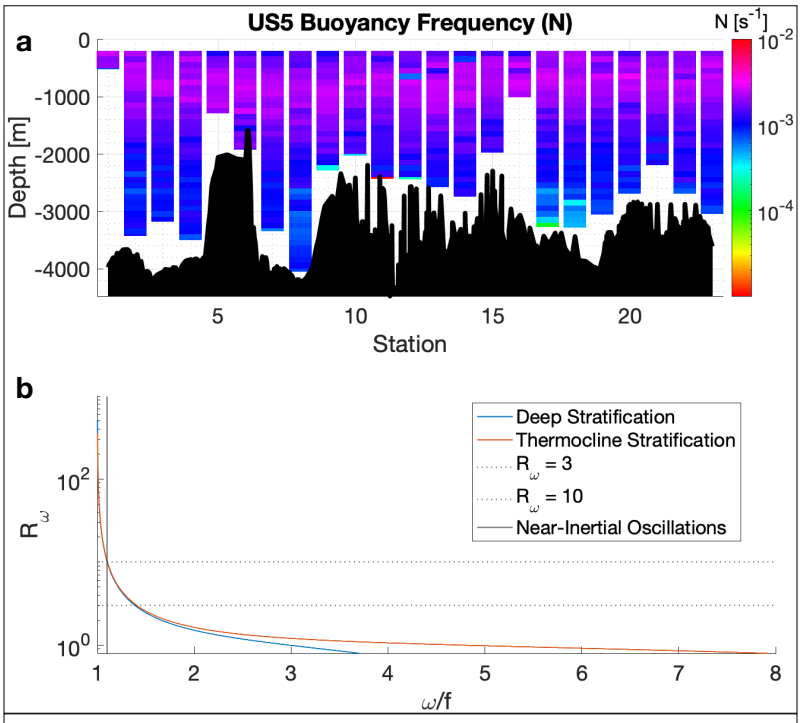

Figure 12: (a) Stratification for DIMES US5 and **(b)** estimated shear-to-strain ratios for range of possible internal waves for deep ocean and main thermocline.

is consistent with Nikurashin & Ferrari (2010)'s explanation of high R_ω in the deep Southern Ocean. Intuitively it makes sense that inertial oscillations have greater shear because their motion is predominately in the horizontal direction; there is much kinetic energy with minimal actual raising of fluid elements.

To better contextualize these results to Argo-based FSP (which is a subject of broad community interest), we applied FSP to Argo profiles (Fig. 13a) in region of AUSSOM and DIMES from 2010 through 2020. This was done using 100-meter segments from 200 to 2000m and $R_\omega = 10$ as before, for which an example strain spectrum is given in Fig. 14a. While the Argo program has generally shifted to deploying floats with 1-2m vertical resolution, some older floats with coarser resolution are found in the dataset. We consider "Good data only" profiles the upper 1000m, below which many floats are programed to assume coarser vertical sampling, and eliminate additional floats which transition to coarse sampling shallower than this depth. (To preserve battery while providing adequate hydrographic coverage, the Argo program agreed on a vertically non-uniform sampling scheme; Interestingly this variable and sometimes coarse sampling resolution of Argo floats is what outright prevents their compatibility with Thorpe scale analysis [Mackinnon et al., 2009].) Were this not done, it would be precarious to use the fixed high wavenumber cutoff of 10m; coarse sampling muddles the demarcation between signal and noise near the spectral rolloff point. To be clear, this is not the same collection of Argo profiles used by Whalen et al. (2012) and Whalen et al. (2015) nor an identical application of FSP. Therefore the TKE dissipation values should not be compared between studies.

TKE dissipation rates for each profile are shown in Fig. 13b, along with associated susceptibility to T/S-intrusive features (Fig. 13c). In general the full Argo dataset has fewer segments with density ratios indicative of double diffusive instabilities

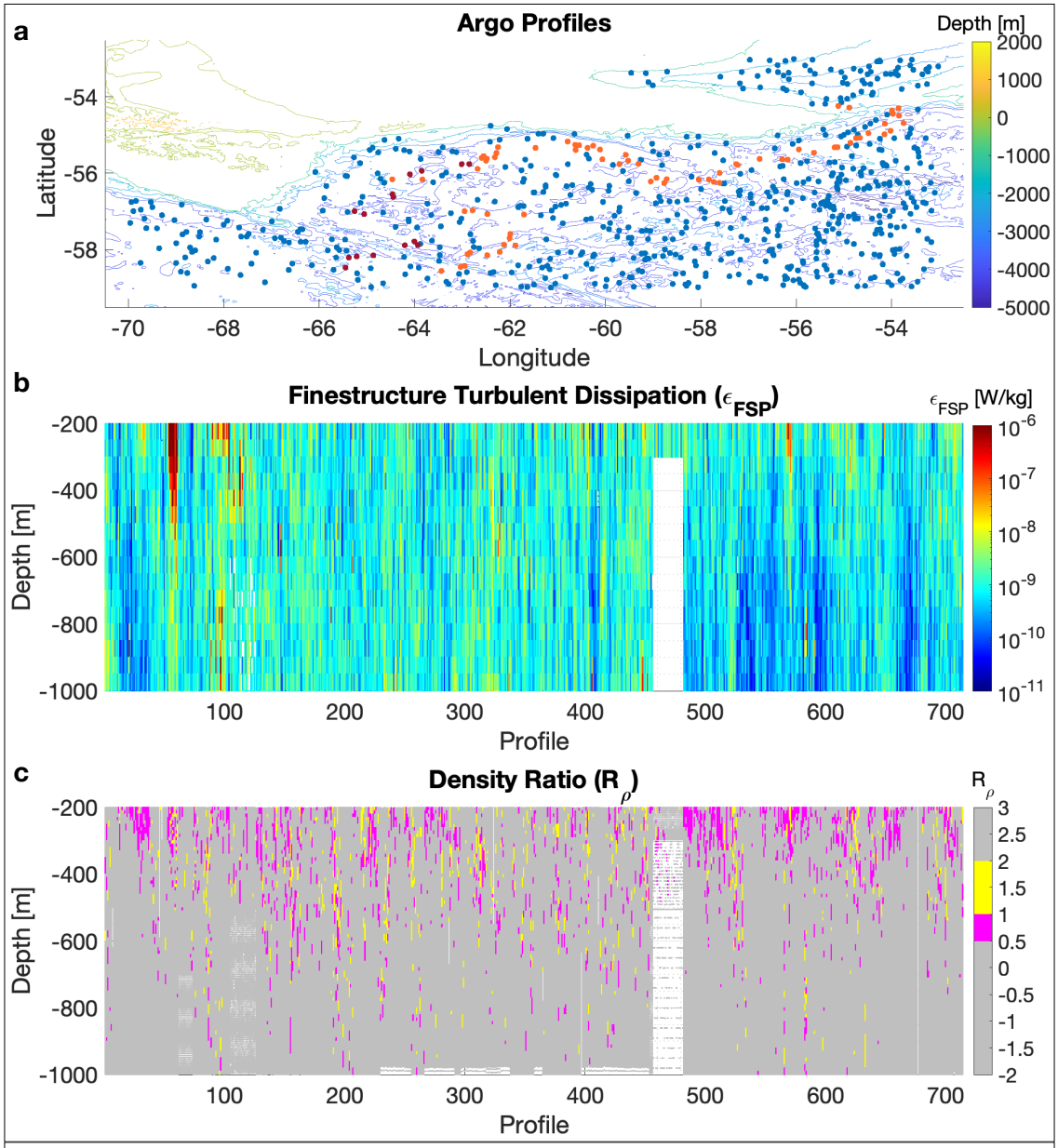

Figure 13: (a) Argo profiles from 2010 through 2020 in region of study (all colors), with subsets for the regions of DIMES US5 (scarlet) and AUSSOM (orange). **(b)** FSP-estimated TKE dissipation rate with $R_\omega=10$. **(c)** Density ratio $R_\rho=(\alpha dT/dz)/(\beta dS/dz)$ for each segment (pink for diffusive regime and yellow for salt fingering regime).

(pink for diffusive regime and yellow for salt fingering regime) relative to DIMES US5 and AUSSOM, which is to be expected given that the latter two studies were both specifically designed to sample in and around the ACC fronts (and thus very likely to capture T/S-intrusive features) contrary to the quasi-random sampling of Argo. The high TKE-dissipation patches around profiles 50 and 550 (Fig. 13b) are believed to be real and associated with frontal features or eddies, based on their TKE dissipation structure. In the absence of collocated microstructure measurements, we make a similar plot to Fig. 7b and Fig. 8b with estimated TKE dissipation rate presented as a relative magnitude $\overline{log10(\epsilon_{FSP}/5\times10^{-9})}$ rather than a true bias $\overline{log10(\epsilon_{FSP}/\epsilon)}$; a normalization value corresponding to when the buoyancy Reynolds number

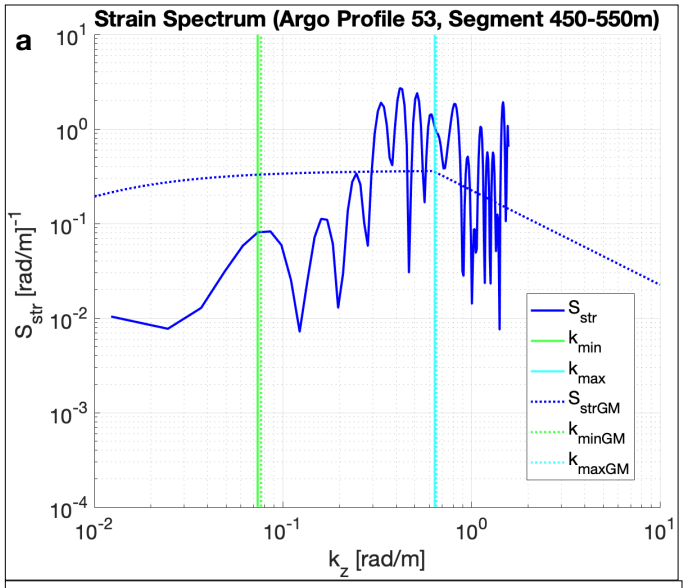

Figure 14: (a) Example strain spectra and limits of integration (Eq. 4) for one segment of Argo, as in Fig. 3. The segment has 2-meter vertical resolution in CTD data. **(b)** Geometric mean strain spectra for all depth levels of AUSSOM glider (blue), DIMES US5 VMP (green) and Argo (purple) datasets with 90% confidence intervals. The mean strain spectrum for the doubly stable region of AUSSOM (after 19-Dec-2017 00:00) is also provided (cyan).

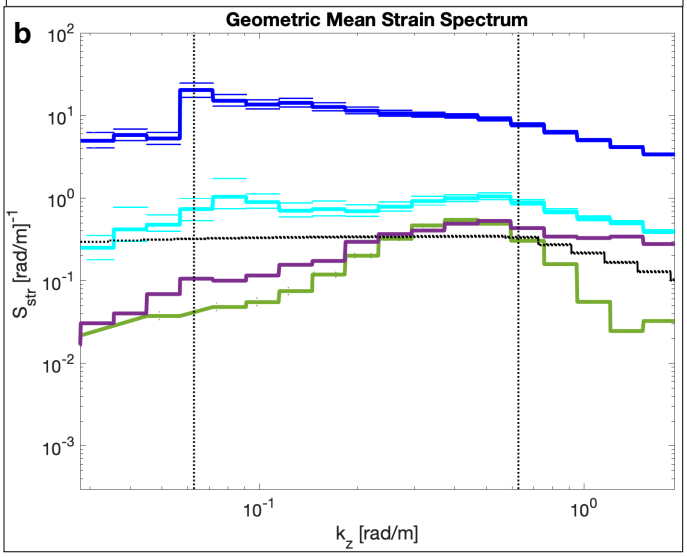

$Re = \epsilon/(\nu N^2)$ takes on a value of 200, a baseline for turbulence of sufficient strength to be isotropic (Gargett et al., 1984). This is for the purpose of exploring the potential impact of T/S-intrusive features on the magnitude of Argo-based FSP in the Southern Ocean. Fig. 15a shows these magnitudes vs. density ratio for a DIMES US5-region subset, a AUSSOM-region subset, and the full region, created using the Matlab toolbox ocean_data_tools (Ferris, 2020a). Few T/S-intrusive features were captured by the DIMES US5 or AUSSOM subset but there were more in the full-region dataset. Though not all T/S-intrusive segments are associated with high values of estimated TKE

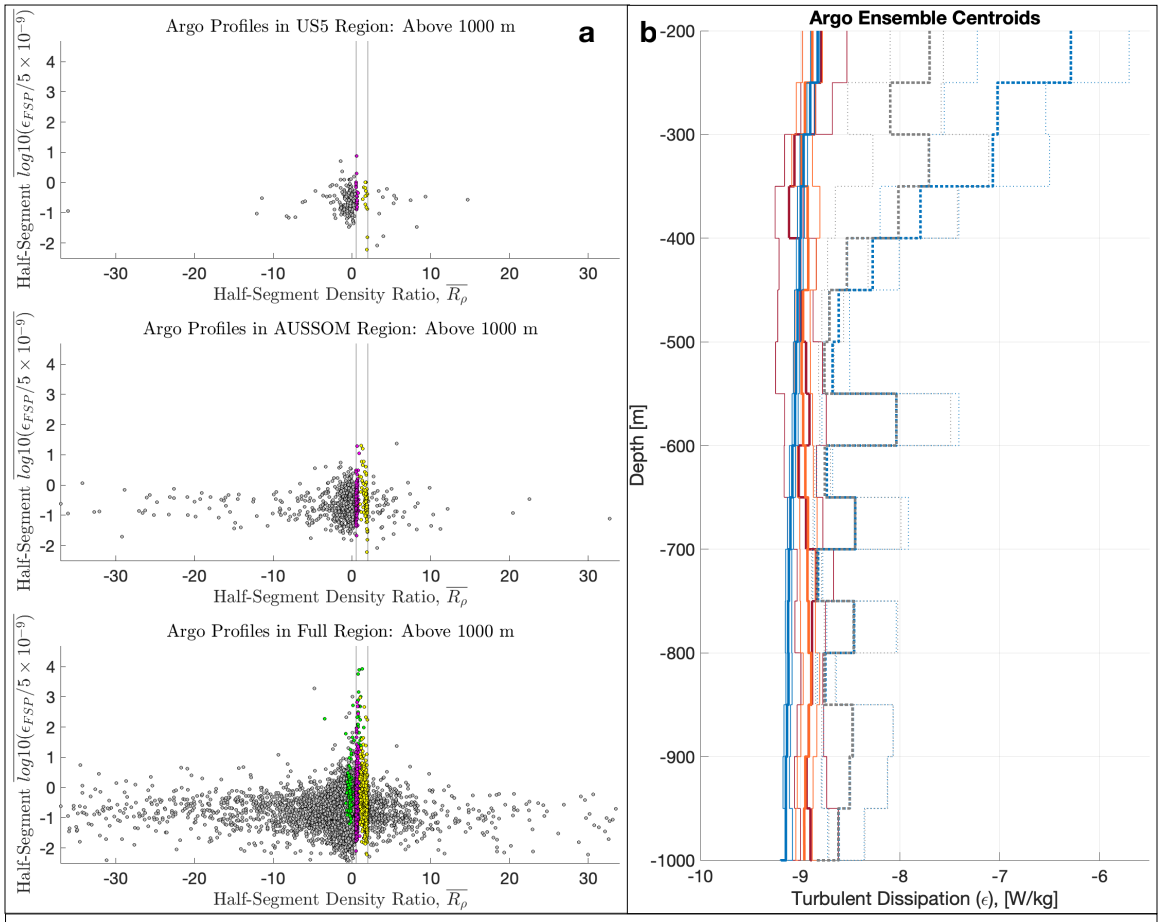

Figure 15: (a) Same as Fig. 7b, 8b but with y-axis as FSP-estimated TKE dissipation rate relative to W/kg. Segments from a float with suspected CTD issues (ID: 1901892), distributed as good data, are highlighted green. **(b)** Ensemble geometric means with 90% confidence intervals (solid lines) corresponding to Fig. 13a, with a full-region arithmetic mean (blue dotted lines). The arithmetic mean is recalculated (grey lines) without the green float, which accounted for 9 of 714 profiles. Yellow and magenta correspond to segment density ratio (Fig. 13c).

dissipation rate, the largest TKE dissipation estimates are associated with T/S-intrusive features. The test for T/S-intrusive density ratio (yellow or magenta points) in Fig. 15a shows the average T/S-intrusive density ratio density ($0.5 < R_\rho < 2$) if present at all in the segment. Not all yellow and magenta points correspond to high TKE dissipation, unlike Fig. 7b and 7b. This is for three reasons: (1) The test is binary and thus agnostic of the number of doubly unstable features in a particular segment, (2) the density ratio measures favorability to double diffusive instability and not its presence, and (3) the y-axis in the figure is a measure of magnitude and not bias — small-magnitude segments could have very large bias if the true TKE dissipation for the segment was also small.

For the Argo array, subtle data quality issues present a second source of bias which appears almost identical to TS-intrusive features but is actually an artifact in the observations. An example of this is presented in Fig. 16, which shows vertical profiles from an Argo float which is experiencing sensor issues but passed automated Argo quality checks and was distributed as “good data.” An issue with the conductivity sensor produced erroneous density features with the same vertical scale as both T/S intrusions and true internal wave strain (Fig. 15a). The consequences of this and similar CTD issues (a reality of long-deployed and unsupervised platforms) are large; Fig. 15b shows an arithmetic mean for the full Argo data set with (blue dotted) and without (grey dotted) the float in question. This illustrates the danger of applying FSP to the global Argo array in an automated fashion, even if the practitioner limits the dataset to "Good data only”.

At this point we wish to underscore the distinction between overestimating TKE dissipation rate (ϵ) and overestimating diffusivity, $K_\rho = \Gamma\epsilon/\overline{N}^2$. Regions prone to double

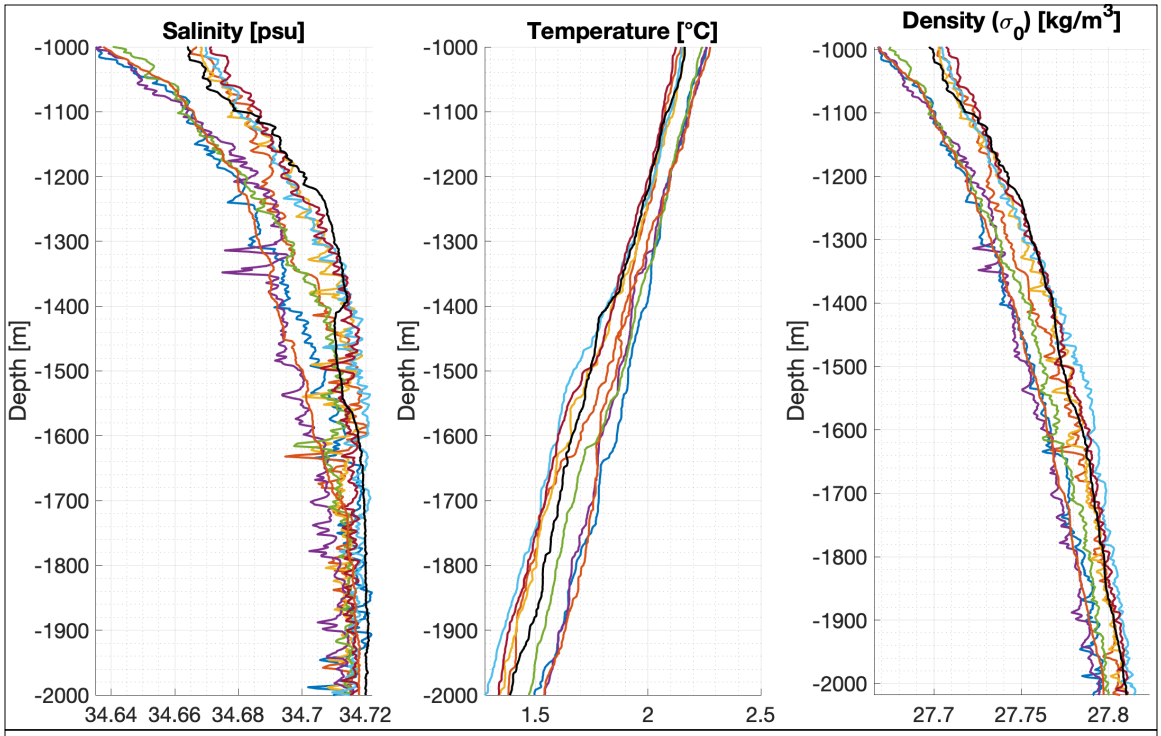

Figure 16: Profiles from the Argo float (ID: 1901892) with suspected CTD issues which corresponds to erroneous doubly diffusive segments (green dots) in Fig. 15. The conductivity sensor appears to become problematic at a depth of 1200m while ascending (black line), perhaps due to intake of biological material, and remain so (colored profiles).

diffusive convective regimes which are biased high in TKE dissipation rate (ϵ) are not biased equivalent high in diffusivity (K_ρ) because double diffusive convective mixing regimes are energetically more efficient that 3-D isotropic turbulence at converting kinetic energy to potential energy. T/S-intrusive features have the potential to influence diffusivity in the opposite sense.

Ensemble centroids for the Argo subsets and full-region dataset are given (Fig. 15b), and we turn our attention to the nuances of averaging mentioned in reference to Eq. 6. The ensemble centroids in Fig. 9, Fig. 11, and Fig. 15 are geometric means - calculated by applying logarithmic transformation prior to averaging. Geometric means are appropriate for representing the centroid of a dataset where data points vary

logarithmically. Arithmetic means (no logarithmic transformation prior to averaging) are appropriate for representing data with no significant outliers or log-scale variation.

The problem with using an arithmetic mean to represent the centroid of TKE dissipation rates is that it is akin to just taking the maximum. The order of logarithmic transformation and averaging determines whether an estimated TKE dissipation rate is simply the maximum value of a given ensemble or whether it is the centroid of all TKE dissipation estimates in the ensemble. Given that TS-intrusive appear as artificial internal wave-attributed strain and bias FSP-derived TKE dissipation rates to be high, the consequences of including these features in an arithmetic mean (dotted blue line in Fig. 15b) are more deleterious than including them in a geometric mean (solid blue line in Fig. 15b). While T/S-intrusive features aren't dominate in the global ocean, they exist and can create large biases in TKE dissipation rate estimated by FSP. To ameliorate this, one should use a geometric mean and/or remove the contaminated segments when attempting FSP analysis; T/S-intrusive features have the potential to introduce large errors if included in either a geometric mean with little contamination but few samples (as in DIMES US5), a geometric mean with much contamination and many samples (as in AUSSOM), or an arithmetic mean of any kind (as in the Argo full-region dataset).

Upon examining TKE dissipation rate estimates derived from Argo profiles, it is reasonable to wonder why AUSSOM (with its superior vertical resolution) had high bias (Fig. 8a) relative to the other datasets, some of which remained even after adjusting the shear-to-strain ratio and removing contaminated segments (Fig. 11c). A well-documented issue in the glider-based CTD is thermal lag, which arises from the displacement between

the thermistor and conductivity cell within a CTD, as well as the thermal inertial of the cell itself. As a glider dives or climbs through sharp gradients, there is a mismatch between temperature and salinity, which can produce erroneous density features (there are excellent examples Garau et al., 2011 or Latarius et al., 2019). Thermal lag acts at 1-10m scale, which falls within the same narrowband finescale structure as T/S-intrusive features and oceanic internal waves. As such, it was important to verify that the thermal lag was not the source of the high strain variance within the T/S-intrusive region of AUSSOM. We applied thermal lag correction after Garau et al. (2011) using https://github.com/socib/glider_toolbox, which is showing in Fig. 17 (dotted lines). We also visually inspected temperature, conductivity, salinity, and

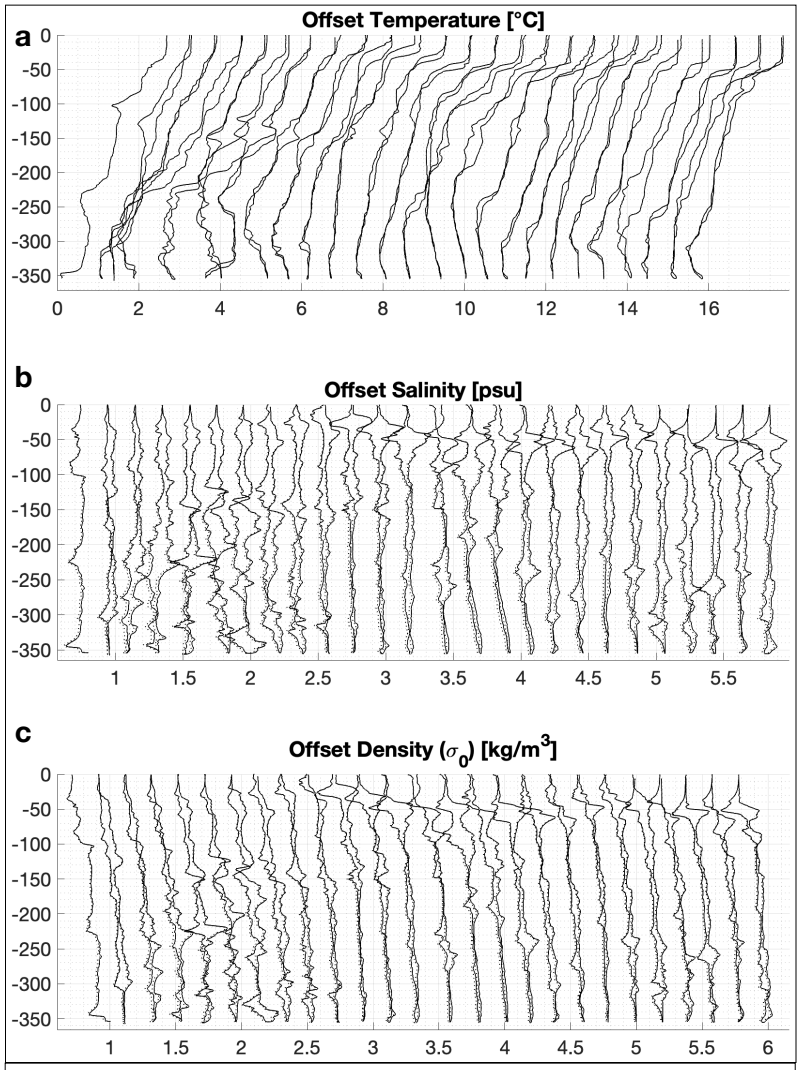

Figure 17: Glider profiles during AUSSOM, corresponding to 01-Dec-2017 20:32:58 through 03-Dec-2017 07:12:53 in which the glider was in the core of the Polar Front and observed elevated TKE dissipation rates. Showing **(a)** offset temperature, **(b)** offset salinity, and **(c)** offset density. Adjacent upcasts and downcasts are paired, and the same variables corrected for thermal lag are provided (dotted lines) for reference.

density profiles. Given that mirroring in adjacent casts is found in both temperature and salinity, is not removed by thermal lag correction, and is consistent with observations of internal waves, we attribute these features to be produced by internal waves aliased with the frequency of glider up and downcasts. Regarding AUSSOM and why that FSP dissipation estimates are still too high after decontaminating: the large biases in AUSSOM are likely intrusive features combined with an intense internal wavefield which perhaps does not dissipate locally (via radiation away or momentum transfer into the mean flow, violating Assumption 3).

Finally, worth discussing is the nuances of the glider, VMP, and Argo float platforms and their impact on the observed strain spectra. The mean AUSSOM spectra (Fig. 14b) is closer to a Garrett-Munk shape than DIMES US5 or Argo, perhaps because it is the upper ocean and relatively immune from the non-GM physics of the ACC at depth. Its magnitude varies inside and outside of the front; the mean AUSSOM spectra for the doubly stable region (December 19th and beyond) is over an order of magnitude lower than that for the full AUSSOM dataset which is dominantly in the front and contaminated by TS-intrusion-like features.

Individual Argo spectra generally have a spectra shape similar to (Fig. 14a), with less strain power in low wavenumbers relative to AUSSOM or DIMES US5. We are unable to determine the cause of this distinctive spectral shape for Argo with our dataset. However, we can speculate that it is either due to a physical reason (e.g. the Argo floats which primarily sample the open ocean away from the front which is less likely to have a GM spectra than Drake Passage) or a technical reason (e.g. an engineering property

specific to the platform causes this). We suspect a technical reason that Argo floats could be problematic is that Argo floats are ballasted to be near-neutral buoyancy, fall slowly, and have little inertia. We speculate that the strain spectrum is depleted in low wavenumbers because the Argo floats are missing low wavenumbers; moving with the longest internal waves instead of measuring their associated strain. The fluid-structure interaction of Argo floats could act as a natural filter to remove certain wavenumbers. However the is only a conjecture. Our dataset alone not enough to ascertain truth of spectra, and this issue deserves future investigation.

A final note is that glider users should pay attention to aliasing and and statistical independence when applying FSP to glider datasets. In this paper, our aim was to examine the efficacy of FSP from a technical perspective. When implementing glider-based FSP to obtain an actual TKE dissipation rate or diffusivity, averaging 10 consecutive profiles implies that the glider is resampling the same feature or water column several times in a row and these are not truly 10 independent estimates. Thus applying FSP to 10 consecutive profiles does not produce 10 statistically-independent estimates of TKE dissipation rate in a region and should be avoided when possible.

5. Conclusions

The application of FSP to estimate TKE dissipation in the Southern Ocean has several layers of vulnerability. To summarize, the most tractable vulnerability is observed T/S features (both double diffusive instabilities and CTD issues) being misidentified as internal wave strain. Even if these features are removed, the second layer is that shear-to-strain ratio (R_ω) is well documented to vary by more than an order of magnitude

throughout the global ocean (producing an error of up to an order of magnitude) and can no longer justifiably be assumed to have a constant value. Finally, even if the R_ω is correctly calibrated, the innermost vulnerability (and most difficult to correct) is that the parameterization assumes the validity of a GM spectrum. With its near spatial universality, basing finescale parameterizations on the GM spectrum to solve global mixing problems seems like an innocuous assumption. However, the spatial scale of energetic regions (such as the Antarctic Circumpolar Current) are not directly proportional to their importances; TKE dissipation varies by orders of magnitude such that its extreme values contribute disproportionately more to ocean mixing than its mean values. The GM spectrum may fail in limited regions of the ocean, but these limited regions of the ocean could be responsible for the majority of turbulent mixing. We are potentially taking the wrong approach by applying uniform internal wave physics to understand, calculate, and build simulations of a spatially heterogenous process. FSP is useful tool for estimating TKE dissipation rates, but it should not be taken as a mathematical truth that solely underlies which can be used to increment our understanding of the turbulence-associated physics.

Frontal physics (as well as data quality issues) mimic the role of internal wave strain. When applying FSP to data from the global Argo array, we must be cautious of data collected in any strong frontal region. The frontal physics discussed in this paper are not unique to the Antarctic Circumpolar Current and extend to global areas such as the Kuroshio Current, Agulhas Current, and Gulf Stream. Referencing the Argo-derived global map of estimated TKE dissipation rate (Fig. 3 of Whalen et al., 2015), it is

noticeable that estimated rates are sharply enhanced ($\epsilon \gg 1 \times 10^{-8}$ W/kg) in these frontal regions as well as much of the Northwest Pacific gyre. We wonder whether the TKE estimates in each of these regions are inflated by frontal physics, data quality issues, or truly due to enhanced internal wave activity. A second quandary is whether an enhanced internal wavefield results in an enhanced TKE dissipation. This hinges on the assumption that the internal wavefield is locally dissipative such that at any given location there is leakage of the internal wave spectrum as TKE dissipation (ϵ). In the case of the Southern Ocean, St. Laurent et al. (2012) found that the most unstable lee wave energy dissipated within the bottom 1000m of topography, while the lower-mode energy in the spectrum escapes upward to produce the Southern Ocean internal wavefield and circulates around the upper ocean (i.e. thermocline and above). Whether this energy dissipates locally or propagates adiabatically without dissipation until encountering a catalyst such as wave-mean flow interaction (restated, the amount of decoupling between the finescale and the microscale) is a key future research question.

The conclusions of this study are that: (1) FSP should not be conducted where double diffusive instabilities are active, (2) an appropriate shear-to-strain ratio R_ω should be tuned from available microstructure data for each distinct region of the global ocean prior to performing FSP, (3) choose the appropriate averaging scheme for FSP-estimated TKE dissipation rate (i.e. arithmetic vs. geometric mean) matters tremendously, (4) subtle data quality issues are an insidious source of bias when applying FSP in an automated manner, and (5) free-falling platforms with a high vertical sampling resolution (such as autonomous underwater gliders) allow the user to integrate over more of the strain

spectrum while avoiding the dissipation scale at $k_{max} > k_c$ (unlike ship-lowered CTD which has a spectral roll-off muddied by heave or Argo which often cannot measure strain down to the 1-meter scale due to variable sampling rate). These results are broadly applicable to energetic currents rich in frontal structure and anywhere T/S-intrusive regimes are active. In order to accurately understand global patterns of mixing—especially in frontal zones, we are best served using direct turbulence measurements. Large eddy simulation (LES) numerical studies are another tool to explore estimates of mixing rates from the finescale energy cascade (Khani, 2018), and advances in theoretical understanding or computational capacity could enable better future finestructure estimates of turbulent mixing.

Autonomous platforms (VMP, gliders, and Argo floats) allow for potentially effective application of FSP with the caveat that, because of the enhanced resolution, we now have the responsibility to check for double diffusive instabilities. As such, the community has several choices to deal with this going forward: to apply more rigorous quality control to Argo-derived TKE dissipation rate estimates, add shear probes to floats (which carries its own suite of technical challenges), or dramatically increase the number of microstructure-equipped glider surveys of frontal regions. The problem with these first options is that FSP can only capture the processes we have designed it to capture. The second presents a technical challenge of implementing durable and biofouling-proof shear probes (which is not yet possible). The third option (true microstructure measurements) is likely the most economical, has the highest level of technical readiness,

and would elucidate undiscovered nuances of forward energy cascade which the community has not yet tackled.

Acknowledgments

Computational resources were provided by the VIMS Ocean-Atmosphere & Climate Change Research Fund. AUSSOM was supported by the OCE Division of the National Science Foundation (NSF); we thank the crew of the R/V Gould for their support during the field program, and Justin Shapiro for glider recovery. DIMES US5 was supported by NSF; we thank the crews on the R/V Palmer. Argo data were collected and made freely available by the Coriolis project and contributive programs (http://www.coriolis.eu.org).

Data Availability Statement

All AUSSOM and DIMES US5 data used in the paper will be shared at microstructure.ucsd.edu, the NSF-funded Microstructure Database.

Endnotes

I gratefully acknowledge the contributions of my collaborators for this project: Donglai Gong (VIMS), Sophia Merrifield (SIO), and Louis St. Laurent (APL-UW).

Chapter 5

Symmetric instability as a mechanism for topographically-enhanced mixing in the Southern Ocean

Abstract

Submesoscale frontal instabilities are well-established by idealized analytical and numerical studies to be a significant source of turbulent kinetic energy (TKE) in the global ocean (Boccaletti et al., 2007; Stamper & Taylor, 2016; Skyllingstad & Samelson, 2019). In particular, symmetric instability (Haine & Marshall, 1998) has gained popularity in mid-latitude literature for explaining enhanced turbulence at energetic oceanic fronts (D'Asaro et al., 2011; Thomas et al., 2013). However, observations of TKE dissipation enhanced by symmetric instabilities are still few, and it is unknown where and to what order in the real ocean this process is important. In this study we use vorticity and buoyancy flux fields from a 1-km Regional Ocean Modeling System (ROMS) hindcast to examine the role of symmetric instability (SI) in Southern Ocean mixing. We show that SI of the centrifugal/inertial variety is widespread along the northern continental margins of the Antarctic Circumpolar Current due to topographic shearing of the anticyclonic side of Polar Front-associated jets, as well as along the Shackelton Fracture Zone.

1. Introduction

The details of downscale energy transfer in the global ocean are an area of active research. Energetic forcing of the global ocean happens at scale of internal tides and wind-generated near inertial (NI) internal waves. While many process are physically possible, the realistic details of ocean energy transfer from the mesoscale to dissipative scale are still largely unknown. Above the thermocline, the energy cascade is driven by a combination of factors including wind stress, mesoscale eddies, submesoscale instabilities, critical layer dynamics, and double diffusive processes. The multiple factors influencing the energy cascade result in a set of complex energetic pathways leading to dissipation, most of which are still poorly observed and quantified. Understanding the physics of how energy moves downscale and produces mixing in the real ocean is necessary for the construction of next-generation operational and climate models, which currently harness diffusivity-profile parameterizations (based on Monin-Obukhov scaling near boundaries and vertical shear in the interior) to accomplish turbulent mixing. With limited computational power, a critical task is elucidating the relative roles and spatial arrangement of the physical processes capable of generating TKE in order to know which to prioritize.

In the surface boundary layer, much of the energy for turbulent mixing comes from buoyancy flux (convection) and wind stress (breaking surface gravity waves and Langmuir circulation) (Mackinnon et al., 2013). In addition to directly driving turbulent dissipation in the actively mixing layer, wind stress generates near-inertial (NI) motions which modulate the base of the mixed layer, sending NI internal waves into the interior ocean (Mackinnon et al., 2013). Convective engulfment of thermocline waters and

entrainment by shear instabilities (e.g. Holmboe instabilities or Kelvin-Helmholtz billows) are active at the bottom of the mixed layer and important for communicating heat and momentum between the atmosphere and interior ocean (Thorpe, 2005).

In the upper ocean and main thermocline, processes that drive mixing and energy transfer are include double-diffusive convection and interleaving/layering, shear-driven instabilities (e.g. Kelvin-Helmholtz), internal wave-eddy interactions (strain of mesoscale features trapping internal wave, critical layers), and internal wave-wave (elastic scattering, induced diffusion, parametric instability) interactions. Internal waves interact with each other until they break and relinquish their energy as turbulent dissipation; this is accepted as the main form of forward energy cascade. Meanwhile, there are other options such as wave-flow interactions, double diffusive instabilities, and baroclinic-symmetric instabilities. For a barotropic instability, the wave draws energy from the current; for a baroclinic instability, potential energy is extracted from the isopycnal slope of the thermal wind balance. Baroclinic frontal instability converts available potential energy (APE) from sharp horizontal buoyancy gradients to eddy kinetic energy (EKE); where wind stress opposing an along-front flow can further destratify the frontal region, enhancing diapycnal mixing through symmetric instability (D'Asaro et al., 2011; Thomas et al., 2013; Mackinnon et al., 2013).

There are a variety of instabilities at the submesoscale. The subsubmesoscale is characterized by flow features with spatial scales of $\mathcal{O}$(1-10km), vertical scales of $\mathcal{O}$ (100m), timescales of $\mathcal{O}$(hrs-days), Richardson numbers $Ri = B_z/(U_z^2 + V_z^2)$ of $\mathcal{O}$(1), and Rossby numbers $Ro = U/fL$ also of $\mathcal{O}$(1). The effects of velocity structure,

stratification, and rotating are all important. In a rotating, stratified framework, overturning instabilities can arise when Ertel potential vorticity (q) opposes Coriolis parameter ($qf < 0$). Several types of overturning instability include baroclinic-symmetric (buoyancy gradient induced) instabilities, gravitational (stratification) instabilities, and inertial/centrifugal (relative vorticity induced) instabilities (Todd et al., 2016). For gravitational instability (GI), energy is extracted from stratification (B_z) when $N^2 \equiv B_z < 0$. For centrifugal instability (CI), energy is extracted from shear (U_y) when $f\zeta_a < 0$. Symmetric instability (SI) is a generalization of gravitational and centrifugal instability and can occur despite convective stability in the vertical and dynamic stability in the horizontal. It arises from the same physical setup as baroclinic instability (along with a convective mode and an inertial critical layer mode) but assumes no along-front variation in the perturbation. SI produces weak restratification (Dong et al., 2021a) by extracting KE through shear production (see Fig. 3 of Stamper & Taylor [2016] for the velocity structure of SI convective cells). On the other hand, ageostrophic baroclinic instability (ABI) assumes quasigeostrophy and no cross-front variation. It generates strong restratification by extracting potential energy and creating kinetic energy. ABI can occur at the submesoscale but is can also act at the mesoscale.

Along-front wind stress causes an Ekman advective transport of buoyancy that can further destratify PF regions by pushing dense water over less dense water, enhancing baroclinic instability; an effect which can be exacerbated by nonlinear Ekman dynamics acting on a nonuniform vorticity field such (as a jet with an cyclonic side and an anticyclonic side) (Thomas et al., 2008). Symmetric instability arises from the same

physical setup as baroclinic instability, but acts at smaller scale; baroclinic instability assumes quasigeostrophy and no cross-front variation while the symmetric instability assumes no along-front variation in the perturbation (Smyth & Carpenter, 2019). Along-front wind (such that Ekman transport destabilizes a front) is not required for SI; rather, it can be one of many agents in reducing (enlarging) the potential vorticity until it is symmetrically unstable. While the instability criterion for SI ($Ri < f/\zeta_a$) is necessary and sufficient condition, the commonly cited condition $Ri < 1$ is not necessary. Literature referencing this condition (e.g., Bocalleti et al., 2007) are generally discussing the basic state of the Eady problem (thermal wind shear, no vertical vorticity) as in Stone (1966). The condition comes from the analytical condition for the maximum growth rate to be real, $Ri < f/\zeta_a = f/(f + V_x - U_y)$. A result of this is that instability can arise for $Ri > 1$ if the relative vorticity acts to reduce the magnitude of the absolute vorticity ($\zeta > 0$), termed *centrifugal-symmetric instability*.

The Southern Ocean is populated with mesoscale eddies and Scotia Sea is an eddy generation hotspot. Shallower than the sill depth of the Drake Passage (~2000m), the ACC cannot support a zonal pressure gradient or meridional geostrophic current. In lieu of this, eddy flux accomplishes meridional water mass transport and upwelling. The mesoscale eddies (~20km), generated by baroclinic instabilities, mediate transfer of momentum between the surface (wind stress) and underlying topography (bottom form stress). These eddies are concentrated along zonal fronts, which coincide with potential vorticity gradients (Thompson, 2008) and deep-reaching geostrophic flow. Potential energy is released from the water column when eddies are pinched off at density fronts

and decay (Ferrari & Wunsch, 2009; Marshall & Speer, 2012). The eddies themselves serve as rotating, curved fronts. Additionally, mesoscale eddies and filaments resulting from dynamic instabilities of ACC fronts are expected to modulate the propagation of internal waves through influence on flow shear variance as well as critical layer dynamics (Sheen et al., 2015). Submesoscale instabilities resulting from the interaction of mesoscale eddies with the Polar Front (PF) have been shown to generate large vertical velocities (~100 m/day) and water mass modification associated with the Sub Antarctic Mode Water (SAMW) on time scale of days; with stability analysis indicating that gravitational, symmetric, and inertial instabilities all contribute to upper ocean mixing (Adams et al., 2017).

Many ACC eddies are beneath a threshold length scale of $L = 2\pi R_d$ and drive a forward energy cascade (Scott & Wang, 2005; Ferrari & Wunsch, 2009; McWilliams, 2016), losing energy to frontal instability and frontogenesis in the surface layer (D'Asaro et al., 2011), as well as to bottom friction (Munk & Wunsch, 1998). However, the reality of Southern Ocean energy cascade is more complicated. Due to weak stratification, large injection of kinetic energy, and the absence of continuous zonal jets, the Southern Ocean is highly influenced by topographic interaction in addition to geostrophic turbulence (Ferrari & Wunsch, 2009). Deep flow impinging on topography generates internal lee waves and other hydraulic features. TKE may dissipate at the site of internal wave generation or internal waves may propagate energy away from the site of generation, dissipating at continental margins (Waterhouse et al., 2014). Elevated TKE dissipation

rates near abyssal bathymetry and along continental margins are often attributed solely to nonlocal TKE dissipation from internal waves.

While the dynamics of topography-enhanced vertical mixing in the ACC are not fully understood, flow-bathymetry interaction and deep ocean mixing are known to key factors. Microstructure measurements of turbulence in the ACC are sparse. St. Laurent et al. (2012) conducted microstructure measurements of turbulent energy dissipation rate in the Drake Passage, as part of the Diapycnal and Isopycnal Mixing Experiment (DIMES). Turbulent dissipation was enhanced by two orders of magnitude to $O(10^{-8})$ W kg^{-1} upwards through 1000m depth along the Southern Antarctic Current Front (SACCF), PF, and Subantarctic Front (SAF); compared to $O(10^{-10})$ W kg^{-1} outside of frontal regions. In addition to the speed and depth of incident flow, the terrain of underlying bathymetry influences enhancement of turbulent mixing and upwelling. Turbulent diffusivity is known to be enhanced over rough topography (Sheen at al., 2013) and abrupt isolated ridges in the abyssal ocean (Polzin et al., 1997; Waterhouse et al., 2014). The geometry of these features is known to be important, with TKE dissipation in abyssal mixing enhanced over ridge crests and bathymetric slopes (Ledwell et al., 2000; Naveira Garabato et al., 2004). However, there has been little investigation beyond internal waves with respect to conjecture about the process responsible. Most studies have suggested internal waves as having principle role, especially near the abyss (Garrett & St. Laurent) and continental margins.

In the real ocean, instability is transient because the flow restores itself to stability through forward energy cascade (at the mesoscale and submesoscale) and mixing (at the

submesoscale and finescale). For example, within a few days of baroclinic instability arising in the Gulf Stream, it sheds an eddy and is no longer an unstable system (Sutyrin et al., 2001). Operational ocean models implement mixing (parameterize diffusivity) via KPP, based in MO scaling with vertical shear. Symmetric instabilities arise from horizontal gradients in velocity/buoyancy and thus can develop in models but cannot be directly removed; thus the effects of these instabilities are generally not represented by existing subgrid scale mixing parameterizations. The significance of frontal instabilities is subgrid scale release of kinetic energy, causing the real ocean to be more homogenized that represented by the model. Understanding the potential relevance of processes (other than vertical shear and internal wave-wave interactions) which supply TKE for mixing, including symmetric instabilities, is important for the computational triage of mixing parameterizations in the development of next generation climate and operational models. It is currently unclear under which circumstances the development of SI parameterizations should be made a priority.

Most model turbulence closures consider vertical shear but neglect SI, which is contingent on horizontal buoyancy and velocity gradients, in both boundary and interior treatments. The existing diffusivity parameterization (to be used with a turbulence closure) that does incorporate SI (Bachman et al., 2016) considers only geostrophic production by forced SI (FSI) in the surface mixed layer. Forced SI (FSI) occurs when wind and buoyancy forcing sustain pre-existing SI ($EBF + J_b > 0$). The instability criterion for SI ($Ri < f/\zeta_a$) is unique in that they are both necessary and sufficient (independent of whether Ekman transport from wind forcing had a role in producing or

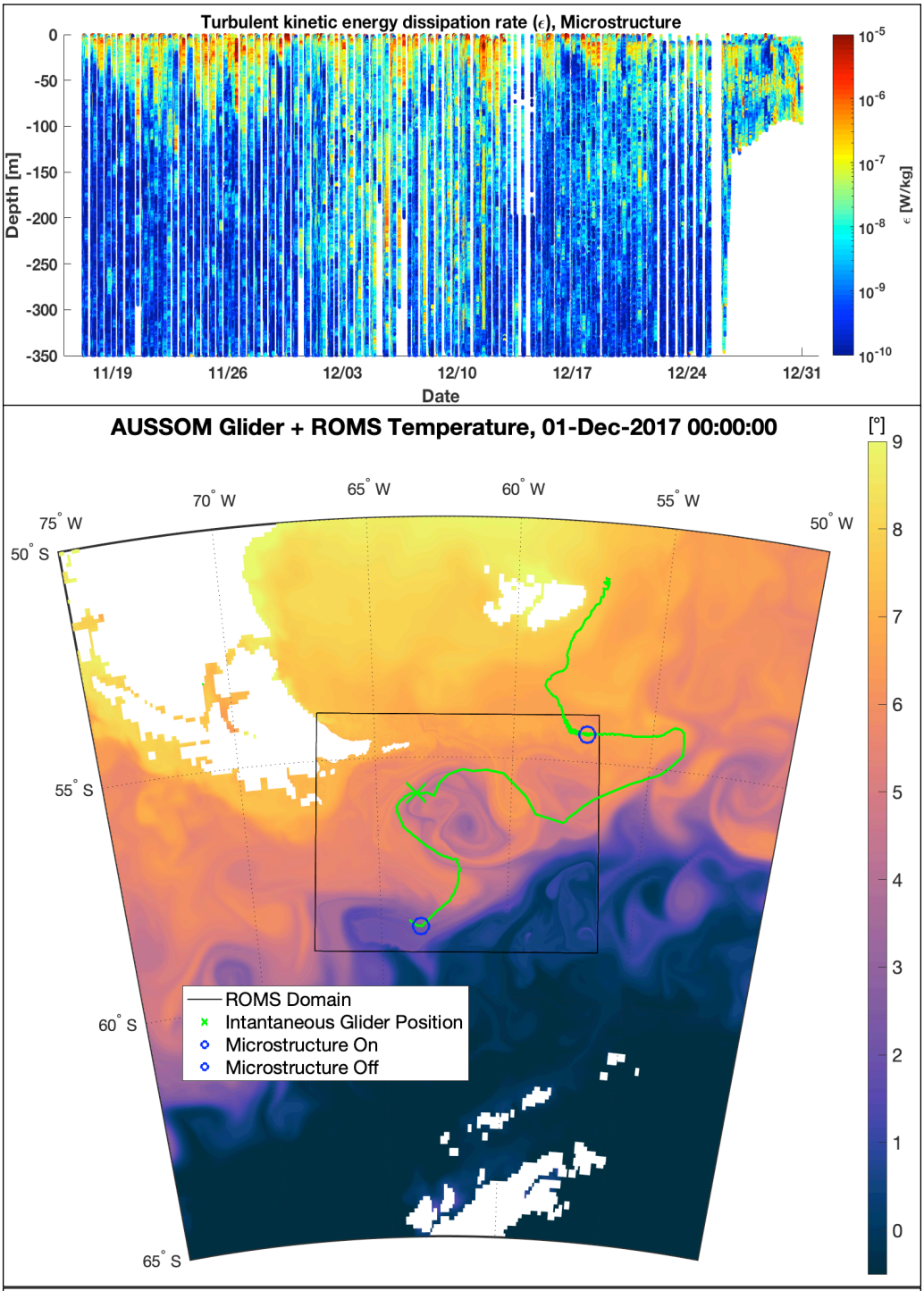

Figure 1: (a) TKE observations and **(b)** associated Slocum glider track along the Polar Front in Scotia Sea during the AUSSOM project in 2017. Elevated TKE dissipation levels were observed in the surface Active Mixed Layer as well as at depths in the core of the Polar Front. **(b)** shows instantaneous temperature from the 1-km ROMS hindcast used in this study nested within a 1/12° Operational Mercator simulation.

perpetuating symmetrically unstable conditions). This is notable because the current SI parameterization in existence (Bachman et al., 2016; Dong et al., 2021a) relies on FSI by checking for bulk negative potential vorticity (PV) in the surface boundary layer, attributing it to SI, and then estimating geostrophic shear production from FSI. The argument for neglecting ageostrophic shear production (Thomas et al., 2013; Bachman et al., 2016) is that makes only a small contribution to the energy budget when vertically integrated over the upper ocean (Taylor & Ferrari, 2010). However, its individual values are a dominant term within the upper ocean (see Fig. 9 from Thomas et al. [2013]). This may be fine for large scale ocean models but have considerable shortcomings when accurate predictions of upper ocean structure are required. In short, neither the effects of non-forced SI, nor shear production by the ageostrophic component of SI, are currently considered important for parameterizations of SI-associated mixing. Both of these aspects must be better understood.

This study was also motivated by the need to understand the elevated TKE dissipation observed from 100 to 350 meters throughout the Polar Front during the AUSSOM (Autonomous Sampling of Southern Ocean Mixing) program (Fig. 1). A comparison of AUSSOM glider CTD + Microstructure and corresponding ROMS variables (where TKE dissipation rate ϵ is estimated from vertical diffusivity AKv) is given in Fig. 2. Because the ROMS output has a highly realistic structure but slightly different Polar Front location from observed, it was decided to analyze the model data independently to provide dynamical context for AUSSOM without limitations of direct comparison.

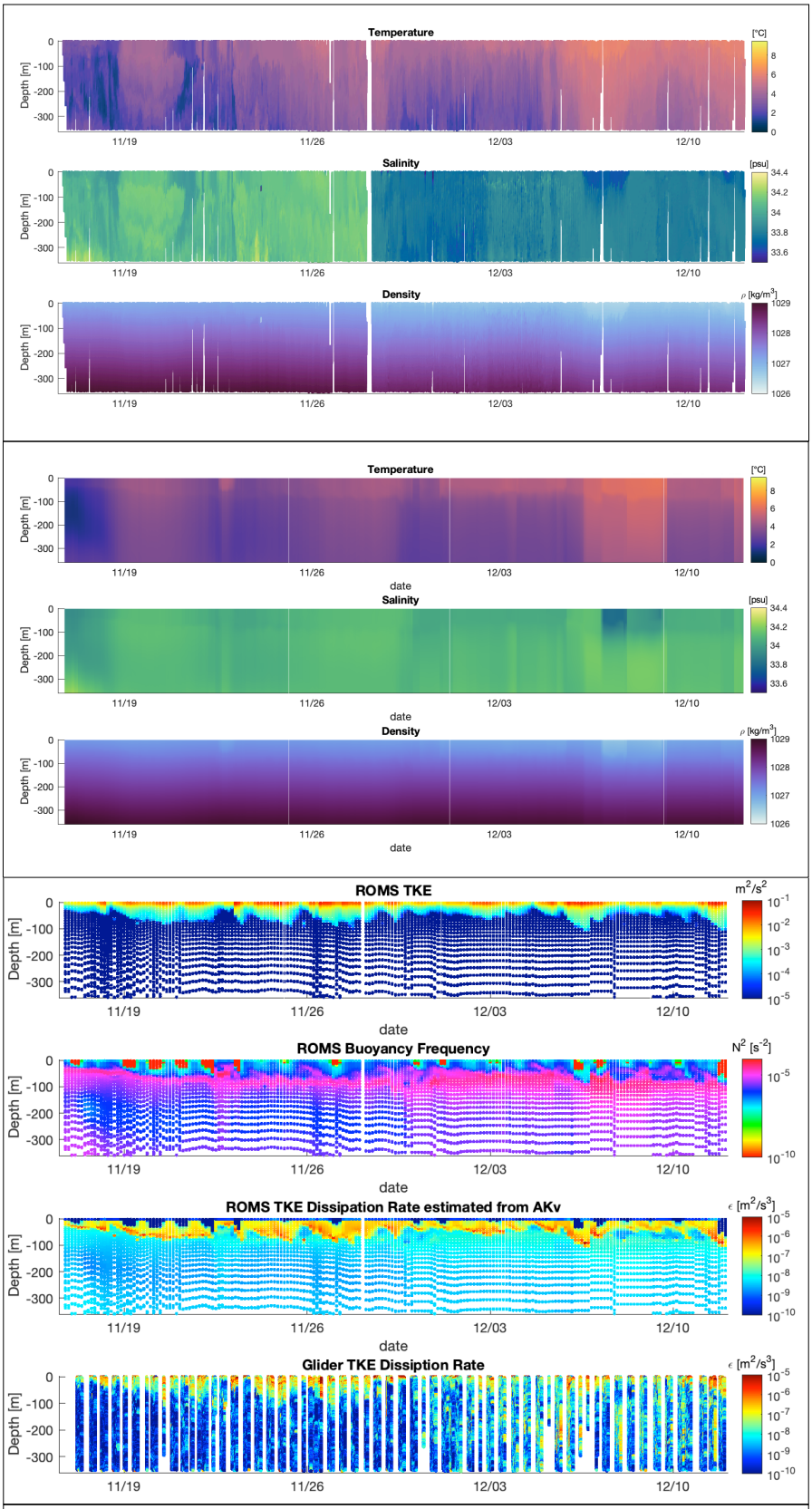

Figure 2: Comparison of AUSSOM glider data and ROMS data extracted along corresponding glider location and time.

Below boundary layer driven turbulence, mechanistic candidates for enhanced dissipation in and above the main thermocline are internal wave-driven mechanisms that can support mixing from below (critical layer interactions or simple internal wave-wave interactions). The other mechanism, less supported by observations, is SI, as popularized by Thomas et al. (2013) or more general mixed layer instability (MLI) events described by Callies et al., 2016. [Note MLI is just specific terminology for eddies formed by ageostrophic baroclinic instability in a surface mixed layer, having weak stratification and a small $\mathcal{O}(0.1)$ Prandtl ratio, with spatial scales $\mathcal{O}$(1-10km) and growth timescales $\mathcal{O}$ (1 day) (Boccaletti et al., 2007).] Most attention has been paid to the modal growth instabilities at stratified unstable fronts (Stone, 1970; Stamper & Taylor, 2017), but its transient effects may also be significant. Zemskova et al. (2020) examined transient (non-modal) growth of instabilities in the hydrostatic Eady problem, finding that associated growth rates are up to two order of magnitude larked that the baroclinic and symmetric modes, likely acting as an non-negligible restratifying agent despite their asymptotic decay. The studies supporting SI and others are heavily analytical and numerical, with limited observational evidence for these instabilities causing enhanced TKE dissipation in the open ocean.

Prior modeling efforts have aimed to elucidate the forward energy cascade from the mesoscale through the submesoscale in major ocean currents. Gula et al. (2016) used a nested Regional Ocean Modeling System (ROMS) model to show that the anticyclonic (eastern) side of the Gulf Stream is topographically sheared by the Bahama Banks, decreasing relative vorticity (amplifying anticyclonic shear) enough to meet criterion

(based on Ertel's potential vorticity) for ageostrophic centrifugal instability. St. Laurent et al. (2019) used 1/12-degree HYCOM simulations of Palau's wake, paired with a microstructure-capable glider, to show only 10% of elevated TKE attributable to wind shear, with the rest likely attributable to shear or instability associate with the relative vorticity field in Palau's wake; vorticity structures in the wake draw energy from mean flow and feed energy to smaller scales, where instability converts it to TKE dissipation (also seen by Simmons et al., 2019). However, lateral strain did not have significant correlation with TKE dissipation, raising questions of whether SI played a significant role (if any). Rosso et al. (2015) used 1/80-degree (1.39 km) hydrostatic MITgcm model to study forward energy cascade in the Southern Ocean, likely one of the first modeling studies looking at topographic effects on the Southern Ocean submesoscale. The authors suggested mesoscale EKE and strain rate could be used to parameterize submesoscale vertical velocity, but the study did not delve into specific mechanisms of downscale energy transfer. Mashayek et al. (2017) used nested 1/100-degree model to show topographic enhancement of mixing over various hotspots in the Drake Passage and Scotia Sea, again confirming the strong role of topography in the ACC forward energy cascade. Finally, Wenegrat & Thomas (2018; 2020) call attention to the importance of baroclinic, centrifugal, and symmetric instability in the bottom boundary layer. While observations of the Kuroshio (D'Asaro et al., 2011) and Gulf Stream (Thomas et al., 2013; Thomas et al., 2016; Todd et al., 2016) have suggested SI might play a role in the ACC, there is to date limited evidence for symmetric instability in ACC fronts. Recent Large Eddy Simulations (LES) has suggested that pure symmetric instability is generally

difficult to recreate, achieved though no wind stress and weak cooling (Skyllingstad & Samelson, 2020).

Centrifugal (or inertial) instability (Jiao & Dewar, 2015) occurs when absolute vorticity destabilizes the flow independent of stratification effects. Interestingly, pure centrifugal instability was thought to be unlikely at high latitude due to planetary stabilization (Haine & Marshall, 1998). However, Adams et al. (2017) observed submesoscale instabilities in the upper 200 meters of a mesoscale cyclonic eddy in the Scotia Sea during the Surface Mixed Layer Evolution at Submesoscales (SMILES) project. The largest patch of centrifugal instability was on the outer edge of a warm core ring on the side near bathymetry in the 100-150 meter depth range, with other areas dominated by gravitational, symmetric, and mixed instabilities. The northern front of the eddy was within 1/2 of a degree of the North Scotia Ridge. With close proximity to the continental rise, it is interesting to consider whether topography had any role in the development of this front-attributed SI. The flanks of currents may be a more promising source than the fronts themselves. Naveira Garabato et al. (2019) uncovered a new mixing mechanism using a microstructure-equipped AUV in an along-slope current of South Orkney Plateau (Antarctica); previously unsuspected submesoscale instabilities (including SI) create a cross-current secondary circulation which transforms water through enhanced boundary layer-interior exchange.

The issue of including SI (either explicitly or through sub grid scale parameterizations) in ocean models is an area of active research. Dong et al. (2021a)

applied the forcing-dependent Bachman et al. (2017) parameterization for mixed layer SI to Coastal and Regional Ocean Community Model (CROCO)-ROMS and found that its inclusion improved simulation results. Yankovsky et al. (2021) have developed a parameterization for SI which does not rely on dimensional parameters as does that of Bachman et al. (2017). With increasing model resolution, parameterizations must be used with caution. Bachman & Taylor (2014) examine the issue of partially-resolved SI and double-counting (resolved and parameterized mixing). KPP and large mixed layer viscosities can squash growing SI modes, called grid-arrested re-stratification. Used a 2D MITgcm model with 5-m vertical resolution to show large horizontal viscosity (80 m^2/s) paired with a fine grid (250-3000m) can prevent mixed layer re-stratification, while smaller horizontal viscosity (10 m^2/s) has been demonstrated to cause excessive restratification due to nonphysical mixing of numerical origin. It should be noted that the vertical structure of this model is not similar to that of ROMS, but still this example illustrates the complexity of parameterizing the mixing in general circulation models for which SI is responsible.

In this study we use an analytical model of an idealized jet to show how topographic shearing drives centrifugal and centrifugal-symmetric instability when the PF jet veers close to the northern boundary of the ACC in the Drake Passage Scotia Sea (Ch. 2, Fig. 1). Next, we utilize vorticity and buoyancy flux fields from a 1-km ROMS hindcast (Fig. 1b) to elucidate the phenomenology of submesoscale frontal instabilities in supplying energy to the ACC microscale. Specifically, we use instability criterion to show phenomenology of difference instabilities in the domain and confirm the findings of the

Table 1. Parameters for 2D model

H: 3500 m
L: 200 km
Nz: 51 ($\Delta z \approx 68.6$ m)
Ny: 301 ($\Delta y \approx 0.66$ km)
Base Lat: 57°S
ρ_0: 1027 kg/m^3

analytical model. Finally, we use numerical solution of the linearized governing equations to explore the growth rates.

2. Analytical Model

2.1 Methods

An 2D idealized model (Table 1), based on a PF-associated jet observed during AUSSOM, was created from the geometry observed via AVISO, wind conditions from CCMP V2.0, and approximate density from the glider to investigate the development of SI. The model is a cross-section of a geostrophic zonal jet with no time evolution. The background density structure (ρ_θ) based on a Drake Passage width of $L_{DP} = 850$ km and potential density anomaly ($\delta\rho_\theta$) which produce the geostrophic jet are given by:

is given by:

$$\rho_\theta(z, y) = (1 + z r_z + y r_y) + \delta\rho_\theta \tag{1a}$$

$$\delta\rho_\theta(z, y) = -0.06(1 + z/H)\tanh((y - y_{0\rho})/\Delta y_\rho) \tag{1b}$$

where $r_z = -1/(H\rho_0)$ and $r_y = -0.3/(L_{DP}\rho_0)$and width of the anomaly (Δy_ρ) is 7 km. The latitude of the density anomaly ($y_{0\rho}$) is chosen to be 100 km (Case O, representing an open ocean jet) or 170km (Case B, representing near-boundary jet). The jet velocity (U_0)

is calculated using thermal wind balance $U_z(z,y) = -B_y/f$, where $B(z,y) = -g\rho/\rho_0$ and subscripts indicate differentiated quantities. A horizontal velocity anomaly (δU) and logarithmic decay function are used to represent the effects of topographic shearing and the topographic boundary layer, respectively.

$$U_0(z,y) = U(z-\Delta z, y) + U_z(z,y)\Delta z \tag{2a}$$

$$\delta U(z,y) = -0.35\tanh((y - y_{0_U})/\Delta y_U) \tag{2b}$$

$$U(z,y) = \begin{cases} U_0 + \delta U, & \text{if } y \le y_{0_U} \\ (U_0 + \delta U)\frac{\ln(L-y)}{\ln(L-y_{0_U})}, & \text{if } y_{0_U} < y \end{cases} \tag{2c}$$

Here $y_{0_U} = 170$ km and $\Delta y_U = 3$ km. Omitting the topographic boundary layer, the transport is similar for both idealized scenarios; 30.73 Sv for Case O and 30.87 Sv for Case B.

A question is what conditions are conducive to forced symmetric instability (FSI) in which Ekman buoyancy flux (EBF) and meteorological buoyancy flux (J_b) can sustain the unstable structure of a symmetrically-unstable front and allow it to persist as it is dissipated by finescale and microscale mixing (Thomas et al., 2013). FSI can occur if $EBF + J_b > 0$ where

$$EBF = \rho_0^{-1}|\tau||U_z|_{z=0}\cos\theta \tag{3}$$

Here τ is the wind velocity and θ is the angle of the wind with respect to the direction of geostrophic shear such that $-90^\circ < \theta < 90^\circ$ indicates a down-front wind component. Using the mean conditions from AUSSOM (Ferris et al., 2020; Ferris et al., in review),

$\tau = 0.3$ N m^{-2} and $J_b = -5.406 \times 10^{-8}$ m^{2}s^{-3}, FSI is possible (Fig. 3), but cannot itself create SI.

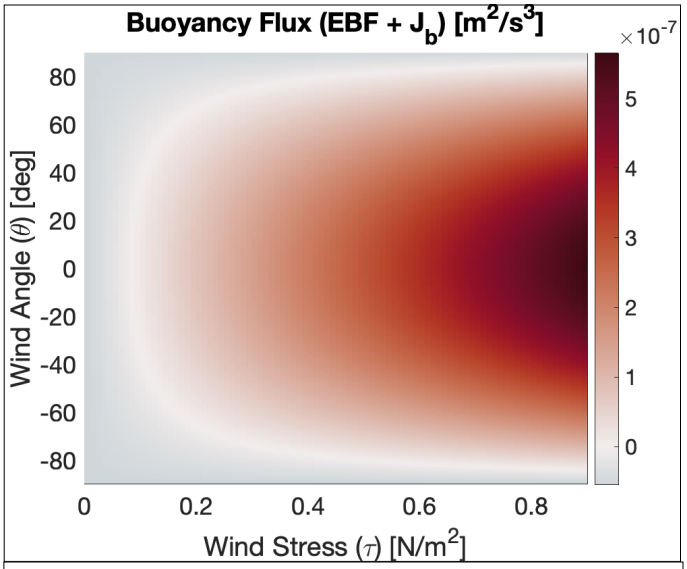

Figure 3: Wind conditions for forced symmetric instability (possible when $EBF + J_b > 0$) for AUSSOM mean buoyancy flux m^2/s^3.

We use instability criteria based on Ertel potential vorticity (q) after Hoskins (1974) and Richardson number $Ri = B_z/(U_z^2 + V_z^2)$ after Thomas et al. (2013); noting $N^2 \equiv B_z$. In the Southern Hemisphere, areas of positive q are inherently unstable (Bachman et al., 2017).

The Ertel PV (q) field is calculated as:

$$q = (f\hat{k} + \nabla \times u) \cdot \nabla b = \left[B_z(f + V_x - U_y)\right]_{vert} + \left[B_y U_z - B_x V_z\right]_{horiz} \quad (4)$$

Here, $b = -g\rho_\theta/\rho_0$. The application of Ri-based instability criteria typically consists of the recasting of the Hoskins (1974) criteria , $qf < 0$, using the assumption of thermal wind balance in the form

$$Ri_B = \frac{N^2}{Uz^2 + Vz^2} \equiv \frac{f^2 N^2}{|\nabla_h b|^2} \quad (5)$$

such that (excluding CI) overturning instabilities arise when $\phi_{Ri_B} < \phi_c$, where $\phi_{Ri_B} = \tan^{-1}(-1/Ri_B)$ and $\phi_c = \tan^{-1}(-\zeta_a/f)$. Here ζ_a is the absolute vorticity. The

hyperbolic tangent function can be partitioned into discretized regimes such that instability types are identified by the relative dominance of terms (Thomas et al., 2013), useful for the compact identification of instability types. These regimes are summarized in Table 2 after Naveira Garabato et al. (2019):

Table 2. Instability Criteria

Type	**Criteria**
Baroclinic Instability	cross-stream gradient of q changes sign with depth
Stratified Shear Instability (SSI)	$Ri < 0.25$
Overturning Instability (OI)*	$qf < 0$
Centrifugal Instability (CI)	$f\zeta_a < 0$ and $B_z > 0$
Gravitational Instability (GI)	$B_z < 0$ or $-180 < Phi_{RiB} < -135$**
Gravitational-Symmetric Instability (GSI)**	$-135 < \phi_{RiB} < -90$
Symmetric Instability (SI)**	$-90 < \phi_{RiB} < \phi_c$ and $\phi_c < -45$ or $-90 < \phi_{RiB} < -45$ and $-45 < \phi_c$
Centrifugal-Symmetric Instability (CSI)**	$-45 < \phi_{RiB} < \phi_c$ and $-45 < \phi_c$
	* includes CI, GI, GSI, SI, CSI ** for $f\zeta_a > 0$

2.2 Results

Cross-sections of the jet in both cases are provided (Fig. 4 and Fig. 5) with centrifugal and centrifugal-symmetric instabilities highlighted over total Ertel potential vorticity in green and red, respectively. In Case O (open-ocean jet, Fig. 4 and Fig. 6a), stratification effects create centrifugal-symmetric instability (red dots) which almost doubles the total amount of overturning instability (plus signs) that would otherwise be limited to centrifugal instability (green dots). In Case B (near-boundary jet, Fig. 5 and Fig. 6b), close proximity of the jet to the northern boundary increases the instances of

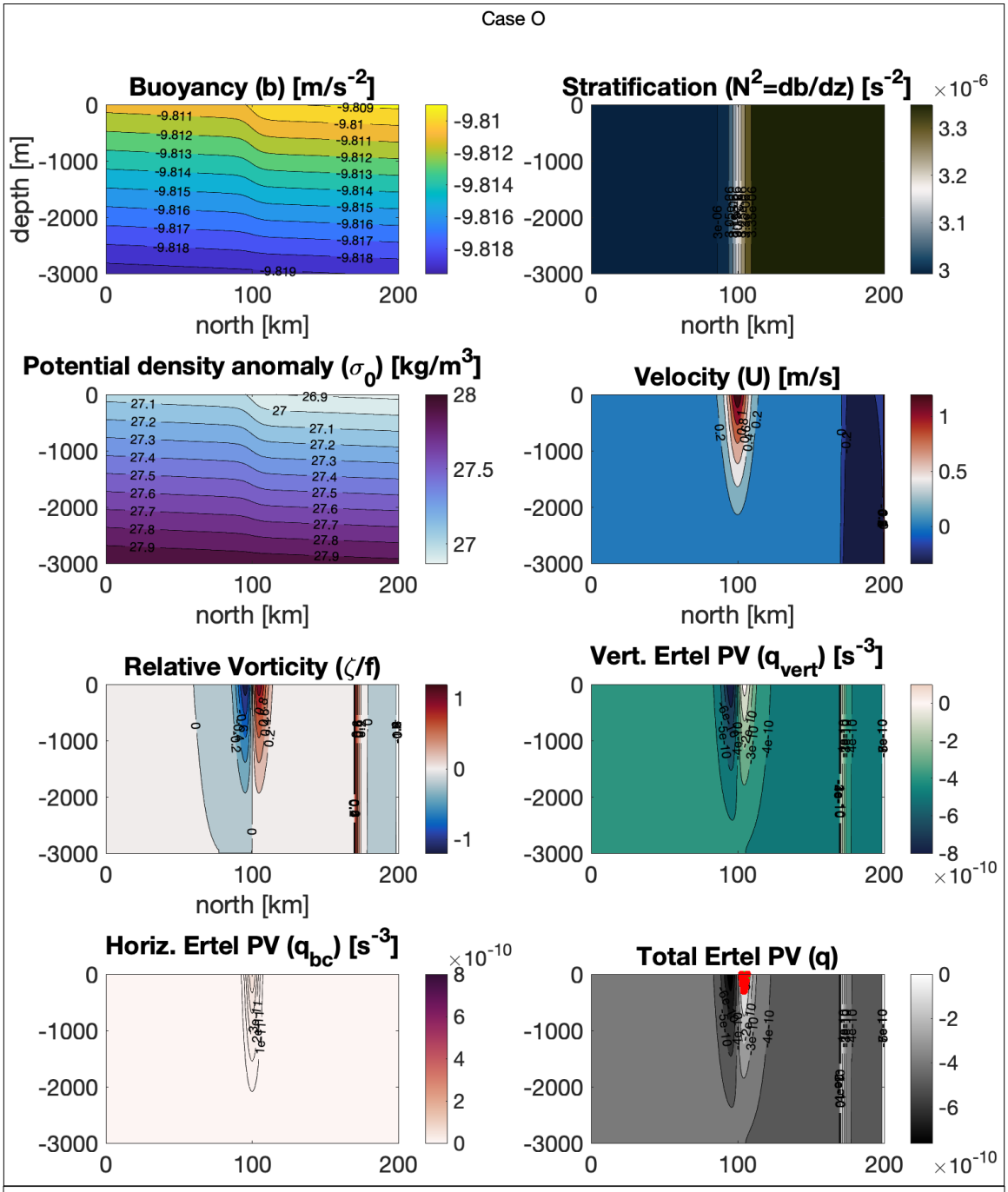

Figure 4: Cross-sections of an idealized jet for the open-ocean case. Nodes satisfying criteria (Table 2) for centrifugal (neon green) and centrifugal-symmetric instability (neon red) are highlighted in **(h)**. There are no instances of pure symmetric instability.

centrifugal instability, which is augmented by a doubling in centrifugal-symmetric instability. The centrifugal-symmetric instabilities extend throughout the

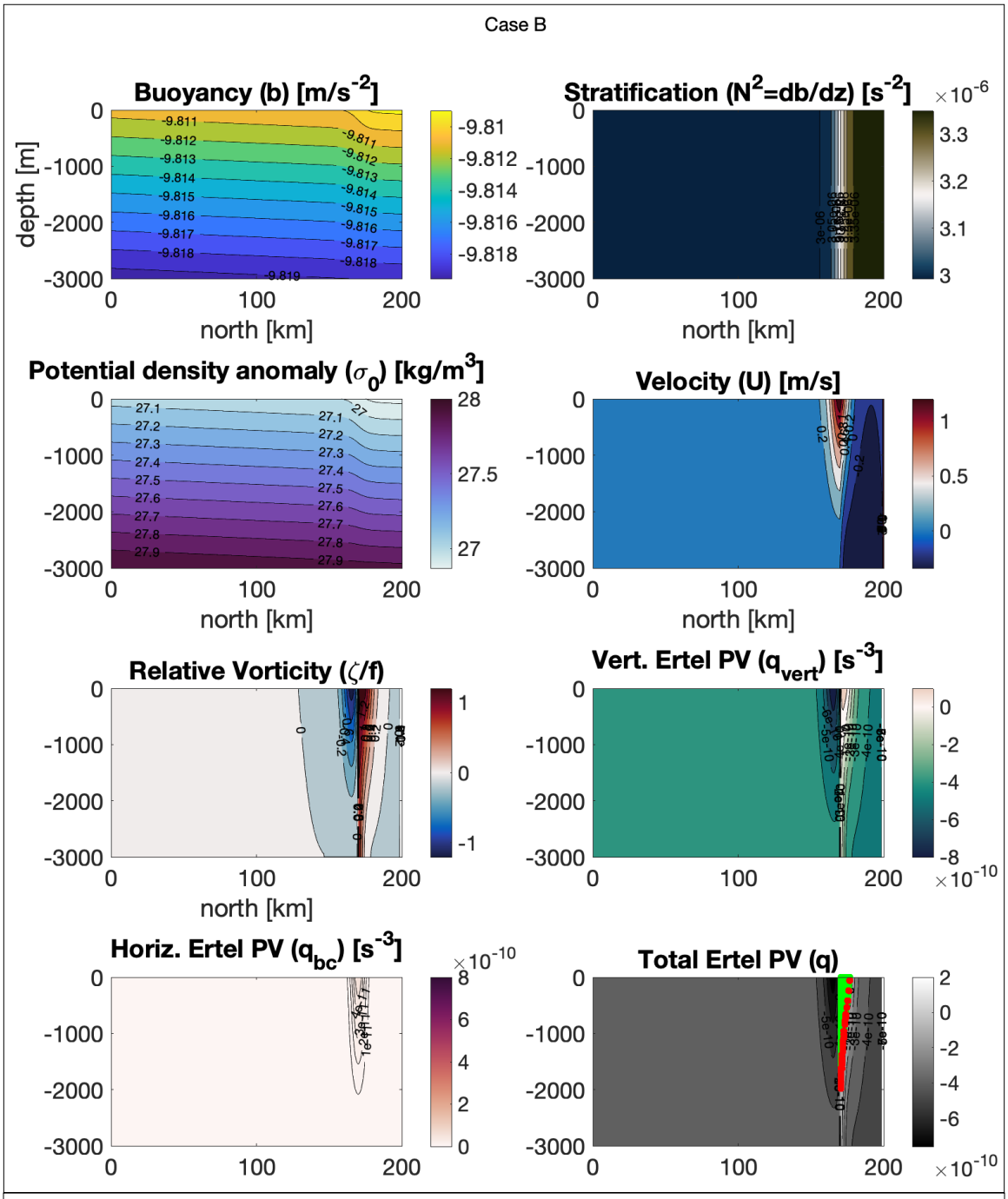

Figure 5: Cross-sections of an idealized jet for the near-boundary case. As in Fig. 4, nodes satisfying criteria (Table 2) for centrifugal (neon green) and centrifugal-symmetric instability (neon red) are highlighted in **(h)**.

water column, illustrating it is not a process specific to the surface ocean or mixed layer as commonly intuited. This idealized scenario demonstrates how an identical jet can produce smaller or greater amounts of submesoscale instabilities in the main thermocline

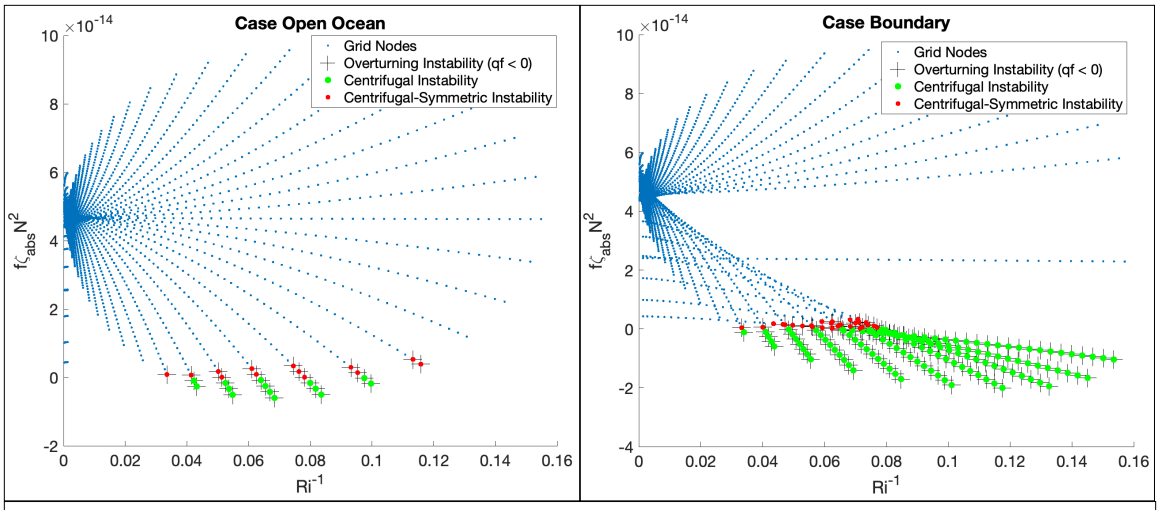

Figure 6: Showing relationship between flow characteristics and presence of submesoscale instabilities for the **(a)** open ocean and **(b)** near-boundary case. Instability can arise in barotropic flows when the y-axis assumes negative values.

depending on its location at a given time, suggesting that the relative role of thermocline submesoscale instability in ACC forward energy cascade depends on temporal variation of the PF in time (unlike mixed layer symmetric instabilities which are not directly contingent on location of the PF and primarily depend on the wind direction and velocity).

3. Numerical Model

3.1 Methods

Model output with 1-km and 3-hr resolution was produced using the Regional Ocean Modeling System (ROMS), a free-surface, hydrostatic, primitive equation model discretized with a terrain following vertical coordinate system (Shchepetkin and McWilliams, 2005). Runs initialize every 7 days and run for 10 days, covering a period from 12-November-2017 though 29-December-2017. The model is initialized using the 1/12° resolution Operational Mercator simulation

(GLOBAL_ANALYSIS_FORECAST_PHY_001_024) and lateral boundary conditions are a radiation/nudging scheme with radiation on outflow and nudging on inflow to Mercator, with a 3-day relaxation timescale (Marchesiello et al., 2001). The purpose of this setup is to limit the model drift, but at the same time allow the ocean to evolve without constraints. The vertical grid is 50 sigma layers, which in the absence of topography appears as depth coordinates in the upper ocean with levels at 0, 3, 8, 12 meters etc. Flux forcing is computed every 3 hours with turbulent fluxes calculated using bulk formulae (Fairall et al., 1996; Large & Pond, 1981) using the evolving model state and specified atmospheric state obtained from MERRA (Gelaro et al 2017) The model uses a K-profile parameterization (KPP) turbulence closure scheme (Large et al., 1994) in the surface and bottom boundary layer and Ri-dependent mixing in the ocean interior. ROMS retains the large-scale mesoscale structures of the Mercator model but admits a cascade to higher wave-numbers with the formation of sharper fronts and filaments. The Charkok-Craig parameter was enabled to incorporate the effects of surface flux of TKE due to wave breaking (Carniel et al., 2009).

Resolving a submesoscale feature (e.g., a symmetrically unstable front) is different from resolving the instability or eddy that grows from it (were model resolution sufficient to let it progress through forward energy cascade). ROMS does not resolve the growing instability; rather it resolves the unstable setup (which is also the basis for subgrid scale parameterizations). To actually resolve these instabilities would require higher resolution; baroclinic MLI has wavelength ~52-2.9 km while SI has wavelength 20-500 m (Dong et al., 2020; 2021). It is important to ensure we attain comparable

resolution and gradients to previous observational and model-based studies of SI. Observations of symmetrically unstable features in the literature range 0.5-km to "few kilometer" towed CTD casts paired with shipboard ADCP (D'Asaro et al., 2011; Thomas et al., 2013; 2016; Adams et al., 2017). Lateral buoyancy gradients used in LES studies have ranged $M^2 = db/dx \approx 1.3 \times 10^{-7} s^{-2}$ to $5 \times 10^{-7} s^{-2}$ (Thomas et al., 2013; 2016;

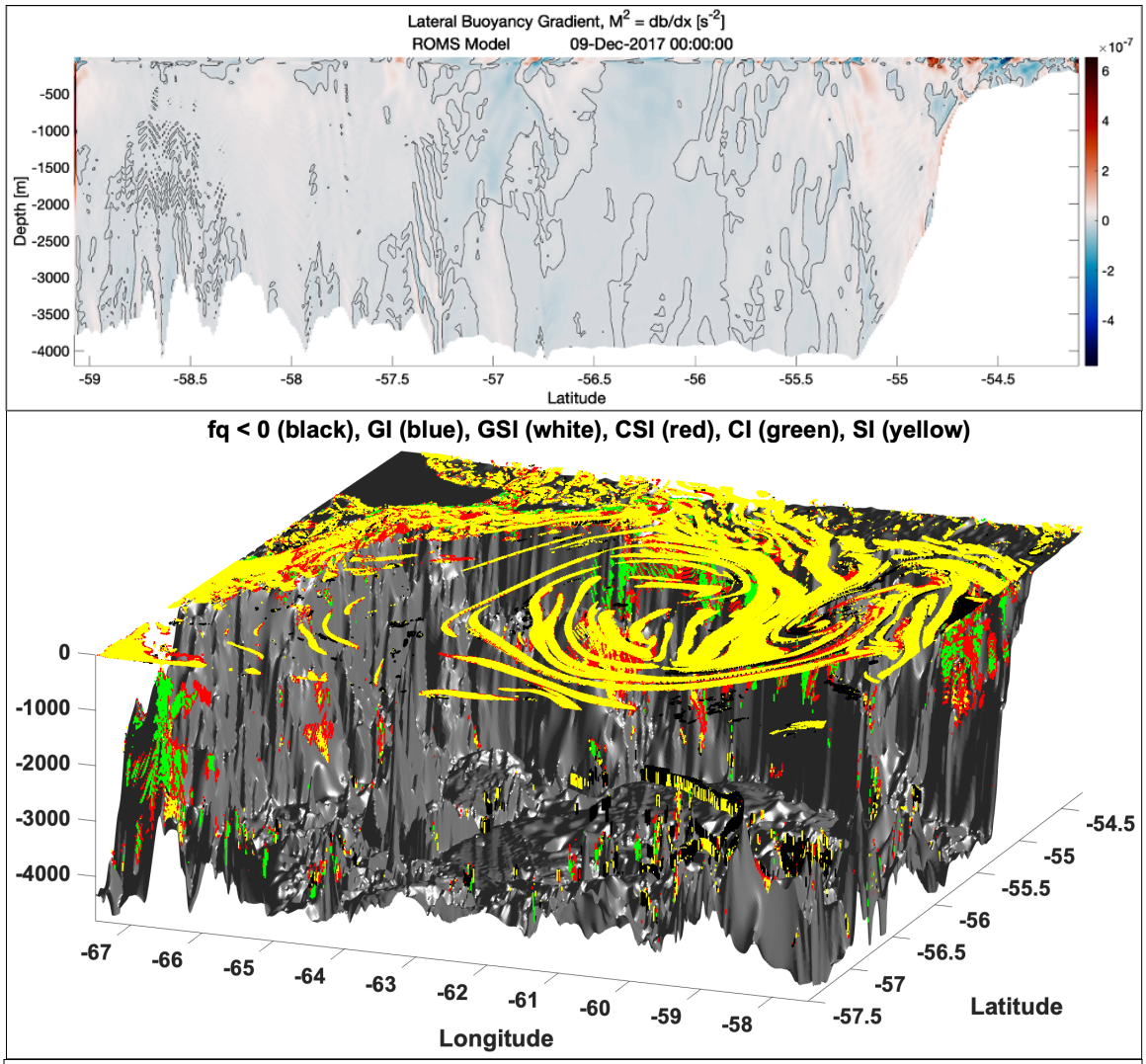

Figure 7: (a) An example of lateral buoyancy gradients found in the ROMS model. The meridional section is taken from 63.5˚W. **(b)** Showing a submesoscale instabilities (Table 2) in the 3-D ROMS domain for one timestep (Run 1, 09-Dec-2017 00:00:00). Unstable nodes are highlighted, including gravitational (blue), gravitational-symmetric (white), any overturning (black), centrifugal (green), centrifugal-symmetric (red), and symmetric (yellow). Instances of overturning instability are overlaid with the other colors when meeting criteria for a specific instability type.

Skyllingstad & Samelson, 2020) which are achieved in the model (Fig. 7a). Another consideration is that ROMS is hydrostatic; however, hydrostacy is not expect to impact resolution of the unstable setup (Mahadevan, 2006).

The typical application of Ri-based instability criteria (Eq. 5) contains assumptions of geostrophic balance (and despite this is has been commonly used in small-scale, high-velocity LES studies). That said, it is straightforward to demonstrate that an assumption geostrophic balance is invalid over Burwood Bank (Ch. 3, Fig. 1) (and other parts of the domain) where velocities on the order of $U \approx 0.5$ m/s and a Coriolis parameter of 1.2×10^{-4} s^{-1} would require features much larger than $L \approx 4$ km to produce a Rossby number ($Ro = U/fL$) of much less than order unity and remain in geostrophic balance. The model resolves ageostrophic features of much less than 4 km and they are present in the northernmost portion of the domain. For the purposes of allowing freedom from the geostrophic assumption, but making use of Ri-based in stability criteria (which are convenient for neatly distinguishing between types of overturning instability, we use the following practical redefinition for the remainder of this paper:

$$Ri_B = \left| \frac{fBz}{By(Uz - Wx) + Bx(Wy - Vz)} \right| \tag{6}$$

which is compatible with the Thomas et al. (2013) Ri-based instability criterion when $By(Uz - Wx) + Bx(Wy - Vz) > 0$. Vertical buoyancy ($B$) and velocity ($U, V$) profiles are linearly interpolated from sigma coordinates to a uniform vertical grid ($\Delta z = 5$m) before calculation of spatial derivatives and the subsequent application of instability criteria (Table 2 with Eq. 6). The model output is considered in two ways: meridional

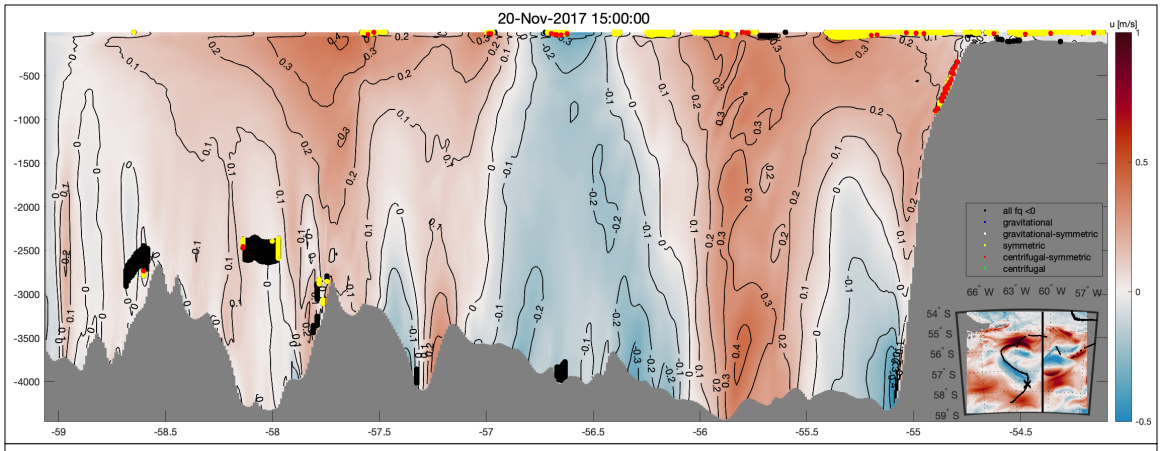

Figure 8: Widespread mixed layer symmetric instability (yellow) associated with Polar Front filaments as well as submesoscale vortices advected from the Tierra del Fuego archipelago. Centrifugal-symmetric instability (red) is seen in the main thermocline along Burwood Bank. Black contours show eastward velocity (u).

sections (conducive to study of the mainly-zonal PF jet) and the full 3-D domain. For meridional sections the PF jet latitude and velocity were obtained by finding the maximum eastward component of velocity ($u(y,z)$) in the general PF latitudinal range ($56.5^{\circ}\text{S} < y < 54.0^{\circ}\text{S}$). The purpose of this latitudinal constraint is to avoid misidentifying the SACCF jet core or (secondary meanders associated with the PF) as the PF jet core. For the 3-D domain, PF jet latitude and velocity metrics were obtained by finding the maximum eastward component of velocity ($u(x,y,z)$) in the general PF latitudinal range for which the front and associated jet are dominantly zonal ($63.0^{\circ}\text{W} < x < 60.0^{\circ}\text{W}$). Instability analysis was restricted ($67.5^{\circ}\text{W} < x < 57.5^{\circ}\text{W}$ and $57.5^{\circ}\text{S} < y < 54.25^{\circ}\text{S}$) to conservatively omit false instability due to slight transport mismatch in the ROMS-Mercator nesting. For consistency, we use a $x = 60.5^{\circ}\text{W}$ example section when discussing the meridional sections, but its associated features were common to the range of longitudes with a zonal PF jet ($63.0^{\circ}\text{W} < x < 60.0^{\circ}\text{W}$) and its selection was somewhat arbitrary.

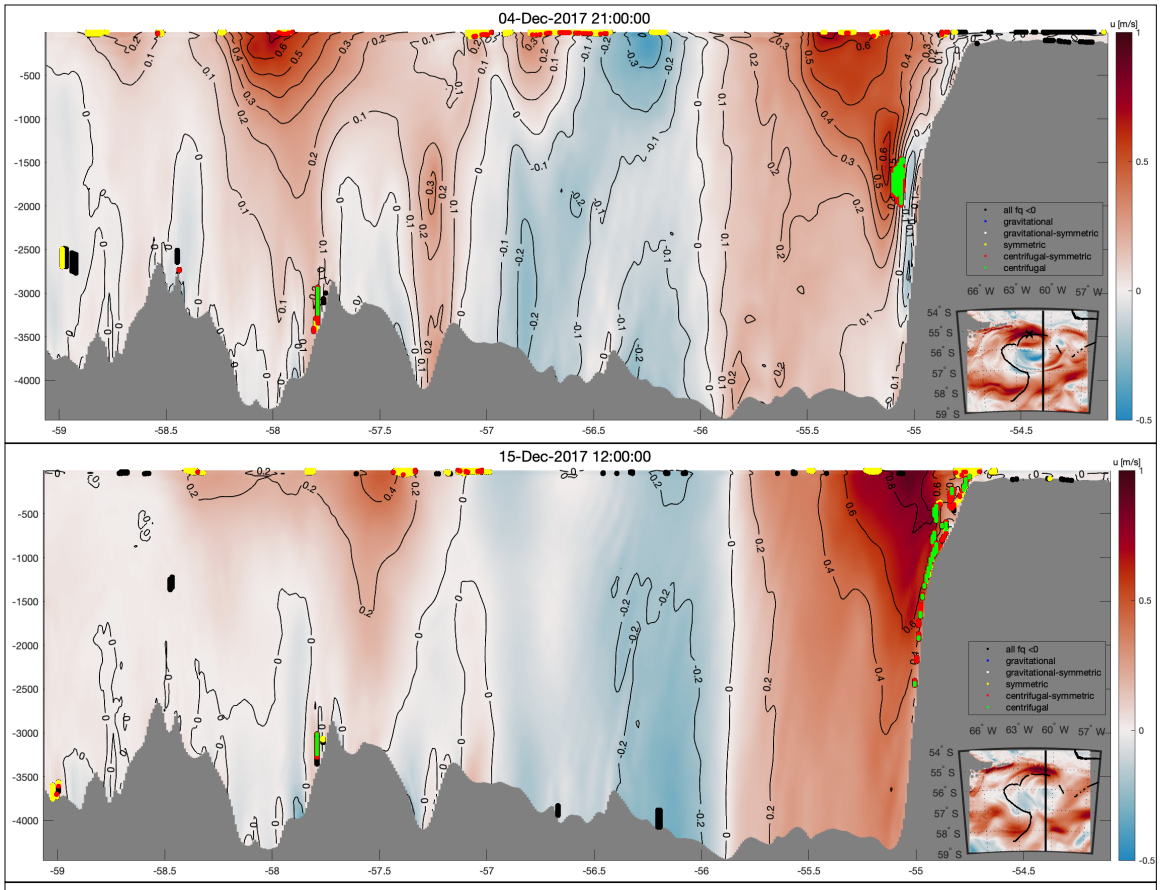

Figure 9: Showing phenomenology of centrifugal (green) and centrifugal-symmetric (red) instabilities for various conditions of the PF jet. associated with a submesoscale vortex produced by shearing of the ACC along Tierra del Fuego and Burwood Bank.

3.2 Results

Centrifugal and centrifugal-symmetric instabilities are present where the PF jet experiences topographic drag along Burwood Bank (Fig. 7b); as well as in the surface boundary layer at open ocean fronts, as limited observations of the Kuroshio (D'Asaro et al., 2011) and Gulf Stream (Thomas et al., 2013) literature suggested would be ubiquitous in the ACC. The mixed layer symmetric instability in the domain (yellow, Fig. 8) is associated with the eastward advection of submesoscale vortices generated by interaction between the ACC and Tierra del Fuego (Fig. 7b) and at the abrupt lateral buoyancy gradients of the Polar Front's numerous filaments. Overall, topographic shearing of

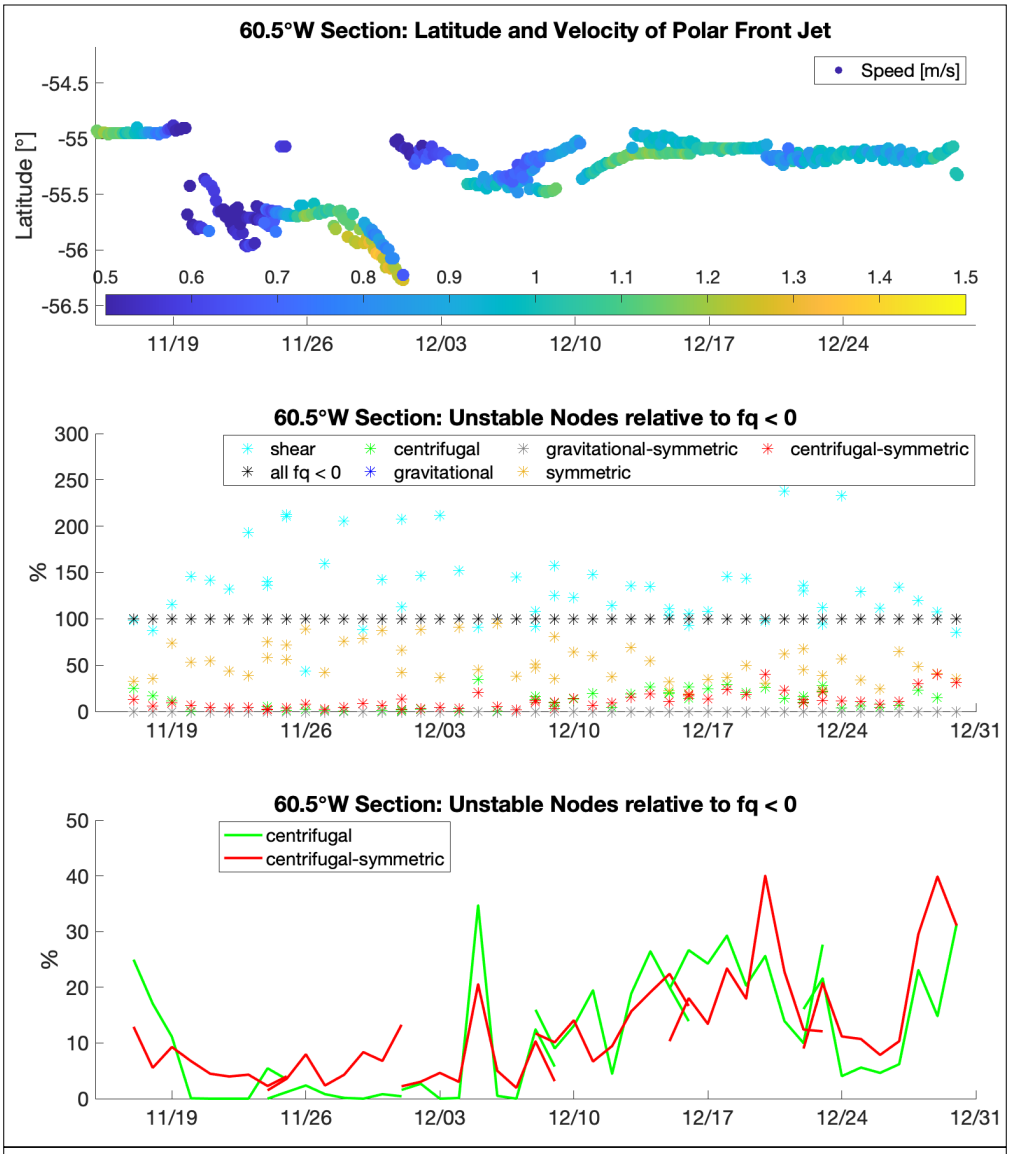

Figure 10: PF characteristics compared to presence of submesoscale instabilities and the relative contribution of centrifugal-symmetric for an example meridional section.

vorticity plays a critical role in the development of submesoscale instabilities. At depth, Instabilities tend to be on the north side of the zonal jet (as theory would predict) but with a larger topographic element than expected. The position of the PF jet (Fig. 9), namely its proximity to the continental rise (Ch. 1, Fig. 1), directly affects the amount of thermocline symmetric instability and its role in ACC mixing. In the southern (northern)

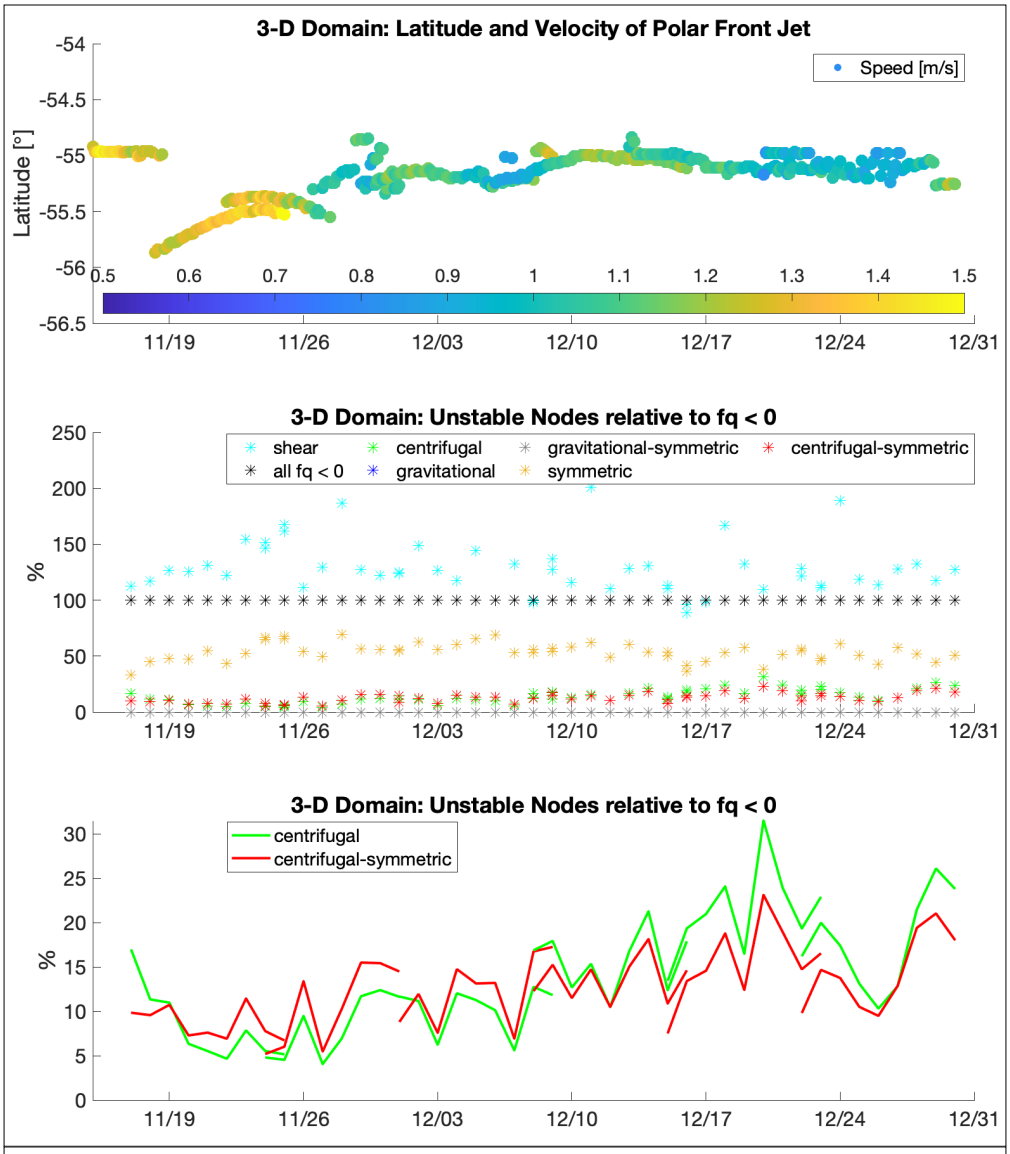

Figure 11: PF characteristics compared to presence of submesoscale instabilities and the relative contribution of centrifugal-symmetric for the full 3-D domain.

hemisphere a process causing an increase (decrease) in relative vorticity would contribute to overall anticyclonic nature of the flow and potentially tip it into the symmetrically unstable realm. In this case, the lateral boundary on the north edge of the ACC (or alternatively, the southern flank of an abyssal topographic feature) produce horizontal shear and thus vertical vorticity to create symmetric instability.

Prevalence of submesoscale instabilities in relation to PF characteristics are given for a meridional section (Fig. 10) and the full domain (Fig. 11). Both of these instability counts demonstrate a trend between the PF jet state (notably, proximity to Burwood Bank at ~55ºS) and the relative role of centrifugal and centrifugal-symmetric instability. The relationship is slightly less pronounced in the full-domain count (Fig. 11) which could be due to the utilized metric PF state (see Section 3.1, i.e. the values for latitude and velocity). The metric of PF state for the 3-D domain (bulk description of PF latitude and velocity) is based on finding the single-point max eastward velocity in proximity of Burwood Bank such that it does not account for curvature of Burwood Bank or the PF jet. While the former cannot be ameliorated in a bulk sense, the latter could be improved by referencing the PF position in kilometers-to-Bank rather than absolute latitude. While symmetric instability appears to be a dominant mode of instability, its phenomenology in the water column suggests otherwise. Though spatially ubiquitous at fronts in the model domain, SI is highly dependent on weak stratification for the production of positive vertically-attributable potential vorticity, q_{vert} (Eq. 4) and for this reason effectively limited to the surface mixed layer (0-100m).

Other limitations of using 1-km ROMS hindcast to study symmetric instability are resolution constraints and presence of partially resolved SI (i.e. the limitation of not resolving the narrowest symmetric instabilities). It is possible that there is mixed layer symmetric instability and other MLIs acting below the 1-km scale in the real ocean which are unresolved by the model. While in the real ocean symmetric instabilities may be sustained by FSI, another limitation worth consideration is that CI, CSI, and SI likely

persists longer in the model than it does in the real ocean due to lack of removal mechanisms, secondary (i.e. shear and convective) instabilities and turbulent dissipation.

4. Numerical Instability Analysis

4.1 Methods

Finally we consider what the potential impact of turbulence on symmetric instability might be. Stability analysis is conducted via numerical solution of normal mode equations to investigate the growth rates and wavelengths of the topographically-sheared instabilities which arise along the northern boundary of the ACC (identified in Section 3). The purpose is to explore the effects of turbulence on growing symmetric instabilities. For this pilot analysis we look at only the fastest-growing mode. We extend the traditional rotating system by implementing isotropic eddy viscosity and diffusivity. The addition of these terms to numerical instability analysis has applications both for completing the physical representation of growing instabilities, as well as stabilizing the numerical algorithms used to solve the normal mode equations due to singular behavior of the normal mode equations (both Taylor Goldstein and Eady forms) in the vicinity of critical layers (Rees & Monahan, 2014; Zemskova et al., 2020)

In general, linear instability analysis (analytical or numerical) is conducted by imposing a small perturbation on the basic equations of motion of the fluid system (linearizing them), deriving a differential equation governing the flow (from the linearized equations of motion), assuming a wave-like solution (with independent variables not appearing in coefficients of the ODE), and examining the integral properties

of the ODE to find where the wave-like solution takes on an exponential growth rate $\sigma = \sigma_r + i\sigma_i$ such that $\sigma_r > 0$ corresponds to a growing instability. Two examples of ODEs are the Rayleigh equation (for a parallel shear flow) and the Taylor-Goldstein equation (for a stratified shear flow). A nonzero imaginary component σ_i means the wave-like solution is oscillatory. Equivalently $\{\sigma\}_i = -\tilde{k}c$ such that an instability has a complex phase speed. The growth rate is related to the e-folding time (for a disturbance to grow by a factor of $e \approx 2.72$) is σ_r^{-1}. Instability analysis can be conducted on real flows through numerical solution of the normal mode equations (using singular value decomposition, a spectral method such as Fourier-Galerkin, or recast as an eigenvalue problem as done below).

We use a stratified, rotating system identical to Smyth & Carpenter (2019) but with the effects of background viscosity and diffusivity added. Assuming perturbation solutions in the form $\phi' = \phi(z)e^{\sigma t + i(kx+ly)}$, we start with the linearized governing equations for a perturbation to a rotating, stratified flow in normal mode form (see Eqs. 8.67-8.71 from Smyth & Carpenter, [2019] for more detail), and add appropriate terms for viscosity (ν) and diffusivity (κ) to obtain the normal mode perturbation equations for a rotating, stratified, viscous, diffusive flow:

$$ik\hat{u} + il\hat{v} + \hat{w}_z = 0 \tag{7a}$$

$$(\sigma + ikU)\hat{u} + U_z\hat{w} = -ik\hat{\pi} + f\hat{v} + \nu\nabla^2\hat{u} \tag{7b}$$

$$(\sigma + ikU)\hat{v} = -il\hat{\pi} - f\hat{u} + \nu\nabla^2\hat{v} \tag{7c}$$

$$(\sigma + ikU)\hat{w} = -\hat{\pi}_z + \hat{b} + \nu\nabla^2\hat{w} \tag{7d}$$

$$(\sigma + ikU)\hat{b} + B_y\hat{v} + B_z\hat{w} = \kappa\nabla^2\hat{b} \tag{7e}$$

Here $\sigma \leftrightarrow \partial/\partial t$, $ik \leftrightarrow \partial/\partial x$, $il \leftrightarrow \partial/\partial y$, and $\nabla^2 \leftrightarrow \partial^2/\partial z^2 - \tilde{k}^2$ and $\tilde{k}^2 = k^2 + l^2$. $\hat{u}$ and $\hat{v}$ are perturbation velocity components, $\hat{b}$ is the buoyancy fluctuation, $\hat{\pi}$ is the pressure fluctuation, k is the wavenumber aligned with the direction of the flow (along-front direction), l is orthogonal to it (across-front direction), U is flow velocity, and B is background buoyancy. After Smyth & Carpenter (2019) the divergence ($\overrightarrow{\nabla}\cdot$) of (Eqs. 7b-d) give pressure equation

$$\nabla^2\hat{\pi} = -2ikU_z\hat{w} + \hat{b}_z + f(ik\hat{v} - il\hat{u}) \tag{8}$$

where viscosity terms vanish due to continuity. Using a change of variables for vorticity $\hat{q} = ik\hat{v} - il\hat{u}$ we cross-differentiate (Eq. 7b) and (Eq. 7c) to obtain

$$(\sigma + ikU)\hat{q} - ilUz\hat{w} = f\hat{w}_z + \nu\nabla^2\hat{q} \tag{9}$$

and take the Laplacian (∇^2) of (Eq. 7d) to obtain

$$(\sigma + ikU)\nabla^2\hat{w} + 2ikU_z\hat{w}_z = -\nabla^2\hat{\pi}_z + \nabla^2\hat{b} + \nu\nabla^4\hat{w} \tag{10}$$

Note the second term in (Eq. 10) comes from using the chain rule twice on the first term of (Eq. 7d) with the assumption that second derivatives of U are negligible (in order to facilitate a solution). By differentiating (Eq. 8) by z and combining with (Eq. 10) to eliminate pressure ($\hat{\pi}$) we obtain

$$(\sigma + ikU)\nabla^2\hat{w} = -\tilde{k}^2\hat{b} - f\hat{q}_z + \nu\nabla^4\hat{w} \tag{11}$$

Finally by recasting (Eq. 7e) again using the vorticity ($\hat{q}$) change of variables we obtain

$$(\sigma + ikU)\tilde{k}^2\hat{b} = ikB_y\hat{q} - ilB_y\hat{w}_z - \tilde{k}^2B_z\hat{w} + \tilde{k}^2\kappa\nabla^2\hat{b} \tag{12}$$

Grouping (Eq. 9), (Eq. 11), and (Eq. 12) gives

$$\sigma \begin{pmatrix} I & 0 & 0 \\ 0 & \nabla^2 & 0 \\ 0 & 0 & I \end{pmatrix} \begin{pmatrix} \hat{q} \\ \hat{w} \\ \hat{b} \end{pmatrix} = \begin{pmatrix} -ikU + \nu\nabla^2 & ilU_z + fD^{(1w)} & 0 \\ -fD^{(1q)} & -ikU\nabla^2 + \nu\nabla^4 & -\tilde{k}^2 \\ \frac{ik}{\tilde{k}^2}B_y & -\frac{il}{\tilde{k}^2}B_y D^{(1w)} - B_z & -ikU + \kappa\nabla^2 \end{pmatrix} \begin{pmatrix} \hat{q} \\ \hat{w} \\ \hat{b} \end{pmatrix} \quad (13)$$

where $D^{()}$ are vertical derivative operators. This system is analogous to the Taylor-Goldstein equation recast as an eigenvalue problem with the effects of rotation, viscosity, and diffusivity added. The pseudocode for this problem is $[\hat{\sigma}, \hat{q}, \hat{w}, \hat{b}] = \mathcal{F}(z, U, B, \kappa, \nu; k, l)$. In the absence of horizontal strain information B_y the user could assume thermal wind balance and estimate it from velocity via $B_y = -fU_z$ but we do not do this. We use fixed boundary conditions for velocity, frictionless boundary conditions for vorticity, and insulating boundary conditions for buoyancy. This derivation assumes isotropic eddy viscosity (ν) and diffusivity (κ). There is a published addition of anisotropic horizontal and vertical values for ν and κ to the Taylor-Goldstein in Lian et al. (2020); to our knowledge there is not published application of viscosity and diffusivity to numerical instability analysis of a rotating stratified system with either isotropic or directionally-distinct values. After solving the eigenvalue problem (13) for growth rate σ and perturbation quantities ($\hat{q}$, $\hat{w}$, and $\hat{b}$), the remaining perturbation quantities are obtained from algebraic solution of the normal mode equations.

$$\hat{v} = i(l\hat{w}_z - k\hat{q})/\tilde{k}^2 \quad (14a)$$

$$\hat{u} = k\hat{v}/l - \hat{q}/(il) \quad (14b)$$

$$\hat{\pi} = -(\sigma\hat{v} + ikU\hat{v} + f\hat{u})/(il) \quad (14c)$$

$$\eta = w/(\sigma + ikU) \quad (14d)$$

The budget for evolution of perturbation kinetic energy (K_t) is obtained from various fluxes using $\overline{a'b'} = \frac{1}{2}\{\hat{a}\hat{b}^*\}_r e^{2\sigma t}$ with $t = 0$ as:

$$K_t = SPZ + SPY - EF_z + BF + \nu K_{zz} - \epsilon \tag{15a}$$

$$K = (|\hat{u}|^2 + |\hat{v}|^2 + |\hat{w}|^2)/4 \tag{15b}$$

$$K_t = 2\sigma_r K \tag{15c}$$

$$SPZ = -U_z\{\hat{u}^*\hat{w}\}_r/2 \tag{15d}$$

$$SPY = -U_y\{\hat{u}^*\hat{v}\}_r/2 \tag{15e}$$

$$EF = \{\hat{w}^*\hat{\pi}\}_r/2 \tag{15f}$$

$$BF = \{\hat{w}^*\hat{b}\}_r/2 \tag{15g}$$

$$\epsilon = \nu/2(|\hat{u}_z|^2 + |\hat{v}_z|^2 + |\hat{w}_z|^2 + 4\tilde{k}^2 K) \tag{15h}$$

Here K is the perturbation kinetic energy, SPZ is vertical shear production, SPY is lateral shear production, EF_z is the divergence of pressure-driven vertical kinetic energy flux, BF is the buoyancy production, and ϵ remains viscous dissipation of TKE [W/kg]. In this case (Eq. 15 and none other, "*" indicates a complex conjugate; in all other cases "*" indicates a dimensionless variable. In general, shear production dominates for CI and SI and buoyancy production dominates for baroclinic and gravitation instability. Both EF_z and νK_{zz} spread but do not create energy (by pressure and viscosity, respectively), causing accumulation at a particular depth.

For the purpose of this pilot analysis we only consider the fastest growing mode. Before solving the problem for vertical profiles, the algorithm is validated by: (1) testing the algorithm for a published idealized non-dimensional with a known Mode 1

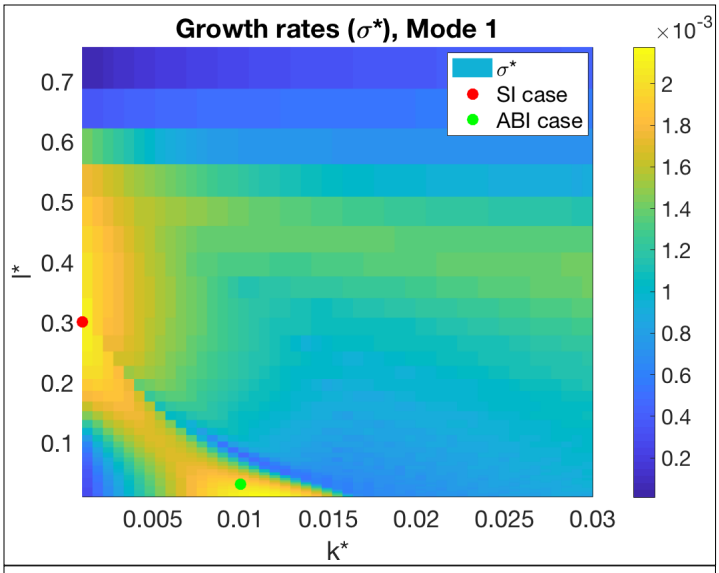

Figure 12: Numerically-obtained growth rate vs. wavenumber for the idealized test case (Table 3) used to validate the non-diffusive inviscid algorithm with Compare to Fig. 8.8 from Smyth & Carpenter (2019). Wavenumbers used to explore the energetics of symmetric instability (SI) and ageostrophic baroclinic instability (ABI) are annotated with dots.

relationship (Fig. 8.8 of Smyth & Carpenter, 2019) for σ^* as a function of wavenumber space (Fig. 12), (2) testing to see whether the summation of right-hand terms in (Eq. 15a) $K_{t\Sigma}$ is equal to (Eq. 15c) indicating the energy budget is balanced, and (3) testing the energy budget once again with an ambient background diffusivity of $\kappa^* = 10^{-6}$ and viscosity of $\nu^* = 10^{-6}$ to verify that it remains in balance. These values are based on mid-to-lower end of the range of diffusivity values $\nu^* = \nu/LU \approx \kappa^*$ observed in the thermocline during AUSSOM (chosen to be conservative due to the isotropic implementation). Parameters for the Smyth & Carpenter (2016) case are given in Table 3.

Table 3. Parameters for Test Case of Rotational Instabilities

$H = 1/2$	$U_z^* = 1$
$z^* = [-H, H]$	$U_y^* = 0$
$P \equiv \lvert f \rvert B_z^{-1/2} = 0.01$	$k^* = [0.1,3]P$
$Ri = 0.94$	$l^* = [1,\pi/z^*]P$
$B_z^* = Ri$	
$f^* = -PRi^{1/2}$	

Here (P) is the Prandtl ratio. Note that this P (based on $B_z \approx 5 \times 10^{-5} s^{-2}$ seen in the

ROMS model and AUSSOM glider dataset, as in Ch. 3 Fig. 2) and Ri of $\mathcal{O}(1)$ are appropriate for submesoscale activity in the parts of thermocline and above (such as Fig. 9). Maximum analytical growth rates are predicted from the well-known expressions

$$\sigma_{BI} = 0.3\,|f|\,Ri^{-1/2} \tag{16a}$$

$$\sigma_{SI} = |f|\,(1/Ri - \zeta_a/f)^{1/2} \tag{16b}$$

$$\sigma_{CI} = \{(-f(f - U_y)^{1/2})\}_r \tag{16c}$$

for idealized cases. From (Eq. 16), $\sigma^*_{BI} = 2.8 \times 10^{-3}$ and $\sigma^*_{SI} = 2.5 \times 10^{-3}$; due to the lack of relative vorticity, the idealized setup (Table 3) is conducive to symmetric and baroclinic but not centrifugal instability.

4.2 Results

The growth rate for symmetric instability for the idealized inviscid, non-diffusive case ($\sigma^* = 2.1 \times 10^{-3}$, Fig. 13a) is remarkably similar to the analytically predicted maximum growth rate for symmetric instability. The velocity structure of the perturbations are qualitatively similar to that of numerical simulations in Stamper & Taylor (2016, Fig. 3). Energetics are reasonable for a constant-U_z and constant-B_z flow, with shear production removed balanced by buoyancy flux, pressure-driven flux (EF) vanishing at the boundaries, and the redundant metrics of kinetic energy (Eq. 15a and Eq. 15c) matching. Shear production is primary energy source as expected for SI; it is opposed rather than augmented by buoyancy, consistent with centrifugal-symmetric variety. Upon adding viscosity and diffusivity (Fig. 13b), the growth rate is reduced by 50% ($\sigma^* = 2.1 \times 10^{-3}$ without viscous/diffusive effects vs. $\sigma^* = 1.2 \times 10^{-3}$ with

viscous/diffusive effects). Shear production removed by buoyancy flux increase, consistent with viscosity configuring perturbation such that it extracts more kinetic energy from mean flow.

For the ageostrophic baroclinic mode (Fig. 14), the addition of viscosity and diffusivity reduces growth rate by only 5% ($\sigma^* = 2.0 \times 10^{-3}$ without viscous/diffusive effects vs. $\sigma^* = 1.9 \times 10^{-3}$ with viscous/diffusive effects). The growth rate for ageostrophic baroclinic instability (Fig. 14a) for the idealized inviscid, non-diffusive case ($\sigma^* = 2.0 \times 10^{-3}$, Fig. 14a) is slightly below the analytically predicted maximum growth rate for baroclinic instability ($\sigma^* = 2.8 \times 10^{-3}$), a result subject to the choice in wavenumber space (Fig. 12). Energetics are dominated by buoyancy production which is reasonable because buoyancy rather than shear is the primary energy source of baroclinic instability.

For the idealized cases, the TKE dissipation structure (Fig. 15) for symmetric instability is distinct from ageostrophic baroclinic instability, with higher dissipation associated with the former; though it is worth noting that the background values for ν and κ affect the resulting ϵ profile. Overall the idealized, non-dimensional cases have well-behaved, believable solutions which match the analytically predicted growth rates for symmetric and baroclinic instability, respectively. The 5-50% disparity in growth rate between the inviscid/non-diffusive and viscous/diffusive cases make a strong case that it is important to consider these effects when applying numerical instability analysis to both observed and idealized flows in order to obtain useful estimates of growth rate.

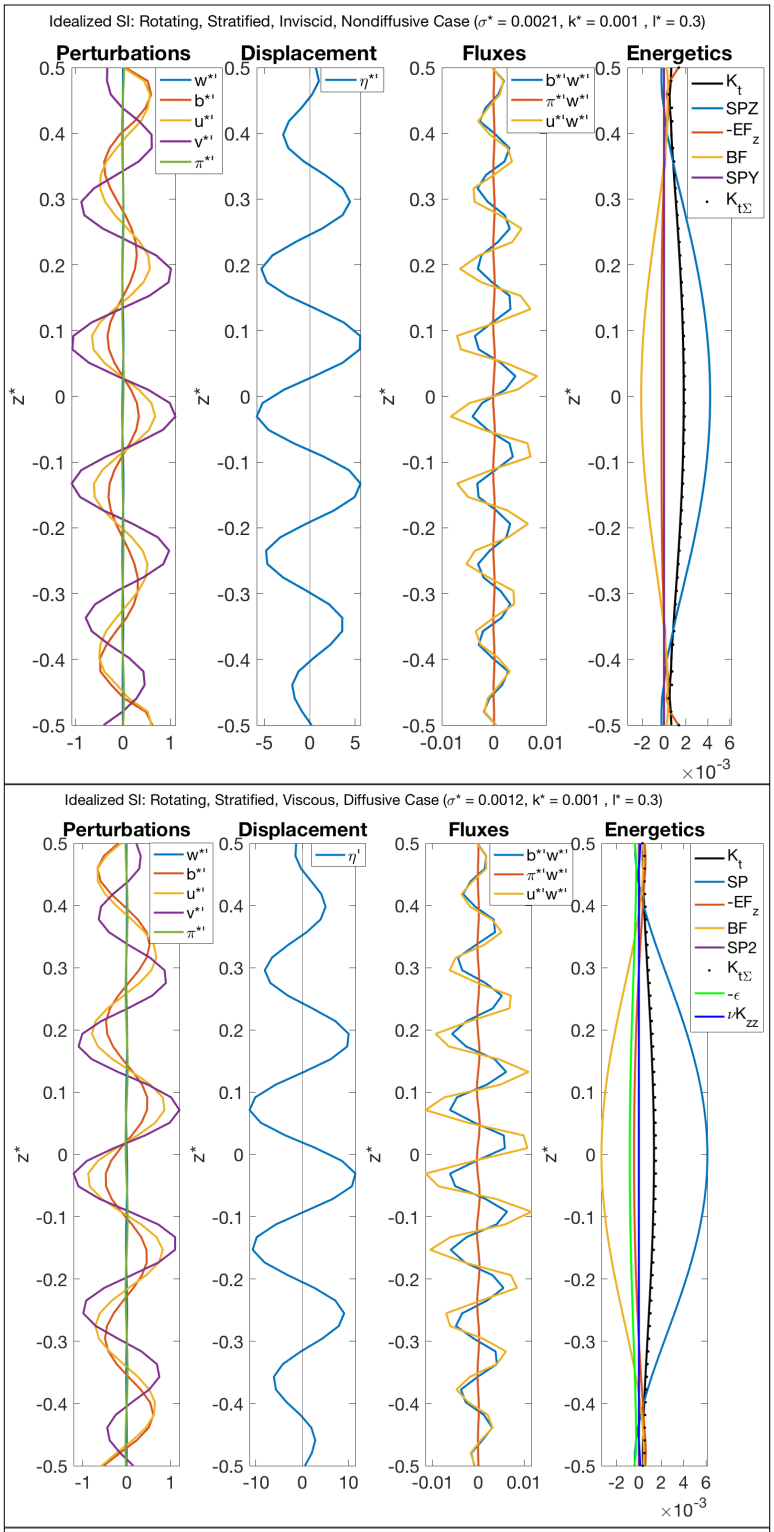

Figure 13: Perturbation quantities, fluxes and energy terms (Eqs. 15a-h) of the symmetrically unstable idealized profile in Fig. 12 without (a) and with (b) a weak viscosity and diffusivity.

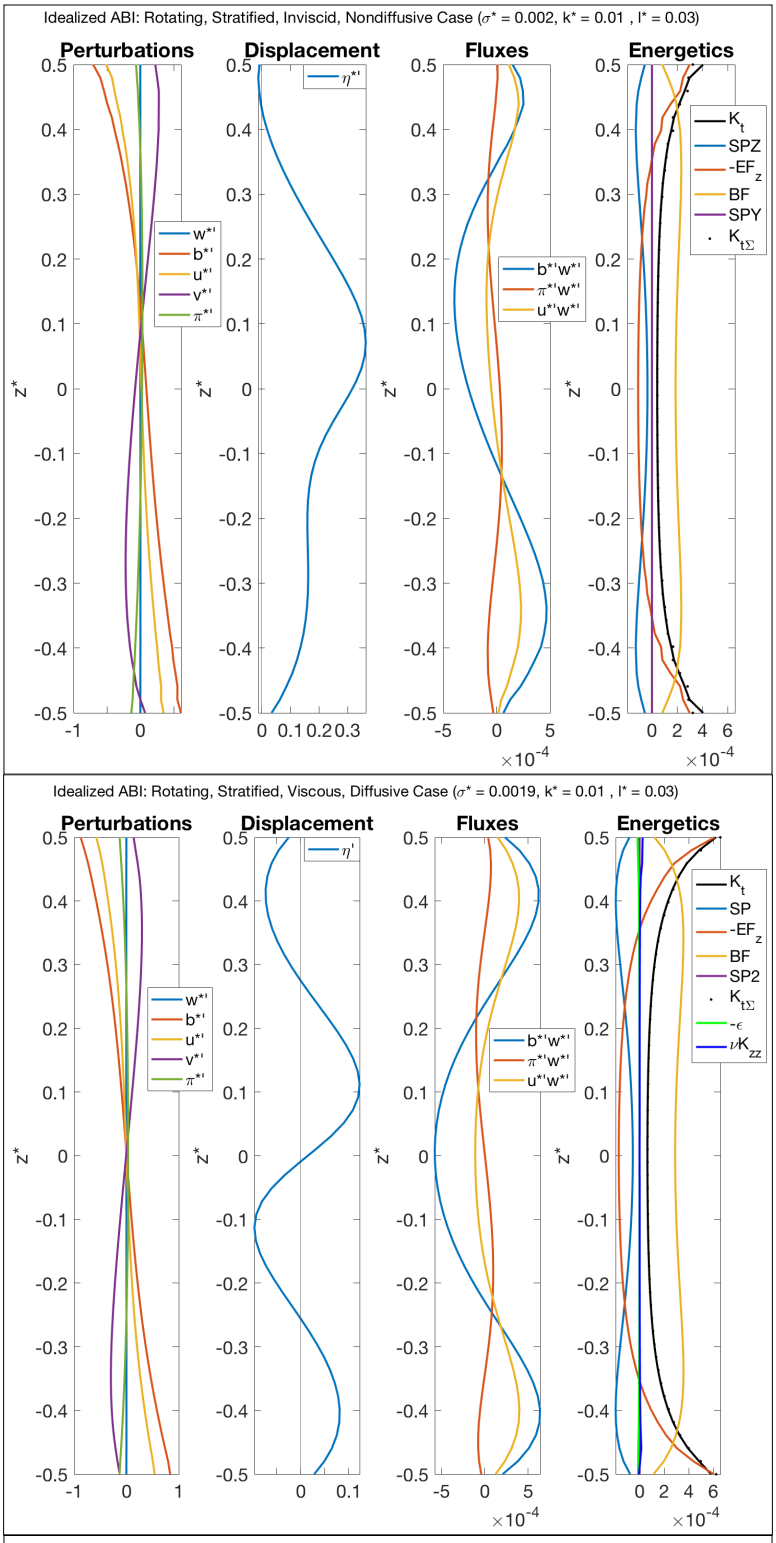

Figure 14: Perturbation quantities, fluxes and energy terms (Eqs. 15a-h) of the ageostrophic baroclinicly unstable idealized profile in Fig. 12 without (a) and with (b) a weak viscosity and diffusivity.

Viscous and diffusive effects restrict wavenumber range (k, l) of the symmetric mode and reduce growth rate (σ*) where it persists (Fig. 16). However, there is minimal impact for the baroclinic mode which acts at larger scale. Support for widespread SI based on idealized, inviscid, non-diffusive Eady-type cases may have less applicability to real ocean mixing than previously thought. In-depth numerical instability analyses (i.e. variation of dimensionless numbers and data sources) are needed to further contextualize this result in the physical ocean.

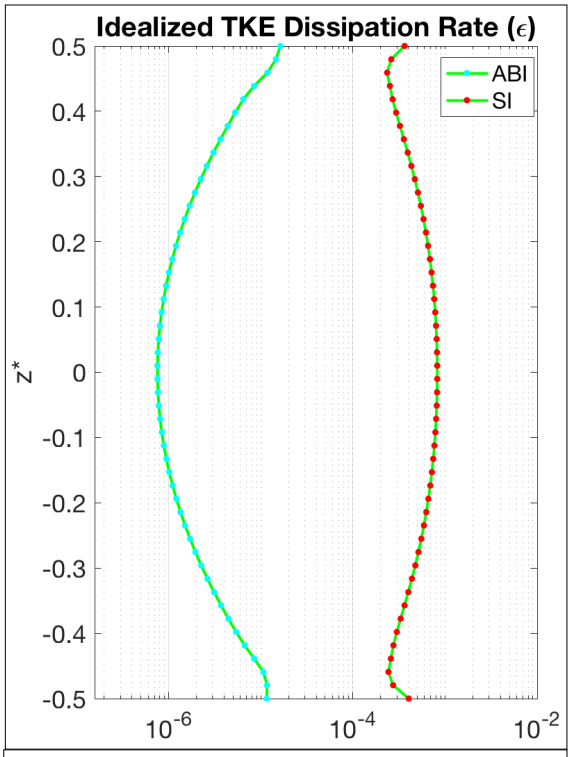

Figure 15: Estimated TKE dissipation rate from idealized (Fig. 13b and Fig. 14b) cases with a weak viscosity and diffusivity.

5. Discussion

5.1 Summary

While symmetric instability is significant to mixing near lateral boundaries in the ACC, we find that (away from sloping topography) it has minimal influence on TKE dissipation below the weakly stratified surface mixed layer. Both the mixed layer and the SI convective layer (estimated using $Ri_{bulk}(z = H) \equiv 1$; Thomas et al., 2013) take on values 0-100 m, rendering this physical process significantly too shallow to explain the high values of glider-observed TKE dissipation (Fig. 1a) extending to and beyond 350 m. Wave-wave interactions, wave-flow interactions, and other pathways likely dominate the

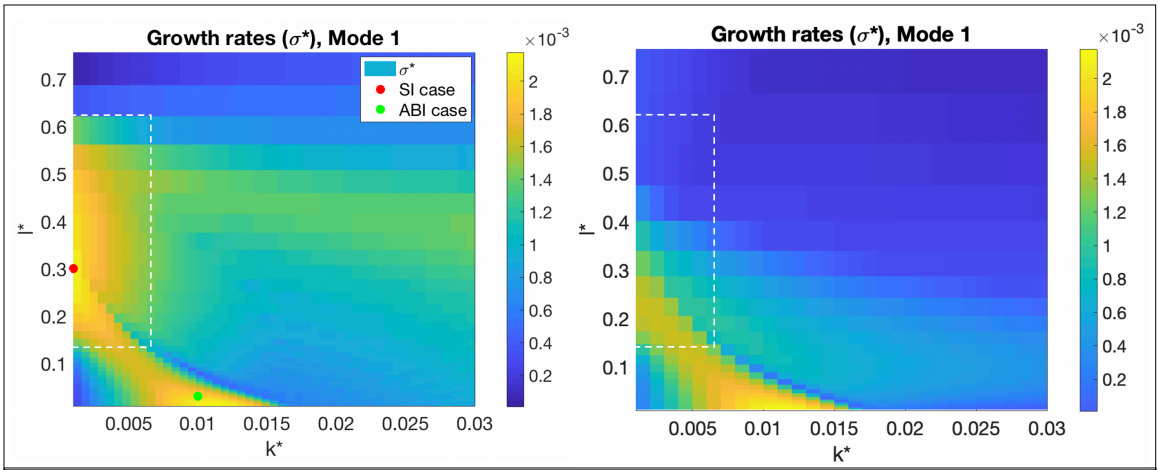

Figure 16: Growth rate in wavenumber space before and after the addition of viscous and diffusive terms. Note **(16a)** is identical to Fig. 12.

forward cascade in those domains. The significance of thermocline symmetric instability to the turbulent kinetic energy budget likely varies temporally along with wind forcing and the locations of ACC frontal jets. Both atmospheric changes such as the Southern Annular Mode and the El Niño Southern Oscillation (ENSO) and internal dynamical variabilities can alter the position of the ACC's fronts (Gille et al., 2016) and thus the positions of their associated jets. Changing position of the polar fronts with respect to Southern Ocean topography will impact SI-associated mixing and thus vertical heat, carbon, and nutrient flux. Additionally, the mechanism for Antarctic Intermediate Water (AAIW) formation is not well known; enhanced mixing at the ACC's northern boundary due to the topographic shearing mechanism presented in this paper may play an important role.

This is not the first finding of topographic shearing facilitating the forward energy cascade by producing submesoscale instabilities in a major current; we observed a similar mechanism to that presented in Gula et al. (2016). SI is created on the anticyclonic side of

the ACC when topographic drag increases relative vorticity enough to create SI of the centrifugal nature. If presence of northern boundary dominates the development of SI, a natural conclusion is that the Drake Passage and Scotia Sea region are unique (perhaps with the exceptions of the Agulhas Bank and Campbell Plateau). Other features such as the Kerguelen Plateau and submerged seamounts can provide topographic drag. Regardless, northern land boundaries renders this region unique to the rest of the ACC. But with strong support for a spatial inhomogeneity of Southern Ocean mixing and the log-scale nature of TKE dissipation, the spatial extend of a mechanism does not directly correspond to its importance.

Symmetric instability may not be a realistic narrative for Southern Ocean frontally enhanced mixing, as least below the surface mixed layer and above 1-km scale (with the caveat that if SI in away from lateral boundaries is prevalent, it is acting at smaller scales and requires sharper horizontal buoyancy gradients than the model can produce). Left unexplained is the physical process responsible for sharply enhanced upper ocean TKE dissipation rates recently observed by the AUSSOM (Autonomous Sampling of Southern Ocean Mixing) glider program (Ferris et al., 2020; Ferris et al., in review), which observed elevated turbulent dissipation rates ($\epsilon = 10^{-7}$ W/kg) for the entire duration for which the glider sampled the core of the Polar Front (Fig. 1a) down to 350 m. We dispute the role of SI and other MLIs in energetic frontal zones (such as the ACC and Kuroshio) as a dominant driver of mixing; they are certainly present in the Southern Ocean but have limited vertical influence and perhaps less relevancy than previous literature has suggested.

Symmetric instability was speculated to be a sourced of elevated subsurface TKE during the AUSSOM glider mission, but further analysis (comparison of AUSSOM glider position with submesoscale instabilities in the ROMS data) has rendered symmetric instability an unlikely candidate to explain this turbulence. Buoyancy flux played a minimal role in forcing the actively mixing layer in the Drake Passage/Scotia Sea region, with buoyancy rarely removed from the upper ocean and energy for near-surface mixing predominately supplied by wind stress (Ferris et al., 2020). This implies that the condition for Ekman buoyancy flux to sustain forced symmetric instability (FSI) is that the wind field have a down front component (true). However, the significance of FSI is to maintain SI as it acts to homogenize the potential vorticity field. This is an observational consideration but not relevant here because the ROMS model is unable to evolve SI (Thomas et al., 2008) and thus remove it through dissipative processes. With suspicion towards symmetric instability minimized, we suspect internal wave interactions, particularly absorption and reflection at critical layers along the Polar Front and its mesoscale eddies to be responsible for this TKE dissipation.

5.2 Critical layer interactions as a mechanism for enhanced dissipation

Particularly in the Southern Ocean, internal lee waves are a key process driving the energy cascade below the thermocline (Bell, 1975; Nikurashin & Ferrari, 2010a; Nikurashin & Ferrari, 2010b; Nikurashin et al. 2014). Internal lee waves generated by flow-topography interactions appear to dissipate only a fraction of the total lee wave energy locally, with most of their energy radiating away (Brearley et al., 2013). Internal lee waves generated through the interaction of flow with topography

($h = h_0 \sin[k(x + Ut)]$) such that waves oscillate with intrinsic frequency $\omega = kU_0$, where k is the topographic wavenumber and U_0 is the velocity of the mean flow; they can propagated when $f < \omega < N$ (Bell, 1995). Waves have the form

$$u = -Umh_0 \cos(kx + mz - \omega t) \tag{17a}$$

$$v = k^{-1} fmh_0 \sin(kx + mz - \omega t) \tag{17b}$$

$$w = Ukh_0 \cos(kx + mz - \omega t) \tag{17c}$$

with dispersion relation and vertical wavenumber

$$\omega^2 = \frac{f^2 m^2 + N^2(k^2 + l^2)}{k^2 + l^2 + m^2} \tag{18a}$$

$$m^2 = \frac{k^2(N^2 - \omega^2)}{\omega^2 - f^2} = \frac{k^2(N^2 - U^2 k^2)}{U^2 k^2 - f^2} \tag{18b}$$

The upward propagations of lee waves [within the hydrostatic rotating wave regime] into the water column can flux energy into the upper ocean from the abyssal ocean. These radiating internal lee waves can interact nonlinearly with the mean flow at critical layers in the ocean, depositing energy into the surface-intensified mean flow without significant turbulent mixing (Waterman et al., 2013).

While internal waves do not require critical layer interactions to redistribute energy, critical layers can expedite and concentrate the process. A critical layer forms where wave frequency matches the local Coriolis parameter ($\omega \approx f$), upward-propagating waves asymptotically approach a near-horizontal ray path, and friction effects cause wave energy to dissipate. Functionally this is when the local flow velocity changes such that $U(z) = f/k$. Using Coriolis parameter f, mean flow velocities U_0, and buoyancy

frequency N, we can solve for the wavenumber range associated with propagating lee waves $f/U_0 < k < N/U_0$ and identify cases which produce a critical layer. Booker & Bretherton (1967; using WKB approximation) found that waves approaching a critical level are refracted by velocity shear such that vertical wavenumber increases without limit, the time for energy associated with the group velocity ray to approach the critical level is infinite, and dissipative effects become important (Warren & Wunsch, 1981; Gill, 1982, Kunze & Lien, 2019). The Eliassen-Palm finding that flux of momentum due to wave-mean interactions should be constant ("non-acceleration result"; Vallis, 2019) is discontinuous at critical levels; momentum transfer can occur (Thorpe, 2005). A discussion on baroclinic critical layers is found in Wang & Balmforth (2016), which are distinct from classical critical layer depths associated with baroclinic instability (Smith & Marshall, 2008; 2009; Chen et al., 2014).

Sheen et al. (2015) observed a deep Southern Ocean mesoscale eddy modulating lee wave propagation and TKE dissipation, with reflection of internal wave energy from the eddy center and enhanced breaking through critical layer processes along eddy boundaries. Examination of the Southern Ocean topographic wavenumber spectrum paired with ROMS near-bottom flow velocities (Fig. 17) suggests critical layer interactions are generally possible for the velocity range $U(z) = [0.1,0.8]$ m/s such that this process is not only possible but likely. Similarly, we can work backwards by starting with the ACC velocity structure $U(z)$, solving for the horizontal wavenumber ($k(z)$) which would be associated the critical layer at a given depth, and rejecting wavenumbers outside of the propagating range. This exercise is conducted on transects of the ROMS

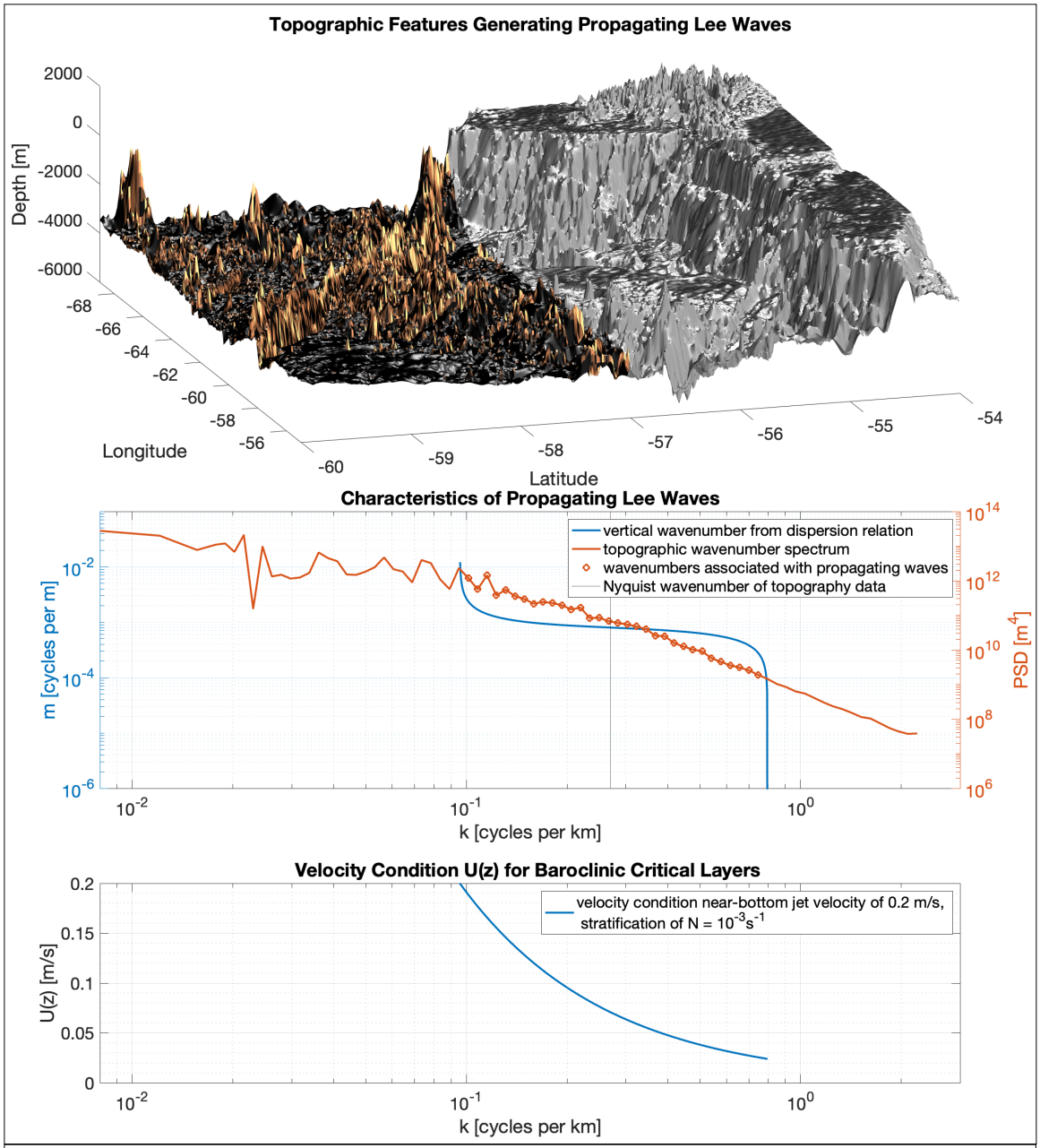

Figure 17: Southern Ocean conditions conducive for critical layer interactions. Showing: **(a)** bathymetry where presence of copper color indicates topographic features within wavenumber range to produced propagating lee waves. Produced by calculating radially averaged surface roughness power spectrum (method adapted from Kanafi, 2021) of Smith & Sandwell (1997) topography and bandpass filtering to remove wavenumber contributions outside of the propagating range. **(b)** characteristics of propagating lee waves (blue) in comparison to topographic spectrum (orange) with wavenumber from (Eq. 18b); with near-bottom jet velocity $U_0 = 0.2$ m/s from typical ROMS section, and $f = 1.2 \times 10^{-4}$ s^{-1} typical for the Southern Ocean, and the horizontal wavenumber range from St. Laurent et al. (2012). **(c)** resulting critical condition. Future analysis will involve narrowing the wavenumber range for spatial subsets based on nearby topography (ignoring non-local production of lee waves).

model which are tangential to the AUSSOM glider track (Fig. 18). Critical layer

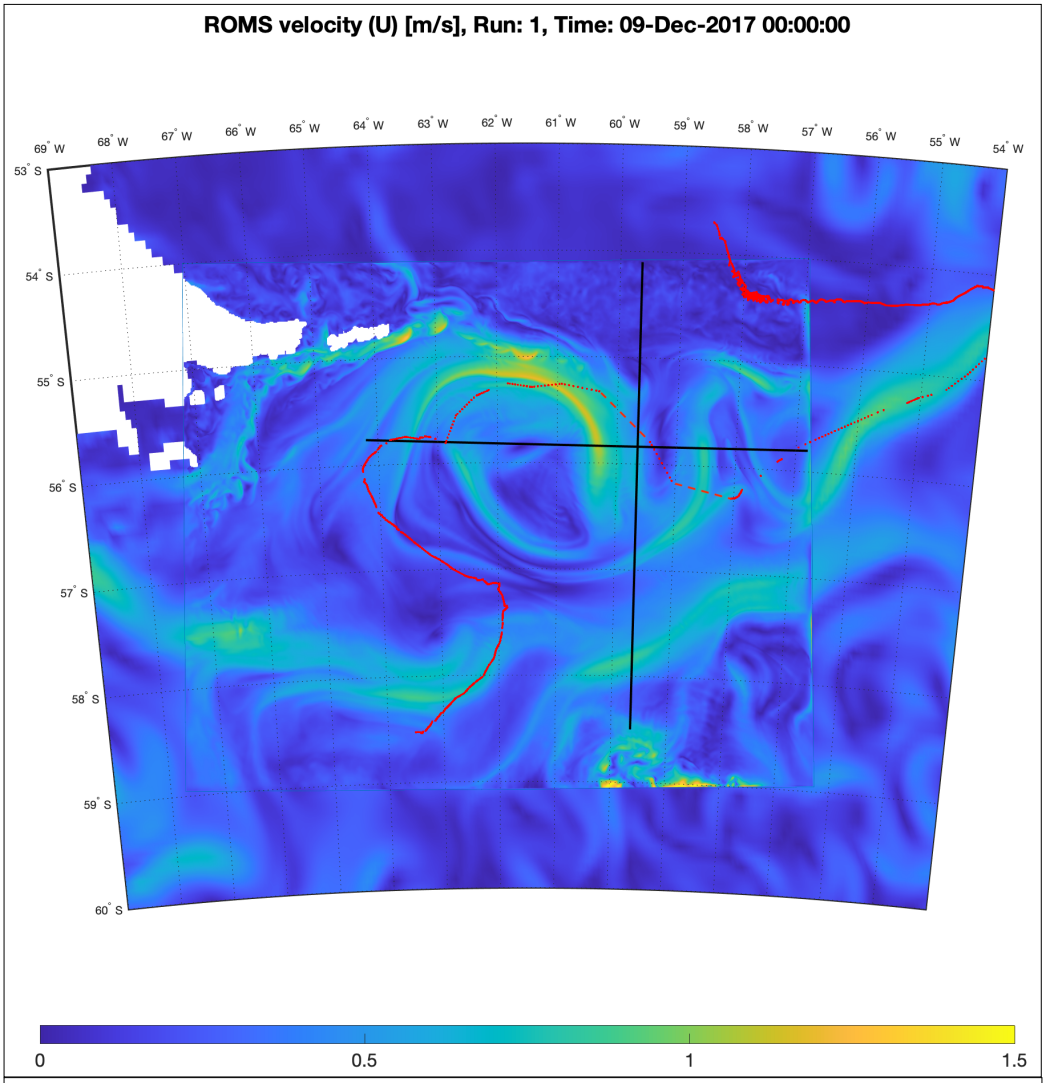

Figure 18: Showing locations of model transects (black lines) used for critical layer analysis. The AUSSOM glider track is shown in red.

interactions were possible in the 0-350 meter depth range (Fig. 19-20) during the time the glider measured elevated TKE dissipation throughout the water column (Fig. 1a), unlike SI which is confined by stratification to the shallowest 100 m. Critical conditions are only apparent outwards of the PF core along the edges of the associated eddy (Fig. 18). Inside of the jet core, the current velocity is too high such that the wavenumber (which would be associated with the critical condition) falls below the propagating range (limited by

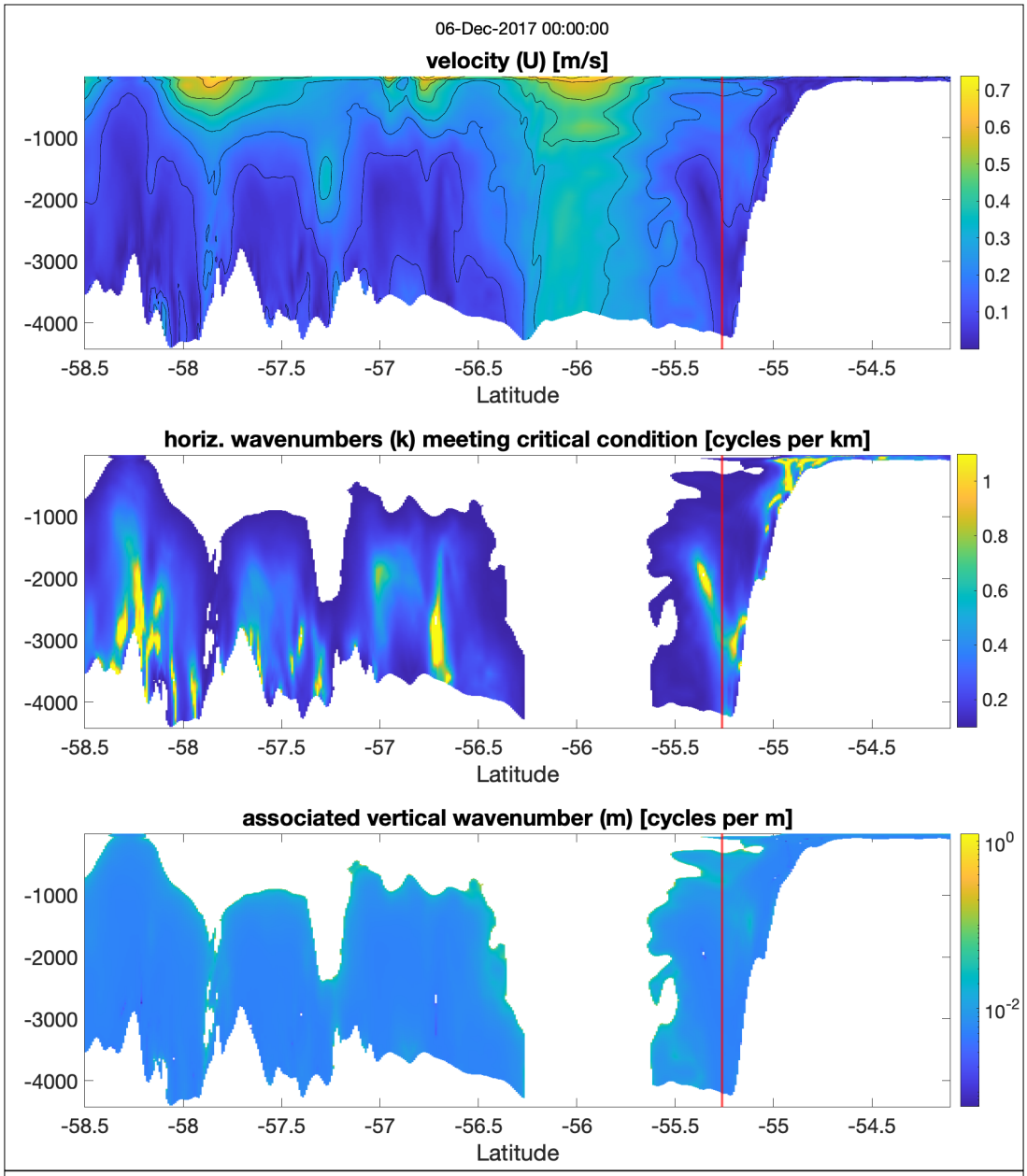

Figure 19: Meridional transect in Fig. 18. Showing velocity (*U*), horizontal wavenumber (*k*) satisfying critical conditions, and associated vertical wavenumber (*m*). The red line indicates the position of the glider during the ROMS timestep.

rotation rather than stratification). Additionally and alternatively, near-inertial wave (NIW) features acting along the edges of a large barotropic eddy in the model (Fig. 21) are further affirmation for the importance of waves interacting with flow along fronts and

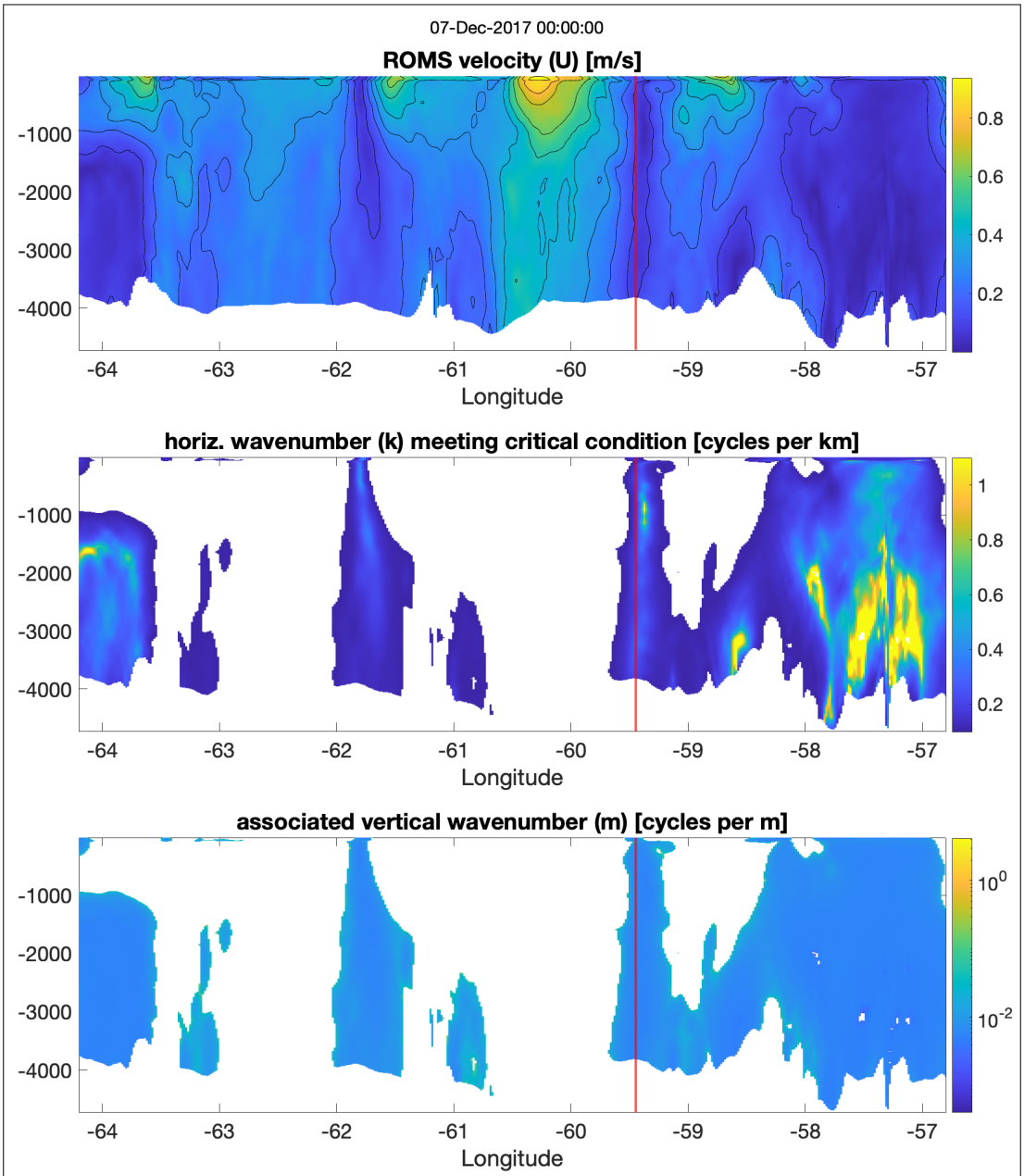

Figure 20: Zonal transect in Fig. 18. Showing velocity (*U*), horizontal wavenumber (*k*) satisfying critical conditions, and associated vertical wavenumber (*m*). The red line indicates the position of the glider during the ROMS timestep.

eddy boundaries (as in Kunze, 1986; 1995; Grisouard & Thomas, 2016; Asselin et al., 2020). The role of internal wave effects will be explored further in a future paper.

5.3 Conclusions

In summary, the conclusions of this study are that: (1) SI is very widespread along the northern boundaries of the ACC due to topographic shearing of the unstable north side of the jet; it is mostly of the centrifugal/ inertial nature. (2) SI also acts along the Shackelton Fracture Zone such that it is worth considering whether some of the near-boundary elevated TKE (over rough topography and along continental margins) which was historically attributed to internal waves could be partially due to submesocale instabilities. (3) The enhanced TKE dissipation during AUSSOM likely was not symmetric instability and was instead related to internal wave interactions, to be addressed in a follow-on paper. (4) The effects of viscosity and diffusivity significantly alter predicted instability growth rate and should be considered when conducting numerical instability analysis on both idealized and analytical cases.

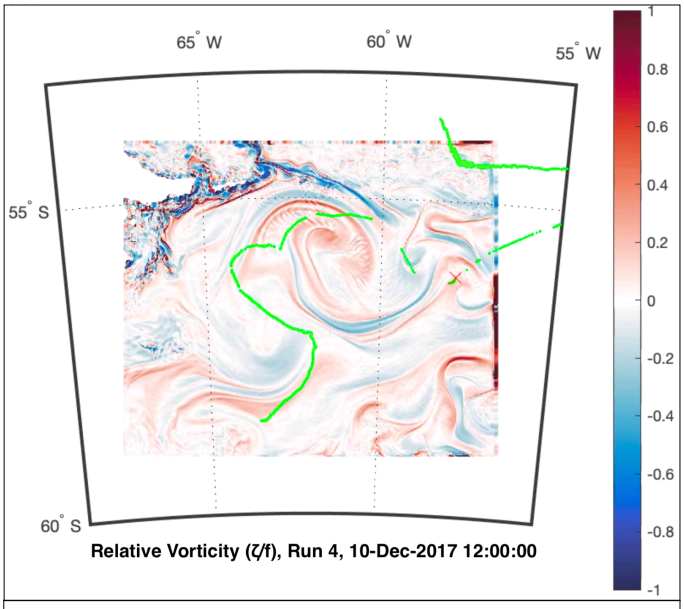

Figure 21: ROMS relative vorticity at 0 m with AUSSOM glider track overlaid. Showing internal wave activity along a Polar Front-associated eddy (ripples).

In this study we have provided insight into the relative role and spatial arrangement of symmetric instabilities in the Southern Ocean, with the finding that symmetric instabilities are as important along the topographic boundaries of the ACC as they are in the surface mixed layer at open ocean density fronts. The results of this work may be applied to other energetic geostrophic currents rich in frontal structure. Published

symmetric instability analysis of the Kuroshio and Gulf Stream are not much more common than that of the ACC, and there has been little submesoscale instability work in the subarctic, also rich in energetic currents and sharp density fronts. The simulation of littoral and coastal regions is probably a more pressing motivator for SI parameterizations than the blue water Southern Ocean. It may be that inclusion of topographically sheared symmetric instabilities are vital for accurately simulating ocean structure in these regions. The community's need to develop realistic SI parameterizations is strong motivation to make further observations in regions suspected of topographically-sheared SI, and to conduct numerical instability analysis on high-resolution observations of buoyancy and velocity in order to better understand the growth rates, depths, and re-stratification timescales associated with these instabilities in the real ocean. At the same time, equal focus should be placed on internal wave phenomena which are likely as important (if not more important) than SI away from boundaries.

Acknowledgments

Computational resources were provided by the VIMS Ocean-Atmosphere & Climate Change Research Fund and UAF.

Endnotes

I gratefully acknowledge the contributions of my collaborators for this project: Harper Simmons (UAF), Donglai Gong (VIMS), John Klinck (CCPO-ODU), and Louis St. Laurent (APL-UW). I also thank Thilo Klenz (UAF) for useful insight.

Chapter 6
Conclusion

1. Significance

This dissertation combines the AUSSOM glider turbulence record with satellite-based meteorology, DIMES VMP, Argo floats, and a ROMS hindcast to elucidate forward energy cascade, turbulence, and its parameterizations in an energetic frontal region of the global ocean. Through it we have addressed three guiding questions:

1. *How does energy transfer between the atmosphere and interior ocean in the Polar Front and does it match our law-of-the-wall understanding?*

2. *How realistic is assumption that energy in internal wave field smoothly transfers to turbulent dissipation in the Southern Ocean?*

3. *Which processes are responsible for energy transfer into the microscale in the Antarctic Circumpolar Current?*

The significance of this research is to elucidate downscale energy transfer in the Southern Ocean. Achieving a better understanding of energy transfer across scales in the Southern Ocean, and determining which physical processes deserve the most attention, is necessary for the community to build accurate models of ocean circulation. The next great challenge is accurately building turbulent mixing into predictive ocean models. But in order to do this, we must understand the physics of how energy moves downscale and

creates mixing in the real ocean. Not just which processes are physically possible; but their relative roles and spatial arrangement.

2. The predictive application of observing oceanic turbulence

Turbulence homogenizes density gradients in a fundamentally inhomogeneous ocean, profoundly altering its structure. It provides the fuel (kinetic energy) for mixing (which raises the potential energy of the fluid) and thus its inclusion in ocean models is vital to model accuracy. Moore's Law dictates (as it stands) a rate limit for obtaining faster computers (see Fox-Kemper et al., 2019; Dong et al. 2020; 2021b for interesting discussion) such that modelers are computationally limited in choice of model grid resolution; a limitation that impacts the mathematical representation of turbulence in Reynolds-averaged Navier-Stokes (RANS) type models. When Reynolds averaging the Navier-Stokes equations, a necessary prerequisite for any grid scale larger than the scale of the smallest turbulent motions (~1 cm) a nonlinear advective term arises, $\partial \overline{u_i' u_j'} / \partial x_j$. This quantity cannot explicitly be determined from flow characteristics at or above the scale of averaging (there is no exact solution for the advective effects of fluid motion below grid scale down to 1cm scale) and must be recast as a diffusive effect, $(\partial/\partial x_j)\nu_E(\partial \overline{u}_i/\partial x_j)$. From Cushman-Roisin & Beckers (2011), Boussinesq hydrostatic RANS equations for x-momentum (Eq. 1a) and energy (Eq. 1b) are

$$\frac{\partial u}{\partial t} + u\frac{\partial u}{\partial x} + v\frac{\partial u}{\partial y} + w\frac{\partial u}{\partial z} - fv = -\frac{1}{\rho_0}\frac{\partial p}{\partial x} + \frac{\partial}{\partial x}\left(\mathscr{A}\frac{\partial u}{\partial x}\right) + \frac{\partial}{\partial y}\left(\mathscr{A}\frac{\partial u}{\partial y}\right) + \frac{\partial}{\partial z}\left(\nu_E\frac{\partial u}{\partial z}\right) \quad (1a)$$

$$\frac{\partial \rho}{\partial t} + u\frac{\partial \rho}{\partial x} + v\frac{\partial \rho}{\partial y} + w\frac{\partial \rho}{\partial z} = \frac{\partial}{\partial x}\left(\mathscr{A}\frac{\partial \rho}{\partial x}\right) + \frac{\partial}{\partial y}\left(\mathscr{A}\frac{\partial \rho}{\partial y}\right) + \frac{\partial}{\partial z}\left(\kappa_E\frac{\partial \rho}{\partial z}\right) \quad (1b)$$

where u, v, w, ρ in this case are averaged quantities. The mixing effect of sub grid scale motions are represented using enlarged eddy viscosity and diffusivity terms ($\nu_E, \mathscr{A}, \kappa_E$) with units m²/s. What happens below grid scale, and the specific choices for $\nu_E, \mathscr{A}, \kappa_E$ must be parameterized using model turbulence closures.

Assumptions about the physical sources of turbulences are embedded in these closures, which are based on first- or higher-order characteristics of the flow and either diagnostic (i.e a Prandtl closure) or prognostic (i.e. a one- or two-equation turbulence model). A second-order, two-equation $k-\epsilon$ model, adapted from Cushman-Roisin & Beckers (2011), is reproduced (Eq. 2) for the sake of discussion:

$$\frac{dk}{dt} = P_s + P_b - \epsilon + \nu_E\frac{\partial^2 k}{\partial z^2} \quad (2a)$$

$$\frac{d\epsilon}{dt} = \frac{\epsilon}{k}\left(c_1 P_s + c_2 P_b - c_3\epsilon\right) + \nu_E\frac{\partial^2 \epsilon}{\partial z^2} \quad (2b)$$

$$\nu_E = c_\mu k^2/\epsilon \quad (2c)$$

$$\kappa_E = c'_\mu k^2/\epsilon \quad (2d)$$

In this model turbulence closure, ν_E and κ_E are determined from the evolution equation for TKE (k) and dissipation (ϵ), where P_s is shear production, P_b is buoyancy production, and variables in the form $c_{\_}$ are empirical constants. The prognostic equation for ϵ is embedded with numerous hypotheses and assumptions about which physical processes are relevant contributors to TKE dissipation (and to what magnitude). The model

turbulence closure prescribes—rather than describes—where, how, and when mixing occurs in an ocean simulation.

In practice, ν_E and κ_E profiles are determined from published implementations such as K-Profile Parameterization (KPP; Large et. al, 1994), Mellor-Yamada (Mellor & Yamada, 1982), Generic Length Scale (GLS; Umlauf & Burchard, 2003). Mellor-Yamada leverages a $k - kl_m$ model. KPP leverages boundary layer similarity scaling (BLS, the subject of Ch. 3) in the upper ocean and three interior processes: shear instability (from Richardson number Ri), double diffusive instability (addressed in Ch. 4), and internal wave-wave interactions (implemented using a constant eddy viscosity). GLS can take on numerous two-equation forms. Some implementations have additional parameterizations for the effects of wave breaking (Carniel et al., 2009), Langmuir circulation (Sinha et al., 2015; Chor et al., 2021), or other physical processes. All implementations include boundary treatment (based on Monin-Obukhov theory/BLS/law-of-the-wall) as well as interior treatment.

Taking KPP for example, what happens to the model solution (and its applicability to model-informed operations in the real ocean) when physical processes other than shear instability, double diffusivity instability, or internal wave-wave interactions is a significant contributor to mixing? How should we deal with the spatial inhomogeneity of internal wave-wave interactions, and where might internal-flow interactions be even more important? The practical application of this work is that predictive (and hindcast) ocean models have mixing parameterizations designed from our understanding of the physics and phenomenology of turbulence. To improve model

accuracy (while dealing with computational limitations and having no closed-form solution to the Navier-Stokes equations), we must improve our understanding of turbulence in the real ocean. Chapters 3, 4, and 5 have direct consequences for model turbulence closures, some of which are highlighted:

- Chapter 3 found that strong wind, breaking waves, Langmuir circulation have minimal effect on bias associated with boundary layer similarity scaling in deepest 90% of actively mixing layer. ***Wave breaking & Langmuir circulation alone cannot fix vertical structure of turbulence closures.***

- Chapter 4 found that double diffusive instability at fronts can cause internal wave strain-based estimates of turbulence and diffusivity to be up to 10^8 too high. ***Global diffusivity patterns derived from finescale strain estimates likely have severely inflated mixing in frontal zones.***

- Chapter 5 found that symmetric instability (SI) is more relevant to topographic boundaries than open ocean fronts of the major currents. ***Closures for SI-attributable mixing should not be limited to geostrophic shear production by surface-forced SI.***

The (sometimes unexpected) findings of this dissertation underscore the extreme value of observing oceanic turbulence through direct microstructure measurements to understanding physical processes which existing theory, turbulence parameterizations, or modeling alone would have missed. A graphic illustrating the iterative process of making observations, using them in conjunction with turbulence parameterizations, and

improving model turbulence closures is given in Fig. 1. As a community, we use turbulence observations to improve our understanding of turbulence physics; which ultimately is incorporated into the machinery of models and used for predictive applications. This process cannot be conducted using large eddy simulation (LES) alone and must continue utilizing turbulence measurements from the actual ocean. LES and direct numerical simulation (DNS) are ideal for small-scale processes studies but are coverage-limited in their ability to realistically include the horizontal processes and across-scale interactions affecting turbulence, and thus complement the analysis of true measurements of TKE dissipation rate.

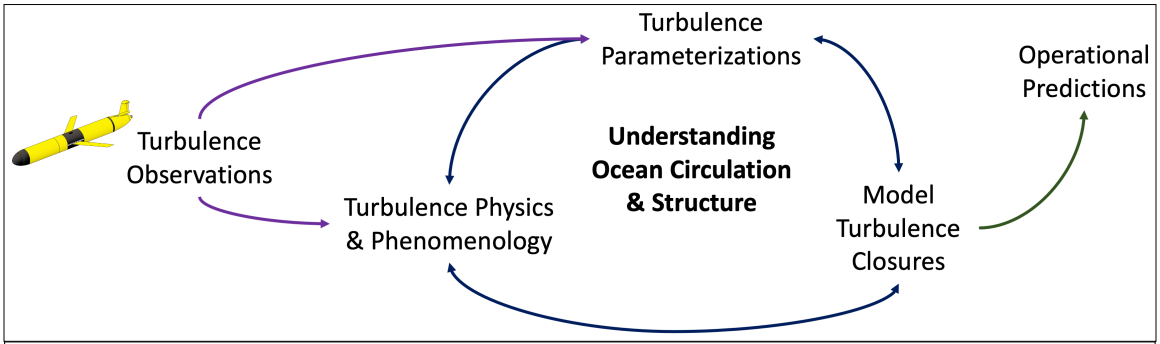

Fig. 1: The cycle of using physical observations to improving mathematical and numerical representations of ocean mixing.

3. Broader impacts

The results of this work may be applied to other energetic geostrophic currents rich in frontal structure. The results of this work are also important to other disciplines of oceanography and climate. Turbulent mixing, upwelling, and subduction in the Southern Ocean are thought to play central roles in the global overturning circulation and Earth's climate system (Naveira Garabato et al., 2004; Sallee et al., 2010). They set the rates of water mass transformation and ventilation for the various deep and intermediate water

masses. These processes also control the supply of nutrients to the upper ocean (Anderson et al., 2009; Tagliabue et al., 2014), the rate of ocean-atmospheric exchange of carbon (Lenton & Matear, 2007), the duration and extent of Antarctic sea ice (Gordon et al., 2000; Marshall & Speer, 2012), as well as the basal melting rates of Antarctic glacial ice sheets by oceanic heat (Holland et al., 2008; Pritchard et al., 2012). Palter et al. (2010) find the level of vertical mixing used in MOM3 simulations of the Southern Ocean fundamentally alter the model-observed dominant nutrient pathways. Dufour et al. (2015) highlight the importance of mesoscale eddies in transporting heat, carbon, oxygen, and phosphate across the PF core; as well as the uncertainty associated with using a constant eddy diffusivity κ_E in quantifying the role of eddy diffusive transport (relative to advective transport), particular around sloping topography. For these reasons, it is critical that we understand the physical processes that downscale energy transfer, driving the variability in the rates of mixing, upwelling, and subduction in the Southern Ocean.

4. Future research questions

Some future research questions pertaining to the investigation of Southern Ocean forward energy cascade are as follows:

- What specific type of internal wave interaction acts along the Polar Front-associated eddy observed during AUSSOM to produce elevated TKE dissipation through 350 meters?

- Are the internal wave features observed in the ROMS model (Ch. 5, Fig. 21) related to distortion of near inertial waves (NIWs), critical layer interactions involving topographic lee waves, or another mechanism?

- How does the vorticity wavenumber spectrum and EKE wavenumber spectrum evolve over time, and do their slopes correspond with the submesoscale activity (e.g -3~mesoscale, -8/3~frontal collapse, -2~submesoscale, -5/3~3D turbulence) in the model domain identified using instability criteria and vorticity fields? How do eddy kinetic energy (EKE) and TKE in the model evolve over time in comparison? Does this relationship change for different Polar Front regimes (i.e. near-boundary or open-ocean)?

- How useful is the common assumption that criteria for forced symmetric instability (FSI) are a reasonable proxy for symmetric instability (SI). Using its Ekman buoyancy flux (EBF) and surface buoyancy flux (J_b) diagnostics, how does phenomenology of FSI in the ROMS model compare to near-surface SI?

While located in the Southern Ocean, the conclusions of this dissertation are applicable to other energetic frontal zones, especially in high-latitude regions. As the Arctic becomes increasingly ice-free, intense frontal regions such as the high northern oceans have become a focal point of shipping, security, and sustainability. The community's existing oceanographic predictive models are embedded with parameterizations developed based largely on the available observations (and thus oceanography) of more quiescent and blue-water regions. At the same time, the high-

northern oceans are defined by energetic storm events, strong fronts, intense seasonal cycles, and close connectivity between complex littoral (shelf, slope, and its adjacent deep) topography and open-ocean dynamics. There is increased need to understand (sub)mesoscale physical processes (on timescales of weeks and shorter) in the high-latitude oceans. Predicting ocean structure leverages a combination of resolved and parameterized dynamics. Central to this is turbulence and mixing, which alters ocean structure on spatial scales down to 1 cm and timescales down to 20 minutes. Future work will focus on applying findings from this dissertation and AUSSOM to the study of forward energy cascade and mixing in models. Some future research questions beyond the Southern Ocean i.e. the subarctic are as follows:

- Where else in the global ocean does topographic shearing of a jet along a lateral boundary produce a substantial centrifugal-symmetric instability contribution?
- How does double diffusive instability in the upper ocean impact acoustic propagation?
- What is the prevalence of NIW interactions and critical layer interactions topographic lee waves in other parts of the global ocean with intense frontal structures, such as the high North Atlantic?

Bibliography

Abernathey, R. P., Cerovecki, I., Holland, P. R., Newsom, E., Mazloff, M., & Talley, L. D. (2016). Water-mass transformation by sea ice in the upper branch of the Southern Ocean overturning. Nature Geoscience, 9(8), 596.

Adams, K. A., Hosegood, P., Taylor, J. R., Sallée, J. B., Bachman, S., Torres, R., & Stamper, M. (2017). Frontal circulation and submesoscale variability during the formation of a Southern Ocean mesoscale eddy. Journal of Physical Oceanography, 47(7), 1737-1753.

Adler, R., J.-J. Wang, M. Sapiano, G. Huffman, D. Bolvin, E. Nelkin, and NOAA CDR Program, 2017: Global Precipitation Climatology Project (GPCP) Climate Data Record (CDR), Version 1.3 (Daily). NOAA National Centers for Environmental Information, doi:10.7289/V5RX998Z.

Agrawal, Y. C., E. A. Terray, M. A. Donelan, P. A. Hwang, A.J. Williams, W. M. Drennan, K. K. Kahma, and S. A. Krtaigorodskii,1992: Enhanced dissipation of kinetic energy beneath surface waves. Nature, 359, 219-220.

Alford, M. H. & Pinkel, R., 2000: Observations of overturning in the thermocline: The context of ocean mixing. J. Phys. Oceanogr., 30, 805-832.

Anderson, R. F., Ali, S., Bradtmiller, L. I., Nielsen, S. H. H., Fleisher, M. Q., Anderson, B. E., & Burckle, L. H. (2009). Wind-driven upwelling in the Southern Ocean and the deglacial rise in atmospheric CO2. science, 323(5920), 1443-1448.

Asselin, O., Thomas, L. N., Young, W. R., Rainville, L., 2020. Refraction and Straining of Near-Inertial Waves by Barotropic Eddies. Journal of Physical Oceanography, 50, 3439-3454.

Bachman, S.D., Fox-Kemper, B., Taylor, J.R. and Thomas, L.N., 2017. Parameterization of frontal symmetric instabilities. I: Theory for resolved fronts. Ocean Modelling, 109, pp.72-95.

Bachman, S.D. and Taylor, J.R., 2014. Modelling of partially-resolved oceanic symmetric instability. Ocean Modelling, 82, pp.15-27.

Bartello, P., Tobias, S. M., 2013: Sensitivity of stratified turbulence to the buoyancy Reynolds number. J. Fluid Mech., 725, 1-22.

Beaird, N., Fer, I., Rhines, P., Eriksen, C., 2012: Dissipation of turbulent kinetic energy inferred from Seagliders: An application to the eastern Nordic Seas overflows. J. Phys. Oceanogr., 42, 2268-2282.

Belcher, S. E., Grant, A.L., Hanley, K. E., Fox−Kemper, B., Van Roekel, L., Sullivan, P.P., Large, W. G., Brown, A., Hines, A., Calvert, D., Rutgersson, A., 2012: A global

perspective on Langmuir turbulence in the ocean surface boundary layer. Geophys. Res. Lett., 39.

Bell Jr., T. H., 1975: Topographically generated internal waves in the open ocean. J. Geophys. Res., 80, 320-327.

Bemis, K. E., Tyler, J. C., Psomadakis, P. N., Ferris, L. N., & Kumar, A. B. (2020). Review of the Indian Ocean spikefish genus Mephisto (Tetraodontiformes: Triacanthodidae). Zootaxa , 4802 . doi:10.11646/zootaxa.4802.1.5

Boccaletti, G., Ferrari, R. and Fox-Kemper, B., 2007. Mixed layer instabilities and restratification. Journal of Physical Oceanography, 37(9), pp.2228-2250.

Booker, J. R., & Bretherton, F. P. (1967). The critical layer for internal gravity waves in a shear flow. Journal of Fluid Mechanics, 27(3), 513-539.

Brearley, J. A., Sheen, K. L., Naveira Garabato, A.C., Smeed, D.A., Waterman, S., 2013: Eddy-induced modulation of turbulent dissipation over rough topography in the Southern Ocean. J. Phys. Oceanogr., 43, 2288-2308.

Cael, B. B., Mashayek, A., 2021: Log-Skew-Normality of Ocean Turbulence. Phys. Rev. Lett. 126, 224502.

Callies, J., Flierl, G., Ferrari, R. and Fox-Kemper, B., 2016. The role of mixed-layer instabilities in submesoscale turbulence. Journal of Fluid Mechanics, 788, pp.5-41.

Carniel, S., Warner, J.C., Chiggiato, J. and Sclavo, M., 2009. Investigating the impact of surface wave breaking on modeling the trajectories of drifters in the northern Adriatic Sea during a wind-storm event. Ocean Modelling, 30(2-3), pp.225-239.

Chen, R., McClean, J. L., Gille, S. T., Griesel, A., 2014. Isopycnal Eddy Diffusivities and Critical Layers in the Kuroshio Extension from an Eddying Ocean Model. Journal of Physical Oceanography, 44, 2191-2211.

Chinn, B. S., Girton, J. B., Alford, M. H., 2016: The impact of observed variations in the shear-to-strain ratio of internal waves on inferred turbulent diffusivities. J. Phys. Oceanogr., 46, 3299-3320.

Chor, T., McWilliams, J. C., & Chamecki, M. (2021). Modifications to the K-Profile parameterization with nondiffusive fluxes for Langmuir turbulence. Journal of Physical Oceanography, 51(5), 1503-1521.

Clayson, C. A., and J. Brown, 2016: NOAA Climate Data Record Ocean Surface Bundle (OSB) Climate Data Record (CDR) of Ocean Heat Fluxes, Version 2. Climate Algorithm Theoretical Basis Document (C-ATBD). NOAA National Center for Environmental Information, doi:10.7289/V59K4885.

Clayson, C. A., J. Brown, and NOAA CDR Program, 2016a: NOAA Climate Data Record (CDR) of Sea Surface Temperature - WHOI, Version 2. NOAA National Climatic Data Center. doi:10.7289/V5FB510W.

Clayson, C. A., J., Brown, and NOAA CDR Program 2016b: NOAA Climate Data Record Ocean Surface Bundle (OSB) Climate Data Record (CDR) of Ocean Near Surface Atmospheric Properties, Version 2. NOAA National Center for Environmental Information, doi:doi:10.7289/V55T3HH0.

Craig, P. D. and M. L. Banner, 1994: Modeling wave-enhanced turbulence in the ocean surface layer. J. Phys. Oceanogr., 24, 2546-2559.

Crear, D. P., Watkins, B. E., Saba, V. S., Graves, J. E., Jensen, D. R., Hobday, A. J., & Weng, K. C. (2020). Contemporary and future distributions of cobia, Rachycentron canadum. Divers Distrib., 00. doi:10.1111/ddi.13079

Cushman-Roisin, B., & Beckers, J. M. (2011). Introduction to geophysical fluid dynamics: physical and numerical aspects. Academic press.

D'Asaro, E. A., 2014: Turbulence in the upper-ocean mixed layer. Annu. Rev. Mar. Sci., 6, 101-115.

D'Asaro, E., Lee, C., Rainville, L., Thomas, L., & Harcourt, R. (2011). Enhanced turbulence and energy dissipation at ocean fronts. science, 1201515.

D'Asaro, E. A., J. Thomson, A. Y. Shcherbina, R. R. Harcourt, M. F. Cronin, M. A. Hemer, and B. Fox-Kemper, 2014: Quantifying upper ocean turbulence driven by surface waves. Geophys. Res. Lett., 41, 102-107.

Danabasoglu, G., and Coauthors, 2012: The CCSM4 Ocean Component. J. Climate, 25, 1361-1389.

Derakhti, M., J. Thomson, and J. T. Kirby, 2020: Sparse Sampling of Intermittent Turbulence Generated by Breaking Surface Waves. J. Phys. Oceanogr., 50, 867-885.

Dillon, T. M., 1982: Vertical overturns: A comparison of Thorpe and Ozmidov length scales. J. Geophys. Res. Oceans, 87, 9601-9613.

Dohan, K., and R. E. Davis, 2011: Mixing in the Transition Layer during Two Storm Events. J. Phys. Oceanogr., 41, 42-66.

Dong, J., Fox-Kemper, B., Zhang, H., & Dong, C. (2020). The scale of submesoscale baroclinic instability globally. Journal of Physical Oceanography, 50(9), 2649-2667.

Dong, J., Fox−Kemper, B., Zhu, J. and Dong, C., (2021a). Application of symmetric instability parameterization in the Coastal and Regional Ocean Community Model (CROCO). Journal of Advances in Modeling Earth Systems, 13(3), p.e2020MS002302.

Dong, J., Fox-Kemper, B., Zhang, H., & Dong, C. (2021b). The Scale and Activity of Symmetric Instability Estimated from a Global Submesoscale-Permitting Ocean Model. Journal of Physical Oceanography, 51(5), 1655-1670.

Dong, S., J. Sprintall, S. T. Gille, and L. Talley, 2008: Southern Ocean mixed-layer depth from Argo float profiles. J. Geophys. Res., 113.

Dufour, C. O., Griffies, S. M., de Souza, G. F., Frenger, I., Morrison, A. K., Palter, J. B., ... & Slater, R. D. (2015). Role of mesoscale eddies in cross-frontal transport of heat and biogeochemical tracers in the Southern Ocean. Journal of Physical Oceanography, 45(12), 3057-3081.

du Plessis, M., S. Swart, I. J. Ansorge, A. Mahadevan, and A. F. Thompson, 2019: Southern Ocean Seasonal Restratification Delayed by Submesoscale Wind–Front Interactions. J. Phys. Oceanogr., 49, 1035-1053.

Edson, J. B., and Coauthors, 2013: On the exchange of momentum over the open ocean. J. Phys. Oceanogr., 43, 1589-1610.

Fairall, C. W., Bradley, E. F., Rogers, D. P., Edson, J. B., & Young, G. S. (1996). Bulk parameterization of air−sea fluxes for tropical ocean−global atmosphere coupled−ocean atmosphere response experiment. Journal of Geophysical Research: Oceans, 101(C2), 3747-3764.

Fer, I., Peterson, A. K., & Ullgren, J. E. (2014). Microstructure measurements from an underwater glider in the turbulent Faroe Bank Channel overflow. Journal of Atmospheric and Oceanic Technology, 31(5), 1128-1150.

Ferrari, R., & Wunsch, C. (2009). Ocean circulation kinetic energy: Reservoirs, sources, and sinks. Annual Review of Fluid Mechanics, 41.

Ferris, L. N. (2020). Zenodo. doi:10.5281/zenodo.4151538

Ferris, L., 2020a: ocean_data_tools: A MATLAB toolbox for interacting with bulk freely-available oceanographic data. J. Open Source Softw., 5, 2497.

Ferris, L. N., D. Gong, T. Ijichi, S. T. Merrifield, J. Shapiro, L. St. Laurent, 2020: Turbulent Dissipation Rate and Mixing Variations in the Polar Front of the Southern Ocean. Ocean Sciences Meeting 2020, San Diego, CA, American Geophysical Union, PS51A-04, https://agu.confex.com/agu/osm20/meetingapp.cgi/Paper/648069.

Ferris, L. N., Gong, D., Merrifield, S. T., Clayson, C. A., St. Laurent, L. Assessing surface boundary layer scalings of shear turbulence in the high-wind Southern Ocean using direct measurements. (in revision)

Fox-Kemper, B., Adcroft, A., Böning, C.W., Chassignet, E.P., Curchitser, E., Danabasoglu, G., Eden, C., England, M.H., Gerdes, R., Greatbatch, R.J. and Griffies, S.M., 2019. Challenges and prospects in ocean circulation models. Frontiers in Marine Science, 6, p.65.

Fox-Kemper, B., Johnson, L., Qiao, F (In press): Ocean Near-Surface Layers, Ocean Mixing, Elsevier.

Frants, M., Damerell, G. M., Gille, S. T., Heywood, K. J., MacKinnon, J., Sprintall, J., 2013: An assessment of density-based finescale methods for estimating diapycnal diffusivity in the Southern Ocean. J. Atmos. Ocean. Technol., 30, 2647-2661.

Freeman, N.M. and Lovenduski, N.S., 2016. Mapping the Antarctic Polar Front: weekly realizations from 2002 to 2014. Earth System Science Data, 8(1), pp.191-198.

Frenger, I., Münnich, M., Gruber, N., & Knutti, R. (2015). Southern Ocean eddy phenomenology. Journal of Geophysical Research: Oceans, 120(11), 7413-7449.

Garau, B., Ruiz, S., Zhang, W. G., Pascual, A., Heslop, E., Kerfoot, J., Tintoré, J., 2011: Thermal lag correction on Slocum CTD glider data. J. Atmos. Ocean. Technol., 28, 1065-1071.

Gargett, A. E., 1990: Do we really know how to scale the turbulent kinetic energy dissipation rate ε due to breaking of oceanic internal waves?. J. Geophys. Res. Oceans, 95, 15971-15974.

Gargett, A., & Garner, T., 2008: Determining Thorpe scales from ship-lowered CTD density profiles. J. Atmos. Ocean. Technol., 25, 1657-1670.

Gargett, A. E., Osborn, T. R., Nasmyth, P. W., 1984: Local isotropy and the decay of turbulence in a stratified fluid. J. Fluid Mech., 144, 231-280.

Garrett, C. J., and W. Munk, 1972: Space–time scales of internal waves. Geophys. Fluid Dyn., 2 , 255–264.

Garrett, C. J., and W. Munk, 1975: Space–time scales of internal waves: A progress report. J. Geophys. Res., 80 , 291–297.

Garrett, C. and St. Laurent, L., 2002. Aspects of deep ocean mixing. Journal of oceanography, 58(1), pp.11-24.

Gelaro, R., McCarty, W., Suárez, M. J., Todling, R., Molod, A., Takacs, L., ... & Wargan, K. (2017). The modern-era retrospective analysis for research and applications, version 2 (MERRA-2). Journal of Climate, 30(14), 5419-5454.

Gemmrich, J. R., T. D. Mudge, and V. D. Polonichko, 1994: On the energy input from wind to surface waves. J. Phys. Oceanogr., 24, 2413-2417.

Gerbi, G. P., J. H. Trowbridge, E. A. Terray, A. J. Plueddemann, and T. Kukulka, 2009: Observations of Turbulence in the Ocean Surface Boundary Layer: Energetics and Transport. J. Phys. Oceanogr., 39, 1077-1096.

Gill, A. E., 1982: Atmosphere-Ocean Dynamics. Academic Press., 662 pp.

Gille, S.T., McKee, D.C. and Martinson, D.G., 2016. Temporal changes in the Antarctic Circumpolar Current: Implications for the Antarctic continental shelves. Oceanography, 29(4), pp.96-105.

Greene, C. A., Thirumalai, K., Kearney, K. A., Delgado, J. M., Schwanghart, W., Wolfenbarger, N. S., Thyng, K. M., et al. (2019). The Climate Data Toolbox for MATLAB. Geochemistry, Geophysics, Geosystems . doi:10.1029/2019GC008392

Gregg, M. C., 1989: Scaling turbulent dissipation in the thermocline. J. Geophys. Res. Oceans, 94, 9686-9698.

Gregg, M. C. & Kunze, E., 1991: Shear and strain in Santa Monica basin. J. Geophys. Res. Oceans, 96, 16709-16719.

Gordon, C., Cooper, C., Senior, C. A., Banks, H., Gregory, J. M., Johns, T. C., Mitchell, J. F. B., & Wood, R. A. (2000). The simulation of SST, sea ice extents and ocean heat transports in a version of the Hadley Centre coupled model without flux adjustments. Climate dynamics, 16(2-3), 147-168.

Grisouard, N., Thomas, L. N., 2016. Energy Exchanges between Density Fronts and Near-Inertial Waves Reflecting off the Ocean Surface. Journal of Physical Oceanography, 46, 501-516.

Gula, J., Molemaker, M.J. and McWilliams, J.C., 2016. Topographic generation of submesoscale centrifugal instability and energy dissipation. Nature communications, 7(1), pp.1-7.

Haine, T.W. and Marshall, J., 1998. Gravitational, symmetric, and baroclinic instability of the ocean mixed layer. Journal of physical oceanography, 28(4), pp.634-658.

Holland, P. R., Jenkins, A., & Holland, D. M. (2008). The response of ice shelf basal melting to variations in ocean temperature. Journal of Climate, 21(11), 2558-2572.

Hoskins, B.J., 1974. The role of potential vorticity in symmetric stability and instability. Quarterly Journal of the Royal Meteorological Society, 100(425), pp.480-482.

Huussen, T. N., Naveira Garabato, A. C., Bryden, H. L., & McDonagh, E. L., 2012: Is the deep Indian Ocean MOC sustained by breaking internal waves?. J. Geophys. Res. Oceans, 117.

Hwang, P. A., 2009: Estimating the effective energy transfer velocity at air-sea interface. J. Geophys. Res., 114.

Jiao, Y., & Dewar, W. K. (2015). The energetics of centrifugal instability. Journal of Physical Oceanography, 45(6), 1554-1573.

Johnston, T. S., & Rudnick, D. L., 2015: Trapped diurnal internal tides, propagating semidiurnal internal tides, and mixing estimates in the California Current System from sustained glider observations, 2006–2012. Deep Sea Res. Part II: Top. Stud. Oceanogr., 112, 61-78.

Kanafi, M. M. (2021). Radially averaged surface roughness/topography power spectrum (PSD) (https://www.mathworks.com/matlabcentral/fileexchange/54297-radially-

averaged-surface-roughness-topography-power-spectrum-psd), MATLAB Central File Exchange. Retrieved August 24, 2021.

Kantha, L. H., and C. Anne Clayson, 2004: On the effect of surface gravity waves on mixing in the oceanic mixed layer. Ocean Modelling, 6, 101-124.

Khani, S., 2018: Mixing efficiency in large-eddy simulations of stratified turbulence. J. Fluid Mech., 849, 373-394.

Khani, S., Waite, M. L., 2013: Effective eddy viscosity in stratified turbulence. J. Turbul., 14, 49-70.

Kimura, Y., Herring, J. D., 2012: Energy spectra of stably stratified turbulence. J. Fluid Mech., 698, 19-50.

Klymak, J. M., Moum, J. N., 2007: Oceanic isopycnal slope spectra. Part I: Internal waves. J. Phys. Oceanogr., 37, 1215-1231.

Kundu, P. K., 1990: Fluid Mechanics. Academic Press, 638 pp.

Kunze, E. (1986). The mean and near-inertial velocity fields in a warm-core ring. Journal of physical oceanography, 16(8), 1444-1461.

Kunze, E., Firing, E., Hummon, J. M., Chereskin, T. K., Thurnherr, A. M., 2006: Global abyssal mixing inferred from lowered ADCP shear and CTD strain profiles. J. Phys. Oceanogr., 36, 1553-1576.

Kunze, E., & Lien, R. C. (2019). Energy Sinks for Lee Waves in Shear Flow. Journal of Physical Oceanography, 49(11), 2851-2865.

Kunze, E., Schmitt, R.W. and Toole, J.M., 1995. The energy balance in a warm-core ring's near-inertial critical layer. Journal of physical oceanography, 25(5), pp.942-957.

Large, W. G., J. C. McWilliams, and S. C. Doney, 1994: Oceanic vertical mixing: A review and a model with a nonlocal boundary layer parameterization. Rev. Geophys., 32, 363-403.

Large, W. G., Patton, E. G., du Vivier, A. K., Sullivan, P. P., Romero, L., 2019.: Similarity theory in the surface layer of large-eddy simulations of the wind-, wave-, and buoyancy-forced southern ocean. Journal of Physical Oceanography, 49, 2165-2187.

Large, W. G., & Pond, S. (1981). Open ocean momentum flux measurements in moderate to strong winds. Journal of physical oceanography, 11(3), 324-336.

Latarius, K., Schauer, U., Wisotzki, A., 2019: Near-ice hydrographic data from Seaglider missions in the western Greenland Sea in summer 2014 and 2015. Earth Syst. Sci. Data, 11, 895-920.

Ledwell, J. R., Montgomery, E. T., Polzin, K. L., St. Laurent, L., Schmitt, R. W., & Toole, J. M. (2000). Evidence for enhanced mixing over rough topography in the abyssal ocean. Nature, 403(6766), 179.

Lenton, A., & Matear, R. J. (2007). Role of the southern annular mode (SAM) in Southern Ocean CO2 uptake. Global Biogeochemical Cycles, 21(2).

Li, Q., and Coauthors, 2019: Comparing Ocean Surface Boundary Vertical Mixing Schemes Including Langmuir Turbulence. J. Adv. Model., 11, 3545-3592.

Lian, Q., Smyth, W., Liu, Z., 2020. Numerical Computation of Instabilities and Internal Waves from In Situ Measurements via the Viscous Taylor–Goldstein Problem. Journal of Atmospheric and Oceanic Technology, 37, 759-776.

Lindborg, E., 2006: The energy cascade in a strongly stratified fluid. J. Fluid Mech., 550, 207-242.

Lombardo, C. P. and M. C. Gregg, 1989: Similarity scaling of viscous and thermal dissipation in a convecting surface boundary layer. J. Geophys. Res. Oceans, 94, 6273-6284.

Lueck, R. G. (2016). RSI technical note 028 calculating the rate of dissipation of turbulent kinetic energy. Victoria, BC, Canada: Rockland Scientific International. Retrieved from http://rocklandscientific. com/support/knowledge-base/technical-notes.

MacKinnon, J., Alford, M., Bouruet-Aubertot, P., Bindoff, N., Elipot, S., Gille, S., Girton, J., Gregg, M., Hallberg, R., Kunze, E. and Naveira Garabato, A., 2009: Using global arrays to investigate internal-waves and mixing. Proceedings of the OceanObs09 Conference: Sustained Ocean Observations and Information for Society, Venice, Italy (Vol. 2).

MacKinnon, J. A., & Gregg, M. C., 2003: Mixing on the late-summer New England shelf —Solibores, shear, and stratification J. Phys. Oceanogr., 33, 1476-1492.

MacKinnon, J. A., and Coauthors, 2017: Climate process team on internal wave–driven ocean mixing. Bull. Am. Meteorol. Soc., 98, 2429-2454.

MacKinnon, J., St Laurent, L., & Garabato, A. C. N. (2013). Diapycnal mixing processes in the ocean interior. In International Geophysics (Vol. 103, pp. 159-183). Academic Press.

Marshall, J., & Speer, K. (2012). Closure of the meridional overturning circulation through Southern Ocean upwelling. Nature Geoscience, 5(3), 171.

Mashayek, A., Ferrari, R., Merrifield, S., Ledwell, J.R., St Laurent, L. and Garabato, A.N., 2017. Topographic enhancement of vertical turbulent mixing in the Southern Ocean. Nature communications, 8(1), pp.1-12.

Mater, B. D., Venayagamoorthy, S. K., St. Laurent, L. and Moum, J. N., 2015. Biases in Thorpe-scale estimates of turbulence dissipation. Part I: Assessments from large-scale overturns in oceanographic data. J. Phys. Oceanogr., 45, 2497-2521.

Mauritzen, C., Polzin, K. L., McCartney, M. S., Millard, R. C., West−Mack, D.E., 2002: Evidence in hydrography and density fine structure for enhanced vertical mixing

over the Mid−Atlantic Ridge in the western Atlantic. Journal of Geophysical Research: Oceans, 107(C10), pp.11-1.

McDougall, T. J., & Barker, P. M. (2011). Getting started with TEOS-10 and the Gibbs Seawater (GSW) Oceanographic Toolbox, SCOR/IAPSO WG127, ISBN 978-0-646-55621-5.

McWilliams, J.C., 2016. Submesoscale currents in the ocean. Proceedings of the Royal Society A: Mathematical, Physical and Engineering Sciences, 472(2189), p.20160117.

Mellor, G. L., & Yamada, T. (1982). Development of a turbulence closure model for geophysical fluid problems. Reviews of Geophysics, 20(4), 851-875.

Merckelbach, L., Berger, A., Krahmann, G., Dengler, M., & Carpenter, J. R. (2019). A dynamic flight model for Slocum gliders and implications for turbulence microstructure measurements. Journal of Atmospheric and Oceanic Technology, 36(2), 281-296.

Merrifield, S. T., 2016: Mechanisms for enhanced turbulence in the Drake Passage Region of the Southern Ocean. Doctoral dissertation, Massachusetts Institute of Technology, 134 pp.

Merrifield, S. T., Laurent, L. S., Owens, B., Thurnherr, A. M., & Toole, J. M. (2016). Enhanced diapycnal diffusivity in intrusive regions of the Drake Passage. Journal of Physical Oceanography, 46(4), 1309-1321.

Monin, A. S. and A. M. Obukhov, 1954: Basic laws of turbulent mixing in the surface layer of the atmosphere. Contrib. Geophys. Inst. Acad. Sci. USSR, 151, 163-187.

Munk, W., 1981: Internal waves and small scale processes. In Evolution of Physical Oceanography, B. Warren and C. Wunch, Ed., MIT Press, 264–291.

Munk, W., & Wunsch, C. (1998). Abyssal recipes II: Energetics of tidal and wind mixing. Deep Sea Research Part I: Oceanographic Research Papers, 45(12), 1977-2010.

Newman, J. N., 2018: Marine Hydrodynamics. The MIT Press, 402 pp.

Naveira Garabato, A. C., Leach, H., Allen, J. T., Pollard, R. T., & Strass, V. H. (2001). Mesoscale subduction at the Antarctic Polar Front driven by baroclinic instability. Journal of Physical Oceanography, 31(8), 2087-2107.

Naveira Garabato, A. C., Polzin, K. L., King, B. A., Heywood, K. J., & Visbeck, M. (2004). Widespread intense turbulent mixing in the Southern Ocean. Science, 303(5655), 210-213.

Nikurashin, M., & Ferrari, R., 2010: Radiation and dissipation of internal waves generated by geostrophic motions impinging on small-scale topography: Application to the Southern Ocean. J. Phys. Oceanogr., 40, 2025-2042.

Nikurashin, M., & Ferrari, R. (2010). Radiation and dissipation of internal waves generated by geostrophic motions impinging on small-scale topography: Theory. Journal of Physical Oceanography, 40(5), 1055-1074.

Nikurashin, M., Ferrari, R., Grisouard, N., & Polzin, K. (2014). The impact of finite-amplitude bottom topography on internal wave generation in the Southern Ocean. Journal of Physical Oceanography, 44(11), 2938-2950.

Naveira Garabato, A.C., Frajka-Williams, E.E., Spingys, C.P., Legg, S., Polzin, K.L., Forryan, A., Abrahamsen, E.P., Buckingham, C.E., Griffies, S.M., McPhail, S.D. and Nicholls, K.W., 2019. Rapid mixing and exchange of deep-ocean waters in an abyssal boundary current. Proceedings of the National Academy of Sciences, 116(27), pp.13233-13238.

Naveira Garabato, A.C., Polzin, K.L., King, B.A., Heywood, K.J. and Visbeck, M., 2004. Widespread intense turbulent mixing in the Southern Ocean. Science, 303(5655), pp.210-213.

Orsi, A. H., Whitworth III, T., & Nowlin Jr, W. D. (1995). On the meridional extent and fronts of the Antarctic Circumpolar Current. Deep Sea Research Part I: Oceanographic Research Papers, 42(5), 641-673.

Palter, J. B., Sarmiento, J. L., Gnanadesikan, A., Simeon, J., & Slater, R. D. (2010). Fueling export production: nutrient return pathways from the deep ocean and their dependence on the Meridional Overturning Circulation. Biogeosciences, 7(11), 3549-3568.

Pujiana, K., Moum, J.N. and Smyth, W.D., 2018. The role of turbulence in redistributing upper-ocean heat, freshwater, and momentum in response to the MJO in the equatorial Indian Ocean. Journal of Physical Oceanography, 48(1), pp.197-220.

Polzin, K. L., & Lvov, Y. V. (2011). Toward regional characterizations of the oceanic internal wavefield. Rev. Geophys., 49.

Polzin, K. L., Naveira Garabato, A. C., Huussen, T. N., Sloyan, B. M., Waterman, S., 2014: Finescale parameterizations of turbulent dissipation. J. Geophys. Res. Oceans, 119, 1383-1419.

Polzin, K. L., Toole, J. M., Schmitt, R. W., 1995: Finescale parameterizations of turbulent dissipation. J. Phys. Oceanogr., 25, 306-328.

Polzin, K. L., Toole, J. M., Ledwell, J. R., & Schmitt, R. W. (1997). Spatial variability of turbulent mixing in the abyssal ocean. Science, 276(5309), 93-96.

Pritchard, H., Ligtenberg, S. R. M., Fricker, H. A., Vaughan, D. G., Van den Broeke, M. R., & Padman, L. (2012). Antarctic ice-sheet loss driven by basal melting of ice shelves. Nature, 484(7395), 502.

Rees, T., Monahan, A., 2014. A General Numerical Method for Analyzing the Linear Stability of Stratified Parallel Shear Flows. Journal of Atmospheric and Oceanic Technology, 31, 2795-2808.

Rosso, I., Hogg, A. M., Kiss, A. E., & Gayen, B. (2015). Topographic influence on submesoscale dynamics in the Southern Ocean. Geophysical Research Letters, 42(4), 1139-1147.

Sallée, J. B., Speer, K., Rintoul, S., & Wijffels, S. (2010). Southern Ocean thermocline ventilation. Journal of Physical Oceanography, 40(3), 509-529.

Schmitt, R. W. (1994). Double diffusion in oceanography. Annual Review of Fluid Mechanics, 26(1), 255-285.

Scott, R. B., & Wang, F. (2005). Direct evidence of an oceanic inverse kinetic energy cascade from satellite altimetry. Journal of Physical Oceanography, 35(9), 1650-1666.

Scotti, A., 2015: Biases in Thorpe-scale estimates of turbulence dissipation. Part II: Energetics arguments and turbulence simulations. J. Phys. Oceanogr., 45, 2522-2543.

Shchepetkin, A. F., & McWilliams, J. C. (2005). The regional oceanic modeling system (ROMS): a split-explicit, free-surface, topography-following-coordinate oceanic model. Ocean modelling, 9(4), 347-404.

Sheen, K. L., Brearley, J. A., Naveira Garabato, A. C., Smeed, D. A., Waterman, S., Ledwell, J. R., Meredith, M. P., St. Laurent, L., Thurnherr, A. M., Toole, J. M., & Watson, A. J., 2013: Rates and mechanisms of turbulent dissipation and mixing in the Southern Ocean: Results from the Diapycnal and Isopycnal Mixing Experiment in the Southern Ocean (DIMES). J. Geophys. Res. Oceans, 118, 2774-2792.

Sheen, K. L., Brearley, J. A., Naveira Garabato, A. C., Smeed, D. A., St. Laurent, L., Meredith, M. P., Thurnherr, A. M., & Waterman, S. N. (2015). Modification of turbulent dissipation rates by a deep Southern Ocean eddy. Geophysical Research Letters, 42(9), 3450-3457.

Schlining, B., Signell, R., & Crosby, A. (2009). nctoolbox. GitHub repository . GitHub. Retrieved from https://github.com/nctoolbox/nctoolbox

Skyllingstad, E.D. and Samelson, R.M., 2020. Instability processes in simulated finite-width ocean fronts. Journal of Physical Oceanography, 50(9), pp.2781-2796.

Simmons, H.L., Powell, B.S., Merrifield, S.T., Zedler, S.E. and Colin, P.L., 2019. Dynamical downscaling. Oceanography, 32(4), pp.84-91.

Smith, K. S., Marshall, J., 2009. Evidence for Enhanced Eddy Mixing at Middepth in the Southern Ocean. Journal of Physical Oceanography, 39, 50-69.

Smith, W. H., & Sandwell, D. T. (1997). Global sea floor topography from satellite altimetry and ship depth soundings. Science, 277. doi:10.1126/science.277.5334.1956

Sinha, N., Tejada-Martínez, A. E., Akan, C., & Grosch, C. E. (2015). Toward a K-profile parameterization of Langmuir turbulence in shallow coastal shelves. Journal of Physical Oceanography, 45(12), 2869-2895.

Smyth, W.D. and J. R. Carpenter, 2019: Instability in Geophysical Flows. Cambridge University Press, 327 pp.

Smyth, W.D, Moum, J. N., Li, L., Thorpe, S. A., 2013. Diurnal Shear Instability, the Descent of the Surface Shear Layer, and the Deep Cycle of Equatorial Turbulence. Journal of Physical Oceanography, 43, 2432-2454.

Smyth, W. D., Moum, J. M., Nash, J. D., 2011. Narrowband Oscillations in the Upper Equatorial Ocean. Part II: Properties of Shear Instabilities. Journal of Physical Oceanography, 41, 412-428.

Stamper, M.A. and Taylor, J.R., 2016. The transition from symmetric to baroclinic instability in the Eady model. Ocean Dynamics, 67(1), pp.65-80.

St. Laurent, L., Ijichi, T., Merrifield, S.T., Shapiro, J. and Simmons, H.L., 2019. Turbulence and vorticity in the wake of Palau. Oceanography, 32(4), pp.102-109.

St. Laurent, L., & Merrifield, S. (2017). Measurements of near-surface turbulence and mixing from autonomous ocean gliders. Oceanography, 30(2), 116-125.

St. Laurent, L., Naveira Garabato, A. C., Ledwell, J. R., Thurnherr, A. M., Toole, J. M., & Watson, A. J. (2012). Turbulence and diapycnal mixing in Drake Passage. Journal of Physical Oceanography, 42(12), 2143-2152.

Stone, P. H. (1966). On non-geostrophic baroclinic stability. Journal of the Atmospheric Sciences, 23(4), 390-400.

Stone, P. H. (1970). On non-geostrophic baroclinic stability: Part II. Journal of Atmospheric Sciences, 27(5), 721-726.

Sullivan, P. P., J. C. McWilliams, and W. K. Melville, 2007: Surface gravity wave effects in the oceanic boundary layer: large-eddy simulation with vortex force and stochastic breakers. J. Fluid Mech., 593, 405-452.

Sutherland, G., Christensen, K.H., Ward, B., 2014: Evaluating Langmuir turbulence parameterizations in the ocean surface boundary layer. J. Geophys. Res. Oceans, 119, 1899-1910.

Sutherland, G., Marié, L., Reverdin, G., Christensen, K.H., Broström, G., Ward, B., 2016: Enhanced turbulence associated with the diurnal jet in the ocean surface boundary layer. J. Phys. Oceanogr., 46, 3051-3067.

Sutherland, G., Ward, B., Christensen, K. H., 2013: Wave-turbulence scaling in the ocean mixed layer. Ocean Sci., 9, 597-608.

Sutyrin, G. G., Ginis, I., & Frolov, S. A. (2001). Equilibration of baroclinic meanders and deep eddies in a Gulf Stream–type jet over a sloping bottom. Journal of physical oceanography, 31(8), 2049-2065.

Tagliabue, A., Sallée, J. B., Bowie, A. R., Lévy, M., Swart, S., & Boyd, P. W. (2014). Surface-water iron supplies in the Southern Ocean sustained by deep winter mixing. Nature Geoscience, 7(4), 314-320.

Talley, L. D. (1996). Antarctic intermediate water in the South Atlantic. In The South Atlantic (pp. 219-238). Springer, Berlin, Heidelberg.

Talley, L. D. (2013). Closure of the global overturning circulation through the Indian, Pacific, and Southern Oceans: Schematics and transports. Oceanography, 26(1), 80-97.

Talley, L. D. (2011). Descriptive physical oceanography: an introduction. Academic press.

Tamsitt, V., Drake, H. F., Morrison, A. K., Talley, L. D., Dufour, C. O., Gray, A. R., Griffies, S. M., Mazloff, M. R., Sarmiento, J. L., Wang, J., & Weijer, W. (2017). Spiraling pathways of global deep waters to the surface of the Southern Ocean. Nature Communications, 8(1), 172.

Terray, E. A., M. A. Donelan, Y. C. Agrawal, W. M. Drennan, K. K. Kahma, A. J. Williams, P.A. Hwan, and S. A. Kitaigorodskii, 1996: Estimates of kinetic energy dissipation under breaking waves. J. Phys. Oceanogr., 26, 792-807.

Thomas, L. N. (2017). On the modifications of near-inertial waves at fronts: Implications for energy transfer across scales. Ocean Dynamics, 67(10), 1335-1350.

Thomas, L.N., Tandon, A. and Mahadevan, A., 2008. Submesoscale processes and dynamics. Ocean modeling in an Eddying Regime, 177, pp.17-38.

Thomas, L.N., Taylor, J.R., D'Asaro, E.A., Lee, C.M., Klymak, J.M. and Shcherbina, A., 2016. Symmetric instability, inertial oscillations, and turbulence at the Gulf Stream front. Journal of Physical Oceanography, 46(1), pp.197-217.

Thomas, L.N., Taylor, J.R., Ferrari, R. and Joyce, T.M., 2013. Symmetric instability in the Gulf Stream. Deep Sea Research Part II: Topical Studies in Oceanography, 91, pp.96-110.

Thompson, A. F. (2008). The atmospheric ocean: Eddies and jets in the Antarctic Circumpolar Current. Philosophical Transactions of the Royal Society of London A: Mathematical, Physical and Engineering Sciences, 366(1885), 4529-4541.

Thomson, J., M. S. Schwendeman, S. F. Zippel, S. Moghimi, J. Gemmrich, and W. E. Rogers, 2016: Wave-Breaking Turbulence in the Ocean Surface Layer. J. Phys. Oceanogr., 46, 1857-1870.

Thorpe, S. A., 1977: Turbulence and mixing in a Scottish loch. Philos. Trans. A Math. Phys. Eng. Sci., 286, 125-181.

Thorpe, S. A., 2004: Langmuir circulation. Annu. Rev. Fluid Mech., 36, 55-79.

Thorpe, S. A, 2005: The Turbulent Ocean. Cambridge University Press, 439 pp.

Thorpe, S. A., 2012: Measuring overturns with gliders. J. Mar. Res., 70, 93-117.

Thyng, K. M., Greene, C. A., Hetland, R. D., Zimmerle, H. M., & DiMarco, S. F. (2016). True colors of oceanography. Oceanography, 29. doi:10.5670/oceanog.2016.66

Todd, R.E., Owens, W.B. and Rudnick, D.L., 2016. Potential vorticity structure in the North Atlantic western boundary current from underwater glider observations. Journal of Physical Oceanography, 46(1), pp.327-348.

Umlauf, L., & Burchard, H. (2003). A generic length-scale equation for geophysical turbulence models. Journal of Marine Research, 61(2), 235-265.

Umlauf, L., H. Burchard, and K. Bolding, 2005: General Ocean Turbulence Model. Source Code Documentation, Baltic Sea Research Institute Warnemünde Technical Report, 346 pp.

Vallis, G. K. (2019). Essentials of Atmospheric and Oceanic Dynamics. Cambridge University Press.

Wang, C, Balmforth, N, 2016. Instability Associated Baroclinic Critical Layers in Rotating Stratified Shear Flow. VIIIth Int. Symp. on Stratified Flows, San Diego, USA, Aug. 29 - Sept. 1, 2016

Warren, B. A., & Wunsch, C. (Eds.). (1981). Evolution of physical oceanography (p. 623). Cambridge: MIT press.

Waterhouse, A. F., and Coauthors, 2014: Global patterns of diapycnal mixing from measurements of the turbulent dissipation rate. J. Phys. Oceanogr., 44, 1854-1872.

Waterman, S., Naveira Garabato, A. C., Polzin, K. L., 2013: Internal waves and turbulence in the Antarctic Circumpolar Current. J. Phys. Oceanogr., 43, 259-282.

Welch, P., 1967: The use of fast Fourier transform for the estimation of power spectra: a method based on time averaging over short, modified periodograms. IEEE Trans. Signal Process., 15, 70-73.

Wenegrat, J. O., Callies, J., & Thomas, L. N. (2018). Submesoscale baroclinic instability in the bottom boundary layer. Journal of Physical Oceanography, 48(11), 2571-2592.

Wenegrat, J.O. and Thomas, L.N., 2020. Centrifugal and symmetric instability during Ekman adjustment of the bottom boundary layer. Journal of Physical Oceanography, 50(6), pp.1793-1812.

Wentz, F. J., J. Scott, R. Hoffman, M. Leidner, R. Atlas, and J. Ardizzone, 2015: Remote Sensing Systems Cross-Calibrated Multi-Platform (CCMP) 6-hourly ocean vector wind analysis product on 0.25 deg grid, Version 2.0. Remote Sensing Systems, Santa Rosa, CA, www.remss.com/measurements/ccmp.

Whalen, C. B., MacKinnon, J. A., Talley, L. D., & Waterhouse, A. F. (2015). Estimating the mean diapycnal mixing using a finescale strain parameterization. Journal of Physical Oceanography, 45(4), 1174-1188.

Whalen, C. B., Talley, L. D. and MacKinnon, J. A., 2012: Spatial and temporal variability of global ocean mixing inferred from Argo profiles. Geophys. Res. Lett., 39.

Wunsch, C. (1998). The work done by the wind on the oceanic general circulation. Journal of Physical Oceanography, 28(11), 2332-2340.

Yankovsky, E., Legg, S. and Hallberg, R., 2021. Parameterization of submesoscale symmetric instability in dense flows along topography. Journal of Advances in Modeling Earth Systems, p.e2020MS002264.

Zemskova, V. E., Passaggia, P. Y., White, B. L., 2020. Transient energy growth in the ageostrophic Eady model. Journal of Fluid Mechanics, 885.

Zippel, S. F., Farrar, J. T., Zappa, C. J., Miller, U., Laurent, L. S., Ijichi, T., Weller, R. A., McRaven, L., Nylund, S. and Le Bel, D., 2021: Moored turbulence measurements using pulse-coherent Doppler sonar. J. Atmos. Ocean. Technol.